Design and Synthesis of Discrete Coordination Driven Self-Assemblies Supported by P-N Scaffolds and their Functional Studies

A Thesis Submitted in Partial Fulfilment of
Requirements for the Degree of

Doctor of Philosophy

by

Rishabh Gupta

Roll no.: 20153367

Department of Chemistry

Indian Institute of Science Education and Research,
Pune, 411008

2022

Dedicated to

“*My Mother” (Mammi)*

(Shakuntala Gupta)

भारतीय विज्ञान शिक्षा एवं अनुसंधान संस्थान, पुणे

INDIAN INSTITUTE OF SCIENCE EDUCATION AND RESEARCH (IISER), PUNE

(An Autonomous Institution, Ministry of Human Resource Development, Govt. of India)
Dr.r.Homi Bhabha Road, Pune 411008.

Prof. R. Boomi Shankar

Department of Chemistry

IISER PUNE

Certificate

I certify that the candidate worked under my direction on the tasks included in the thesis ***"Design and synthesis of discrete coordination driven self-assemblies supported by P-N scaffolds and their functional studies"*** that Mr. Rishabh Gupta submitted. Any portion of the material provided here has never been a part of a thesis that was previously submitted for a degree or diploma from another university or institution.

Prof. R. Boomi Shankar
(Research Supervisor)

Date: 08 Aug 2022
Place: Pune

भारतीय विज्ञान शिक्षा एवं अनुसंधान संस्थान, पुणे

INDIAN INSTITUTE OF SCIENCE EDUCATION AND RESEARCH (IISER), PUNE

(An Autonomous Institution, Ministry of Human Resource Development, Govt. of India)
Dr.r.Homi Bhabha Road, Pune 411008.

Declaration

I hereby declare that this written submission fully expresses my views in my own words and that I have adequately acknowledged and referenced all sources used. Furthermore, I affirm that I have followed all rules governing academic honesty and integrity and that I have not created or faked any idea, data, fact, or source in my work. I am aware that breaking any of the rules mentioned above will result in disciplinary action from the Institute and may also result in penalties from the sources who were improperly cited or whose proper permission was not obtained when necessary.

Date: 08 Aug 2022

Place: Pune

Rishabh Gupta

Roll No. 20153367

Acknowledgment

My seven years, arduous, and brilliant journey for a doctorate is coming to a close. I learned a lot throughout this time and it had a significant impact on my life. During this time, I gained, lost, and achieved a lot. It gave me the chance to interact with a variety of people who supported me no matter how things went for me, making the voyage joyous, enjoyable, and unforgettable.

I want to thank my thesis advisor, Prof. R. Boomi Shankar, for his superb direction, priceless suggestions, and support of my study with ideas and critiques during my whole Ph.D. I am grateful to him for providing me the freedom to live out my beliefs on my own terms and for his encouragement and faith in me. I want to also thank him for his expertise in numerous scientific disciplines, for delivering the project on time, and for helping me to write papers. I am sincerely grateful for his assistance during my difficult times.

I would like express my sincere gratitude to Prof. K. N. Ganesh, the IISER Pune's former director, and present director Prof. Jayant B. Udgaonkar, for their excellent research facilities and lovely research environment. I would like also to express my sincere gratitude to my RAC members Dr. R. Vaithdhyanathan (IISER Pune) and Dr. Rajesh Gonnade (NCL Pune) for their support, encouragement, and helpful ideas. Many thanks go to all the faculties of the IISER Pune specially faculties of the department of chemistry.

I also want to thank to Dr. Rakesh pant and Prakash Panwaria for helping me to understand how to run the job in PARAM BRAHMA cluster. I also want thank to my collaborators Dr. Jeetender Chugh and Dr. Harshad for allowing me to collect data from 600 MHz NMR instrument and also help me to understand the structures through multiple NMR studies. I am also thanful my collaboraters Virender and Dr. Mayurika Lahiri for anticancer activities data. For the dielectric and Piezoelectric measurements, I would like to thank my lab mates Supriya, Vikash, Namo Narayan and Neetu Parjesh.

I would like to thank the technical staff at IISER Pune, namely Mrs. Archana (SCXRD), Mr. Parveen Nasa (SCXRD and PXRD), Mr. Yatish (SEM), Mr. Swati M. Dixit and Suresh Prajapati and Sandip Kanade (MALDI-TOF, CHN analysis ESI-MS and (IR). Sekhar, Dr. V. S. Rao, and others, for their assistance.

I want to thank the Dean Doctoral Studies Office employees, especially Ms. Dipali Dalvi and Mr. Tushar, for their ongoing support. I also acknowledge the administrative staff of IISER Pune, particularly Col. (Ret.) G. Raja.

My sincere gratitude is extended to my lab colleagues Supriya, Neetu, Vikash Meghamala, Cavya, Nilotpal, Rishu, Nanonarayan, Abhradeep, Pratiksha, Hrithik, Rani, Abhay, Akshaya, Saurabh, Anupriya, and Swati for their helpful research discussions and support that made it possible. Especially, I want to thank Supriya for her support during my difficult time. I also wish to thank Vikash for his help in recording the piezoelectric data.

I am grateful that I could spend my free time with friends on the IISER's cricket field and badminton court during my doctoral studies.

There are no words to express my love for my mother, who continually stands and supports me in any condition and encourages me, and my elder sister Mamata gupta, who has faith in me. I am very thankful to my family, who always be my side. I want to express my gratitude and love to my elder brothers, Amit Gupta, Mukesh Gupta, Nilesh Gupta and my sisters.

I am pleased to spend time with my all-time friends Ravindra, Alka, Rathore, Jitender, Rohit, Anupam, Rakesh, Mohit, Satish, Vikash, Praghal, Piyush, Sachinder, Manu, Aman, Samraj, Devanjan, Rahul , Pranjal, Umashankar, Virender, Veeresh.

I would like to express my gratitude to UGC for fellowship and IISER Pune for assisting me. I am appreciative of DST India's for financial assistance. I also appreciate the MTIC for giving me the chance to share my findings. Thank the American Chemical Society (ACS), Royal Society of Chemistry (RSC), Elsevier Science Ltd., John Wiley & Sons, Springer, and others for publishing my research works and granting permission to reproduce under copyright.

Rishabh Gupta

Contents

Contents

Contents

Contents

Abbreviations

Anal.	Analysis
Calcd.	Calculated
ccMOF	Cage Connected Metal-Organic Framework
CCDC	Cambridge Crystallographic Data Centre
DFT	Density Functional Theory
DMF	N, N-Dimethyl Formamide
DMSO	Dimethyl Sulphoxide
DOSY	Diffusion Ordered Spectroscopy
COSY	Homonuclear Correlation Spectroscopy
TOCSY	Total Correlation Spectroscopy
ESI	Electron Spray Ionization
FT-IR	Fourier Transform Infrared Spectroscopy
HRMS	High-Resolution Mass Spectroscopy
Hz	Hertz
KDP	Potassium Dihydrogen Phosphate
KBr	Potassium Bromide
M.P	Melting Point
MALDI-TOF	Matrix-Assisted Laser Desorption/Ionization- Time of Flight
MeOH	Methanol
MeCN	Acetonitrile
mg	Milligram
min	Minutes
L	Microliter
mL	Milliliter
mm	millimeter
mmol	Millimoles
MOF	Metal-Organic Framework
NMR	Nuclear Magnetic Resonance
NLO	Non-Linear Optical
RT	Room Temperature
Ph	Phenyl
P_r	Remnant Polarization
P_s	Saturation Polarization
Py	Pyridyl
PXRD	Power X-ray Diffraction
SCXRD	Single Crystal X-ray Diffraction
T_c	Curie Temperature
TGA	Thermogravimetric Analysis
VT-PXRD	Variable Temperature Powder X-ray Diffraction
SCCs	Supramolecular Coordination complexes

Synopsis

This thesis entitled **"*Design and synthesis of discrete coordination driven self-assemblies supported by P-N scaffolds and their functional studies*"** is focused on the synthesis of noble coordination driven discrete self-assemblies based on the dipodal and tripodal flexible ligands and exploited and their use in the field of material to biology chemistry.

Chapter 1: Introduction

In this chapter, we have provided the history of supramolecular chemistry especially, coordination driven metal-organic complexes. In the past 30 years, significant findings have been made for supramolecular coordination complexes (SCCs). Most of the designed principles like, "directional bonding" and "symmetry approaches" for the formation of SCCs with examples are mentioned in chapter 1. Further, classification of discrete supramolecular coordination complexes such as 2D macrocycles and 3D polyhedras such as, Platonic and Archimedean with examples are also discussed. Mass, NMR and SXRD techniques have known to confirm the formation of supramolecular architectures. These supramolecular architectures find their applications in host-guest chemistry, catalysis, biology, and material chemistry.

Chapter 2: Construction of entropically favored metal-ligand supramolecular trimeric assemblies supported by flexible pyridylaminophosphorous (V) scaffolds.

Synthesis of trimeric supramolecular assemblies by utilizing dipodal ligands and tetratopic metal acceptors has been challenging; however, many reports are available on the tetramer formation. Here, we have reported the preferential formation of trimer $[Pd_3(\mathbf{L^1})_6.(BF_4)_6]$ (**1a**) assembly over tetramer $[Pd_4(\mathbf{L^1})_6.(BF_4)_8]$ (**1b**) assembly by utilising the flexible dipodal ligand [PhPO(NH(3-aminopyridine)$_2$)] (**L^1)** and metal acceptor $[Pd(CH_3CN)_4.2BF_4]$ in DMSO solvent. Trimeric assembly **1a** has been observed as the predominant architecture at room temperature and in DMSO solvent. By changing the external factors such as temperature and solvent, adverse effects have been observed. At higher temperature, **1a** was found to be the only product. However, by Changning the polarity of solvent by addition of MeCN (Acetonitrile) into DMSO, we have observed the more concentration of tetramer species in solution.

In the solvent mixture DMSO: MeCN (1:1), the preferred species was found to be tetramer assembly **1b**, confirmed by ^{31}P NMR and ESI-MS. Interestingly, when we treated a more flexible ligand [MePO(NH(3-aminopyridine)$_2$)] (**L^2)** with the same metal acceptor, only trimeric assembly **2** was observed in the solution, which confirmed by NMR and Mass spectroscopy.

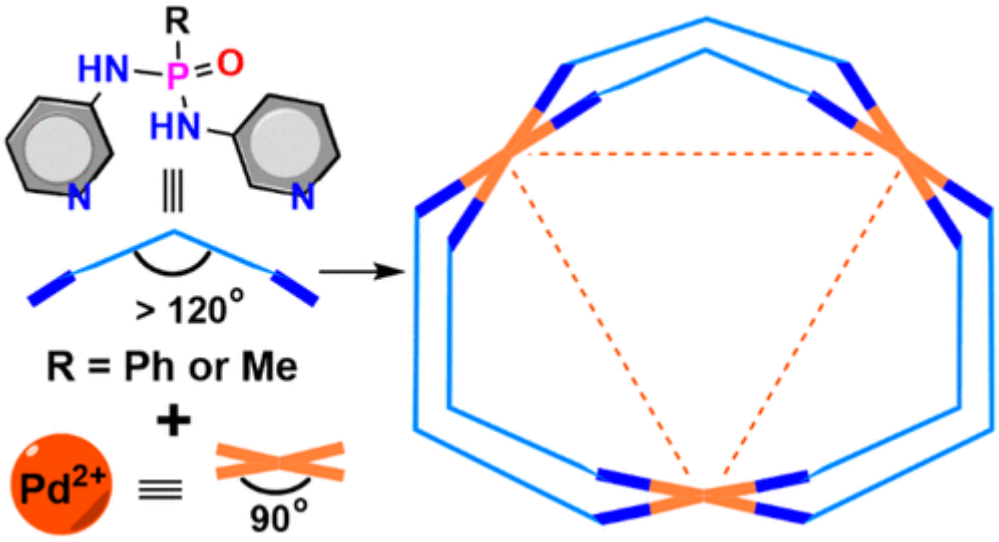

Figure 1 *Schematic presentation of formation of trimeric assemblies by utilizing the flexible dipodal ligands with tetratopic metal acceptor.*

Chapter 3: Piezoelectric polymer composites of M_6L_8 discrete cages and their energy harvesting applications

In this chapter, we have synthesized two self-assembled octahedron cage1 {[Ni_6L_8.12H_2O][12.NO_3]}.xH_2O and cage2 {[Ni_6L_8.12H_2O][12.NO_3]}.xH_2O by self-assembly reaction of tripodal ligand (L) [PO(NH^{3}Py)$_3$] with Ni(NO_3) and Zn(NO_3), respectively. Both the cages were crystalized in the non-centrosymmetric polar *I4* space group, which motivated us to explore their dielectric and piezoelectric properties. Maximum peak-to-peak output voltages of 8.2 and 11.3 V were recorded for the best performing composite devices of 10wt%_1_PDMS and 10wt%_2_PDMS, respectively. Using a 4 MΩ resistor, the maximum peak-to-peak currents were calculated to be 2.06 μA and 2.84 μA for the corresponding 10wt % composite devices of 1 and 2.

The calculated current densities for both 10wt%_1_PDMS and 10wt%_2_PDMS composite devices are 0.41 and 0.57 $\mu Acm^{-2,}$ and the respective power densities are 3.39 and 6.45 μWcm^{-2}. Further, these composite films have been utilized to charge a 10 µF capacitor by channelling the generated output voltages through a four diode bridge rectifier circuit.

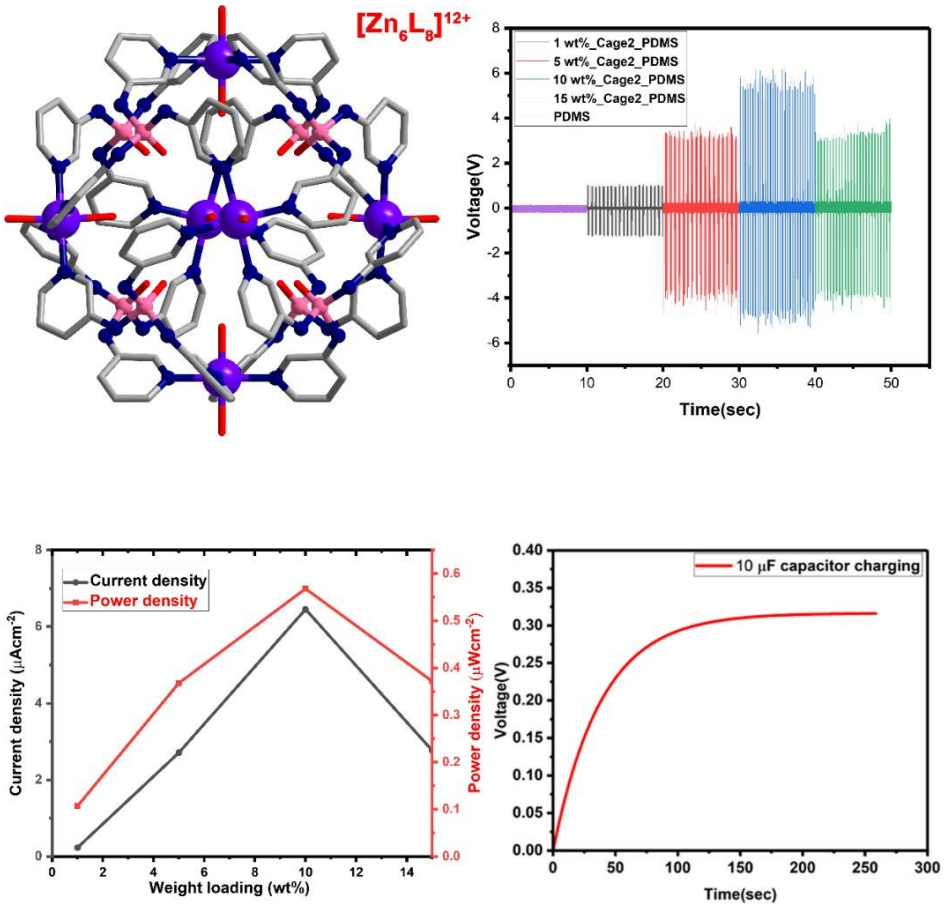

Figure 2 *View of the discrete octahedron cage* $[Zn_6L_8]^{12}$ *, Peak-to-peak output voltage* (V_{OC}) *of 2 of different weight percentages in PDMS, calculated power density and current density of 10wt%_2 and 10 µF capacitor charging by channelling the generated output voltages through a bridge rectifier diode circuit.*

Chapter 4

Synthesis of Pd_6L_8 discrete cages and their role in anticancer activities

Herein, we present the synthesis and anticancer studies of three octahedral $Pd_6L_8]^{+12}$ type metallocages 1, 2 and 3 starting from Pd(II) ions and the amide (or phosphoramide) derived ligands of tris(3-pyridinyl) phosphoramide (L1), tris (3-pyridinyl) benzene 1,3,5 tricarboxamide (L2), and tris (6-aminoquinonyl) benzene 1,3,5 tricarboxamide (L3) ligands, respectively. Further, cytotoxicity experiments against human cancer cell lines have been performed for the MOCs 1, 2 and 3 and their efficacies were compared with their

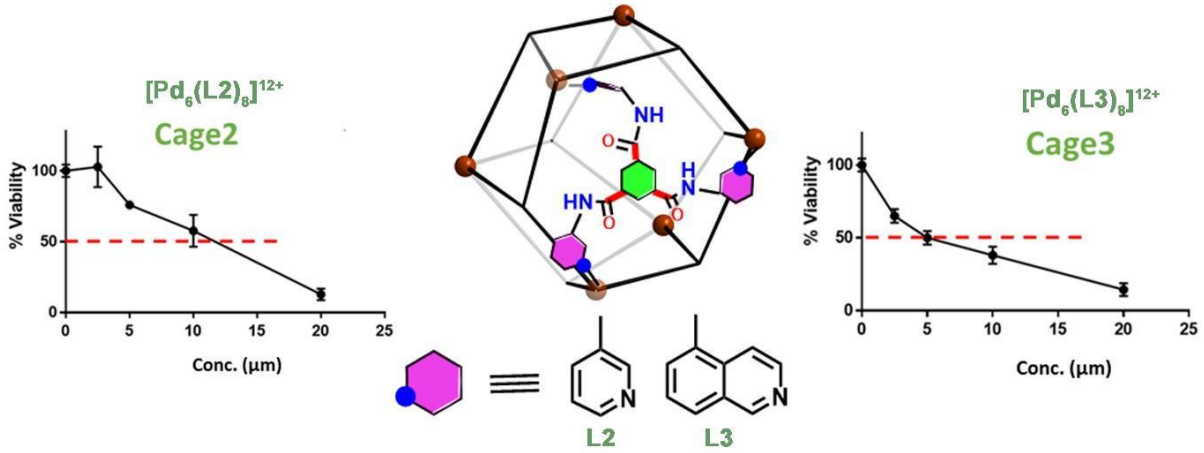

Figure 4 *Schematic presentation of octahedron cage2 $[Pd_6(L2)_8]^{12+}$ and cage3 $[Pd_6(L3)_8]^{12+}$ and their respective anticancer activities plots.*

corresponding ligand motifs. Also, the activities of these MOCs and ligands were tested against the normal cell lines, where excellent selectivity was observed for 3. The IC_{50} values of >20, 11.5 and 5 µm were observed for the compounds 1, 2 and 3, respectively. The IC_{50} value for compound 3 is lowest among other compounds which is 5 µM for breast cancer cell and the high value of IC_{50} for compound 3 towards normal kidney HEK29 cell line. The selectivity index (SI) is defined as the ratio of IC_{50} value of normal cells and cancer cells. The SI ratio for 3 was calculated to be 4. This result indicates that the large self-assembled 3 is ableto kill cancer cells more effectively and selectively than the well-known cisplatin. The Western blotting experiment suggested that 3 is responsible for damaging double-strand DNA thatcauses the possible cell apoptosis.

Rights and Permissions

Chapter 2

Chapter 5 (Appendix)

List of publications

(1) Construction of Entropically Favored Supramolecular Metal-Ligand Trimeric Assemblies Supported by Flexible Pyridylaminophosphorus(V) Scaffolds., **Gupta Rishabh,** Paithankar Harshad, Chugh Jeetender, Boomishankar,Ramamoorthy., *Inorg. Chem.*, **2021**, *60*, 10468-10477.

(2) A Flexible Energy Harvestor from an Organic Ferroelectric Ammonium Salt. **Rishabh Gupta**, Supriya Sahoo, Swati Deswal, Prem Kumar Kothavade, Prashant Dixit, Jan K. Zareba, Kadhiravan Shanmuganathan and Ramamoorthy Boomishankar., *Chem, Asian, J.*, **2021**, *16*, 4122-4129.

CHAPTER 1

Introduction

Chapter 1 Introduction

Background of the metal-ligand coordination complexes

Ever since the discovery of metal complexes by Alfred Werner in 1893, coordination compounds have become an integral part of chemistry and essential to organometallic, bioinorganic and materials chemistry. Werner is the first person to describe the oxidation state, coordination number, and geometry of the coordination complexes, which later helped the researchers to design and synthesize metal complexes using various ligands.[1] Tremendous progress has been made in the past century for coordination complexes relevant to their structures, synthesis is and reactivity, spanning from simple complexes of metal and ligand to metallopolymers to catalysts of organo-metal complexes and bioinorganic systems.

In the past 30 years, significant findings have been made for supramolecular coordination complexes (SCCs) and metal-organic frameworks (MOFs). The SCCs are the discrete and ordered self-assembled structures formed by the covalent coordination bonds between the metal ions and ligands with multiple binding sites. On the other hand, the MOFs are the infinite array of metal centers or metal clusters and multi-topic ligands supported by metal-ligand dative bonds. The present thesis deals with the syntheses of discrete supramolecular coordination complexes such as macrocycles, cages and cavitands and their utility for specific materials and biological targets. Therefore, the introduction provides an account of the existing design strategies to form such assemblies and their utility modes towards the said applications.

1.1 Discrete metal-ligand coordination-driven self-assemblies

Pederson and co-workers discovered discrete supramolecular polygons and polyhedra in the 1960s and demonstrated their utility in molecular recognition via non-covalent interaction.[2] Crown ethers and related molecules were of subsequent interest due to the ease of their synthetic simplicity and ability to bind and encapsulate simple guest ions. In parallel, Lehn and Cram showed interest in the host-guest chemistry of cryptands and spherands and employed them as host molecules to encapsulate various small guest molecules.[3-4] In these systems driving force for encapsulation of guest molecules was non-covalent interactions, namely, π-π interactions, van der Waals forces, hydrogen bonding, and other weak interactions.

The supramolecular coordination complexes (SCCs) are discrete architectures constructed from the mixing of metal ions with organic ligands, which can be neutral or anionic, generating stable thermodynamic products in a coordination-driven self-assembly process.[5-18] As a result, the complexes formed from this process are usually called supramolecular coordination complexes (SCCs). In 1983, Verkade and co-workers reported the first example of discrete self-assembly as a 20-membered macrocycle consisting of a bridging diphosphine ligand $P(OCH_2)_3P$ and metal-carbonyl fragments of transition metals such as Cr, Mo and W (figure 1.a(a)).[19]

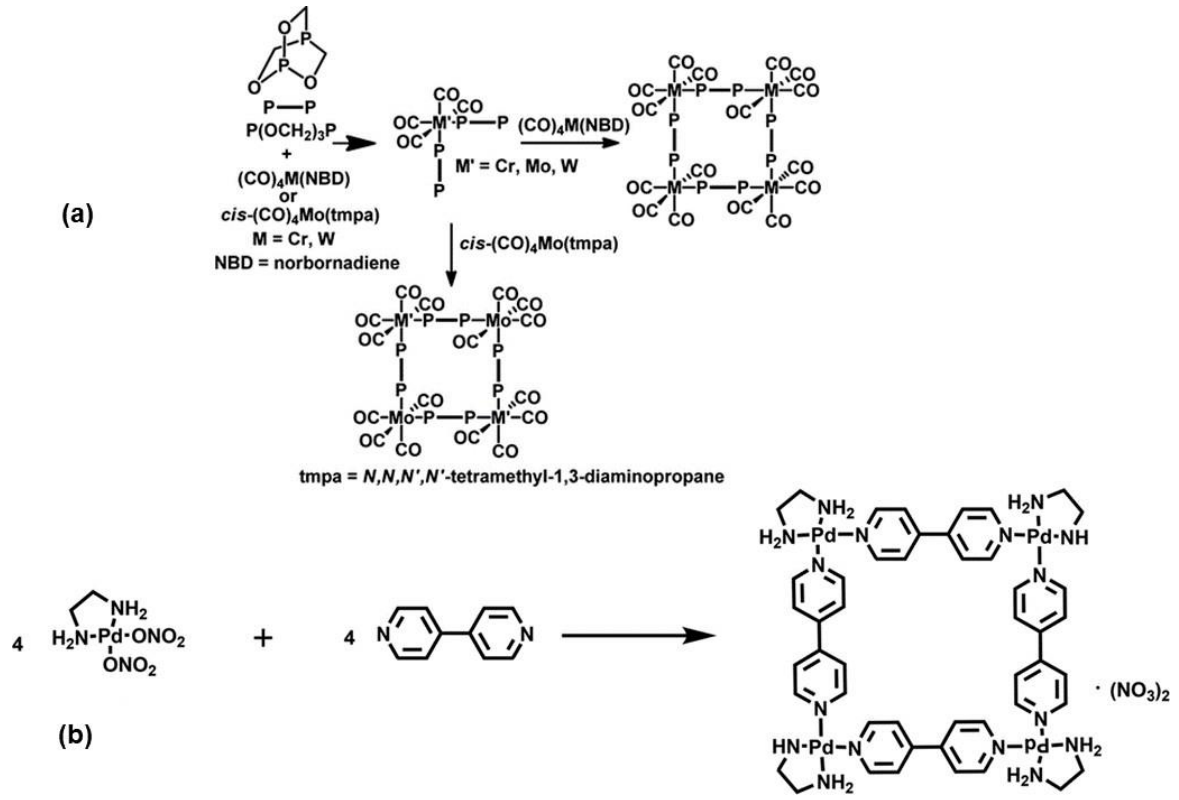

Figure 1.1 *(a) Early examples of supramolecular coordination complexes. (b) First example for the rational design and synthesis of a Pd_4L_4 macrocycle (Copyright permission© 2011, American Chemical Society, Chem. Rev., 2011, 38, 6810*

Later, in the early 1990s, the synthesis of supramolecular square macrocycles were realized by using linear dipodal ligands, for example, 4,4-bipyridine and cis-protected Pd(II) units (with ethylenediamine spectators) containing two free coordination sites (Figure 1.1(b))[20]. Fujita and co-workers have reported numerous examples of supramolecular macrocycles including

molecular squares and triangles starting from both cis blocked Pd (II) ditopic centers as well as unprotected Pd(II) tetratopic units.[20-21] Stang and co-workers' were studying the rational design and synthesis approaches toward discrete metal-ligand supramolecules and developed several macrocycles using transition metals, particularly with Pt (II) as acceptor units. Apart from these two-dimensional (2D) macrocycles, several methods have been established by Fujita, Stang, Raymond, Mirkin and Cotton for the rational design of three-dimensional (3D) metal-organic polyhedra, polygons, and prisms, in the past three decades.[22-29] These design approaches not only gave access to higher 2D-polygons beyond triangles, squares and rectangles but also to 3D architectures such as tetrahedra, cubes, octahedra, cuboctahedra anddodecahedra as well by employing either cis-blocked ditopic or ligand-free tetrtopic metal acceptors. Most of these 3D assemblies or architectures are popularly termed as metal-organicpolyhedra (MOPs).[30-45] These MOPs are special types of 3D structures and are found to exhibitPlatonic, Archimedean, Faceted and Stellated polyhedral structures. Apart from their structuralnovelty, these assemblies can serve as models for the construction of several discrete inorganic,organic, and metal-organic nano-scale structures.[46-62]

1.2 Design principles or approaches of discrete assemblies

The geometry of the metal ions in a coordination-driven supramolecule is octahedron or square planar with vacant anti-bonding orbitals that make them as acceptor units that makes rational bonds with donor ligands and for the desired self-assembled structures. The shape and size of a supramolecular structure are determined by the information implied in the building blocks (ligands and metal acceptors) that form the self-assembly. The important thing of the metal-ligand coordination bond is that, it is highly directional in nature, which help to design the desired product. The typical bond energies of metal-ligand coordination bonds are in the range of 15-50 kcal/mol. This energy range is in between those of covalent bonds (ca. 60-120 kcal/mol) and weak interactions (ca. 0.5-10 kcal/mol). The energy of a coordination bond helps in the introduction of both rigidity and reversibility for the self-assembled products. Moreover, reversibility between building units assisted by the coordination kinetics allows self-correcting of the assembled products. This implies that unwanted or incorrectly coordinated building units can undergo dissociation to facilitate the re-association leading to a thermodynamically more stable single product over its precursor components and other intermediates with kinetic stability. The last two decades have witnessed several new

synthesized supramolecules and numerous strategies to obtain their intricate frameworks. In recent years, various strategies have been developed for the synthesis of coordination driven self-assemblies. These are majorly categorized as directional bonding, symmetry interaction and molecular panelling approaches. In addition, few more protocols such as weak link and dimetallic building block approaches have also been adopted during the design of the discrete self-assemblies.[63-67]. It is to be noted that for all of these design strategies, the metal-ligand coordination bond remains as the key element in controlling their structures. A brief summary of each of these approaches are given in the following discussions.

1.2.1 Directional bonding approach

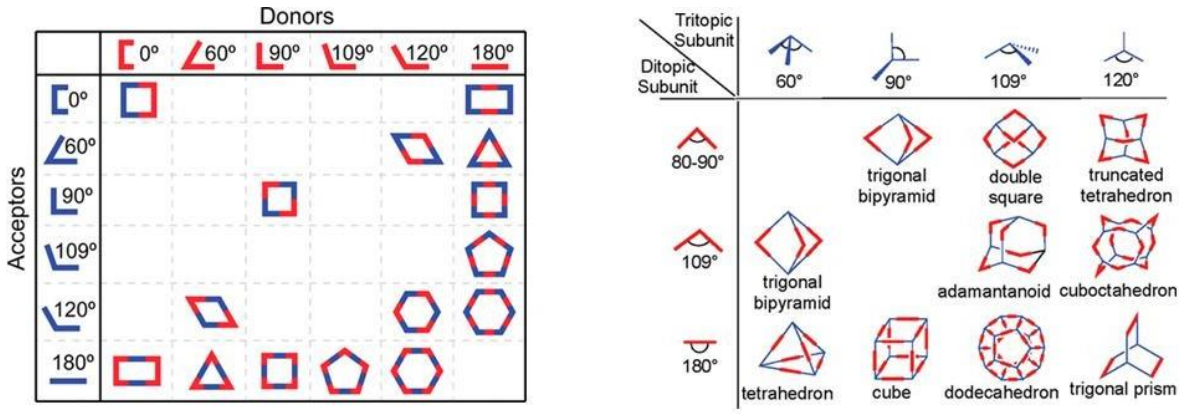

Figure 1.2 Utilization of directional bonding approach for the formation of many types of architectures in 2D macrocycles (left) and 3D polyhedra (right) by combining donor and acceptor units in particular angles to each other. (Copyright permission© 2011, American Chemical Society, Chem. Rev., 2011, 38, 6810)

This approach or method has been widely used by supramolecular researchers to obtain a variety of 2D and 3D supramolecular assemblies, which are known to form high-yield products (Figure 1.2).[63] Since the rational design of supramolecular squares in the early 1990s by Fujita and Stang groups, wide range of coordination driven metallo-macrocycles and -cages have been discovered using this design approach.[20,68-69] Two elemental structural necessities are there to use this approach: (i) both starting building units must have proper bite angles and structurally not too flexible; (ii) the complementary units must be added in a solvent with proper stoichiometric ratio (see again Figure 1.1) . The organic linker ligands usually consist of two or more donor sites in the bite angles in the range of 0 to 180° (Figure 1.2). The metal acceptor units which generally have free coordination sites with fixed angles between them.

The shape of the targeted assembly depends upon the symmetry and binding sites within each building units. For instance, a supramolecular rectangle can be designed by the combination of two acceptor units placed at an angle of 0° and two donor units having 180° bite angle and vice versa. In the same way, the molecular square can be prepared by using at least three approaches by combining (i) two acceptors and two donors, each having 0° bite angles (ii) two acceptors and two donors, each having 90° bite angles and (iii) four ditopic 90° angular units and four 180° linear units. The 3D polyhedral structures can be formed by utilizing angular and linear sub units where one of starting units have more than two coordination sites (Figure 1.2). For instance, a tetrahedral cage-molecule can be formed by taking four tridentate sub unitsseparated at an angle of 60°, with six ditopic units having a bite angle of 180 °. A cubic structurecan be formed by combining eight tripodal donor ligands or metal acceptors having 90 ° bite angle with twelve dipodal units having 180 ° bite angle. Though no changes are expected in the bite angle of the starting units in the obtained assemblies, in most instances it has been observed that the angles distort up to several degrees due to the complexity of the other organicco-ligands present in the assembly and other strain effects in the designed ligands.

1.2.2 Symmetry interaction approach

This rational synthetic approach has been used for the construction of highly symmetric coordination driven architectures. The symmetry interaction approach is based on the geometric connection between the chelating donor ligands and the metal ions used. This approach is basically, applied on the branched multi-site chelating ligands with rigid backbones in combination with naked metal ions of main group or transition elements. Symmetry and rigidity of the building components that are fixed on the binding sites is important to get a particular geometry of the self-assembly and to avoid polymerization. Though this method is similar to the directional bonding approach, it gives additional thermodynamic control by providing error-checking and self-correction via kinetic reversibility. Raymond and co-workers have employed this approach extensively to define the basics of design principles regarding the geometric relationship between building components using symmetry considerations.[64] The plane of symmetry on the chelating ligand is considered orthogonal to the major symmetry axis of the self-assembled structure. Thus, the symmetry of the chelate planes and geometry at the metal acceptor sites decides the geometry of the highly symmetrical self-assembled coordination structure. For instance, to get a triple helicate M_2L_3

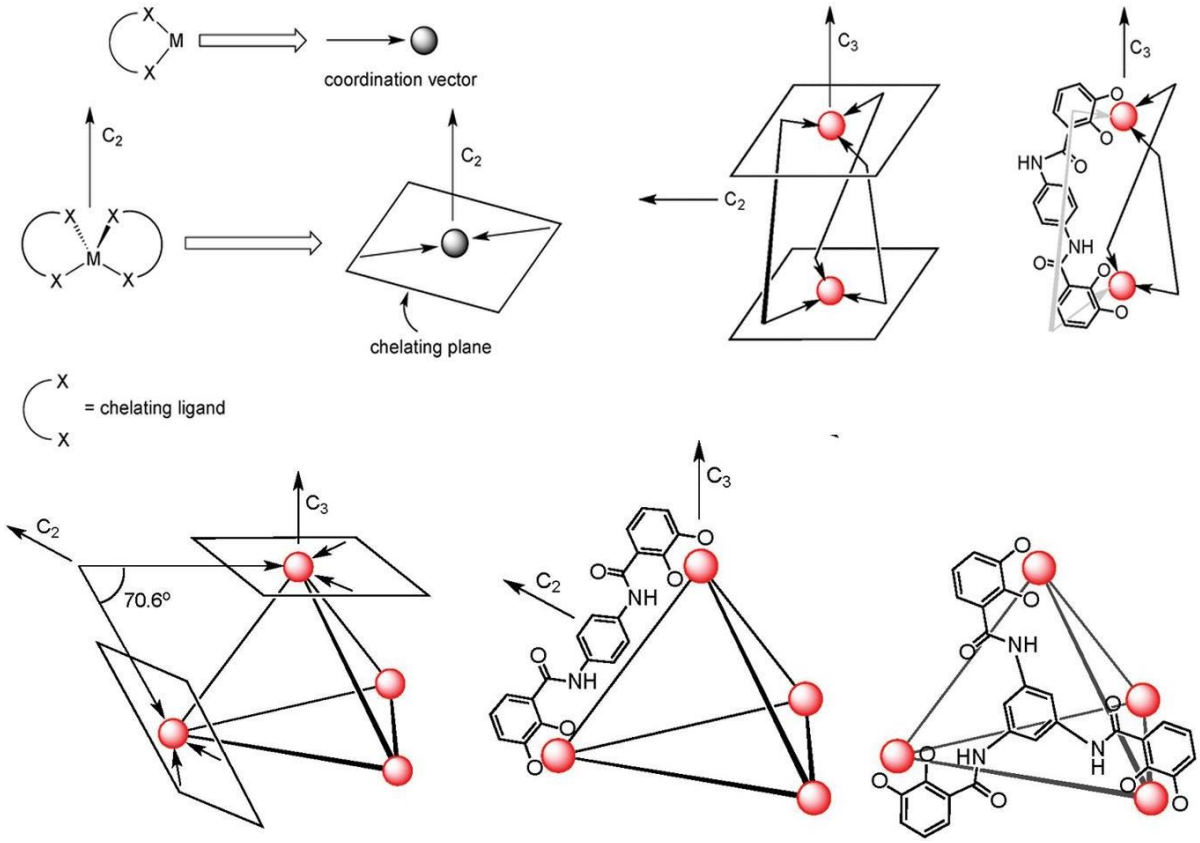

Figure 1.3 Symmetry interaction approach for the formation of an M_2L_3, M_4L_6 and M_4L_4.) (Copyright permission© 2011, American Chemical Society, Chem. Rev., 2011, 38, 6810)

assembly having an idealized point group symmetry of D_{3h}, the principle C_3 axis of the assembly must lie perpendicular to the C_2 axes that runs parallel to the chelating plane of the ligands (Figure 1.3). Since C_3 axis passes through two metal centers, the two chelating planes must be parallel to C_2 axes to achieve the M_2L_3. An approach similar to this can be adopted for the construction of M_4L_6-type tetrahedrons. In such tetrahedron, the four vertices are occupied

by the metal atoms having a C_3 symmetry and six C_2 symmetric ligands lie on its edges. Another way to generate the geometric structure of tetrahedron is by the combination of four

metal atoms which lie at the vertices of the cage with four tripodal chelating ligands located on the four tetrahedral faces. In this way, the C_3 axis passes through the metal and ligand centers.

1.2.3 Paneling approach

Synopsis

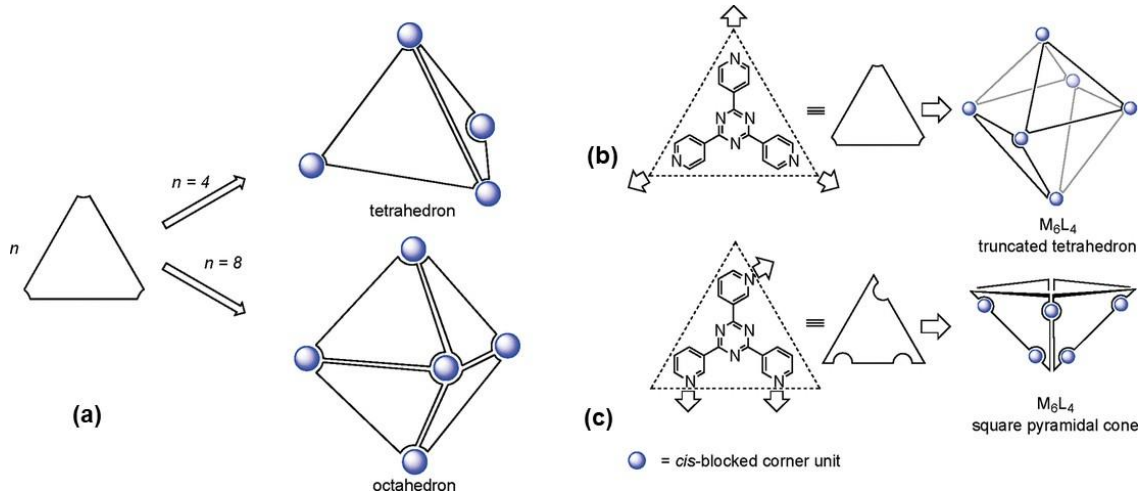

Figure 1.4 (a) Illustration for formation of a tetrahedron and an octahedron architectures exploitation triangular-panels. (b) Using paneling approach, formation of an M_6L_4 truncated tetrahedron and (c) an M_6L_4 square-pyramidal cone by assembling triangular panels. (Copyright permission© 2011, American Chemical Society, Chem. Rev., 2011, 38, 6810)

This rational synthetic approach, established by Fujita and co-workers, has been used for the construction of highly symmetric 2D and 3D coordination architectures, especially those resembling platonic architectures, using metal-ligand coordination bonds. In this protocol, planar panel-like organic ligands with more than two binding sites can be paneled together using suitable structural corner units. These molecular panels, like triangular or square motifs acts as facial ligands in the resulted platonic architectures and the metal atoms work as corner units. For instance, a tetrahedral structure can be planned by combining together four triangular panels, while an octahedron can also be prepared by employing eight triangular panels (Figure 1.4). Similarly, the formation of cubes and prisms can be achieved by taking the squares which have four binding sites.

Keeping the minimum number of free coordination sites helps in the efficient formation of discrete cages instead of polymeric products. For instance, combining the triangular molecular panels having three coordination sites with the cis-blocked Pd(II) corner units, which have only two free coordination sites, result in various supramolecular architectures ranging from M_6L_4truncated tetrahedral cage, the M_6L_4 square pyramidal cone, M_8L_4 tetrahedra and cones. Other supramolecular architectures can also be designed using this method by applying square and rectangular panels which have four coordination sites in combination with cis blocked Pd

(II) or Pt (II) salts that results in the formation of cubes, parallelopipeds, and prisms. Here, we are presenting one of the example for formation of an M_6L_4 truncated tetrahedron by using four tridentate molecular triangular panels at the vertices and six cis blocked Pd(II) corner units. By slightly changing the bite angle of the triangular panel can give rise to the formation of different M_6L_4 assembly as a bowl-like square pyramidal cone.[68] Similarly, square panel ligands having four coordination sites at D_4h symmetry can lead to different topologies in combination with cis blocked corners by varying the positions of the donor atoms on the panel (Figure 1.4). It has been observed from the literature that the use of this strategy lead to discrete self-assemblies which usually have more intrinsic cavity. The intrinsic pores in these cages were utilized for molecular recognition, guest encapsulation and release and catalysis in the confined space.

1.2.4 Weak link and dimetallic building block approaches

These two weak-link and dimetallic building block approaches are slightly different from other approaches that are mentioned above. The weak link approach, first established by Mirkin and co-workers, also produced so many 2D and 3D supramolecular assemblies.[66] It involves the use of hemilabile ligands, which are flexible in nature and coordinate in a bi-dentate chelating mode to the metal center. These ligands offer some sort of coordination with the metal center in such a way that one of the chelating metal-ligand bonds is relatively weaker than the other one. In this way, kinetically controlled products with a more condensed structure are formed at the initial stages. Further treatment of these kinetic-controlled products with small non-chelating ancillary ligands or simple mono-atomic ions having higher affinity towards the metal centres leads the formation of thermodynamic stable and open-structured product (figure1.5).

The dimetallic building block approach was pioneered by Cotton's group.[67] In this approach dimetallic metal centers are used as corner units in which some of the coordination sites are blocked by non-labile chelating ligands and other sites are occupied with labile ligands such as chloride ions and solvent molecules. Treatment of these dimetallic precursors with suitable linker ligands leads to the formation of the desired supramolecular assemblies.

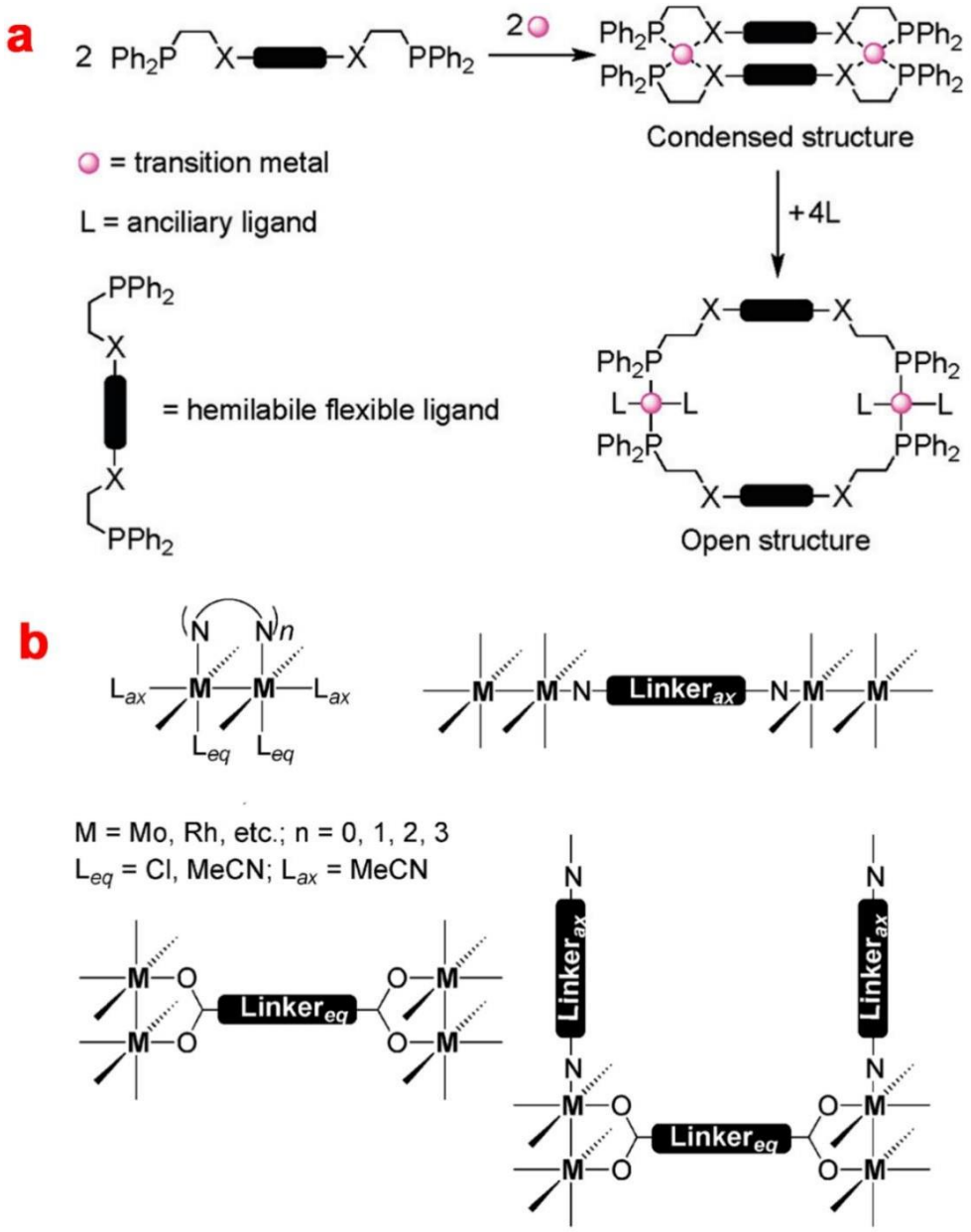

Figure 1.5 (a) Weak link and (b) dimetallic building block approaches exhibit the formation of metal-ligand coordination driven architectures. (Copyright permission© 2011, American Chemical Society, Chem. Rev., 2011, 38, 6810)

Types of discrete self-assemblies

The coordination-driven self-assemblies are majorly classified into two categories; two-dimensional (2D) architecture of macrocycles and polygons and three-dimensional (3D)

architectures such as cages and polyhedra. Polyhedral 3D architectures are further known to resemble Platonic and Archimedean solids. A brief summary of the design principles involved in the construction of some of the critical structures from each of these classes is provided below in this chapter.

1.3 2D discrete self-assemblies

Inspired by the first report on the formation of supramolecular squares by Fujita and his coworkers[20] and Stang and co-workers [70] in 1990, a wide range of 2D metallomacrocycles consisting of various geometries and sizes ranging from rhomboids, squares, rectangles, hexagons, and triangles have been reported in the literature. Most of these attractive molecular 2D assemblies were synthesized by using directional bonding, symmetry interactions and paneling approaches.

1.3.1 Supramolecular rhomboids

Supramolecular dinuclear rhomboids represent the simplest 2D metallacycles known among all the macrocycles. These type of low-nuclearity self-assemblies are typically synthesized by the use of flexible dipodal bridging ligands and cis-blocked acceptor corner units.[71-74] Figure 1.6a shows a suitable example of a dinuclear rhomboid, which has been formed by the reaction of a cis blocked Pd (II) unit, with two vacant acceptor sites at 90 ° bite angles, with a pyridine based dipodal ligand, which has a wide bite angle of 120 °, in methanol-water medium.

1.3.2 Supramolecular trimers/triangles

Supramolecular triangle can be formed mainly in three different ways by using directional bonding approach, (i) by the combination of linear metal acceptors having bite angle 180° with donor ligands having 60°, (ii) by using metal acceptors having bite angle 60° with donor ligands having 180° and finally (iii) by employing metal acceptor units having bite angle range from 80-90° with flexible donor units which have angle 120-180 (Figure 1.6b).[75]

Here, we are presenting one example of a supramolecular triangle using one of the approaches mentioned above. (Figure 1.6b). A mixed Pd(II)-Pt(II) containing cationic supramolecular triangle has been reported by Lippet and coworkers by the treatment of a 60° dipodal metallo-ligand, built from a cis blocked Pd (II) unit (with a cis-coordinated ethylenediamine motif) attached to a pendant bipyrazine ligand (from one side) and trans Pt (II) diamine motif having 180 bite angles in 1: 1 ratio.[76]

Some more molecular triangles have been reported by several research groups by treating cis-blocked Pd (II) or Pt (II) units with flexible pyridine-based ligands having a bridging amide backbone.[77-78] NMR, ESI-MS and Single crystal X-ray diffraction techniques have been used to confirm the formation of the structures.[79]

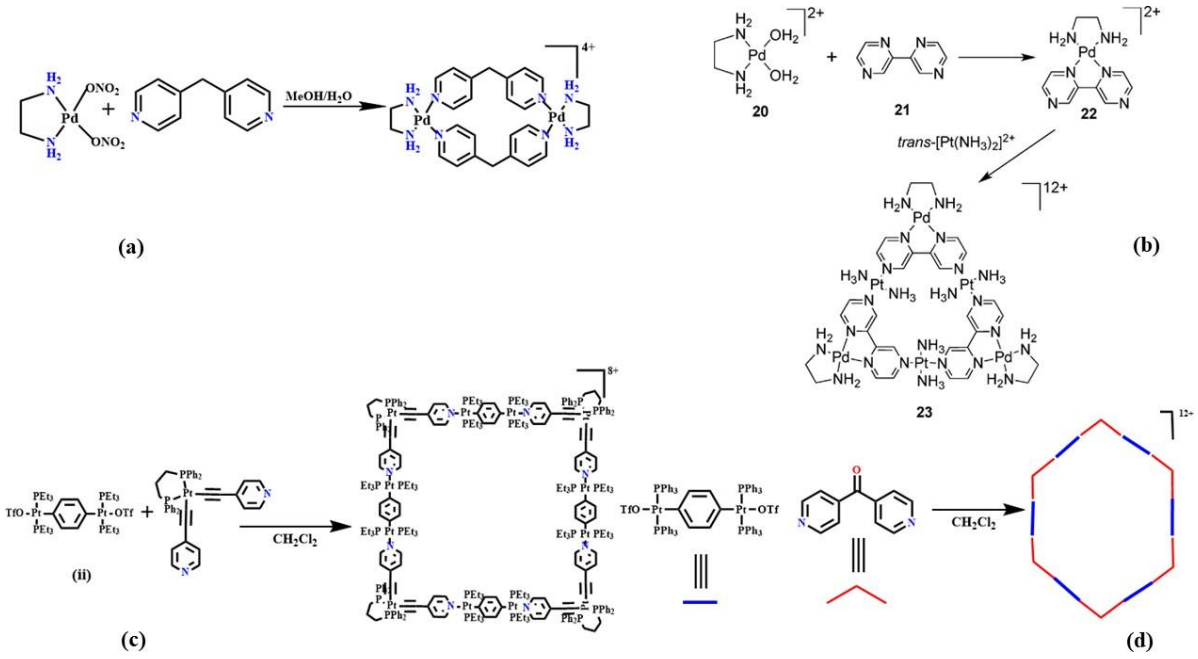

Figure 1.6 (a) Supramolecular rhomboids formed by utilizing dipodal angular ligands and cis-blocked metal acceptor units. (b) A Molecular triangle is formed by the combination of linear metal acceptor units and angular metallo-ligands. (c) Formation of the supramolecular square from a metallo-ligand having a 90 ° bite angle and linear metal acceptor units (d) Formation of a molecular hexagon by using a dipodal ligand with a bite angle range of 120° and linear metal-acceptor units.

1.3.3 Supramolecular tetramers/squares

Supramolecular metal-ligand based squares are one of the most prevalent structures among all polygons. The first report on the design and synthesis of a molecular square is by Fujita and co-workers.[20] Supramolecular squares can be easily designed by using the direction bonding approach by appropriately choosing metallo-corner units with linear ligands. There are two main methods were adopted to synthesize the molecular squares. In the first method, dipodal ligands having bite angle of 180° can be combined with 90° metal-containing acceptor corner units having two free coordination sites. In a complementary way, metal acceptors having 180° bite angle can be combined with dipodal 90° donor ligands to obtain the molecular tetramer.

The simplest of a molecular square was synthesized by Fujita and co-workers in a reaction involving 90 ° cis-blocked Pd (II) acceptors with rigid linear (180°) 4,4 -bipyridine linker ligands at room temperature in water medium.[20] Stang and coworkers have synthesized such molecular square by treating linear Pt(II) metal acceptors combined with dipodal 90° metalloligands at higher temperatures (Figure 1.6 c). Formation of Pt(II) based macrocycles required higher temperatures due to the kinetic inertness of the Pt-N bonds over the Pd-N bonds. Therefore, Pt (II)-based supramolecular assemblies are stabler than Pd (II) based assemblies.[80-81]

1.3.4 Supramolecular hexagons

Other than trimer and tetramers, supramolecular hexagons or other higher order 2D macrocycles have been obtained by employing directional bonding approach. Stang and co-workers have designed and synthesized such types of polygons. For example, to get the macrocyclic hexagon one of the building units should have 180 ° bite angle and the second unit must have 120° bite angle (figure 1.6d). [85]

1.3.5 Triangle-Square or Trimer-Tetramer Equilibrium in Solution

Though all these approaches can lead to definite supramolecular macrocycles, there are several instances where formation of one supramolecule is preferred over the other or their solutions can consist of more than one product. Several factors such as chemical exchange between the corresponding building blocks and certain intermediates, may decide the final composition of the self-assembled products. More often, these steps permit the system to self-correct, yielding the products controlled by the thermodynamic stability where one of the products has sufficiently less energy than the other possible products. However, there have been instances when two or more products could exist in dynamic equilibrium in solution because of the lack of a clear thermodynamic inclination for any one of the species in solution. The triangle-square equilibrium in solution is a well-studied phenomenon for supramolecular self-assembled systems (figure 1.7).[82] Importantly, the concentration of triangles and molecular squares in solution has been understood well from the point of view of thermodynamics regulated by the subtle changes in the entropy and enthalpy. The supramolecular squares are favored by the enthalpy of the system because of their lower conformational strain over triangles. In contrast, entropic factors support the formation of triangles as they are built from a smaller number of components over squares. The external factors which affect the equilibrium between both

trimer and tetramer are temperature, concentration, solvents, and flexibility of the starting building units.[82, 83-84.] Nevertheless, the number of ligand assemblies that support trimeric assemblies over tetrameric assemblies is far less in the literature.

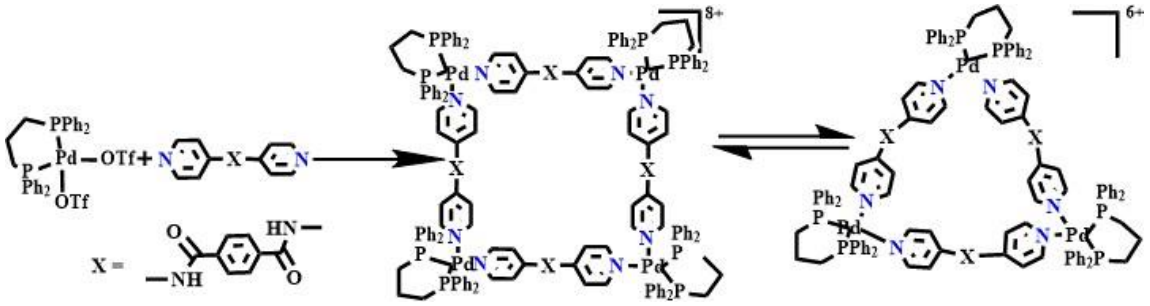

Figure 1.7 Schematic showing the square-triangle equilibrium in a macrocyclic Pd(II) self-assembly reaction.

1.4 3D supramolecular cages

It is well-known in nature that viral capsids exhibit 3D polyhedral structures of icosahedron and dodecahedron, which inspires the synthesis of such assemblies using metal-ligand bonds. However, some of the synthetically known 3D structures are the results of serendipity and does not conform to any rational design approach.[30-85] Research in the past three decades has paved the way for various design principles for the self-assembly of highly symmetrical coordination cages. This leads to numerous classes of 3D architectures in both platonic and Archimedean topologies. The following sections in this chapter will elaborate on the design of some representative examples for these structures.

1.4.1 Examples of platonic architectures

A simpler and widely known platonic solid is a tetrahedron. It can be formed mainly in two ways. The M_4L_6 type tetrahedral structures can be formed by combination of six edge-directed ligands with four metal acceptors vertices. The M_4L_4 type tetrahedral structure can be formed by a combination of four face-directed ligands with four metal ions at the vertices. The first example of the formation of a 3D metal-organic coordination driven tetrahedron architecture is the assembly of Mg_4L_6 cage supported by an in-situ generated bis di-ketonate ligand formed in a serendipitous reaction.[30] Subsequently, several tetrahedral assemblies were designed and synthesized. Raymond and co-workers have synthesized several tetrahedral cages using symmetry interactions approach. They employed tri- and tetravalent-metal ions such as Ga(III),

Al(III), In(III), Fe(III), Ti(IV), and Sn(IV) as corner acceptor units and bis-chelating dianionic ligands as the edges leading to the formation of anionic M_4L_6 type cages (Figure 1.12 (left side)).[86-88] Organic substituted ammonium cations act as the charge-balancing counter cations as well as the guest-molecules at the intrinsic cavities of these cages.

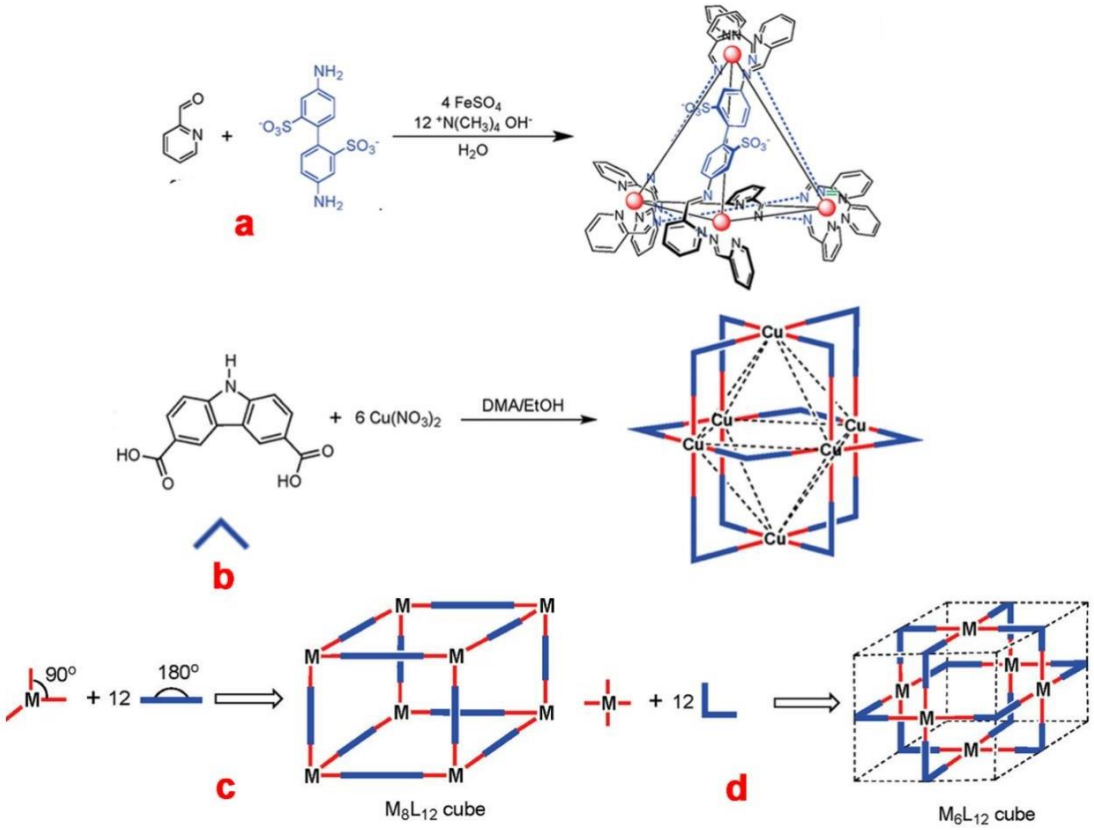

Figure 1.8 (a) Formation of a tetrahedral Fe_4L_6 cage via the condensation of 2-formylpyridine and 4,4′-diaminobiphenyl-2,2′-disulfonic acid subcomponents with Fe (II) in water. (b) Formation of 3D metal-organic coordination driven octahedron architecture derived from a 90° dicarboxylate ligand and a paddle wheel $Cu_2(COO)_4$ cluster. (Copyright permission© 2011, American Chemical Society, Chem. Rev., 2011, 38, 6810)

Cages with intrinsic chirality have been found to be formed in several instances starting from achiral building units. Nitschke and co-workers constructed examples of cationic cages built from imine-based chelating ligands, which form coordinative bonds with the transition metal centres yielding tetrahedral M_4L_6 type assemblies. For example, the tetrahedral assembly Fe_4L_6, was attained in a sub-component self-assembly process via the combination of Fe (II) ions, 2-formylpyridine and 4,4′-diaminobiphenyl-2,2′-disulfonic acid in water (Figure 1.8 a).[89] An ammonium salt has been used in this reaction for the charge balance in the framework.

Other groups like Fujita and co-workers and Lindoy and co-workers have also synthesized examples of cationic and neutral tetrahedral cages.[90-91]

Many research groups have widely explored the formation of supramolecular octahedral architectures worldwide. The construction of supramolecular octahedra is mainly achieved via edge-directed or face-directed design procedures. Zhou and co-workers have employed dicarboxylate ligands having donor sites positioned at a bite angle of around 90° bite angles with paddle wheel $Cu_2(COO)_4$ cluster for the formation of edge-directed charge-neutral M_6L_{12} type octahedral cages (Figure 1.8b).[92]

Similarly, platonic cube architectures can be achieved by designing (i) edge-directed and (ii) face-directed self-assemblies. These platonic solids are very well known in the literature. In the edge-directed self-assembly model, the combination of twelve dipodal linear (180 °) edge-directed donor ligands can meet at the vertices of a cube, which are occupied by the tritopic 90 ° metal acceptor units. To design the face-directed self-assembled cubes, tetratopic metal acceptor units having 90 ° bite angles need to occupy the cubic faces and all their coordination sites are filled with bonds from twelve dipodal 90 ° donor ligands or vice versa.

1.4.2 Archimedean architectures

The smallest of the 13 Archimedean solids (Truncated tetrahedron, truncated octahedron, cuboctahedron, icosidodecahedron, truncated icosahedron, truncated dodecahedron, truncated cube, snub dodecahedron, snub cube, small rhombicosidodecahedron, small rhombicuboctahedron, great rhombicuboctahedron and great rhombicosidodecahedron) is the truncated tetrahedron. To design the truncated tetrahedron architecture, we need to utilize the tritopic unit, which can have 120° bite angles, in combination with the corner unit, which can be either donor or metal acceptor. This combination leads the four hexagonal faces. Here one of example for the formation of a truncated tetrahedron is given that employs a cis-blocked, Pd (II) unit in combination with tripodal donor ligands which have planar geometry with 120° bite angle (figure 1.9a).[93]

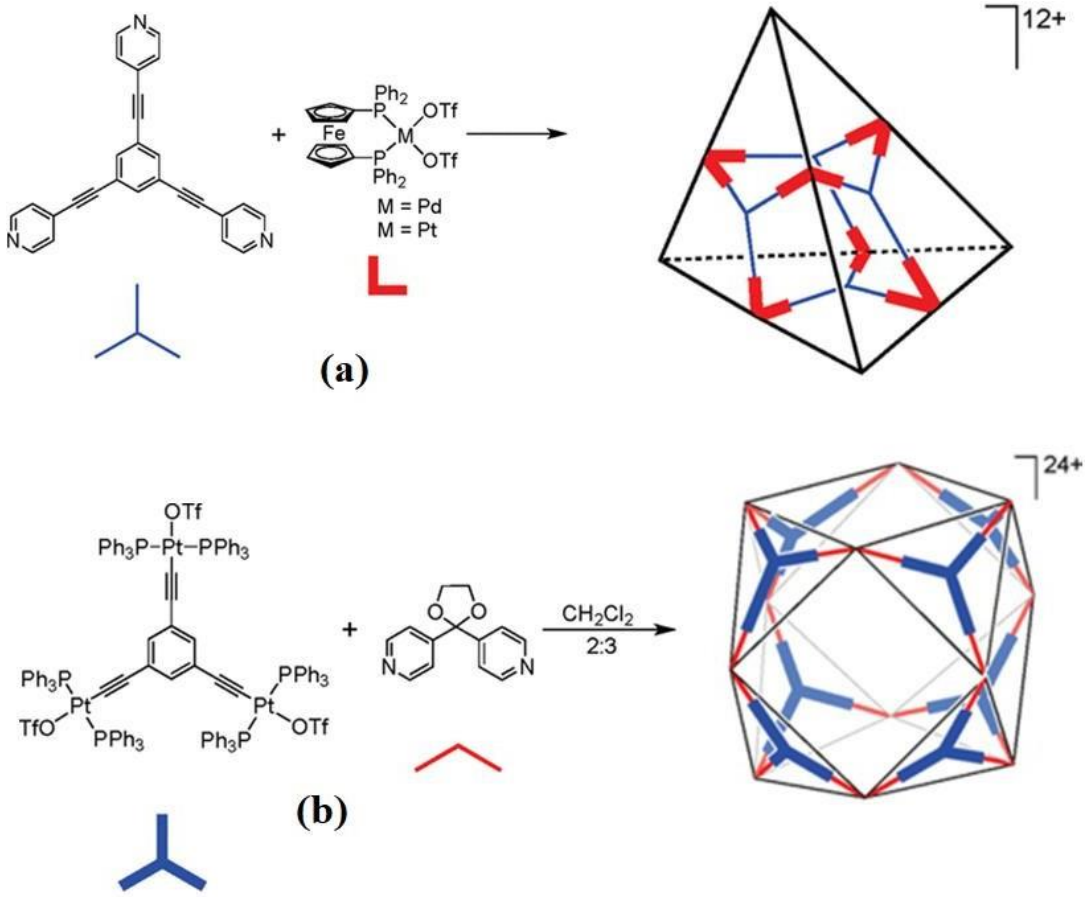

Figure 1.9 (a) Formation of a truncated tetrahedron by using cis-blocked Pd (II) in combination with planar tripodal donor ligands having 120° bite angle. (b) Formation of a cuboctahedron architecture by using angular dipodal ligands in combination with planar acceptor units having 120° bite angle. (Copyright permission© 2011, American Chemical Society, Chem. Rev., 2011, 38, 6810)

The cuboctahedron is one of the rare Archimedean solids that display the structure of a semiregular polyhedron containing two different, triangle and square, faces. The typical procedure for synthesizing cuboctahedra assemblies involves the directional bonding approach. It can be produced by coupling planar tridentate metal acceptors with 120° bite angles with the dipodal rigid ligands having bite angles of around 108-109°, as shown by the example of a cuboctahedral cage reported by Stang and co-workers (figure 1.9b).

1.5 Special characterization method

In the initial stages of their research, only a limited number of techniques were known to self-assembled products in solution, apart from probing their structure in the solid-state by single-crystal X-ray diffraction analysis. However, enormous technological progress has bee

made in the past two decades that saw numerous breakthroughs in the development of metal-ligand based coordination assemblies. The emergence of such novel characterization methods has uncovered some of the key underlying phenomena related to the formation and reactivities of these materials. In this section we present a brief account of some of the fundamental and advanced techniques that are employed in the characterization of these self-assembled compounds using the mass-spectrometry and NMR spectroscopy techniques.

1.5.1 Mass spectrometry

Mass spectrometric techniques are one of the most reliable and widely employed tools for determining the compositions of coordination-driven assemblies in the solution phase. It helps in the understanding of the exact masses, charge states, isotopic patterns and stoichiometry of the obtained assemblies. It also provides the necessary information to recognize the impurities in the solution mixture.[94-95] However, the earlier techniques of ionization, such as fast atom bombardment and matrix-assisted laser desorption/ionization (MALDI) are sometimes incompatible with metal-ligand assemblies. Their ionization methods are harsh for the coordination bonds because large internal energies are infused to the parent and fragment ions of the molecule that leads to the incoherent cleavage of the fragments. A rather new softer ionization technique that has been developed is based on electrospray ionization (ESI).[96] This technique has been wide used in the last two decades and is as a crucial tool for analyzing metal-ligand based supramolecular assemblies. In this technique, charged droplets are generated via electrospray dispersion of a solution of the self-assembled compound. Desolvated ions are formed from the charged droplets first by coulombic repulsion which makes even smaller droplets and subsequently through a number of evaporation cycles, which further form the desolvated ions.[97] This technique is superior to other ionization techniques for analyzing metal-ligand coordination assemblies because of it suppresses the fragmentation and makes intact ionization. Nevertheless, this technique in its preliminary form is efficient for only charged molecular fragments. To achieve the accuracy of identifying higher molecular weight complexes, the ESI sources were coupled with time-of-flight mass analyzer, which improves the ion separation time. Furthermore, investigation of the isotopic patterns of the metal complexes can be achieved by a combination of ESI source with Fourier transform-ion cyclotron resonance systems. Other techniques, which adopt the softer variants of ESI such as sonic spray ionization-mass spectrometry (SSI-MS) and Cold-spray ionization spectrometry (CSI-MS) have also been developed to characterize larger and labile self-assembled species.[98-

[99] A new ESI derived technique, Ion mobility spectrometry-mass spectroscopy (IMS-MS) has emerged in the past few years to characterize elusive fragments of the self-assembled cages and supramolecules.[100] A special variant of this technique called as Travelling Wave Ion Mobility Mass Spectrometry (TWIM-MS) can be used to identify mixture of compounds, where fragments of same mass and different charges, originate from two different supramolecules, exist in the solution.[101]

1.5.2 NMR spectroscopy

NMR spectroscopic techniques have been in the forefront of research in the last three decade for the analysis of supramolecular complexes.[102] This technique can be used to analyze supramolecular complexes in solution and in the solid state and provide evidence to a number of events that take place at the molecular level. Both ^{1}H and ^{13}C NMR techniques are prevalent in coordination-driven self-assemblies, although other heteronuclear NMRs such as ^{11}B, ^{19}F and ^{31}P and ^{195}Pt, etc., can also be routinely used for analysis. The application of NMR spectroscopy is to understand the presence of all the important species and functional groups in the metal-complexes. The details pertaining to the integration, intensity, broadening, and chemical shifts are the tools, which help to understand the composition of the assemblies. The first evidence of the formation of metal-ligand supramolecular from solution state NMR spectra is via the comparison of spectra of the starting components with the self-assembled species. Broadening of the peaks confirms about formation of the bigger molecule than starting component, while changes in chemical shifts suggested the formation of coordination interaction of the complementary components. The use of 2D NMR spectroscopic investigations is required in several instances when the 1D NMR techniques cannot determine the structural features of a self-assembled species and to understand the complex system and dynamics. Also, all these NMR techniques complement the other techniques such as mass spectrometry and single-crystal X- ray diffraction is given complete idea about the supramolecular structure. One of the most convenient techniques to characterize the structural details of complex supramolecule is by the Diffusion ordered NMR spectroscopy (DOSY NMR). The DOSY NMR helps to understand the size of the product and also determine the number of side products through calculation of diffusion coefficient. Bigger molecule shows the lower diffusion coefficient and based on this idea it is possible to calculate the final assembly size via Stokes-Einstein equation.[103]

Apart from solution-based measurements, the solid-state NMR spectroscopy can also be used to determine the structural features of supramolecular assemblies. It is a more convenient technique when solution samples of the complex molecules cannot obtain or screen for measurements. Finally, the single crystal X-ray diffraction technique is very useful for correctly determine structure, although growing single crystals of appropriate dimensions are very challenging for these types of larger molecules. More recently, solution-phase X-ray measurements (SAXS and WAXS) provide a handy method to characterize supramolecular architectures. Especially this technique is very helpful when conventional techniques such as mass spectrometry, NMR spectroscopy and single-crystal X-ray diffraction fail to determine the structures and sizes of the complex assemblies.[104]

1.6 Applications of coordination driven discrete self-assemblies

Metal-ligand coordination driven self-assemblies have now found applications in various branches of science. Some of the prominent application domains for these materials include host-guest chemistry, catalysis, sensing, materials for potential electronic devices and biological probes. Particularly, polyhedral 3D architectures serve as an efficient platform for most of these applications owing to their facile synthesis over conventional container molecules prepared with covalent contacts. The advantages of 3D cages include easy synthesis, accessibility of a large number of building blocks, and the ability to display selective guest encapsulation and transport. The metal-ligand bonds, owing to their controlled directionalities, result in the formation of robust designer coordination architectures and with nanoscale internal cavities. Interestingly, the intrinsic cavities of these coordination driven cages could generate a unique environment in comparison with those found in the bulk of the species in solution. Such uncommon micro environments provided by the cage cavities could also be exploited. For the stabilization of short-lived intermediates and for performing reactions in their confined space to yield uncommon products. In this section, we describe some notable findings on the application of metal-ligand cages in some key frontiers such as host-guest chemistry, catalysis, ferroelectric studies and as biological probes, especially targeting cancer cells.

1.6.1 Host-guest chemistry (molecular encapsulation and recognition)

In order for a self-assembled metal-ligand supramolecule to exhibit host-guest chemistry, it should possess a well-defined cavity and exhibit suitable interactions with the incoming guest molecules. A clear understanding of the host-guest mechanisms is the crucial aspect for the

application of host-guest chemistry in various frontiers such as catalysis and drug delivery. There are many types of interactions such as hydrophobic, van der Waals, hydrogen bonding, ion-association forces, and steric interactions are found in the host-guest systems based on coordination-driven assemblies. There are two major pathways with which these supramolecular systems can encapsulate the guest molecules. The first one is an associative mechanism, where guest molecules replace the molecules or solvents located in the intrinsic void of the cage or macrocycle. The second one is a dissociative mechanism, where removal of solvents or ions is done to produce a guest-free assembly, which could then trap the entering guest molecule.[105]

In this context, Raymond and co-workers synthesized several anionic M_4L_6 tetrahedron assemblies.[88,106-107] The tetrahedral assembly of $[Ga_4(L)_6]^{12-}$ is soluble in water and exhibits a hydrophobic cavity, which makes it the perfect host to encapsulate the hydrophobic guest molecules.[108] Further, they were able to encapsulation of various mono-cationic guest molecules (figure 1.10a).[109] Van't Hoff thermodynamic analysis performed on the host-guest systems reveals that that the encapsulation of cationic guest molecules in this case is an entropically driven processes as both the ΔH and ΔS of the process exhibit positive values.[110]

Nitschke and co-workers have synthesized a range of cationic and anionic tetrahedral cages and utilized them for host-guest application. Here, we are presenting one example from their studies for a Fe (II) based tetrahedron anionic cage supported by peripherally functionalized sulphonate groups.

This cage is soluble in water and the nature of the cavity is found to be hydrophobic. This assembly is pH sensitive and breaks upon decreasing the pH and reforms upon increasing the pH of the solution, demonstrating its reversible disassembly and assembly process.[111] Thus, the addition of *p*-toluenesulfonic acid in the aqueous solution lead breaking of the cage that allows the entrapped cyclohexane to come out into the bulk solution (figure 1.10b). Upon addition of sodium bicarbonate, the reassembly of the cage takes place along with theencapsulation of cyclohexane inside the cage.

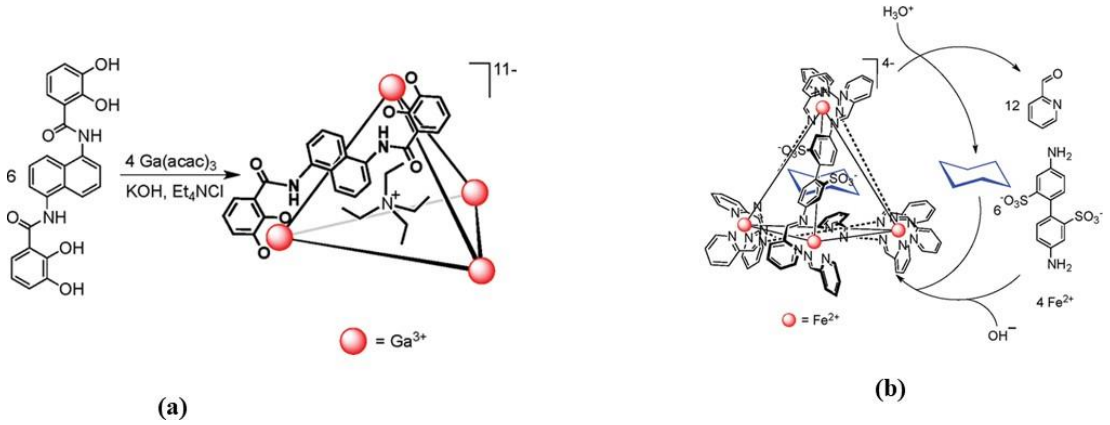

Figure 1.10 (a) An anionic tetrahedral cage $[Ga_4(L)_6]^{12-}$, showing the encapsulation of a hydrophilic guest molecule. (b) Reversible encapsulation and release of a hydrophobic guest molecule assisted by the reversible cage formation and cleavage. (Copyright permission© 2011, American Chemical Society, Chem. Rev., 2011, 38, 6810)

1.6.2 Catalytic reactions

Fujita and coworkers have utilized a number of discrete cages for catalytic reactions. Here we are giving one example, where they have utilized a 3D truncated tetrahedral cage to accomplish a rare Diels–Alder reaction with uncommon regio- and stereoselective preferences.[112] This cage encapsulates both the precursors of a Diels-Alder reaction involving 9-hydroxymethylanthracene and *N*-cyclohexyl maleimide in an aqueous solution. Upon heating the reaction mixtures to 80 °C, the formation of an unusual stereo- and regioselective a [2 + 2] cycloaddition product was observed. Such types of a [2 + 2] cycloaddition product under thermal conditions is a very unusual process under the bulk phase in the absence of a confined cage (figure 1.11). These types of discrete cages have been probed as efficient reaction nano vessels for various catalytic reactions because of the unique micro environments within nano vessels. However, in some cases where cavity-mediated reactions which produced large size product which could have strong complexation with the cage, resulting in a low catalytic turnover. Judicious choice of the host and substrate can prevent such product inhibition, leading to truly catalytic systems.[113]

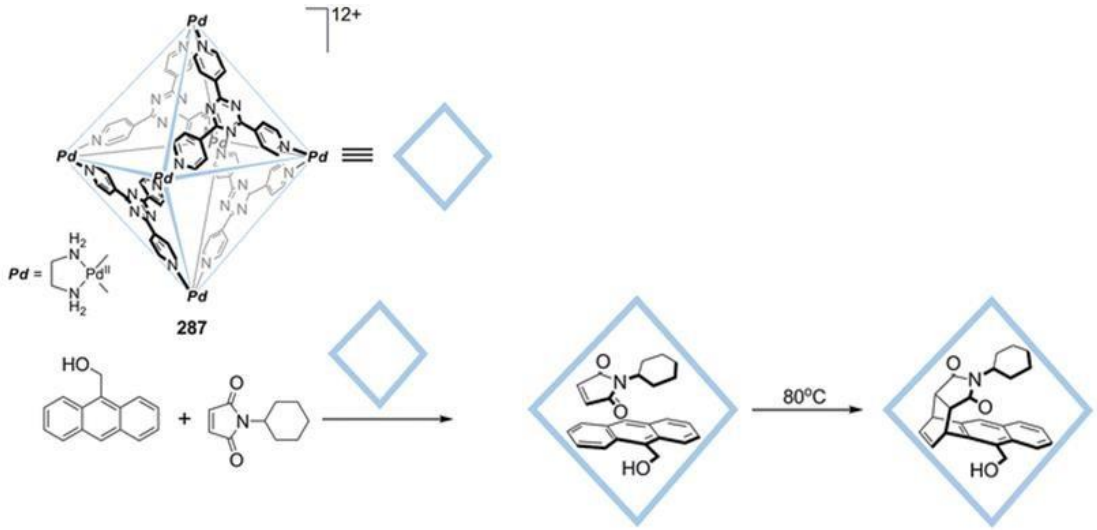

Figure 1.11 *A 3D truncated tetrahedral M_6L_4 cage was utilized for the unusual cycloaddition reaction. (Copyright permission© 2011, American Chemical Society, Chem. Rev., 2011, 38, 6810)*

1.6.3 Biological applications

Ever since the discovery of cisplatin as an anti-cancer agent, inorganic metal complexes have received considerable attention for their potential biological applications. However, the use of self-assembled metal-ligand assemblies in this domain as anticancer drugs, drug vehicles, and DNA binding probes are still in its early stages. Looking at the pace with which the new examples of metal-ligand cages are reported, the number of such cages being utilized for these applications is very little. Some key reports have been made from the laboratories of Stang, Therr in, and co-workers using Pt and Ru-based supramolecular ensembles as anti-tumor agents and delivery vehicles for existing drugs.[114] It is to be noted that the functions of the drug delivery vehicles are typically nontherapeutic. One of the possible advantages of drug vehicles based on coordination-driven 2D or 3D structures, with inherent anti-tumor properties, which can enhance their anticancer properties.

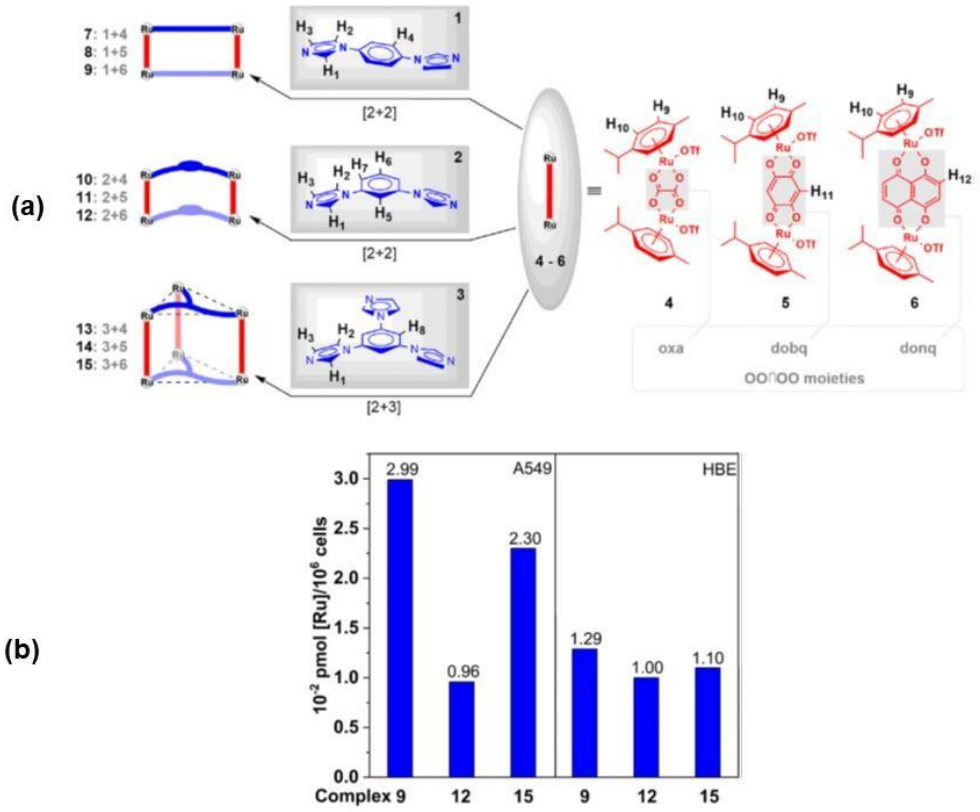

Figure 1.12 *(a) Formation of six tetranuclear 2D metallocycles and three 3D metallcages from dipodal and tripodal flexible imidazole-based ligands in combination with dinuclear half sandwich p-cymene Ru (II) acceptors and suitable linkers. (b) Cellular accumulation plots of complexes for some representative complexes.*

As mentioned earlier, a limited number of metal-ligand based discrete self-assemblies have been investigated for their efficacy towards various tumors present in liver, lung, cervical, breast, colon, prostate, ovarian, brain, stomach, bone, skin, mouth, and thyroid.[115-121] Several studies indicate that the anticancer properties of discrete cage materials operate via mechanisms such as DNA damage, membrane damage, cell apoptosis and autophagy.[115-118] One such as study examining the anti-proliferative activity of a series of self-assemblies based on Ru(II) metal ions is described here. Stang and co-workers have synthesized six trinuclear 2D metaloacycles have been synthesized by treating dipodal flexible imidazole-based ligands and carboxylate derived linkers with dinuclear half sandwich Ru (II) acceptors (figure 1.12). In a similar way, three other hexanuclear trigonal prismatic metallocages were synthesized through a combination of 1,3 imidazole based tripodal ligands with Ru (II) acceptors along with similar

linker ligands (figure 1.12a). Notably, the self-assembled macrocycles and metallocages built using the 5,8-dioxido-1,4-naphtoquinonato (donq) spacers acceptor exhibited good anticancer activity against cell lines such as HCT-116, MDA-MB-231, MCF-7, HeLa, A549, and HepG-2, as confirmed by MTT assay experiments. It has been noticed that the complex 12 performed very well against cancer cells in comparison with known drugs like cisplatin and doxorubicin. The cytotoxicity of the Complex 3 was found to be very low for normal cells such as HBE and THLE-2. Also, the cellular accumulation studies have shown good results for complex 9 in comparison with all other complexes (figure 1.12b).

1.6.4 Dielectric and ferroelectric materials

One of the emerging applications of discrete and self-assembled metal organic structures is in the domain of non-linear dielectric materials dealing with the dielectric, ferroelectric and piezoelectric properties. In this effort, few research group including that of ours have contributed to emergence of such materials. One of the challenges in this field of research is the understanding of the mechanisms of polarization. Typical mechanism of polarization by ceramics and their polymeric and small molecule derived systems involves the displacing mechanism or order-disorder type mechanisms. However, the metal-organic materials generally cannot exhibit such mechanisms as it requires the ordering of the large molecular entity. Hence, the polarization reversals and mechanisms in metal-organic systems are controlled by the nature of metal-ions, nature and types of ligand systems, charge on the framework, nature of the anions and the guest-molecules are ions present in the framework. In this regard, our group has developed a number of charge-separated self-assembled structures based on pyridyl functionalized di- and tripodal ligands. Thus, by choosing the nature of coordinating sites at the pyridyl backbone in the dipodal ligand backbone, we were able to obtain discrete metallo-cavitands, 1D-helical chains and 2D-sheet like assembles that show tuned ferroelectric responses depending on the nature of anions, dimensionality of the framework and the guest molecules present in them.[122-124] Utilizing a tripodal pyridyl phosphoramide ligand, our group has also developed a series of octahedral M_6L_8 type cationic cages and their hierarchical cage-connected frameworks. All these assemblies showed a ferroelectric anisotropic behavior assisted by the toggling of the nitrate ions present in their packing cavities along the crystallographic ab-plane.[125-126] All these findings emphasize our group's contribution to new polarization mechanisms in metal-ligand self-assembled systems.

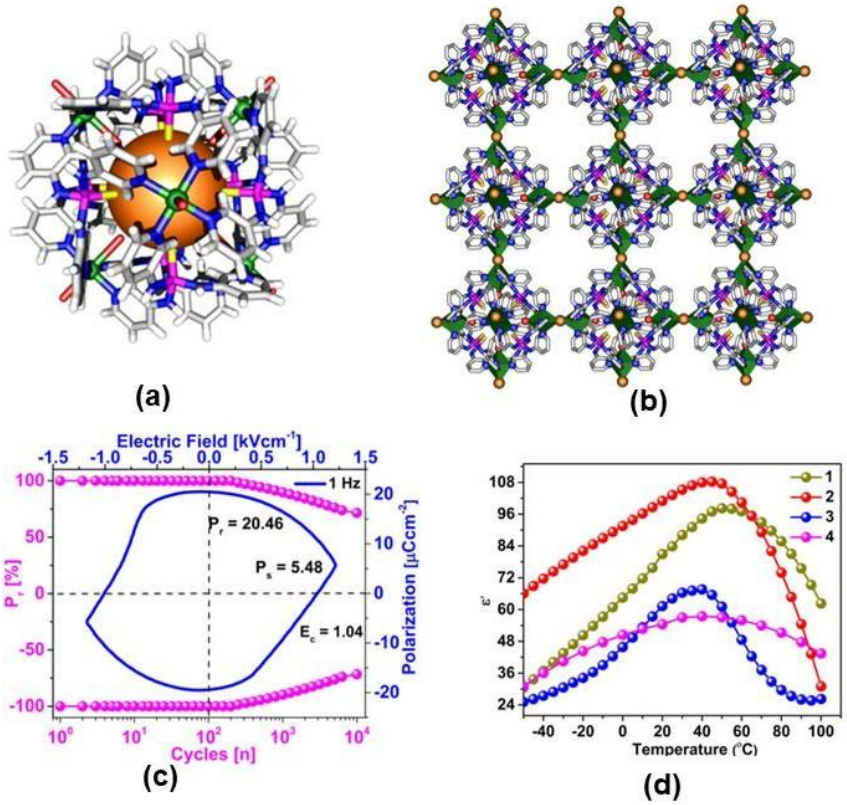

Figure 1.13 (a) View of a cationic discrete octahedral M_6L_8 cage supported by the tripoldal [PS(NH^{3}Py)$_3$] ligand. and its two-dimensional M_6L_8 connected-cage framework obtained by the replacement of the axial aqua ligands with bridging chloride ligands. (c) Ferroelectric hysteresis P-E loop of and fatigue data up to 10^4 cycles for discrete M_6L_8 cage (d) Dielectric constant vs temperature plot showing the desolvation assisted dielectric relaxation behavior.

Scope of the Present Thesis

The present thesis aims at the design and synthesis of metal-ligand cages supported by pyridyl donor ligands based on P-N platforms and planar aromatic ligands and investigated their potential in material chemistry as well as biological activities. It aims to probe the preferential formation of one assembly over the other assisted by the subtle steric and/or electric effects provided by the ligand backbone. The second chapter deals with the coordination of a dipodal pyridyl donor ligand with tetratopic Pd(II) acceptors and its control in the formation of entropically favoured trimeric assembly over the enthalpically controlled tetrameric product. The third chapter is on the development of transition metal-based piezoelectric M_6L_8 cages supported by tripodal pyridyl donor ligands and their utility as mechanical energy harvesters.

The last chapter of the thesis probes the various small and big Pd_6L_8 cages supported by tripodal ligands derived from the P-N backbone and other larger aromatic backbone containing ligands and their utility as cytotoxic agents. Finally, the thesis concludes with a summary and outlook.

The following objectives are realized in this present thesis.

- Synthesis of P (V) based dipodal N-donor containing phosphoramide ligands and their use in the formation of discrete trimeric cages
- Understand the role of the external factors such as, flexibility, temperature and solvents in the discrete coordination driven self-assembly reactions.
- Study of various materials properties of the discrete cages such as dielectric and piezoelectric and their energy harvesting applications.
- Study the role of metal-ligand-based coordination cationic cages in anticancer activities.

References

(1) Bowman-James, K. Alfred Werner Revisited: The Coordination Chemistry of Anions. *Acc. Chem. Res.* **2005**, *38*, 671–678.

(2) J. Pedersen, C. Cyclic polyethers and their complexes with metal salts. *Journal of the American Chemical Society*, **1967**, *89*, 7017–703.

(3) Cram DJ, Cram JM. Host-Guest Chemistry: Complexes between organic compounds simulate the substrate selectivity of enzymes. *Science*. **1974,**183, 803-9.

(4) Lehn, J. M. Cryptates: inclusion complexes of macro polycyclic receptor molecules *Pure and Applied Chemistry*, **1978**, *50*, 871-892.

(5) Murakami, Y, Kikuchi, JI, Hisaeda, Y & Hayashida, O, 'Artificial enzymes', *Chem. Rev.*, **1996**, 96, 2, 721-758.

(6) Hsiao, J. S.; Krueger, B. P.; Wagner, R. W.; Johnson, T. E.; Delaney, J. K.; Mauzerall,D.C.; Fleming, G. R.; Lindsey, J. S.; Bocian, D. F.; Donohoe, R. J. Soluble Synthetic Multiporphyrin Arrays. 2. Photodynamics of Energy-Transfer Processes. *J. Am. Chem. Soc.* **1996**, *118* (45), 11181–11193.

(7) Breslow R, Dong SD. Biomimetic Reactions Catalyzed by Cyclodextrins and Their Derivatives. Chem. Rev. **1998**, 98, 1997-2012.

(8) French, R. R.; Holzer, P.; Leuenberger, M. G.; Woggon, W. D. *Angew. Chem. Inter. Ed.* **2000**, *39*, 1267-1269.

(9) Balzani, V. Light-harvesting dendrimers. *Current Opinion in Chemical Biology.*, **2003**, *7*, 657–665.

(10) Ungar, G.; Liu, Y.; Zeng, X.; Percec, V.; Cho, W.-D. *Science* **2003**, *299*, 1208-1211

(11) Fiedler D, Leung DH, Bergman RG, Raymond KN. Selective molecular recognition, C-H bond activation, and catalysis in nanoscale reaction vessels. Acc. Chem. Res. **2005,** 38, 349-58.

(12) Mukherjee, B., Mohanta, K., & J. Pal, A. Tuning of Molecular Rectification in Donor/Acceptor Assemblies via Supramolecular Structures. *Chem. Mater*. **2006**. *18*, 3302–3307.

(13) Song, Y., Yang, Y., J. Medforth, C., Pereira, E., K. Singh, A., Xu, H., Jiang, Y., Jeffrey Brinker, C., van Swol, F., & A. Shelnutt, J. Controlled Synthesis of 2-D and 3-D Dendritic Platinum Nanostructures. *J. Am. Chem. Soc.*, **2003**, *126*, 635–645.

(14) A. Palacios, M., Nishiyabu, R., Marquez, M., & Anzenbacher, P. Supramolecular Chemistry Approach to the Design of a High-Resolution Sensor Array for Multianion Detection in Water. *J. Am. Chem. Soc.*, **2007**, *129*, 7538–7544.

(15) V. Kumar, C., & R. Duff, Michael. DNA-Based Supramolecular Artificial Light Harvesting Complexes. *J. Am. Chem. Soc.*, **2009**. *131*, 16024–16026.

(16) D. Pluth, M., G. Bergman, R., & N. Raymond, K., Proton-Mediated Chemistry and Catalysis in a Self-Assembled Supramolecular Host. *Acc. Chem. Res.* **2009**, *42*, 1650–1659.

(17) Wessendorf, F., Grimm, B., M. Guldi, D., & Hirsch, A. Pairing Fullerenes and Porphyrins: Supramolecular Wires That Exhibit Charge Transfer Activity. *J. Am. Chem. Soc.*, **2010**, *132*, 10786–10795.

(18) N. Dsouza, R., Pischel, U., & M. Nau, W. Fluorescent Dyes and Their Supramolecular Host/Guest Complexes with Macrocycles in Aqueous Solution. *Chem. Rev.*, **2011**, *111*, 7941–7980.

(19) Stricklen, P., & Verkade, J. Novel homo and heterometallic coordination macrocycles. *J. Am. Chem. Soc.*, **2002**, *105*, 2494–2495.

(20) Fujita, M., Yazaki, J., & Ogura, K. Preparation of a macrocyclic polynuclear complex, [(en)Pd(4,4’-bpy)]4(NO3)8 (en = ethylenediamine, bpy = bipyridine), which recognizes an organic molecule in aqueous media. *J. Am. Chem. Soc.*, **1990**, *112*, 5645–5647.

(21) J. Stang, P., & H. Cao, D. Transition Metal Based Cationic Molecular Boxes. Self-Assembly of Macrocyclic Platinum(II) and Palladium(II) Tetranuclear Complexes. *J. Am. Chem. Soc.*, **1994,** *116*, 4981–4982.

(22) Leininger, S., Olenyuk, B., & J. Stang, P., Self-Assembly of Discrete Cyclic Nanostructures Mediated by Transition Metals. *Chem. Rev.*, **2000**, *100*, 853–908.

(23) Albert Cotton, F., Lin, C., & A. Murillo, C., Supramolecular Arrays Based on Dimetal Building Units. *Acc. Chem. Res.*, **2001**, *34*, 759–771.

(24) Fujita, M., Tominaga, M., Hori, A., & Therrien, B. Coordination Assemblies from a Pd(II)-Cornered Square Complex. *Acc. Chem. Res.*, **2005,** *38*, 369–378.

(25) C. Gianneschi, N., S. Masar, M., & A. Mirkin, C., Development of a Coordination Chemistry-Based Approach for Functional Supramolecular Structures. *Acc. Chem. Res.*, **2005**, 825–837.

(26) Pluth (2007) Reversible guest exchange mechanisms in supramolecular host-guest assemblies', Chem. Soc. rev., **2007**, 36, 161–171.

(27) Li, S.-S., H. Northrop, B., Yuan, Q.-H., Wan, L.-J., & J. Stang, P. Surface Confined Metallosupramolecular Architectures: Formation and Scanning Tunneling Microscopy Characterization. *Acc. Chem. Res.*, **2008**, *42*, 249–259.

(28) Northrop, B. H.; Yang, H.-B.; Stang, P. J. Coordiantion driven self-assembly of functionlized supramolecular metallacycles. *Chem. Comm.* **2008**, 5896-5908

(29) G. Oliveri, C., A. Ulmann, P., J. Wiester, M., & A. Mirkin, C., Heteroligated Supramolecular Coordination Complexes Formed via the Halide-Induced Ligand Rearrangement Reaction. *Acc. Chem. Res.*, **2008**, *41*, 1618–1629.

(30) Saalfrank, R. W.; Stark, A.; Peters, K.; von Schnering, H. G. The First "Adamantoid" Alkaline Earth Metal Chelate Complex: Synthesis, Structure, and Reactivity. *Angew. Chem. Int. Ed. English* **1988**, *27*, 851–853

(31) Simard, M.; Su, D.; Wuest, J. D. LAH/Et20. **1991**, *1991*, 4696–4698.

Synopsis

(32 Beissel, T.; Powers, R. E.; Raymond, K. N. Symmetry-Based Metal Complex Cluster Formation.Pdf. *Angew. Chem. Int. Ed.* **1996**, *35*, 1084

(33) J. Stang, P., E. Persky, N., & Manna, J., Molecular Architecture via Coordination: Self-Assembly of Nanoscale Platinum Containing Molecular Hexagons. *J. Am. Chem. Soc.*, **1997**, *119*, 4777–4778.

(34) Roche, S.; Haslam, C.; Adams, H.; Heath, S. L.; Thomas, J. A. Self-Assembly of a Supramolecular Cube. *Chem. Comm.* **1998**, 1681–1682.

(35) Jude, H., Disteldorf, H., Fischer, S., Wedge, T., M. Hawkridge, A., M. Arif, A., Frederick Hawthorne, M., C. Muddiman, D., & J. Stang, P. Coordination-Driven Self-Assemblies with a Carborane Backbone. *J. Am. Chem. Soc.*, **2005,** *127*, 12131–12139.

(36) Olenyuk, B., D. Levin, M., A. Whiteford, J., E. Shield, J., & J. Stang, P., Self-Assembly of Nanoscopic Dodecahedra from 50 Predesigned Components. *J. Am. Chem. Soc.*, **1999,** *121*, 10434–10435.

(37) Olenyuk, B.; Whiteford, J. A.; Fechtenkötter, A.; Stang, P. J. Self-Assembly of Nanoscale Cuboctahedra by Coordination Chemistry. *Nature* **1999**, *398*, 796–799.

(38) D. Levin, M., & J. Stang, P. Insights into the Mechanism of Coordination-Directed Self-Assembly. *J. Am. Chem. Soc.*, **2000**, *122*, 7428–7429.

(39) K. Kryschenko, Y., Russell Seidel, S., C. Muddiman, D., I. Nepomuceno, A., & J. Stang, P., Coordination-Driven Self-Assembly of Supramolecular Cages: Heteroatom-Containing and Complementary Trigonal Prisms. *J. Am. Chem. Soc.*, **2003**, *125*, 9647–9652.

(40) Lang, J.-P., Xu, Q.-F., Chen, Z.-N., & F. Abrahams, B. (2003). Assembly of a Supramolecular Cube, [(Cp*WS3Cu3)8Cl8(CN)12Li4] from a Preformed Incomplete Cubane-like Compound [PPh4][Cp*WS3(CuCN)3]. *J. Am. Chem. Soc.*, **2003,** *125*, 12682–12683.

(41) Würthner, F.; You, C. C.; Saha-Möller, C. R. Metallosupramolecular Squares: From Structure to Function. *Chem. Soc. Rev.* **2004**, *33*, 133–146.

(42) Thanasekaran, P.; Liao, R. T.; Liu, Y. H.; Rajendran, T.; Rajagopal, S.; Lu, K. L. Metal-Containing Molecular Rectangles: Synthesis and Photophysical Properties. *Coord. Chem. Rev.* **2005**, *249* (9–10), 1085–1110.

(43) P. Argent, S., Adams, H., Riis-Johannessen, T., C. Jeffery, J., P. Harding, L., & D. Ward, M., High-nuclearity Homoleptic and Heteroleptic Coordination Cages Based on Tetra-Capped Truncated Tetrahedral and Cuboctahedral Metal Frameworks. *J. Am. Chem. Soc.*, **2005**, *128*, 72–73.

44) Zangrando, E., Casanova, M., & Alessio, E., Trinuclear Metallacycles: Metallatriangles and Much More. *Chem. Rev.*, **2008**, *108*, 4979–5013.

45) Suzuki, K.; Tominaga, M.; Kawano, M.; Fujita, M. Self-Assembly of an M6L12 Coordination Cube. *Chem. Comm.*, **2009**, 13, 1638–1640.

46) Ward, M. D. Polynuclear Coordination Cages. *Chem. Comm.*, **2009**, 4487–4499.

(47) Smulders, M. M. J.; Riddell, I. A.; Browne, C.; Nitschke, J. R. Building on Architectural Principles for Three-Dimensional Metallosupramolecular Construction. *Chem. Soc. Rev.* **2013**, *42* , 1728–1754.

(50) Compounds, C. Nyholm Memorial Lecture. **1979**

(51) Feldman, Y., L. Frey, G., Homyonfer, M., Lyakhovitskaya, V., Margulis, L., Cohen, H., Hodes, G., L. Hutchison, J., & Tenne, R. Bulk Synthesis of Inorganic Fullerene-like MS2 (M = Mo, W) from the Respective Trioxides and the Reaction Mechanism. *J. Am. Chem. Soc.*, **1996**, *118*(23), 5362–5367.

(52) Rebek, J. Assembly and Encapsulation with Self-Complementary Molecules. *Chem. Soc. Rev.* **1996**, *25*, 255–264.

(53) L. Caulder, D., & N. Raymond, K. (1999). Supermolecules by Design. *Acc. Chem. Res.*, **1999**, *32*(1, 975–982.

(54) MacGillivray, L. R.; Atwood, J. L. Structural Classification and General Principles for the Design of Spherical Molecular Hosts. *Angew. Chemie - Int. Ed.* **1999**, *38*, 1018–1033.

(55) Muller, A.; Kogerler, P.; Kuhlmann, C. Erratum: A Variety of Combinatorially Linkable Units as Disposition: From a Giant Icosahedral Keplerate to Multi-Functional Metal-Oxide Based Network Structures. *Chem. Comm.*, **2000**, *21*, 2173.

(56) Leininger, S.; Fan, J.; Schmitz, M.; Stang, P. J. Archimedean Solids: Transition Metal Mediated Rational Self-Assembly of Supramolecular-Truncated Tetrahedra. *Proc. Natl. Acad. Sci. U. S. A.* **2000**, *97*, 1380–1384.

(57) Hof, F.; Craig, S. L.; Nuckolls, C.; Rebek, J. Molecular Encapsulation. *Angew. Chemie - Int. Ed.* **2002**, *41*, 1488–1508.

(58) Müller, A.; Beckmann, E.; Bögge, H.; Schmidtmann, M.; Dress, A. Inorganic Chemistry Goes Protein Size: A Mo 368 Nano-Hedgehog Initiating Nanochemistry by Symmetry Breaking. *Angew. Chemie - Int. Ed.* **2002**, *41*, 1162–1167.

(59) Alvarez, S. Polyhedra in (Inorganic Chemistry). *Dalt. Trans.* **2005**, *13*, 2209–2233.

(60) Biros, S. M.; Rebek, J. Structure and Binding Properties of Water-Soluble Cavitands and Capsules. *Chem. Soc. Rev.* **2007**, *36*, 93–104.

(61) Schwedtmann, K.; Hennersdorf, F.; Bauzá, A.; Frontera, A.; Fischer, R.; Weigand, J. J. Isolation of Azadiphosphiridines and Diphosphenimines by Cycloaddition of Azides and a Cationic Diphosphene. *Angew. Chemie - Int. Ed.* **2017**, *56*, 6218–6222.

(62) Forbes, T. Z.; McAlpin, J. G.; Murphy, R.; Burns, P. C. Metal-Oxygen Isopolyhedra Assembled into Fullerene Topologies. *Angew. Chemie - Int. Ed.* **2008**, *47*, 2824–2827.

(63) J. Stang, P., & Olenyuk, B. Self-Assembly, Symmetry, and MolecularArchitecture: Coordination as the Motif in the Rational Design of Supramolecular Metallacyclic Polygons and Polyhedra. *Acc. Chem. Res.*, **1997**, *30*, 502–518.

(64) L. Caulder, D., Brückner, C., E. Powers, R., König, S., N. Parac, T., A. Leary, J., & N. Raymond, K. (2001). Design, Formation and Properties of Tetrahedral M4L4 and M4L6 Supramolecular Clusters1. *J. Am. Chem. Soc.*, **2001**, *123*, 8923–8938.

(65) Fujita, M. Metal-Directed Self-Assembly of Two- and Three-Dimensional Synthetic Receptors. **1997**.

(66) Holliday BJ, Mirkin CA. Strategies for the Construction of Supramolecular Compounds through Coordination Chemistry. *Agnew. Chem. Int. Ed.,* **2001**,40, 2022-2043.

(67) Cotton FA, Lin C, Murillo CA. Supramolecular arrays based on dimetal building units. Acc Chem Res. **2001** ,34, 759-71.

(68) Poyac, L., Rose, C., Wahiduzzaman, M., Lebrun, A., Cazals, G., H. Devillers, C., G. Yot, P., Clément, S., & Richeter, S. Synthesis, Characterization, and Encapsulation Properties of Rigid and Flexible Porphyrin Cages Assembled from N-Heterocyclic Carbene–Metal Bonds. *Inorganic Chemistry*, **2021**, *60*, 19009–19021.

(69) Chakrabarty, R., Mukherjee, P. S., & Stang, P. J. Supramolecular coordination: Self-assembly of finite two- and three-dimensional ensembles. In *Chem. Rev.* **2011**, *111*, 6810–6918.

(70) J. Stang, P., & H. Cao, D. Transition Metal Based Cationic Molecular Boxes. Self-Assembly of Macrocyclic Platinum(II) and Palladium(II) Tetranuclear Complexes. *J. am. Chem. Soc.* **2002**, *116*(11), 4981–4982.

(71) Fujita, M.; Aoyagi, M.; Ogura, K. Macrocyclic Dinuclear Complexes Self-Assembled from (En)Pd(NO3)2 and Pyridine-Based Bridging Ligands. *Inorganica, Chim. Acta* **1996**, *246* ,53–57.

(72) Fujita, M.; Ibukuro, F.; Hagihara, H.; Ogura, K. L l 1. *Quant. self-assembly a [2]catenane from two preformed Mol. rings* **1994**, *367*, 720–723.

(73) Fujita, M., Ibukuro, F., Seki, H., Kamo, O., Imanari, M., & Ogura, K., Catenane Formation from Two Molecular Rings through Very Rapid Slippage. A Möbius Strip Mechanism *J. am. Chem. Soc.* **1996**, *118*(4), 899–900.

(74) Fujita, M., Ibukuro, F., Yamaguchi, K., & Ogura, K. A Molecular Lock. *J. am. Chem. Soc.* **2002**, *117*(14), 4175–4176.

(75) Zangrando, E., Casanova, M., & Alessio, E. Trinuclear Metallacycles: Metallatriangles and Much More. *Chem. Rev.***2008**, *108*(12), 4979–5013.

(76) Ukai, K., Oshima, K., & Matsubara, S. Preparation of Cyclopropanediol: Novel [2 + 1] Cycloaddition Reaction of Bis(iodozincio)methane with 1,2-Diketones. *J. am. Chem. Soc.* **2000**, *122*, 12047–12048.

(77) Lippert, B.; Sanz, P. J.; Miguel, P. J. S.; Sanz, P. J. Chem Soc Rev Metallatriangles and Metallasquares : The Diversity behind Structurally Characterized Examples and the Crucial Role of Ligand Symmetry. **2011**, *40*, 4475–4487.

(78) Burchell, T. J.; Eisler, D. J.; Jennings, M. C.; Puddephatt, R. J. Ring-Opening Polymerization of Gold Macrocycles and Self-Assembly of a Coordination Polymer through Hydrogen-Bonding. **2003**, 2228–2229.

(79) Bar, A. K., Chakrabarty, R., Chi, K-W., Batten, S. R., & Mukherjee, P. S. Synthesis and characterisation of heterometallic molecular triangles using ambidentate linker: Self-selection of a single linkage isomer. *Dalton. Trans.* **2009**, 3222.

(80) J. Stang, P., Chen, K., & M. Arif, A. Modular Assembly of Hybrid Iodonium-Transition Metal Cationic Tetranuclear Macrocyclic Squares. Single Crystal Molecular Structure of {[(Et3P)2Pd(OTf)2][(NC5H4C6H4)2I(OTf)]}. *J. am. Chem. Soc.* **2002**, *117*, 8793–8797.

(81) Manna, J., J. Kuehl, C., A. Whiteford, J., J. Stang, P., C. Muddiman, D., A. Hofstadler, S., & D. Smith, R. Nanoscale Tectonics: Self-Assembly, Characterization, and Chemistry of a Novel Class of Organoplatinum Square Macrocycles. *J. am. Chem. Soc.* **1997**, *119*(48), 11611–11619.

(82) Oguraa, K. On the Structure of Transition-Metal-Linked Molecular Squares. *Chem. Commu.*, **1996**, *20*, 1535–1536.

(83) Ferrer, M., Mounir, M., Rossell, O., Ruiz, E., & Angel Maestro, M. Equilibria between Metallosupramolecular Squares and Triangles with the New Rigid Linker 1,4-Bis(4-pyridyl)tetrafluorobenzene. Experimental and Theoretical Study of the Structural Dependence of NMR Data. *Inorg. Chem.* **2003**, *42*, 5890–5899.

(84) Weilandt, T., W. Troff, R., Saxell, H., Rissanen, K., & A. Schalley, C. Metallo-Supramolecular Self-Assembly: the Case of Triangle-Square Equilibria. *Inorg. Chem.* **2008**, *47*, 7588–7598.

(85) J. Stang, P., E. Persky, N., & Manna, J. Molecular Architecture via Coordination: Self-Assembly of Nanoscale Platinum Containing Molecular Hexagons. *J. am. Chem. Soc.* **1997**, *119*, 4777–4778.

(86) Beissel, T.; Powers, R. E. Symmetry-Based Metal Complex Cluster Formation. *Angew. Chem. Int. Ed.* **1996**, 35, 1084.

(87) Beissel, T., E. Powers, R., N. Parac, T., & N. Raymond, K. Dynamic Isomerization of a Supramolecular Tetrahedral M4L6 Cluster1. *J. am. Chem. Soc.* **1999**, *121*, 4200–4206.

(88) Cluster, T. M. L. S.; Caulder, D. L.; Powers, R. E.; Parac, T. N.; Raymond, K. N. The Self-Assembly of a Predesigned. **1998**, 1840–1843.

(89) Mal, P.; Nitschke, J. R. Sequential Self-Assembly of Iron Structures in Water. *Chem. Comm.* **2010,** *46*, 2417.

(90) Kusukawa, T., & Fujita, M. Self-Assembled M6L4-Type Coordination Nanocage with 2,2‘-Bipyridine Ancillary Ligands. Facile Crystallization and X-ray Analysis of Shape-Selective Enclathration of Neutral Guests in the Cage. *J. am. Chem. Soc.* **2002**, *124* 13576–13582.

(91) Clegg, J. K.; Lindoy, L. F.; Moubaraki, B.; Murray, K. S.; McMurtrie, J. C. Triangles and Tetrahedra Metal Directed Self-Assembly of Metallosupramolecular Structures Incorporating Bis-Diketonato. Dalton Trans. **2004**, 2417.

(92) Li, J.; Timmons, D. J.; Zhou, H. Interconversion between Molecular Polyhedra and Metal - Organic Frameworks. *J. am. Chem. Soc.*, **2009**, *131*, 6368–6369.

(93) Zheng, Y.; Zhao, Z.; Kim, H.; Wang, M.; Ghosh, K.; Pollock, J. B.; Chi, K.; Stang, P. J. Coordination-Driven Self-Assembly of Truncated Tetrahedra Capable Of. **2020**, 10238–10240.

(94) Schalley CA. Molecular recognition and supramolecular chemistry in the gas phase. *Mass Spectrom Rev.* 2001, 253-309.

(95) Schalley, C.; Schalley, C. A. Analytical Methods in Supramolecular Chemistry. **2012**

(96) Fenn, J. B.; Mann, M.; Meng, C. K.; Wong, S. F. Electrospray Ionization-Principles and Practice. Mass Spectrom. rev. **1990**, *9*, 37.

(97) Baytekin, B.; Baytekin, H. T.; Schalley, C. A. Mass Spectrometric Studies of Non-Covalent Compounds : Why Supramolecular Chemistry in the Gas Phase. Org. Biomol. Chem. **2006**, 2825–2841.

(98) Yamaguchi, K. Cold-Spray Ionization Mass Spectrometry: Principle and Applications. *J. Am. Soc. Mass Spectrom*, **2003**, *1*, 473–490.

(99) Liang, X.; Han, H.; Xia, Y.; Mcluckey, S. A. A Pulsed Triple Ionization Source for Sequential Ion / Ion Reactions in an Electrodynamic Ion Trap. *J. Am. Soc. Mass Spectrom*,, **2007,** *18*, 369-376.

(100) Kanu AB, Dwivedi P, Tam M, Matz L, Hill HH Jr. Ion mobility-mass spectrometry. *J Mass Spectrom.* **2008,** *43*,1-22.

(101) Kaczorowska, M.A., Hotze, A.C.G., Hannon, M.J. *et al.* Electron capture dissociation mass spectrometry of metallo-supramolecular complexes. *J. Am. Soc. Mass Spectrom.,* **2010**, *21***,** 300–309.

(102) Shapiro, Y. E. Progress in Polymer Science Structure and Dynamics of Hydrogels and Organogels : An NMR Spectroscopy Approach. *Prog. Polym. Sci.* **2011**, *36*, 1184–1253.

(103) Ramalhete SM, Nartowski KP, Sarathchandra N, et al. Supramolecular Amino Acid Based Hydrogels: Probing the Contribution of Additive Molecules using NMR Spectroscopy. *Chemistry*. **2017**, 23, 8014-8024.

(104) Mertens HD, Svergun DI. Structural characterization of proteins and complexes using small-angle X-ray solution scattering. *J. Struct. Biol.* **2010**,172,128-41.

(105) Pluth, M. D.; Raymond, K. N.; Raymond, K. N. Reversible Guest Exchange Mechanisms in Supramolecular Host – Guest Assemblies and a Distinguished Teaching. **2007**, 161–171.

(106) L. Caulder, D., & N. Raymond, K. (1999). Supermolecules by Design. *Acc. Chem. Res.*, **1999**, *32*, 975–982.

(107) L. Caulder, D., Brückner, C., E. Powers, R., König, S., N. Parac, T., A. Leary, J., & N. Raymond, K. Design, Formation and Properties of Tetrahedral M4L4 and M4L6 Supramolecular Clusters1. *J. Am. Soc.**2001**,123,* 8923–8938.

(108) N. Parac, T., L. Caulder, D., & N. Raymond, K. Selective Encapsulation of Aqueous Cationic Guests into a Supramolecular Tetrahedral [M4L6]12- Anionic Host1. *J. Am. Soc.* **1998**, *120*, 8003–8004.

(109) Pluth, M. D., Johnson, D. W., Szigethy, G., Davis, A. v., Teat, S. J., Oliver, A. G., Bergman, R. G., & Raymond, K. N. Structural consequences of anionic host-cationic guest interactions in a supramolecular assembly. *Inorg. Chem.* **2009**, *48*, 111–120.

(110) D. Pluth, M., G. Bergman, R., & N. Raymond, K. (2007). Making Amines Strong Bases: Thermodynamic Stabilization of Protonated Guests in a Highly-Charged Supramolecular Host1. *J. Am. Soc. 129*, 11459–11467.

(111) Mal, P.; Schultz, D.; Beyeh, K.; Rissanen, K.; Nitschke, J. R. An Unlockable – Relockable Iron Cage by Subcomponent. **2008**, 8297–8301.

(112) Yoshizawa M, Tamura M, Fujita M. Diels-alder in aqueous molecular hosts: unusual regioselectivity and efficient catalysis. *Science*. **2006**, 312, 251-4.

(113) Fiedler, D.; Bergman, R. G.; Raymond, K. N. Supramolecular Catalysis of a Unimolecular Transformation: Aza-Cope Rearrangement within a Self-Assembled Host. **2004**, 6748–6751.

(114) Sepehrpour, H.; Fu, W.; Sun, Y.; Stang, P. J. Biomedically Relevant Self-Assembled Metallacycles and Metallacages. **2019,** *141***,** 14005-14020.

(115) Schmidt, A.; Hollering, M.; Drees, M.; Casini, A.; Kühn, F. E. Supramolecular Exo-Functionalized Palladium Cages: Fluorescent Properties and Biological Activity. **2016**, 8556–8565.

(116) Grishagin, I. V; Pollock, J. B.; Kushal, S.; Cook, T. R.; Stang, P. J.; Olenyuk, B. Z. In Vivo Anticancer Activity of Rhomboidal Pt(II)Metallacycles. *PNAS*, **2014,** 111,18448-18453**.**

(117) Therapy, P.; R, M.; Singlet, M.; Sensitizer, O.; Chem, T.: Therapy. **2016**.

(118) Sun, Y.; Ding, F.; Zhou, Z.; Li, C.; Pu, M.; Xu, Y.; Zhan, Y.; Lu, X. Nanoprobe for Tumor Diagnosis and Image- Guided Therapy. **2019**, 1–

(119) Gupta, G.; Kumar, J. M.; Garci, A.; Nagesh, N.; Therrien, B. Exploiting Natural Products to Build Metalla-Assemblies: The Anticancer Activity of Embelin-Derived Rh(III) and Ir(III) Metalla-Rectangles. **2014**, 6031–6046.

(120) Zhao, Y.; Zhang, L.; Li, X.; Shi, Y.; Ding, R.; Teng, M.; Zhang, P.; Cao, C. Metallacages with Imidazole-Based Ligands and Their in Vitro Anticancer Activity. Natl. Acad. Sci. U S A. **2019**, *116*, 4090-4098.

(121) Mun, J.; Mandal, N.; Chi, K.; Lee, C. Y. Self-Assembled Novel BODIPY-Based Palladium Supramolecules and Their Cellular Localization. *Inorg. Chem.*, **2017**, *56*, 1–7.

(122) Srivastava, A. K.; Vijayakanth, T.; Divya, P.; Praveenkumar, B.; Steiner, A.; Boomishankar, R. Metallo-Cavitands by Varying Hydrated. **2017**, 7352–7359.

(123) Anant Kumar Srivastava, B. Praveenkumar, Indra Kumar Mahawar, Pillutla Divya, S. Shalini, and R. B. Anion Driven [CuIIL2]n Frameworks: Crystal Structures, Guest-Encapsulation, Dielectric, and Possible Ferroelectric Properties. *Chem. Mater.*, **2014**, *12*, 3811–3817.

(124) Srivastava, A. K.; Divya, P.; Praveenkumar, B.; Boomishankar, R. Potentially Ferroelectric {CuIIL2}n Based Two-Dimensional Framework Exhibiting High Polarization and Guest-Assisted Dielectric Anomaly. *Chem. Mater.* **2015**, *27*, 5222–5229.

(125) Yadav, A.; Srivastava, A. K.; Kulkarni, P.; Divya, P.; Steiner, A.; Praveenkumar, B.; Boomishankar, R. Anion-Induced Ferroelectric Polarization in a Luminescent Metal-Organic Cage Compound. *J. Mater. Chem. C.*, **2017**, *5*, 10624–10629.

(126) Yadav, A.; Kulkarni, P.; Praveenkumar, B.; Steiner, A. Hierarchical Frameworks of Metal – Organic Cages with Axial Ferroelectric Anisotropy. **2018**, 14639–14643.

END of CHAPTER 1

CHAPTER 2

Construction of Entropically Favoured Supramolecular Metal-Ligand Trimeric Assemblies Supported by Flexible P (V) Scaffolds

2.1 INTRODUCTION

The first example of tetrameric square assembly was reported by Fujita and co-workers by employing a cis-blocked Pd (II) acceptors moiety with 4,4'- bipyridine dipodal ligands.[1] However, Hong and coworkers observed the existence of supramolecular square along with molecular triangle in the solution. These molecules exist in solution and equilibrium between them controlled by induced-fit molecular recognition. The equilibrium ratio is pushed toward triangle molecule in the presence of small guest; however, the concentration of molecular square has been dominated in presence of bigger guest molecules.[2-3] In several examples square structures reported,[4-9] molecular triangle structures are much less common, mainly due to strain that created inside the structure.[10-11] Most often, the driving force for all such reactions is under thermodynamic control.[12] The supramolecular tetramer (or molecular square) is wider and less strained compared to the trimer, and thus enthalpy drives the formation of the tetramer. In contrast, entropy favors the formation of molecular trimers (or triangles), because the number of trimers that can be formed is more in comparison with the tetramers for the same number of structural components at the beginning of the reaction.[13-17] One more factor which prevalent in the formation of molecular trimer is flexibility of the starting components such as ligands.[18-20] Owing to this balance in thermodynamics, the molecular tetramer is the preferred product of the equilibrium when rigid ligands are employed in the reaction.[4-9,21] Molecular trimers can be favourably obtained if the linker moieties are flexible and reduce the strain in the complex.[18-19, 22] Nevertheless, molecular trimers are less common, mainly due to the strain in the structures.[18-22] Factors such as solvents, temperature, concentration, nature of metal ions, nature of the metal-bound ancillary ligands, counter anions, and most importantly, nature of the linkers were found to play a crucial role in affecting the trimer/tetramer (square/triangle) preferences.[4-10, 23] In fact, formation of molecular trimers for tetratopic metal acceptors is veryrare, although there are a few examples known in the literature.[22] Further studies on similar types of systems, with and without cis-blocking ancillary ligands, reveal the existence of molecular trimers and tetramers and their mixtures in equilibria.[8] In addition, there are severalexamples in which the directional preference of the components is not fulfilled. Therefore, themixing of linkers with ditopic Pd^{2+} acceptors lead to mixtures of molecular trimers and tetramers, which may or may not be in equilibrium.[10-18] In some rare cases, the formation of supramolecular triangles was observed exclusively both in solution and in the solid state.[10]

There are also reports for the existence of trimeric structure in the solid-state, while the identity of the species in the solution was unclear.[14] To avoid the strain which creates in the molecular trimer, flexibility of the ligand can play important role to fix the problem. Till date, most of the research on this issue being published by using bipyridine and carboxamide based ligands as building units. Our group has been focused on synthesis of phosphoramide based dipodal and tripodal ligands and their coordination complexes. The general formula of these dipodal and tripodal ligands are [XPYNHR], (X = Ph; Y = O, S; R = 3- pyridine, 4- pyridine, 2- pyridine) and [PYNHR], (Y = O, S; R = R = 3- pyridine, 4- pyridine, 2- pyridine, 6-quinoline). Phosphoramide ligands are more similar to carboxamide ligands and flexibility of P-N-C played very important role to get coordination complexes.[24-27] Using a semi-rigid 3-pyridyl substituted phenyl phosphoramide ligand, $PhPO(3\text{-}Py)_2$ (**L^1**), our group has recently reported the structures of the molecular tetramers for the octahedral metal ions such as Ni(II) and Co(II).[25] However, for the Cu(II) acceptors, both tetrameric and trimeric structures were observed in solid-state depending upon the reaction conditions.[25] Hence, we set out to probe the propensity of this (**L^1**) and a similar methyl-substituted ligand $MePO(3\text{-}Py)_2$ (**L^2**) for the formation of trimeric and tetrameric assemblies in solution using diamagnetic metal ions such as Pd(II). Treatment of **L^1** with tetratopic Pd(II) ions in DMSO yielded the trimeric species $[Pd_3(\mathbf{L^1})_6\cdot(BF_4)_6]$ (**1a**) in solution as a major product with a small amount of the tetrameric species $[Pd_4(\mathbf{L^1})_8\cdot(BF_4)]_8$ (**1b**) as a minor product. At higher temperatures, the trimeric assembly of **1a** was preferentially observed in the solution. Upon reducing the polarity of the medium by adding MeCN to the DMSO solution, **1b** was found to be prevalent. Further, the molecular structure of trimeric assembly was established by single crystal X-ray diffraction analysis of **1a**. Interestingly, when **L^2** was used as the ligand, the trimeric species $[Pd_3(\mathbf{L^2})_6.(BF_4)_6\}$ (**2**) was the only product in the solution at room temperature. These findings support the role of the non-rigid and flexible ligand backbone in obtaining entropically driven products in supramolecular self-assembly reactions.

2.2 EXPERIMENTAL SECTION

2.2.1 General remarks

All the solvents and reagents were purchased from commercial sources and used as received. Toluene was dried freshly distilled over sodium. The reagents 3-aminopyridine, $PhPOCl_2$, $MePOCl_2$, $[Pd(CH_3CN)_4\cdot 2(BF_4)]$ and the NMR-grade solvents such as DMSO-d_6, MeCN-d_3,

and MeOH-d_4 were purchased from Sigma Aldrich and used as received. The NMR spectra were recorded on Bruker 400, Jeol 400, (^{1}H NMR, 400.13 MHz), ^{13}C{^{1}H} NMR, 100.62 MHz, and ^{31}P{^{1}H} NMR, 161.12 MHz) and Bruker 600 MHz spectrometer (^{1}H NMR, 600.4 MHz, and ^{31}P{^{1}H} NMR, 243.05 MHZ) using $SiMe_4$ (^{1}H, ^{13}C NMR) and 85% H_3PO_4 (^{31}P NMR) as standards. The ESI-MS spectra were obtained on the Waters Synapt G2 Q-TOF spectrometer. The MALDI-TOF spectra were recorded on an Applied Biosystem MALDI-TOF/TOF system. FT-IR spectra were recorded on a Perkin-Elmer spectrophotometer in the ATR mode. The Circular Dichroism (CD) were measured in JASCO J815 spectrometer from 450 nm to 180 nm. The optical rotation measurements were performed at 20 °C. Elemental analyses were performed on a Vario-EL cube elemental analyzer. Melting points were analyzed using an Electrothermal melting point apparatus and were uncorrected.

2.2.2 Syntheses

L^1: The ligand **L^1** was synthesized by a slight modified procedure reported by us earlier.[25] To a stirred suspension of 3-aminopyridine (1.48 g, 15.7 mmol) and triethylamine (2.4 ml, 16 mmol) in 100 mL of dry toluene kept at 0 °C in argon atmosphere, $PhPOCl_2$ (1 ml, 7.5 mmol) in toluene (10 mL) was added dropwise over a period of 10 minutes. The reaction mixture was refluxed for 10 hours. The resulting precipitate was collected, washed with water several times, and dried in a vacuum desiccator. Yield: 1.9 g (85%) ^{1}H NMR: (600 MHz, DMSO-d_6) δ = 8.38 (d, 2H), 8.32 (d, NH, 2H), 8.05 (dd, 2H), 7.84 (m 2H), 7.57 (dd, 1H), 7.51 (m, 4H), 7.14 (dd, 2H). ^{31}P{1H} NMR: (242.95 MHz, DMSO-d6) δ= 10.06 (s). MALDI- TOF m/z = 310.30. Anal. calcd. for $C_{16}H_{15}N_4OP$: C, 61.93; H, 4.87; N, 18.06. Found: C, 61.55; H, 4.93; N, 17.89. FT-IR data (cm^{-1}): 3088, 1587, 1477, 1386, 1197, 1121, 1061, 938, 810, 699, and 514.

L^2: To a stirred solution of 3-aminopyridine (1.48 g, 15.7 mmol) and triethylamine (2.4 ml, 16 mmol) in 100 mL of toluene kept at 0° C in argon atmosphere, $MePOCl_2$ (1 gm, 7.5 mmol) in dry toluene (10 mL) was added drop wise over a period of 10 minutes. The reaction mixture was refluxed for 24 hours. The resulting precipitate was collected, washed with dichloromethane several times and dried in a vacuum desiccator. Isolated yield: 1.3 g (75%) ^{1}H NMR: (400 MHz, DMSO-d_6): δ = 8.35 (d, 2H), 8.05 (dd, 2H), 8.03 (d, 2H, NH), 7.48 (dd, 2H), 7.20 (m, 2H), 1.69 (d, 3H). ^{13}C{^{1}H} NMR (DMSO-d_6, 100.62 MHz): δ= 141.88, 138.10, 138.95, 124.14, 15.16. ^{31}P{^{1}H} NMR (DMSO-d_6, 161.97 MHz): δ =17.57(s). ESI-MS: m/z = 249.09 for $(M+H^+)^+$. Anal. calcd. for $C_{11}H_{13}N_4OP$: C, 53.30; H, 5.28; N, 22.57. Found: C,

53.21; H, 5.28; N, 22.44. FT-IR data (cm^{-1}): 3075, 1584, 1499, 1387, 1276, 1196, 941, 798, 750, 689, and 622.

1: $[Pd(CH_3CN)_4 \cdot 2(BF_4)]$ (22.2 mg, 0.05 mmol) was added to a solution of the ligand $\mathbf{L^1}$ (23.5 mg, 0.095 mmol) in DMSO (1 mL) and stirred at 70 °C for 18 h. The resultant light orange colored solution was cooled to room temperature and poured into a conical flask containing cold ethyl acetate (15 mL). The obtained yellow precipitate was collected through filtration. The residue was washed with ethyl acetate and diethyl ether and dried under vacuum to yield the compound **1**. Isolated yield: 44.3 mg (54%). ^{1}H NMR (600 MHz, DMSO-d_6): δ = 8.75 (d, 6H, NH), 8.53 (d, 6H), 8.47 (d, 6H), 8.31 (d, 6H, NH), 7.57-7.47 (m, 48H), 7.36 (dd, 6H), 7.15 (d, 6H), 6.88 (t, 6H). ^{31}P{^{1}H} NMR (242.95 MHz, DMSO-d_6): δ = 6.94 (s), 12.78(s). ESI-MS calculated m/z= 453.07, 482.50, 498.07, 597.12, 513.40, 633.06, and 813.3 for $[Pd_3(\mathbf{L^1})_6+BF_4]^{5+}$, $[Pd_3(\mathbf{L^1})_6+7DMSO+10H_2O]^{6+}$, $[Pd_3(\mathbf{L^1})_6+9DMSO+6H_2O]^{+6}$, $[Pd_3(\mathbf{L^1})_6+BF_4+7DMSO+10H_2O]^{+5}$ $[Pd_4(\mathbf{L^1})_8 \cdot 2(BF_4)]^{6+}$, $[Pd_4(\mathbf{L^1})_8 \cdot 3(BF_4)]^{5+}$, and $[Pd_3(\mathbf{L^1})_6 \cdot 4(BF_4)]^{4+}$, respectively. Anal. calcd. for $C_{96}H_{90}N_{24}O_6P_6B_6F_{24}Pd_3$: C, 42.68; H, 3.36; N, 12.44. Found: C, 43.80; H, 3.85; N, 12.10. FT-IR data (cm^{-1}): 3298, 1580, 1497, 1395, 1282, 1021, 935, 805, 759, 693, and 627**.**

2: To a solution of ligand $\mathbf{L^2}$ (29.5 mg, 0.095 mmol) in DMSO (1 mL), $[Pd(CH_3CN)_4 \cdot 2(BF_4)]$ (22.2 mg, 0.05 mmol) was added and stirred at 70 °C for 24 h. The resultant solution was cooled to ambient temperature and poured into a conical flask containing cold ethyl acetate (25 ml). The obtained yellow precipitate was collected through filtration.

The residue was washed with ethyl acetate and diethyl ether and dried under vacuum to yield compound **2**. Isolated yield: 45.3 mg (47%). ^{1}H NMR (600 MHz, DMSO-d_6): δ = 8.16 (s, broad, 12H), 8.13 (d, 12H), 7.21 (m 12H), 7.08 (d, 12H), 1.25 (d, 18H). ^{31}P{^{1}H} NMR (242.95 MHz, DMSO-d6): δ= 25.02 (s). ESI-MS calculated m/z= 495.05, and 689.07 for $[Pd_3(\mathbf{L^2})_6 \cdot 2(BF_4)]^{+4}$, and $[Pd_3(\mathbf{L^2})_6 \cdot 3(BF_4)]^{+3}$. Anal. calcd. for $C_{66}H_{78}N_{24}O_6P_6Pd_3$: C, 34.03; H, 3.38; N, 14.43. Found: C, 33.55; H, 3.31; N, 14.10. FT-IR data (cm^{-1}): 3273, 1582, 1483, 1394, 1278, 1189, 1019, 930, 807, 763, and 691.

2.2.3 NMR studies

The 2D-COSY and TOCSY and 1D-TOCSY NMR experiments were recorded on Bruker 600 MHz spectrometer. Diffusion ordered spectroscopy (DOSY) NMR experiments were

performed on Bruker 600MHz NMR at a constant temperature of 298 K. The DOSY experiments were performed by varying gradient strength between 2-95%. Diffusion time (Δ) and length of the gradient (δ) was optimized for each system, so as to get ~90-95 % signal reduction in peak of interest at 95 % gradient strength with a maximum gradient strength of 42.58 G/cm. Sixteen data points were collected between 2-95 % of gradient strength with 32 scans for each gradient step. The DOSY data collected was processed and extracted as separate 1D corresponding to each gradient field strength. Peak picking was done in topspin 3.2. The Fitting of the intensities was done in OriginPro 8.5.0 using two parameters mono-exponential fit.

$$I = I_0 \exp\left[-D\gamma^2 g^2 \delta^2 \left(\Delta - \frac{\delta}{3}\right)\right]$$

Where I am the observed integral, I_0 the reference or un-attenuated integral, D the diffusion coefficient, γ the gyromagnetic magnetic ratio of the observed nucleus, g the gradient strength, δ the length of gradient pulse and Δ the diffusion time. 1D- TOCSY experiments were carried out by irradiating Ha or Ha´ protons in the molecule using a selective pulse sequence in the Bruker library with 80 ms TOCSY mixing time.

2.2.4 Crystallography

The single-crystal diffraction data of **1a** was collected using Bruker D8 Venture diffractometer with Microfocus X-ray source and photon detector. Suitable single crystals were mounted, and the data were collected using graphite -monochromatic Cu Kα radiation (1.5418Å) at 100 K. The structure was solved by the direct method using SHELX-2014.[28] Due to the very small size of the crystals and its opaque nature, only the heavier elements of Pd and P and the O-atoms attached to the P-atoms were refined anisotropically. All the remaining atoms of B, F, N, C and solvated O-atoms were refined isotropically. The hydrogen atoms were fixed at the geometric positions using a riding model. Two of the three BF_4 anions in the asymmetric unit were disordered. Atom positions of the disordered fragments were refined using the same distance and similar U-restraint (SAME/SIMU) commands of the SHELX. Details pertaining to the crystallographic refinement, selected bond-lengths and angles and hydrogen bond parameters are listed in the supporting information (Table 2.1, A1-A3, Appendix 2).

Table 2.1: Crystallographic information table of compound **1a.**

Details of crystallographic data and structural refinements of compound_1a	
Identification code	compound_1a
Empirical formula	C96 H102 B6 F24 N24 O12 P6 Pd3
Formula weight	2809.89
Temperature	100(2) K
Wavelength	1.54178 Å
Crystal system	Orthorhombic
Space group	A b a 2
Unit cell dimensions	a = 21.6122(19) Å α= 90° b = 21.9302(19) Å β = 90°.
Volume	c = 25.345(2) Å γ = 90°.
	12012.4(18) Å3
Z	4
Density(calculated)	1.554 Mg/m3
Absorption coefficient	5.247 mm-1
F(000)	5664
Crystal size	0.02 x 0.01 x 0.01 mm3
Theta range for data collection	8.923 to 66.777°.
Index ranges	-23<=h<=25, -25<=k<=26, -30<=l<=30
Reflections collected	39076
Independent reflections	10120 [R(int) = 0.2150]
Completeness to theta = 66.777°	97.9 %
Absorption correction	Semi-empirical from equivalents
Max. and min. transmission	0.753 and 0.597
Refinement method	Full-matrix least-squares on F2
Data / restraints / parameters	10120 / 575 / 326
Goodness-of-fit on F2	1.047
Final R indices [I>2sigma(I)]	R1 = 0.1145, wR2 = 0.2755
R indices (all data)	R1 = 0.1988, wR2 = 0.3300
Absolute structure parameter	0.12(3)
Extinction coefficient	n/a
Largest diff. peak and hole	1.071 and -0.637 e.Å-3

2.2.5 Computational Methods

All the calculations were performed by Gaussian 09 suit programmed. The molecular core structures of [**1a**]$^{6+}$, [**1b**]$^{8+}$ and [**2**]$^{6+}$ were optimized by the density functional theory (DFT) methods by using the RB3LYP basis sets for all the atoms. The geometry-optimization data for **1a**, **1b**, and **2** are summarized in the supporting information (Tables A4-A6 Appendix 2).

2.3 RESULTS AND DISCUSSION

2.3.1 Syntheses

The ligand $\mathbf{L^1}$ was synthesized from the reaction of 3-aminopyridine with $PhPOCl_2$ precursor in the presence of basic medium in dry toluene solvent. Further, synthesis the ligand $\mathbf{L^2}$ was done by following the similar procedure as used for ligand $\mathbf{L^1}$. We used the different workup procedure for $\mathbf{L^2}$ ligand as it was soluble in water solvent. Therefore, the resulted precipitate was washed many times by the dichloromethane (DCM) solvent to remove the ammonium salt (Figure A1-A9, Appendix 2). The self-assembled bulk products of **1** consisting of $[Pd_3(L^1)_6\cdot(BF_4)_6]$ (**1a**) and $[Pd_4(L^1)_8\cdot(BF_4)_8]$ (**1b**) and $[Pd_3(L^2)_6\cdot(BF_4)_6]$ **2** can be gained by combination of $[Pd(CH_3CN)_4\cdot 2(BF_4)]$ with the ligands $\mathbf{L^1}$ and $\mathbf{L^2}$, respectively. To shed more light on the formation of the tri- and tetrameric assemblies, NMR studies were performed for the in-situ reaction of $\mathbf{L^2}$ with $[Pd(CH_3CN)_4\cdot 2(BF_4)]$ in DMSO-d_6 in the 2:1 ratio. The resulting mixture was heating at 70 ^oC and equilibrated for 20 h to obtain a red wine solution

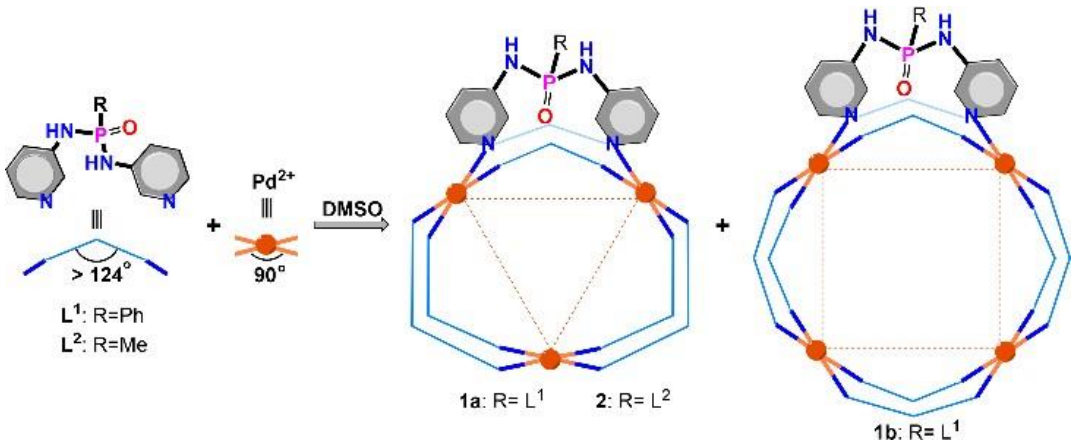

Scheme 2.1: *Schematic representation for the preparation of molecular trimers* $[Pd_3(\mathbf{L^1})_6.6BF_4]$ ***(1a)*** *and* $[Pd_3(\mathbf{L^2})_6\cdot 6BF_4]$ ***(2)*** *and tetramer* $[Pd_4(\mathbf{L^1})_8\cdot 8BF_4]$ ***(1b)***.

2.3.2 Mass analysis

The sample were prepared for the ESI-MS spectral analyses by diluted DMSO with few drops of MeCN solution of **1** exhibited a prominent peak at m/z = 453.05 that can be assigned to the species $[Pd_3(\mathbf{L^1})_6+BF_4]^{5+}$. In addition, a peak centered at 813.09 appear for the species corresponding to $[Pd_4(\mathbf{L^1})_8+4BF_4]^{4+}$ (Figure 2.1). Furthermore, additional peaks pertaining to

both the trimeric and tetrameric species were observed in the ESI-MS spectrum of **1** (FigureA10, Appendix 2). Therefore, ESI-MS analysis suggested the existence of mixture of both **1a** and **1b** in product **1**. To calculate mass of each peak of the trimeric and tetrameric complexes by using molecular weight calculator software and matched with the experimental mass (Figure 2.1). The change in polarity of the solution was further subjected for the mass-spectral analysis, which gave major peaks with m/z values centered at 353.3, 513.4, 633, and 813.3 that are predominantly associated with the tetrameric species **1b** (Figure A11 Appendix 2). The ESI-MS spectrum of **2** gave peaks at m/z = 495.05, and 689.07, corresponding to the $[Pd_3(\mathbf{L^2})_6{\cdot}2BF_4]^{4+}$, and $[Pd_3(\mathbf{L^2})_6{\cdot}3BF_4]^{3+}$ (Figure A12, Appendix 2). The absence of peaks pertaining to the tetrameric species clearly suggests the formation of the trimeric assembly of **2** as a single product

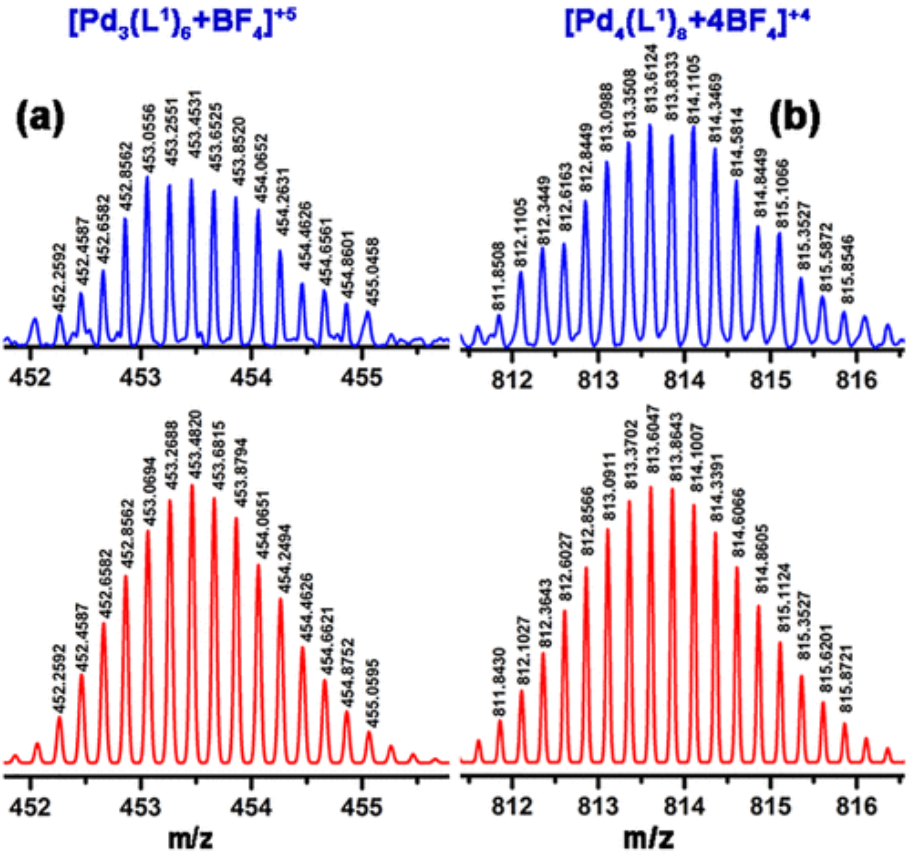

Figure 2.1*: The representative m/z fragments of* ***1a*** *(A) and* ***1b*** *(B) obtained from the ESI-MS analysis. The blue and red graphs are the isotopic distribution of peaks derived from the experimental (top) and simulated (below) profiles.*

2.3.4 NMR analysis

To further, probe the existence of these species in solution, a series of NMR experiments were carried out on the reaction mixture of **L^1** and [Pd(CH$_3$CN)$_4$·2(BF$_4$)] in DMSO-d$_6$ in the 2:1 ratio. Prior to the measurements, the yellowish color mixture was heated for 18 h at 70 ^{o}C to obtain a red wine solution. The ^{1}H NMR spectrum of the resulting solution consists of two sets of signals with similar integration ratio for the pyridyl protons of ligand **L^1**. Chemical shifts of the proton peaks have been observed perhaps, due to the metal-ligand coordination. The closest protons to the pyridine nitrogen, Ha and Ha' are considerably deshielded and appear at 8.47 and 8.53 ppm, respectively (Figure 2.2a). We have also observed the two sets of -NH proton

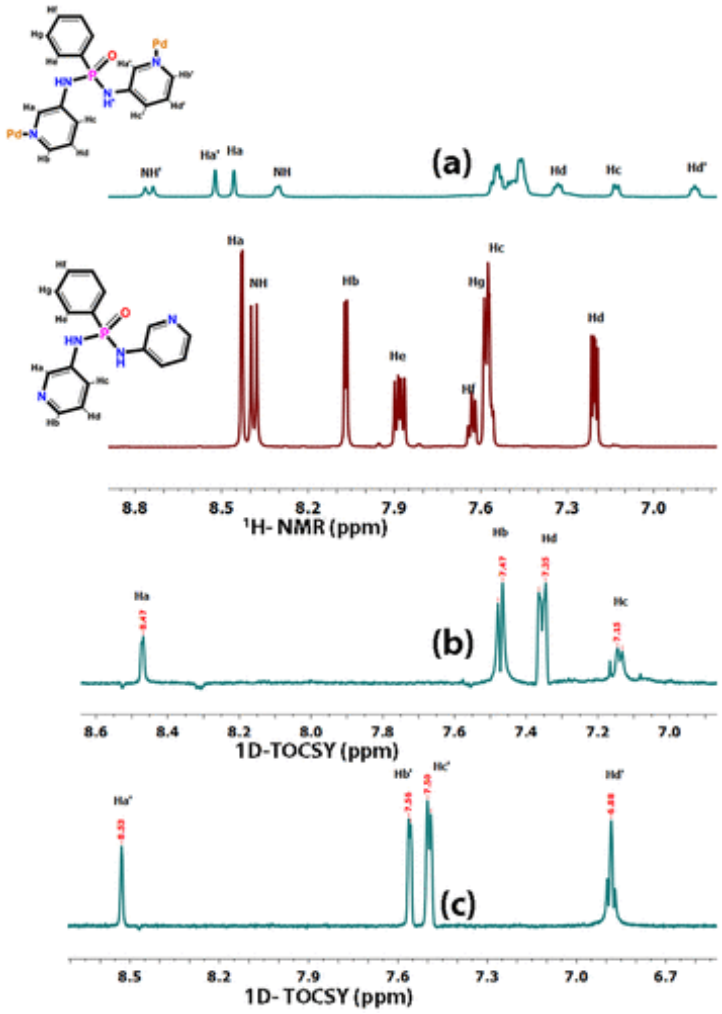

Figure 2.2: *(a) Stacked ^{1}H-NMR of **L^1** (bottom) and **1** (top) in DMSO-d$_6$, (b) and (c), the ^{1}H-^{1}H 1D-TOCSY NMR of **1** showing the correlation of the pyridyl-Ha and pyridyl-Ha' protons respectively.*

peaks as we named NH and NH′ with considearable change in chemical shifts. The chemcal shift changes occurred for NH proton which has been shielded by 0.15 ppm and for deshielded NH proton, chemical shift changes happened by 0.4 ppm. To examine the other proton peaks, proton NMR experiment was unable to give idea about them. The selective ^{1}H-^{1}H 1D-selective-TOCSY spectra was obtained to identify the positions of the remaining pyridyl protons with respect to Ha and Ha'. The selective irradiation of Ha of pyridine ring yields the signals due to Hb, Hc, and Hd in the slightly shielded regions at 7.47, 7.15, and 7.35 ppm, respectively (Figure2.2b). Similarly, the protons of Hb', Hc', and Hd' appeared at 7.56, 7.50, and 6.88 ppm, respectively, upon the selective irradiation of Ha' (Figure 2.2c). Furthermore, the protons of the phenyl ring, He, Hg, and Hf, were identified with a sequence of ^{1}H-^{1}H 2D-TOCSY and ^{1}H-^{1}H 2D-COSY experiments (Figure A13-A14, Appendix 2). Further, ^{31}P-NMR spectrum of the metal-ligand mixture exhibited two new peaks at 6.97 ppm (major) and 12.71 ppm (minor) of same solution with complete disappearance of the peak due to **L^{1}** at 10.06 ppm (Figure A15, Appendix 2). To find out the simultaneous existence of supramolecular tri- and tetrameric assemblies of **1a** and **1b**, the diffusion ordered NMR spectroscopy (DOSY) experiment was performed. In the ^{1}H-2D-DOSY experiment, the diffusion coefficient (D) for the protons Ha (8.47 ppm) and Ha' (8.53) came in the same range with a D-value of 6.27 x e^{-11} $m^{2}s^{-1}$ (Figure 2.3a and Figure A16, Appendix 2). However, the 1D-TOCSY data showed that the protons Ha and Ha' belong to two different pyridine rings, the 2D-DOSY indicate that they belong to only one supramolecular assembly. These NMR studies suggested that both set of proton peaks might belongs to one complex with asymmetric chemical interactions around the pyridine rings make them chemically inequivalent in nature resulted the two sets of proton peaks of the pyridine rings. To understand effect of solvents which is an important factor that influences the equilibrium between trimers and tetramers in the solution,[10] and hence its effect for the assignment of peaks due to **1a** and **1b** was probed in the ^{31}P-NMR experiments. Interestingly, control experiment has been done by changing the polarity of the solution by adding acetonitrile. When the reaction mixture was heated in the three NMR tubes with different polarity of the solution at 70 °C for 14 h in a mixture of MeCN-d_3 and DMSO-d_6 ((0.1: 0.5) mL), ((0.2: 0.4) mL), and ((0.3: 0.3) mL). In case of equivolume of solvent mixtures of DMSO and MeCN, ^{31}P NMR signal at 12.71 ppm appeared as the major peak, while the signal at 6.97 ppm is almost diminished (Figure 2.3b).

These observations suggest that a change in polarity favors the formation of the tetrameric assembly of **1b**.[20]

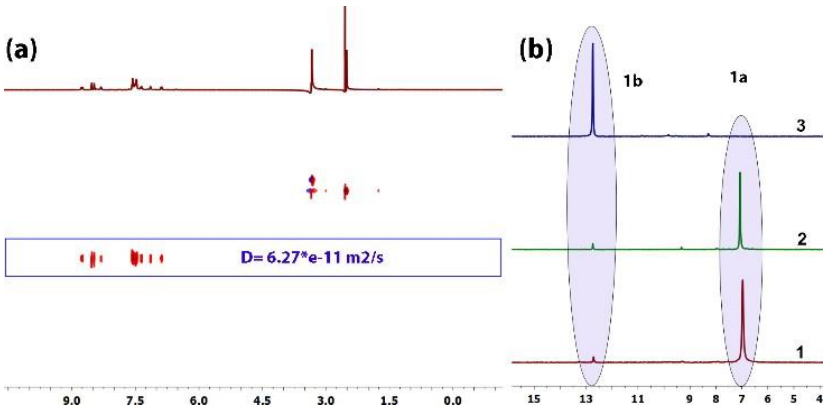

Figure 2.3: *(a) The ^{1}H 2D-DOSY spectra of **1** in DMSO-d_6. (b), solvent dependent ^{31}P NMR spectra of **1** in pure DMSO-d_6 (0.6 mL) (1), 0.2 mL CD_3CN+ 0.4 mL DMSO-d_6 (2), and 0.3* mL *CD_3CN+ 0.3 mL DMSO-d_6 (3).*

This solution was further subjected for the mass-spectral analysis, which gave major peaks with m/z values centered at 353.3, 513.4, 633, and 813.3 that are predominantly associated with the tetrameric species **1b** (Figure A11, Appendix 2). Furthermore, to check the quantitative effect of the temperature on the mixture of the trimeric and tetrameric assemblies in solution, temperature-dependent ^{31}P NMR in DMSO-d_6 has been performed and revealed that the peak at 12.71 ppm starts to disappear as the temperature of the DMSO solution increases and completely vanish above 328 K, (Figure A17, Appendix 2). The temperature- dependent ^{31}P NMR indicates that the species corresponding to the peak at 6.94 ppm is the entropically favored trimeric assembly **1a**. However, temperature-dependent ^{1}H NMR showedshielding of the NH protons due to the weakening of the H-bonding interactions at high temperature (Figure A18, Appendix). The calculated temperature coefficient value -3.2 ppb/Ksuggests the presence of strong hydrogen bonding interactions for the NH proton within the molecule (Figure A19, Appendix 2).[29] However, the concentration-dependent ^{1}H-NMR showsno shift in the peak positions of the NH protons, while the ^{31}P NMR experiments showed a mixture of products **1a** and **1b** in the solution at all the measured concentrations, albeit with minor quantities of **1b** (A20-A21, Appendix 2). Flexibility of the building units can play a vitalrole to get the trimeric assemblies over tetramer.

To probe the flexibility of the ligand leads the formation of the trimeric assembly, we shed more light on the formation of the tri- and tetrameric assemblies, NMR studies were performed for the in-situ reaction of $\mathbf{L^2}$ with $[Pd(CH_3CN)_4 \cdot 2(BF_4)]$ in DMSO-d_6 in the 2:1 ratio. The resulting mixture was heating at 70 ^oC and equilibrated for 20 h to obtain a red wine solution. The ^{1}H-NMR spectrum of **2** gave only one set of protons with chemical shifts in the slightly shielded regions for the methyl and pyridyl protons (Figure 2.4a). The ^{31}P NMR spectrum also showed only one peak at 25.02 ppm (Figure 2.4b). The ESI-MS spectrum of **2** gave peaks at m/z = 495.05, and 689.07, corresponding to the $[Pd_3(\mathbf{L^2})_6 \cdot 2BF_4]^{4+}$, and $[Pd_3(\mathbf{L^2})_6 \cdot 3BF_4]^{3+}$ (Figure A12, Appendix 2).

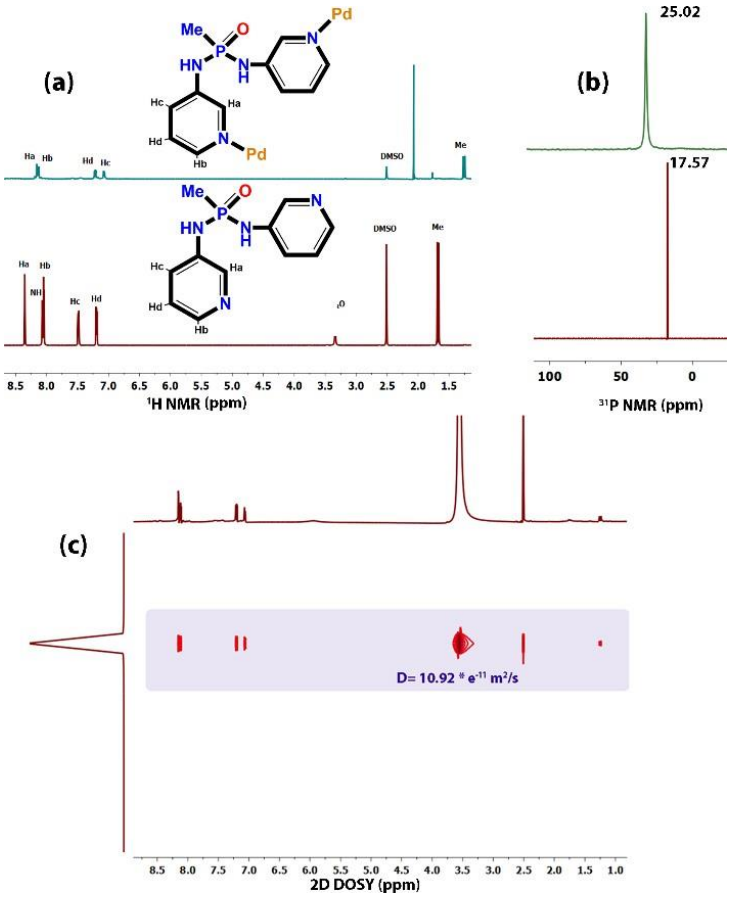

Figure 2.4: (*a) Stacked ^{1}H-NMR of $\mathbf{L^2}$ (bottom) and **2** (top) in DMSO-d_6, (b) stacked ^{31}P NMR of ligand $\mathbf{L^2}$ (bottom) and **2** (top) in DMSO-d_6. (c) The ^{1}H 2D-DOSY profile of **2** in DMSO-d_6.*

The absence of peaks pertaining to the tetrameric species clearly suggests the formation of the trimeric assembly of **2** as a single product. The formation of **2** has also been observed using water as the solvent in the reaction, as revealed by the NMR spectrometric analysis (Figure A22- A23, Appendix 2). The DOSY NMR studies gave a single diffusion coefficient (D) value of 10.92 x e^{-11} m^2s^{-1} in DMSO-d_6, confirming the presence of only one assembly in solution (Figure 2.4c, A24 Appendix 2). Unlike **1**, the DOSY spectrum of **2** revealed the association of the cage with solvent molecules of water and DMSO. This indicates that **2** is more hydrophilic in nature than **1a**. Since the DOSY experiment roughly considers each diffusing particle as a sphere, the observed diffusion coefficient (D) can be correlated with the radius of the sphere using Stokes-Einstein equation.[30] A radius value of 10.05 Å was obtained by feeding the observed D-value of **2** in this equation, which is closely comparable with the observed radius of 9.5 Å from the energy-optimized structure of **2** (Figure A25, Appendix 2).

2.4 Structural Analysis

The structure of the trimeric assembly of **1a** has further been confirmed by single-crystal X-ray diffraction analysis (SC-XRD). Yellow-colored crystals of **1a** were grown from the MeCN/Methanol solution of **1**. Crystals of **1a** also got through (diffusion method) diffusion of ethylaccetate into the concentrated DSMO solution of product **1.** The molecular structure of **1a** was solved in the orthorhombic space group Aba2 (Figure 2.5a). The asymmetric unit consists of three phosphoramide ligands and two Pd (II) atoms, one in a general position and another one in a special position with one-half occupancy. Two of the three $[BF_4]^-$ ions in the asymmetric unit were disordered over five positions. The molecular core consists of a Pd_3L_6 core with a nearly equilateral triangular geometry for the three Pd(II) atoms (Figure 2.5b). The angle between the two adjacent Pd-centers is nearly 60° (<Pd1-Pd2-Pd1 = 58.162(1)°; (<Pd2-Pd1-Pd1 = 60.919(1)°) with an overall angle of 180° for the cage core. The distance between the two adjacent Pd (II) atoms is around 9 Å (*d* (Pd1-Pd2) = 9.21 Å and *d* (Pd2-Pd3 = 8.95 Å)). Each Pd (II)-atom is located in square-planar coordination with four pyridyl groups from four different ligand moieties. The two coordinating N-pyridyl groups at each of these ligands are mutually positioned in a *syn* conformation as the P=O groups are pointing inwards in an *endo* orientation. There are six molecules of solvated water, of which five of them were located at the intrinsic void of the cage exhibiting an axially compressed TBP geometry (Figure 5c). The water molecules at the equatorial positions interact with all the six phosphoramide ligands via H-bonding interactions. The intrinsic void of this cage was calculated to be 74 $Å^3$ by MS Roll

calculations by using a probe radius of 1.4 Å.[31] There are twelve amino protons available on the cage periphery for H-bonding interaction of which ten of them were involved in H-bonding with the $[BF_4]^-$ ions. The remaining two protons are H-bonded to the exo cage solvate water molecules. The $[BF_4]^-$ motifs centered around B2 and B4 atoms tether the adjacent cages that results in the formation of a two-dimensional H-bonded network.

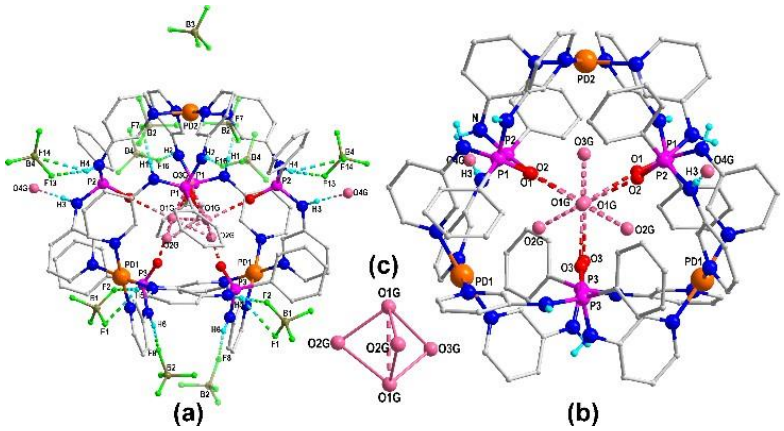

Figure 2.5: (a) *Molecular structure of **1a** showing the cage molecule interacting with the anions and solvate molecules. The BF_4 ions shown as the semi-transparent segments belong to the adjacent cage motifs. (b) View of the $Pd_3L^1{}_6$ core along with the H-bonded solvated and encapsulated water molecules of the cage. (c) View of the pentameric water cluster at the intrinsic void of the cage.*

Furthermore, the core structures of **2** and **1b** were optimized by using DFT methods (Figure A25-A26 Appendix 2). For a better comparison the structure of **1a** has also be optimized, which reveals that the energy minimized structure of **1a** correlates closely with the structure obtained from the single-crystal X-ray diffraction analysis (Figure A27, Appendix 2). The optimized structure of **2** resembles very close to the experimental structure of **1a**. Again, the angle between the two adjacent Pd(II) centers is close to 60 ° and the overall angle of 180 ° for cage core. The cationic core of **1b** has been found to be well-optimized. The structure of **1b** consists of four Pd(II) atoms in a planar configuration that are connected by a pair of dipodal phophoramide ligands above and below the Pd4 plane (Figure 2.6a).

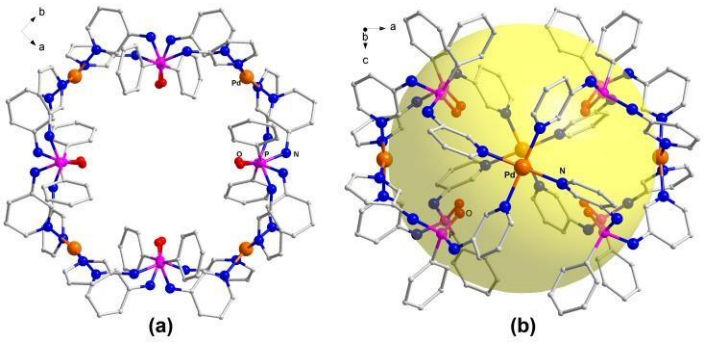

***Figure 2.6**: The structure of the tetrameric core in **1b** optimized by DFT methods. View of the $[Pd_4(\boldsymbol{L^1})_8]^{8+}$ core in **1b** (a) along the c-axis and (b) along the b-axis. The yellow sphere in 'b' shows the presence of a large void in the cavitand-like structure of **1b**.*

Each Pd(II) atom is coordinated with four $N_{pyridyl}$ moieties from four different ligand segments. As observed in **1a**, the ligand $N_{pyridyl}$ groups are positioned in a syn orientation and the P=O group are positioned in an endohedral fashion. While the Pd-Pd-Pd angle in the tetramer is 90°, the P-Pd-P angle that connects the adjacent Pd-centres is 83.20°. The cavitand-like structure of **1b** is very similar to those reported earlier based on L^1 and other 3d-metal ions, except that the metal-bound aqua ligands at the axial positions are absent in the case of **1b**. As a result, the void space inside the cavitands structure of **1b** is expected to be larger than those found in the structurally similar tetrameric assemblies (155 $Å^3$) based on 3d metal ions and L^1 (Figure 2.6b). To probe the chemical inequivalence of the two pyridylamino rings of the ligand L^1 in **1a**, we performed the Circular Dichroism (CD) experiments for **1** in its DMSO solution (1mg/ mL). The DMSO solution of **1**, in which the trimeric species **1a** is predominantly present, shows a somewhat sharp signal at 245 nm and a broad peak ranging from 265-295 nm. These respective peaks could be attributed to the ligand-centered transitions and the metal-ligand charge transfer transitions. This indicates the chirality observed in the solid-state structure of **1a** is retained in solution as well. In contrast, the compound **2** did not show any notable CD profile at the same concentration (Figures A28-A29, Appendix 2). Additionally, the specific rotation ($[\alpha]_D$) values of **1** and **2** were determined by optical rotation measurements in their DMSO solutions (7mg/ 1ml DMSO). The $[\alpha]_D$ value for **1** was found to be -10.24. However, product **2** did not exhibit any optical rotation values. While the ligands, both L^1 and L^2, are achiral, the origin of chirality in **1a** is quite complex to predict. A closer look at the crystal structure of **1a** revealed that the NH protons in four of the six ligands are involved in H-bonding solely with the $[BF_4]^-$ anions,

while two of them are involved in the interactions with mixed $[BF_4]^-$ and H_2O H-bond acceptors. In addition, the NH groups in two of the four L^1 units were involved in H-bonding with a pair of ordered and disordered $[BF_4]^-$ units (those associated with B1 and B2 atoms). Therefore, the diverse nature of the H-bonding interactions and anion disorders could potentially be the cause for the observed asymmetry in **1a**. Furthermore, it is interesting to compare the ligand N_{py}-P-N_{py} angles provided by the ligands L^1 and L^2 in these trimeric and tetrameric assemblies to those observed for their complexes with other metal ions. The earlier reported X-ray structure of the ligand L^1, containing a phenyl ring as a substituent on the phosphorus atom, exhibits an N_{py}-P-N_{py} angle of 80.7°. In metal coordination it was found to flip between *syn* and mixed *syn-anti* orientation. In all the trimeric and tetrameric assemblies known so far, the *syn* coordination of the ligand L^1 was noticed. In the tetrameric assemblies based on octahedral Ni(II) and Co(II) ions, the N_{py}-P-N_{py} angles of around 111.4 – 112.3° were observed, wherein the slightly higher angles were observed for tetrameric cavitands containing hydrated alkali-metal guest cations.[25] Similar N_{py}-P-N_{py} angles (~112.5°) were found for the Cu 1D-helical assemblies, in which the L^1 exhibits a mixed *syn-anti* coordination. However, in the trimeric and tetrameric cages having five coordinate Cu(II) ions, a drastic increase in the N_{py}-P-N_{py} angles were found for L^1; 121° for the trimeric assembly and 117° for the tetramer.[18] Interestingly, the square-planar Pd(II) ion environment supports more flexibility in the ligand backbone as the N_{py}-P-N_{py} angles, as high as, 129 ° (lowest 128.19 °) were observed for **1a** while those computed for **1b** were measured to be 124.64°. The corresponding computed angles in **2** were were in the range of 125.63-126.31° indicating that the wider N_{py}-P-N_{py} angles are favoured for the formation of trimeric assemblies over the tetramers. Also, these findings exemplify the ability of the ligands L^1 and L^2 to adopt a wide range of angles (ranging from 111 to 129 °) in multi-metallic self-assemblies depending on the cage topologies and steric requirements of the metal ions imposed by their coordination geometries. Thus, the ligand L^2 containing a smaller methyl group on the phosphorus atom can conveniently provide the necessary larger linker-angle required to support the trimeric structure of **2**. Nevertheless, the limited availability of the structural data based on L^2 precludes any comparisons between the steric effects of the phosphorus bound phenyl and methyl substituents towards the favourable formation of one self-assembly over the other.

2.5 CONCLUSION

In summary, a detailed study of the formation of supramolecular trinuclear cages have been performed by using dipodal phosphoramide ligands and tetratopic Pd(II) acceptors. The preferential formation of the entropically-favoured trimeric assemblies of $[Pd_3(L^1)_6 \cdot (BF_4)_6]$ (**1a**) and $[Pd_3(L^2)_6 \cdot (BF_4)_6]$ (**2**) over the enthalpically-favoured tetrameric cages has been observed for both L^1 and L^2, respectively. The flexibility and the steric bulk of the ligand backbone was found to play a key role in driving the formation the trimeric species in solution. Hence, the slightly less flexible and more buliker ligand L^1 yields the tetrameric assembly of $[Pd_4(L^1)_8 \cdot (BF_4)_8]$ (**1b**) as a minor product, whereas no tetramer formation was observed in case

L^2, a relatively more flexible ligand. In addition, solvent dependent studies of **1** shows the irreversible conversation of **1a** to **1b** aided by a thermodynamic control. Further, the molecular structure of **1a** was confirmed by single-crystal X-ray diffraction analysis and the structures of **1b** and **2** were visualized by the DFT derived geometry optimization. The triangle- square (or trimer-tetramer) equilibrium is an intriguing problem in supramolecular chemistry and the present results demonstrate the formation of entropically controlled trimeric products for the complex tetratopic Pd(II) acceptors via the topological control of the ligand backbone.

References

(1) Fujita M.; J. Yazaki; O. Katsuyuki. Preparation of a Macrocyclic Polynuclear Complex, $[(en)Pd(4,4,-bpy)]_4(NO_3)_8$, Which Recognizes an Organic Molecule in Aqueous Media. *J. Am. Chem. Soc*. **1990**, *149*, 5645–5647.

(2) Fujita, M.; Sasaki, O.; Mitsuhashi, T.; Fujita, T.; Yazaki, J.; Yamaguchi, K.; Ogura, K. On the Structure of Transition-Metal-Linked Molecular Squares. *Chem. Commun.* **1996**, *20*, 1535–1536.

(3) Ma, G.; Jung, Y. S.; Chung, D. S.; Hong, J. I. Guest-Induced Binding Site Organization of Self-Assembled Pd(II) Complexes. *Tetrahedron Lett.* **1999**, *40*, 531–534.

(4) Fujita, M.; Ogura, K. Transition-Metal-Directed Assembly of Well-Defined Organic Architectures Possessing Large Voids: From Macrocycles to [2] Catenanes. *Coord. Chem. Rev.* **1996**, *148*, 249–264

(5) Stang, P. J. Molecular Architecture: Coordination as the Motif in the Rational Design and Assembly of Discrete Supramolecular Species - Self-Assembly of Metallacyclic Polygons and Polyhedra. *Chem. - A Eur. J.* **1998**, *4* (1), 19–27.

(6) Sun, S. S.; Lees, A. J. Self-Assembly Triangular and Square Rhenium(I) Tricarbonyl Complexes: A Comprehensive Study of Their Preparation, Electrochemistry, Photophysics, Photochemistry, and Host-Guest Properties. *J. Am. Chem. Soc.* **2000**, *122*, 8956–8967.

(7) He, Z.; He, C.; Wang, Z. M.; Gao, E. Q.; Liu, Y.; Yan, C. H. Self-Assembly of Molecular Squares Based on Easy-to-Prepare Multidentate Schiff Base Ligands. *J. Chem. Soc. Dalt. Trans.* **2004**, *4*, 502–504.

(8) Slone, R. V.; Hupp, J. T.; Stern, C. L.; Albrecht-Schmitt, T. E. Self-Assembly of Luminescent Molecular Squares Featuring Octahedral Rhenium Corners. *Inorg. Chem.* **1996**, *35*, 4096–4097.

(9) Liu, D.; Lin, Y. J.; Aznarez, F.; Jin, G. X. Rational Design and Self-Assembly of Molecular Squares Featuring Cp∗M (M = Rh, Ir) Vertices Bridged by Phenanthroline-Derived Ligands. *Cryst. Growth Des.* **2018**, *18*, 6911–6917.

(10) Carina, R. F.; Williams, A. F.; Bernardinelli, G. Molecular Tricorns: Self-Assembly of Trinuclear Palladium(II) Complexes. *Inorg. Chem.* **2001**, *40*, 1826–1832.

(11) Derossi, S.; Casanova, M.; Iengo, E.; Zangrando, E.; Stener, M.; Alessio, E. Self-Assembled Metallacycles with Pyrazine Edges: A New Example in Which the Unexpected Molecular Triangle Prevails over the Expected Molecular Square. *Inorg. Chem.* **2007**, *46*, 11243–11253.

(12) Ferrer, M.; Mounir, M.; Rossell, O.; Ruiz, E.; Maestro, M. A. Equilibria between Metallosupramolecular Squares and Triangles with the New Rigid Linker 1,4-Bis(4-Pyridyl)Tetrafluorobenzene. Experimental and Theoretical Study of the Structural Dependence of NMR Data. *Inorg. Chem.* **2003**, *42*, 5890–5899.

(13) Zangrando, E.; Casanova, M.; Alessio, E. Trinuclear Metallacycles: Metallatriangles and Much More. *Chem. Rev.* **2008**, *108*, 4979–5013.

(14) Schweiger, M.; Seidel, S. R.; Arif, A. M.; Stang, P. J. Solution and Solid State Studies of a Triangle-Square Equilibrium: Anion-Induced Selective Crystallization in Supramolecular Self-Assembly. *Inorg. Chem.* **2002**, *41*, 2556–2559.

(15) Sautter, A.; Schmid, D. G.; Jung, G.; Würthner, F. A Triangle-Square Equilibrium of Metallosupramolecular Assemblies Based on Pd(II) and Pt(II) Corners and Diazadibenzoperylene Bridging Ligands. *J. Am. Chem. Soc.* **2001**, *123*, 5424–5430.

(16) Das, N.; Mukherjee, P. S.; Arif, A. M.; Stang, P. J. Facile Self-Assembly of Predesigned Neutral 2D Pt-Macrocycles via a New Class of Rigid Oxygen Donor Linkers. *J. Am. Chem. Soc.* **2003**, *125*, 13950–13951.

(17) Schnebeck, R.; Randaccio, L.; Lippert, B. Communications [1]. **1998**, 1997–1999.

(18) Cotton, F. A.; Daniels, L. M.; Lin, C.; Murillo, C. A. Square and Triangular Arrays Based on Mo 24 + and Department of Chemistry, UniVersity of Costa Rica Represents an N, N ′ -Diarylformamidinate Anion) May Be Linked by Linear or Quasilinear Dicarboxylate Anions, and This Is Also True of Proceeded T. *J. Am. Chem. Soc.* **1999**, *121*, 4538–4539.

(19) Cotton, F. A.; Liu, C. Y.; Murillo, C. A.; Wang, X. Dimolybdenum-Containing Molecular Triangles and Squares with Diamidate Linkers: Structural Diversity andComplexity. *Inorg. Chem.*, **2006***45*, 2619–2626.

(20) Umakoshi, K.; Yamauchi, Y.; Nakamiya, K.; Kojima, T.; Yamasaki, M.; Kawano, H.; Onishi, M. Pyrazolato-Bridged Polynuclear Palladium and Platinum Complexes. Synthesis, Structure, and Reactivity. *Inorg. Chem.* **2003**, *42*, 3907–3916.

(21) Fujita, M. Metal-Directed Self-Assembly of Two- and Three-Dimensional Synthetic Receptors. **1997**, 17, 417-425.

(22) Zhu, H.; Li, Q.; Shi, B.; Xing, H.; Sun, Y.; Lu, S.; Shangguan, L.; Li, X.; Huang, F.; Stang, P. J. Formation of Planar Chiral Platinum Triangles via Pillar [5] Arene for Circularly Polarized Luminescence. *J. Am. Chem. Soc.* **2020**, *142*, 17340–17345.

(23) Suzuki, K.; Kawano, M.; Fujita, M. Solvato-Controlled Assembly of Pd3L6 and Pd 4L8 Coordination "Boxes." *Angew. Chemie - Int. Ed.* **2007**, *46*, 2819–2822.

(24) Kumar Srivastava, A., Praveenkumar, B., Kumar Mahawar, I., Divya, P., Shalini, S., & Boomishankar, R. Anion Driven [CuIIL2]n Frameworks: Crystal Structures, Guest-Encapsulation, Dielectric, and Possible Ferroelectric Properties. *Chem. Mater.*, **2014**, *26*, 3811–3817.

(25) Kumar Srivastava, A., Divya, P., Praveenkumar, B., & Boomishankar, R. Potentially Ferroelectric {CuIIL2}n Based Two-Dimensional Framework Exhibiting High Polarization and Guest-Assisted Dielectric Anomaly. *Chem. Mater.*, **2015**, *27*, 5222–5229.

(26) Yadav, A.; Srivastava, A. K.; Kulkarni, P.; Divya, P.; Steiner, A.; Praveenkumar, B.; Boomishankar, R. Anion-Induced Ferroelectric Polarization in a Luminescent Metal-Organic Cage Compound. *J. Mater. Chem. C* **2017**, *5*, 10624–10629.

(27) Yadav, A.; Srivastava, A. K.; Balamurugan, A.; Boomishankar, R. A Cationic Copper(I) Iodide Cluster MOF Exhibiting Unusual Ligand Assisted Thermochromism. *Dalt. Trans.* **2014**, *43*, 8166–8169.

(28) Sheldrick GM. A short history of SHELX. Acta Crystallogr A. **2008**, 112-22.

(29) Baxter, N. J.; Williamson, M. P. Temperature Dependence of ^{1}H Chemical Shifts in Proteins. *J. Biomol. NMR.* **1997**, *9*, 359– 369.

(30) T. Edward, J. Molecular volumes and the Stokes-Einstein equation. *Journal of Chemical Education*, **1970**, *47*.

(31) Barbour, L. J. Crystal Porosity and the Burden of Proof. *Chem. Commun.* **2006**, 1163–1168.

END of CHAPTER 2

CHAPTER 3

Piezoelectric polymer composites of M_6L_8 discrete cages and their energy harvesting applications.

3.1 Introduction

Energy harvesting as a technology, is gaining tremendous attention worldwide with rapid technological progression, expanding automation, and spreading electronic networks. Currently, most of these demands are achieved by consuming non-renewable resources such as fossil fuels (coal, oil, petroleum, and natural gas), metal ores, and earth minerals, etc.[1-3] In this regard, researchers have come up with alternative sustainable and highly abundant energy sources of different kind such as solar, heat, wind, biomass, biofuel, tidal and mechanical energy.[4-12] Among these the conversion of mechanical energy into electrical energy is of significant interest due to its easy generation from a variety of external sources such as pressure, fluctuations, bending, folding, and stretching movements. Energy harvesting frompiezoelectric materials is largely explored in recent research where the material does not possess a centre of inversion. In this aspect, ferroelectric materials which are inherently piezoelectric can be used to generate electrical power out of mechanical input. Ferroelectric materials are special type of dielectric materials and subgroup of both piezo- and pyroelectric materials. Dielectric materials are electrically insulating or nonconducting materials; typically,their band gap is greater than 3 eV. However, dielectric materials get polarized when subjectedto an external electric field.[13-15] In general, dielectric materials are classified into two main categories, namely linear and nonlinear dielectrics. The primary applications of nonlinear dielectric materials are in capacitors, transformers, resonators, transducers, semiconductor devices, noise filters, radio frequency transmitters, power cables, gate dielectrics, and liquid crystal displays etc. [16-18]

Piezoelectric devices have been playing key roles in wearable electronics, and will continue to do so in near future, because of their advantages like functioning without any external bias voltage and getting less affected by external conditions like humidity, temperature etc.[19-20] The importance of self-power technology is based on driving a device or sensor by harvesting energy from piezoelectric, triboelectric, thermal gradient, or solar cells methods.[21-24] When a piezoelectric material is subjected to applied stress or mechanical vibration, the induced displacement of ions results in a net electric charge due to a change in the dipole moment of the unit cell, which builds a piezoelectric potential across the material.[25-26]

Nanogenerators using functional materials have been developed as a disruptive innovation, generating voltage in response to mechanical force (vice versa). Conventional piezoelectric materials such as Zinc oxide (ZnO), Barium Titanate ($BaTiO_3$), lead zirconate titanate ($PbTiO_3$) and zinc stannate ($ZnSnO_3$) exhibited very high piezoelectric response however, they contain the toxic and heavy metals which limits their application in flexible electronics.[27-30] Such issues possessed by ceramic materials can potentially be addressed by investigating organic and organic-inorganic hybrid materials, which are flexible in nature.

Earlier, our group has synthesized the family of cationic $[Cu^{II}L_2]_n$, $[Ni^{II}L_2]_4$, and$[Co^{II}L_2]_4$ based coordination assemblies derived from dipodal phosphoramide ligands of the type $[PhPO(NHPy)_2]$, (Py = 3-pyridyl (^{3}Py) or 4-pyridyl(^{4}Py)) and $[PS(NH^3Py)_3]$, which showed tuned ferroelectric responses depending on the counter anions, the dimensionality of the framework and guest molecules present in them.[32-34] Utilizing a similar C_3-symmetric ligand $[PS(NH^3Py)_3]$, our group has synthesized a family of octahedral cages of the type $[M_6L_8]^{12+}$ (point group *O*) and explored their ferroelectric properties[35-36], where the ferroelectric response is generated due to the toggling of the nitrate anions and water moleculesplaced in between two cage moieties. Herein, we report two discrete octahedral cages of formula $\{[Ni_6L_8.12H_2O][12NO_3]\}.xH2O$ (1) and $\{[Zn_6L_8.12H_2O][12NO_3]\}.xH2O$

(2) formed by the self-assembly reaction of a flexible tripodal ligand tris(3-amino- pyridyl) phosphoramide, $[PO(NH^3Py)_3]$ (L), with hydrated $Ni(NO_3)_2$ and $Zn(NO_3)_2$,respectively. Both the cages were crystalized in the non-centrosymmetric polar *I4* space groupthat motivated us to explore their dielectric and piezoelectric properties. We have prepared thecomposites films of both 1 and 2 in PDMS polymers of different weight percentages (1, 5, 10 and 15 wt%) and studied their piezoelectric energy harvesting (nanogenerator) application. Themaximum peak-to-peak output voltages of 8.2 and 11.3 V were recorded for the best performing composite devices of 10wt%_1 and 10wt%_2, respectively. Using a 4 MΩresistor, the maximum peak-to-peak currents were calculated to be 2.06 μA and 2.83 μA for the corresponding 10wt % composite devices of cage1 and cage2. The calculated current densities for both 10wt%_1 and 10wt%_2 composite devices are 0.41 and 0.57 μAcm^{-2} and the respective power densities are 3.38 and 6.45 μWcm^{-2}. Further, these composites filmshave been utilized to charge a 10 μF capacitor by channeling the generated output voltages through a bridge rectifier diode circuit.

3.2 Experimental section:

3.2.1 General remarks

All the solvents and reagents were obtained from commercial sources. $POCl_3$ was freshly distilled prior to the experiment and the solvent toluene was dried over sodium and distilled. The reagent 3-aminopyridine was used without further purification. The NMR-grade solvents such as DMSO-d_6 and MeOH-d_4 were purchased from Sigma Aldrich and were used as received. The NMR spectra were recorded on a Bruker or Jeol 400 MHz spectrometer, (^{1}H NMR, 400.13 MHz), $^{13}C\{^1H\}$ NMR, 100.62 MHz, and $^{31}P\{^1H\}$ NMR, 161.12 MHz), using $SiMe_4$ (^{1}H, ^{13}C NMR) and 85% H_3PO_4 (^{31}P NMR) as standards. The ESI-MS spectra were obtained on a Waters Synapt G2 Q-TOF spectrometer. The MALDI-TOF spectra wererecorded on an Applied Biosystem MALDI-TOF/TOF system. FT-IR spectra were recorded on a Perkin-Elmer spectrophotometer in the ATR mode. Melting points were analyzed using an Electrothermal melting point apparatus and were uncorrected. Dielectric data has been reordered Solartron Analytical 1260 model Impedance Analyzer coupled with a Dielectric Interface 1296A operating with Janis 129610A cryostat sample holder and a Lakeshore 336 model temperature controller. The d_{33} coefficient measurements were performed on a Berlincourt Piezometer. A custom-made impact machine has been used to run all the piezoelectric experiments.

3.2.2 Syntheses

L: The ligand L was synthesized by a slightly modified procedure reported earlier in the literature. A diluted solution of $POCl_3$ (0.5 ml, 5.2 mmol) in 20 ml toluene is added dropwise into a stirred suspension of 3-aminopyridine (1.48 g, 15.7 mmol) and triethylamine (2.4 ml, 16 mmol) in 100 mL of dry toluene at ice-cold conditions in the presence of argon gas flow. A white precipitate was immediately formed upon the addition of $POCl_3$. The mixture was stirred for a further period of 30 minutes at the same conditions and subsequently refluxed for 8 hours under argon atmosphere to allow the reaction to complete. The resulting precipitate was collected by filtration and washed with water several times, and dried in vacuum for 24 hours. Yield: 1.5 g (90%) ^{1}H NMR: (400 MHz, DMSO-d_6) δ = 8.45 (s, 3H, NH), 8.42 (s, 3H, PyNH), 8.08 (d, 3H, PyNH), 7.55 (m 3H, PyNH), 7.24 (dd, 3H, PyNH). $^{31}P\{1H\}$ NMR: (161.12 MHz, DMSO-d_6) δ = -3.77 (s). MALDI- TOF m/z = 326.10. Anal. calcd. for $C_{15}H_{15}N_6OP$: C, 55.21;

H, 4.63; N, 25.76. Found: C, 54.05; H, 4.69; N, 25.84. FT-IR data (cm^{-1}): 3088, 1587, 1477, 1386, 1197, 1121, 1061, 938, 810, 699, and 514.

1: To a stirred solution of the ligand L (32.6 mg, 0.1 mmol) in 1.5 ml of MeOH, a solutionof $Ni(NO_3)_2 \cdot 6H_2O$ (89.2 mg, 0.3 mmol) in 1 ml of H_2O was added. The resulting clear blue colored solution was kept for stirring at room temperature for 2 h and then left for crystallization. After 5 days, blue colored crystals of Cage **1** in hexagonal morphology were obtained. Isolated yield: 85% (28 mg) ESI-MS; We have observed fragmented peaks of the cages instead of mass of whole cage, this could be due to breakage of weak metal-ligand coordination bonds during the ESI experiment. Anal. calcd. for $C_{120}H_{144}N_{60}O_{56}P_8Ni_6$: C, 36.74; H, 3.70; N, 21.42. Found: C, 36.05; H, 3.67; N, 21.84. FT-IR data (cm^{-1}): 3159, 2966, 1640, 1586, 1388, 1263, 961, 689.

2: To a stirred solution of the ligand L (32.6 mg, 0.1 mmol) in 1.5 ml of MeOH, a solutionof $Zn(NO_3)_2 \cdot 6H_2O$ (89.7 mg, 0.3 mmol) in 1 ml of H_2O was added. The resulting clear colourless solution was kept for stirring at room temperature for 2 h and was left for crystallization. After 5 days, colourless crystals of hexagonal morphology were obtained. Isolated yield: 85% (28 mg). δ = 8.48 (d, 24H, NH), 8.45 (d, 24H, PyNH), 8.08 (dd, 24H, PyNH), 7.59 (m, 24H, PyNH), 7.27 (dd, 24H, PyNH). $^{31}P\{^1H\}$ NMR: (242.95 MHz, DMSO-d_6) δ= -4.36 (s). ESI-MS; We have observed fragmented peaks of the cages instead of mass of whole cage, this could be due to breakage of weak metal-ligand coordination bonds during the ESI experiment. Anal. calcd. for $C_{120}H_{144}N_{60}O_{56}P_8Zn_6$: C, 36.37; H, 3.66; N, 21.21. Found: C, 36.10; H, 3.54; N, 21.40. FT-IR data (cm^{-1}): 3155, 2963, 1642, 1586, 1389, 1263, 959, 689.

3.2.3 Crystallography

The single crystal X-Ray diffraction data of cage1 and cage2 were collected using Bruker D8 Venture microfocus diffractometer. Suitable single crystals were mounted, and the data were collected using graphite -monochromatic Mo Kα radiation (1.5418Å) at 100 K. Intrinsic method has been used to solve the both crystals using SHELX-2014.[37] Except hydrogen atoms, all atoms were refined aniosotopically. A loss of crystallinity on removal of the crystals from the mother liquor caused a low-quality data collection. The hydrogen atoms were fixed at the geometric positions using HFIX restrain. Both cages possess disordered nitrates anions and water molecules, which could not be precisely located. Platon software has been used to

squeeze the disordered atoms from both compounds 1 and 2.[38] EADP and ISOR restrains have beenused to fix the carbon atoms of phenyl rings. Details about to the applied crystallographic refinements, selected bond lengths, and angle parameters are listed in the appendix (Table 3.1, Appendix 3).

Table 3.1 Crystallographic information table of compounds 1 and 2.

Compound	**1**	**2**
Empirical formula	C_{120} H_{144} N_{48} O_{20} P_8 Ni_6	C_{120} H_{144} N_{48} O_{20} P_8 Zn_6
Formula weight	3208.34	3172.48
Temperature	100(2) K	100(2) K
Wavelength	0.71073 Å	0.71073 Å
Crystal system	Tetragonal	Tetragonal
Space group	I 4	I 4
Unit cell dimensions	a = 21.1380(17) Å, α = 90°	a = 21.1064(17) Å, α = 90°
	b = 21.1380(17) Å, β = 90°	b = 21.1064(17) Å, β = 90°
	c = 24.705(2) Å, γ = 90°	c = 24.705(2) Å, γ = 90°
Volume	11039(2) $Å^3$	11005(2) $Å^3$
Z	2	2
Density (calculated)	0.925 mg/m^3	0.951 mg/m^3
Absorption coefficient	0.750 mm^{-1}	0.613 mm^{-1}
F(000)	3032	3240

Theta range for data collection	1.268 to 19.873°.	1.649 to 21.619°.
Reflections collected	46535	56157
Independent reflections	5080 [R(int) = 0.0452]	6415 [R(int) = 0.0593]
Completeness to theta	100 %	99.9 %
Refinement method	Full-matrix least-squares on F2	Full-matrix least-squares on F2
Data / restraints / parameters	5080 / 5 / 409	6415 / 1 / 385
Goodness-of-fit on F2	1.046	1.005
Final R indices [I>2sigma(I)]	R1 = 0.0452, wR2 = 0.1115	R1 = 0.0482, wR2 = 0.1237
R indices (all data)	R1 = 0.0502, wR2 = 0.1162	R1 = 0.0550, wR2 = 0.1285
Absolute structure parameter	0.35(3)	0.50(3)
Largest diff. peak and hole	0.602 and -0.640 e.Å^{-3}	0.596 and -0.785 e.Å^{-3}

3.2.4 Dielectric and Piezoelectric measurements:

The dielectric data for compounds 1 and 2 were measured using Solartron Analytical 1260 modelImpedance Analyzer coupled with a Dielectric Interface 1296A operating with Janis 129610Acryostat sample holder and a Lakeshore 336 model temperature controller. The powder samplesof 1 and 2 were compacted in the form of pallets to measure their dielectric properties. Copper adhesive tapes were used as top and bottom electrodes to perform the measurements. The d_{33} coefficient measurements were performed on composite films 10 wt%_1 and 10wt%_2 by using a Berlincourt piezometer. The mechanical energy harvesting performance of the composite devices of 1 and 2 were recorded by using a vertical impact force setup operating in a periodic compression and release function coupled with an

oscilloscope. The fabricated devices were subjected to an impact force of 21 N with a tapping frequency of 8 Hz on an active area of 2.0 × 2.5 cm^2. All of the output voltage and current measurements were recorded on a Keithley DMM7510 7.5 multi meter. The output current density was calculated across various load resistances ranging from 100 kΩ to 30 MΩ. The obtained current density was then multiplied with the maximum output voltage to yield the power density.

3.3 Result and discussion

3.3.1 Synthesis

The ligand L was synthesized by lightly modified literature procedure involving $POCl_3$ and 3-amino pyridine. The formation of ligand L was further confirmed by mass and NMR techniques (Figure A1-A3, Appendix 3).

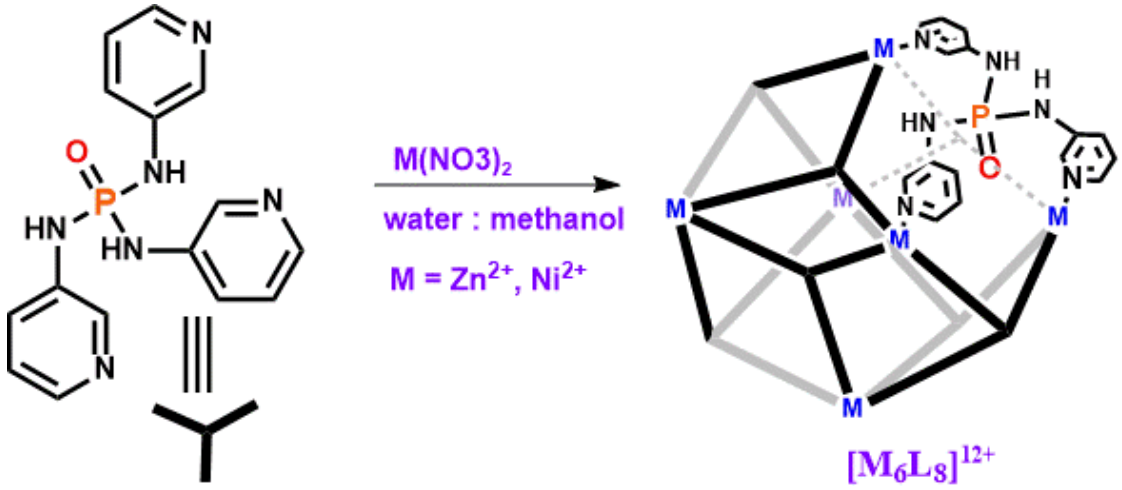

Scheme 3.1 *Schematic representation of synthesis of octahedron $[M_6L_8]^{12+}$ 1 and 2.*

This synthesized ligand L was then treated with the transition metal acceptors in order to get discrete cages. Treatment of 1 eq of ligand L in MeOH with 3 eq of the metal salts $Ni(NO_3)_2$ and $Zn(NO_3)_2$ in H_2O yielded the respective 1 and 2 compounds. Both these cages were isolated as their corresponding hexagonal-shaped crystals.

The crystals of compound 2 were then dissolved in DMSO-d_6 to perform the NMR experiments. The ^1H NMR spectra showed a single set of four proton peaks of the pyridine rings of the ligand Lthat suggested the formation of the symmetric compounds (Figure A4, Appendix 3). Changes

in the chemical shifts have been observed for all peaks suggesting the interaction of the pyridine nitrogen atom to the metal centres and peak broadening for the products over the ligand peaks suggested the formation of complex structure. ^{31}P NMR spectrum of 2 showed a single peak at -4.36 ppm confirming the formation of single self-assembled product (Figure A5 Appendix 3). Further, to understand the composition and mass of the product, ESI-MS experiments have been performed. Unfortunately, fragmentations of the peaks have been observed that suggested the coordination compound is not stable while flying in the mass- chamber during the experiment (Figure A6-A7, Appendix 3). To confirm the bulk purity of both the compounds 1 and 2, powder X-ray diffraction (PXRD) data were collected, which showed a good match with the corresponding simulated patterns obtained from their single crystal X-ray diffraction (Figure A8-A9, Appendix 3). Further, solid state FTIR experiments were performed for ligand L as well as for both the cage1 and cage2 to establish all the functional groups present in these compounds (Figure A10-A12 Appendix 3). Stabilityand desolvation of solvent molecules of both compounds 1 and 2 confirmed by the TGA analysis(Figure A13-A14 Appendix 3). On the single-crystal X-ray diffraction (SCXRD) analyses revealed that both 1 and 2 were found to crystallize in the tetragonal *I4* space group and confirmed the formation of the octahedral cage structures for both of them (Figure 3.1, A15-16, Appendix 3). With the cationic core of both these exhibit $[M_6L_8.12H_2O]^{12+}$ (M = $Ni^{2+}$and Zn^{2+}) composition. All pyridine nitrogen atoms of the ligand L are connected with three different metal atoms and in return, each metal connected with four different ligands. The metal centres have octahedron geometry with two water molecules coordinated on axial position and remaining four equatorial positions are occupied by the ligands, which complete the coordination vacancy of the metals. All eight ligands of the cationic cage $[M_6L_8.12H_2O]^{12+}$oriented in the syn fashion where the P=O moieties oriented towards the cavity of the cages. Each metal ion in the cages reside on a C_4 symmetry axis and the C_3 axes passes through eachof the ligand in the cages. The point group of the cage is cubic 432 representing octahedral (O)symmetry. Both these cages exhibit only the axial symmetric elements (432) and does not contain any mirror plane or inversion symmetry. However, a combination of symmetries invokes the inversion centres in them. Nevertheless, the presence of anions and solvate molecules in the lattice reduces the symmetry of these crystals to tetragonal (4) and thus renderthese cages polar.

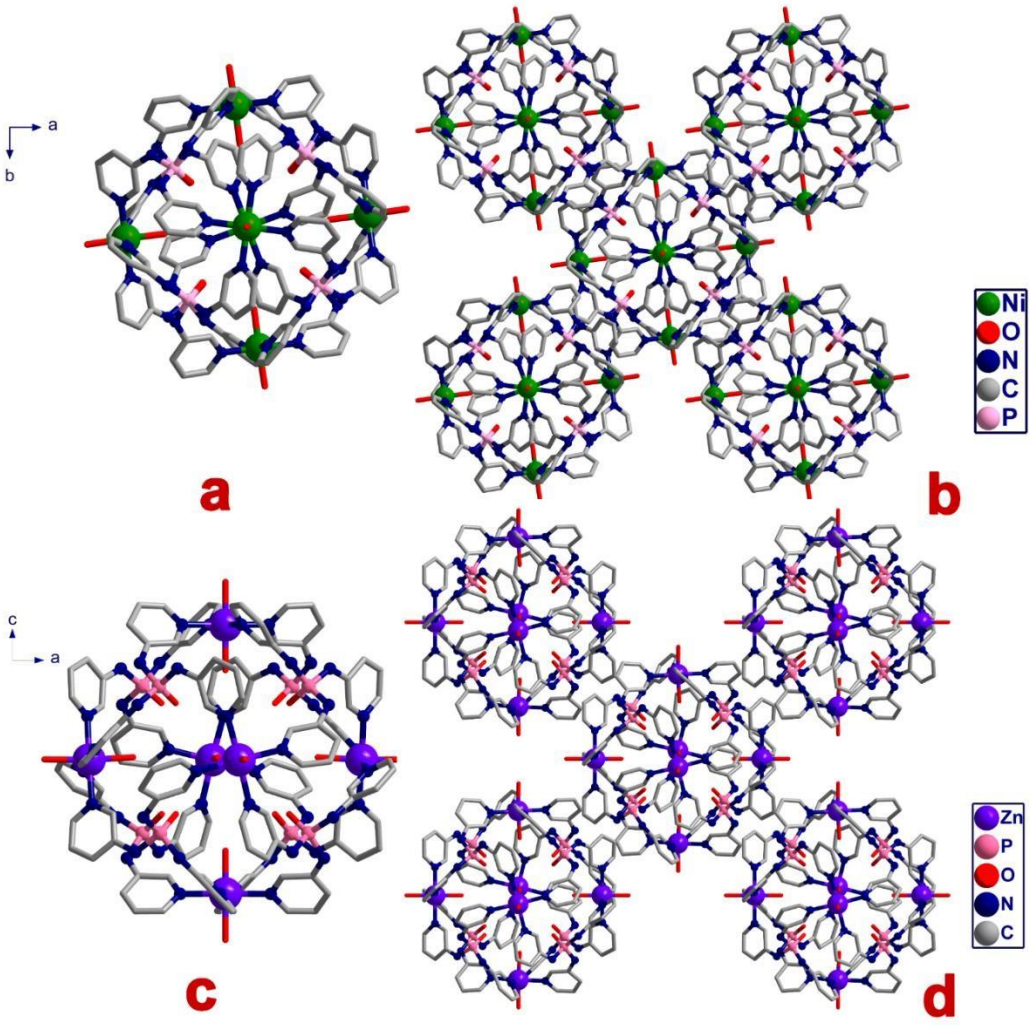

Figure 3.1 *(a) View of the octahedral* $[Ni_6L_8.12H_2O]^{12+}$ *cage core of 1 (b) packing diagram of the cationic* $[Ni_6L_8.12H_2O]^{12+}$ *core along c-axis. (c) View of the octahedral* $[Zn_6L_8.12H_2O]^{12+}$ *cage core of 2 (d) packing diagram of the cationic cage* $[Zn_6L_8.12H_2O]^{12+}$ *core along b-axis.*

3.3.2 Dielectric studies: -

Owing to the rough edges on the surfaces of these crystals, the ferroelectric measurements were not performed on these crystals, while attempts to measure the P-E loops on their compacted pellets did not lead to a saturated rectangular loop. However, based on the prior knowledge about these assemblies, one can presume that these cages would exhibit similar ferroelectric characteristics.[35-36]

Furthermore, dielectric permittivity measurements for cages1 and cage2 were performed on

their 8 mm powder pressed compact pallets. The frequency dependent dielectric permittivity measurements were performed in the temperature range of 298 to 363 K. The real part of dielectric constant (ε′) values at room temperature for compounds 1 and 2, were found to be 19.3and 14.5, respectively at 1 MHz (Figure 3.3). It has also been observed that at lower frequency, the value of dielectric permeability (ε′) increases (figure 3.3) because of the contribution fromall four polarization mechanisms.[34] At room temperature and 100 Hz, the maximum ε′ values were observed to be 43.7 and 63.7 for compounds 1 and 2, which correspond to an anomalous dielectric behaviour. Further a decrease in dielectric permittivity was seen upon increasing thetemperature, indicating the presence of dielectric relaxation behaviour in 1 and 2. These findings imply that the desolvation causes the dielectric anomalies in 1 and 2. (Figure 3.3). Additionally, the low dielectric loss (tan δ) measured at different frequencies reveals the strong dielectric nature of both compounds 1 and 2 (Appendix 3, A17-A18). This couldbe due to the loses of non-covalent interactions at higher temperature which are responsible forthe polarization of these cage assemblies. As the cages possess octahedron symmetry and therefore do not possess any inherent polarization of these compounds are attributed to the disordered nitrate and water molecules, which are found as isolated pockets in the frameworks of the cage molecules. We have earlier reported dielectric permittivity measurements on similarcage assemblies, where the octahedral cage $[M_6(TPTA)_8]^{12+}$ (M = Zn(II) and Cu(II) moleculeas well as the hierarchical connected-cage framework of the Cu(II) system were symmetric innature and origin of the polarization in such materials were attributed to the toggling of the disordered nitrate anions and water molecules within the pockets of cage molecules.[35] As described earlier, the nitrate anion located along the polar axis is ordered, while those located along the ab-plane exhibit a complex disorder. These disordered anions undergo a toggling motion between two different sites under the electric field and produce polarization in these cages.

Interaction of these toggling anions with the coordinated and lattice bound water molecules further establish a long-range polar order in these compounds.[39]

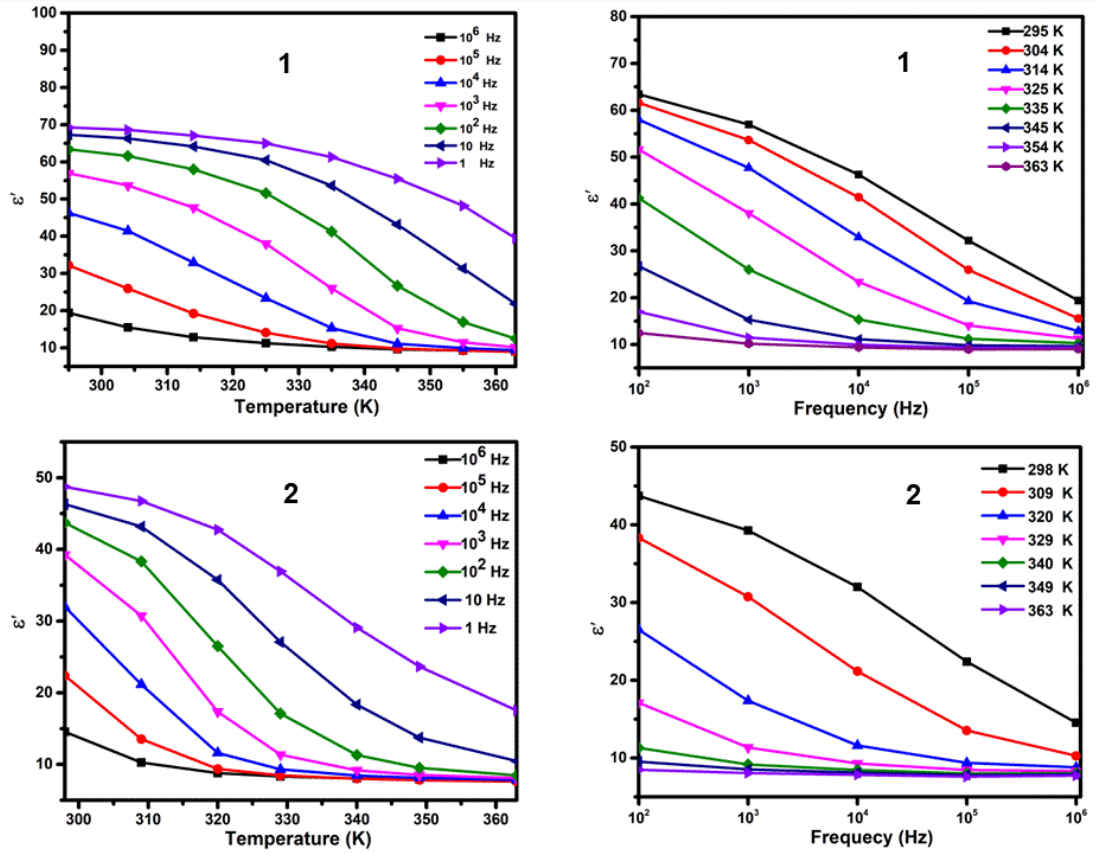

Figure 3.2 *Temperature and frequency dependent dielectric permittivity (ε') profiles for* compounds 1 and 2.

3.3.3 Preparation and characterization of composite films

Inspired by the utility of several two-component ferroelectric materials as high-performance nanogenerators, where the mechanical inputs get converted into electrical outputs, the 1 and 2 were further utilized for piezoelectric energy harvesting applications. For this application purpose, composite films of different weight percentages (1, 5, 10 and 15 wt%) of1 and 2 were prepared in the non-piezoelectric polydimethylsiloxane (PDMS) polymer matrix. Appropriate wt% (1, 5, 10, and 15) of 1 and 2 were added to a mixturecontaining 90 % PDMS and 10 % curing agent and properly mixed with PDMS to yield a homogeneous mixture. After several hours of vigorous stirring, the mixture was then poured on a polyethylene terephthalate (PET) sheet and was left for drying for 7 to 10 days. All PDMScomposite films of 1 and 2 were then peeled off from the PET surface.

The prepared composite films exhibited excellent flexibility and were free towards various

motions of rolling, stretching and multiple folding, etc. (A19, Appendix 3). The phase purity of all the weight percentages (1, 5, 10, and 15 wt%) of 1_PDMS and 2_PDMS films were confirmed from the PXRD analysis (Figure 3.3 b and 3.3 c). From the PXRD analysis, itis evident that the crystalline behaviour of the composite films improve as the weight percentage increases (1 to 15 wt %) for both compounds 1 and 2.

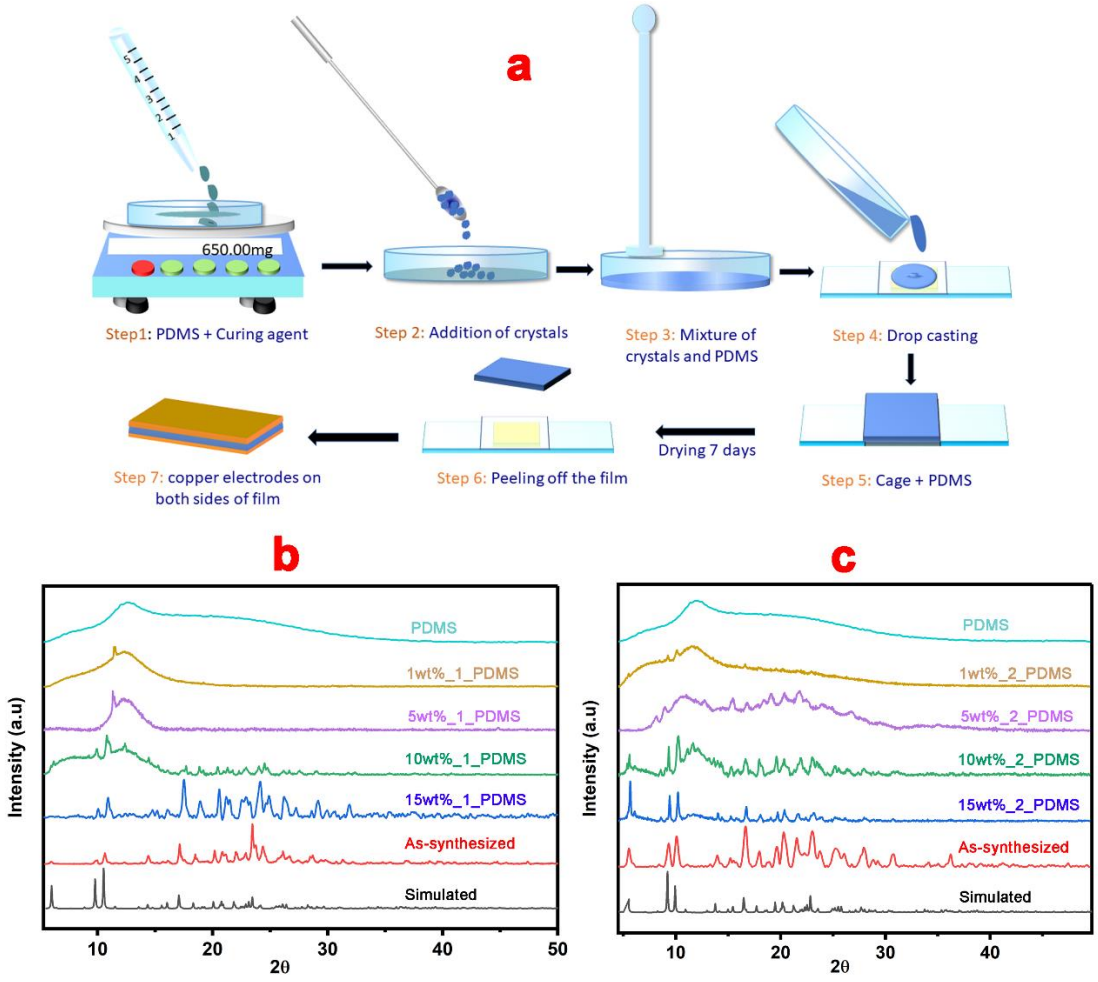

Figure 3.3 *(a) Schematic diagram for the preparation of composite films. (b) Stacked PXRD profile for 1_PDMS composite films along with the simulated and as-synthesized 1profiles, (c) Stacked PXRD profile for 2_PDMS composite along with the simulated andas-synthesized 2 profiles.*

3.3.4 Mechanical energy harvesting outputs of 1_PDMS and 2_PDMS composite devices

After exploring the dielectric and piezoelectric responses, the energy harvesting properties of both compounds 1 and 2 were examined in the form of their PDMS-composite devices.

To complete the device architectures, all the prepared composite films were electroded with Cu tapes as topand bottom electrodes and Cu wires were attached as the contact leads. Further, Kapton tapes were sticked on the upper and lower sides to protect the devices from the external force duringthe mechanical testing. The voltage outputs from the devices were generated from a vertical force from a custom-made impact machine and the signals were collected on an oscilloscope. For every device, the open circuit peak-to-peak voltage (V_{PP}) was recorded at a constant frequency of 8 Hz and 21 N force. The 1_PDMS devices the resulted in V_{PP} values of 1.2,3.9, 8.2 and 5.7 V for the 1, 5, 10, and 15 wt% devices, respectively (Figure 3.4 a, A20, Appendix 3). Similarly, the 2_PDMS devices yielded the V_{PP} values of 2.1, 7.36, 11.3 and 7.4 V for the 1, 5, 10, and 15 wt% devices, respectively (Figure 3.4 b, A21, Appendix 3).

As, PDMS is a nonpiezoelectric polymer, it resulted in very low output voltage of only 300 mV. This confirms the fact that the observed output voltages for different weight percentages of 1_PDMS and 2_PDMS are an outcome of the embedded crystalline cage molecules in the PDMS matrixes. For both 1_PDMS and 2_PDMS devices, the maximum V_{OC} were obtained for the 10 wt% PDMS devices (figure 3.4). However, lower values of V_{PP} were observed for the 15 wt% devices of 1_PDMS and 2_PDMS, this can be due to the agglomeration of cage particles in the PDMS matrix at higher concentration of both compounds 1 and 2. The corresponding output peak-to-peak currents (I_{PP}) were then calculated by attachingthe 4 MΩ resistor across the devices of 1_PDMS and 2_PDMS and voltage drop wererecorded. The resultant output current (I_{PP}) values are 0.31, 0.98, 2.06 and 1.44 μA for 1, 5, 10, and 15 wt% 1_PDMS devices and 0.53, 1.65, 2.83 and 1.68 μA for 1, 5, 10, and 15 wt% 2_PDMS devices respectively (Figure A22-A23, Appendix 3).

It has been observed that the output voltage (V_{PP}) and current (I_{PP}) increased with increasing the load of the cages into the PDMS matrix up to 10 wt% and on further loading of the cage crystallites cause a reduction in the output voltages and currents. This reduction in output voltage and current could be a result of the agglomeration of the particles of compounds 1 and 2 in the PDMS matrix at higher weight percentages, which is also evident from the FE-SEM images (Figure, A24-A25, Appendix 3).

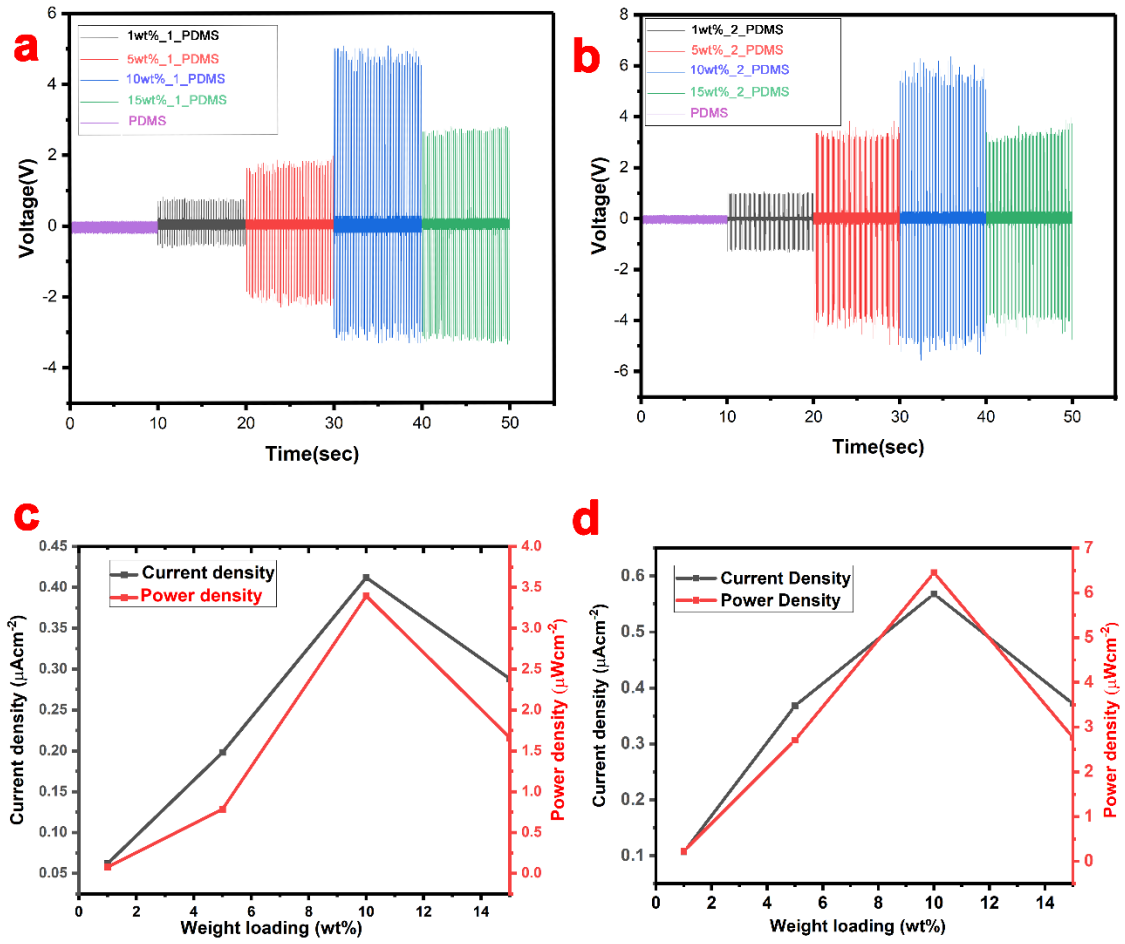

Figure 3.4 *(a) Measured V_{pp} profiles for neat PDMS and all (1, 5, 10, and 15 wt%) composite devices of 1_PDMS. (b) Measured V_{pp} profiles for neat PDMS and all (1, 5,10, and 15 wt%) composite devices of 2_PDMS (c) Comparative current and power density values of 1_PDMS and (d) Comparative current and power density values of 2_PDMS.*

The composites films of the best performing 10 wt%_1_PDMS and 10 wt%_2_PDMSwere subjected to the direct piezoelectric coefficient (d_{33}) measurements, which yielded the d_{33}values of 0.30 and 0.36 pC/N, respectively. Measurements on both films were done by using 'Berlincourt' method on a d_{33} meter. The measurement frequency and force were of the order of 110 Hz and 0.25 N, respectively. The maximum current densities (CD) were calculated to be 0.41 μA/cm^{-2} and 0.57 μA/cm^{-2} for the 10 wt%_1_PDMS and 10 wt%_2_PDMS devices, respectively (Figure 3.4 c and 3.4 d). The power densities (PD) were calculated by

using the formula $PD = \frac{V*I}{Area}$. The maximum PD values for both the 10 wt % devices of 1 and 2 were calculated to be 3.38 and 6.45μW/cm^{-2}, respectively (Figure 3.4 c and 3.4 d). The feasibility of these devices of 10wt % for practical uses were then examined by measuringthe voltage drops across different load resistances ranging from 100 KΩ to 30 MΩ. The voltagedrops were seen to follow an increasing trend while approaching their corresponding open circuit voltages up to 4 MΩ and then saturation was observed. (Figure, A26-A27, Appendix 3).

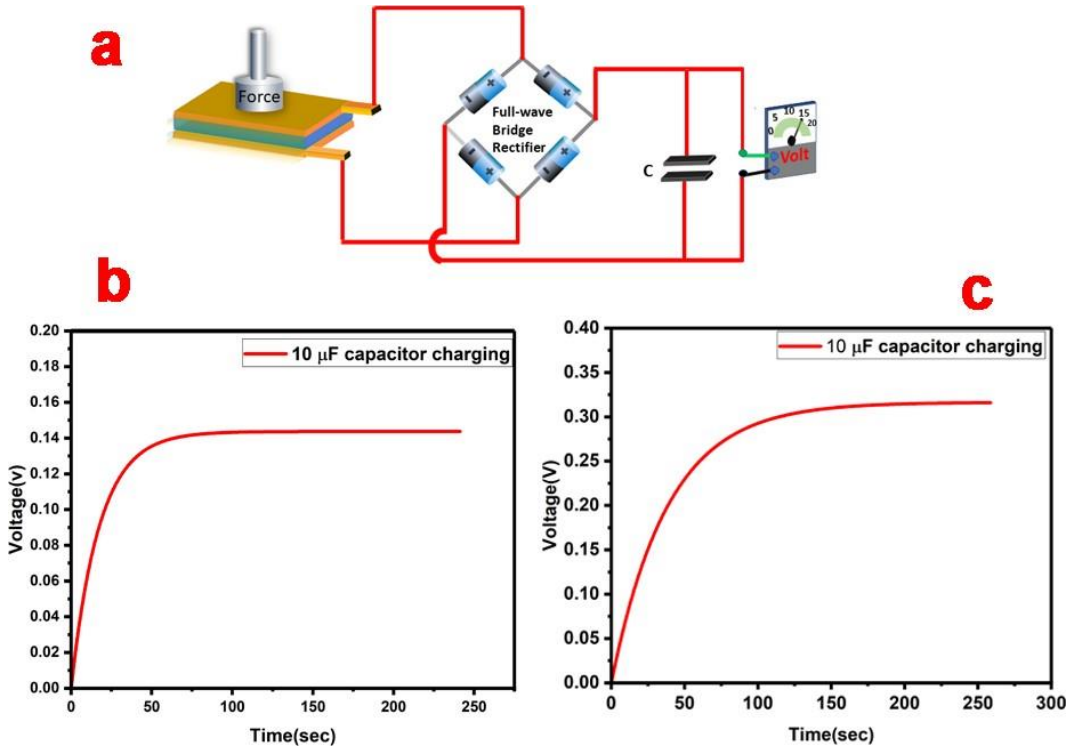

Figure 3.5 *(a) Four diode full wave rectifier circuit used for charging capacitor. Charging curves for the 10 μF capacitor by utilizing the 10 wt%_1_PDMS device (b) and 10 wt%_2_PDMS (c) devices.*

The maximum output voltage obtained from 10wt %_PDMS composites of compounds 1 and 2 were then utilized to charge a 10 μF capacitor using a four-diode full wave bridge rectifier circuit, upon subjecting the devices to a continuous 21 N external force and 8 Hz frequency (Figure 3.5 a). The maximum voltages stored in the respective devices were found to be 140 and 300 mV voltage in 80 and 150 seconds (figure 3.5 b and 3.5 c). As compared to the open

circuit voltage, less voltage was stored in the capacitor, which could be due to the voltage loss during

the rectification of four diodes. The maximum stored energy (E) and charge (Q) were then calculated to be 0.098 μJ and 1.40 μC, respectively, for the 10 wt%_1_PDMS device. Similarly, the maximum stored energy (E) and charge (Q) were 0.45 μJ and 3.0 μC, respectively, for the 10 wt%_2_PDMS device.

3.4 Conclusion

In summary, two new octahedral cages of general formula $[M_6L_8.12H_2O]^{12+}$ were synthesized for Zn(II) and Ni(II) ions and investigated for their dielectric and piezoelectric properties of octahedron $[M_6L_8.12H_2O]^{12+}$ cage assemblies.. These cages were found to crystallize in the polar tetragonal space group *I4*. The polarization in both cage1 and cage2 are attributed to the toggling of disordered nitrate anions and their long-range order assisted by H-bonding with solvated and coordinated water molecules. Polymer composites of these cages were prepared with PDMS and subjected for piezoelectric energy harvesting applications. The 10 wt%_1_PDMS and 10 wt%_2_PDMS, devices gave the maximum output peak to peak voltages of 8.2 and 11.3 V, respectively. The corresponding I_{SC}, CD, and PD values werealso calculated. A 10 μF capacitor was then charged using these two 10 wt% devices of compounds 1and 2 that rapidly charge the capacitor with sizable stored voltages and measured charges. These findings inspire the utility of self-assembled metal-ligand cages for the electrical energy harvesting and storage application from simple mechanical forces.

References

(1) Priya, S.; Inman, D. J. *Energy Harvesting Technologies*; 2009. 1.

(2) Chu, S.; Majumdar, A. Opportunities and Challenges for a Sustainable Energy Future. *Nature* **2012**, *488*, 294–303.

(3) Chu, S.; Cui, Y.; Liu, N. The Path towards Sustainable Energy. *Nat. Mater.* **2016**, *16* , 16–22.

(4) Ellabban, O.; Abu-Rub, H.; Blaabjerg, F. Renewable Energy Resources: Current Status,

Future Prospects and Their Enabling Technology. *Renew. Sustain. Energy Rev.* **2014**, *39*, 748–764.

(5) Tao, P.; Ni, G.; Song, C.; Shang, W.; Wu, J.; Zhu, J.; Chen, G.; Deng, T. Solar-Driven Interfacial Evaporation. *Nat. Energy* **2018**, *3*, 1031–1041.

(6) Shen, S.; Xiao, X.; Xiao, X.; Chen, J. Wearable Triboelectric Nanogenerators for Heart Rate Monitoring. *Chem. Commun.* **2021**, *57*, 5871–5879.

(7) Invernizzi, F.; Dulio, S.; Patrini, M.; Guizzetti, G.; Mustarelli, P. Energy Harvesting from Human Motion: Materials and Techniques. *Chem. Soc. Rev.* **2016**, *45*, 5455–5473.

(8) Tu, Y.; Wang, R.; Zhang, Y.; Wang, J. Progress and Expectation of Atmospheric Water Harvesting. *Joule* **2018**, *2*, 1452–1475.

(9) Ryu, H.; Yoon, H. J.; Kim, S. W. Hybrid Energy Harvesters: Toward Sustainable Energy Harvesting. *Adv. Mater.* **2019**, *31*, 1–19.

(10) Cheng, T.; Gao, Q.; Wang, Z. L. The Current Development and Future Outlook of Triboelectric Nanogenerators: A Survey of Literature. *Adv. Mater. Technol.* **2019**, *4*, 1–7.

(11) Zhang, Y.; Phuong, P. T. T.; Roake, E.; Khanbareh, H.; Wang, Y.; Dunn, S.; Bowen, C. Thermal Energy Harvesting Using Pyroelectric-Electrochemical Coupling in Ferroelectric Materials. *Joule* **2020**, *4*, 301–309.

(12) Lan, L.; Ping, J.; Xiong, J.; Ying, Y. Sustainable Natural Bio-Origin Materials for Future Flexible Devices. *Adv. Sci.* **2022**, *9*, 1–34.

(13) Zhang, W.; Xiong, R. Ferroelectric Metal À Organic Frameworks. **2012**, 1163–1195.

(14) Hosseini, E. S.; Dervin, S.; Ganguly, P.; Dahiya, R. Biodegradable Materials for Sustainable Health Monitoring Devices. *ACS Appl. Bio Mater.* **2021**, *4*, 163–194.

(15) Shi, P. P.; Tang, Y. Y.; Li, P. F.; Liao, W. Q.; Wang, Z. X.; Ye, Q.; Xiong, R. G. Symmetry Breaking in Molecular Ferroelectrics. *Chem. Soc. Rev.* **2016**, *45*, 3811–3827.

(16) Dou, Q.; Wu, N.; Yuan, H.; Shin, K. H.; Tang, Y.; Mitlin, D.; Park, H. S. Emerging Trends in Anion Storage Materials for the Capacitive and Hybrid Energy Storage and Beyond. *Chem. Soc. Rev.* **2021**, *50*, 6734–6789.

(17) Martin, L. W.; Rappe, A. M. Thin-Film Ferroelectric Materials and Their Applications. *Nat. Rev. Mater.* **2016**, *2*, 2.

(18) de Araujo, P.; Cuchiaro, J. D.; McMillan, L. D.; Scott, M. C.; F Scott, B. J. Fatigue-Free Ferroelectric Capacitors with Platinum Electrodes. *Nature* **1995**, *374*, 889–891.

(19) Wang, Z. L. Self-Powered Nanosensors and Nanosystems. *Adv. Mater.* **2012**, *24*, 280–285.

(20) Zhang, R.; Lin, L.; Jing, Q.; Wu, W.; Zhang, Y.; Jiao, Z.; Yan, L.; Han, R. P. S.; Wang, Z. L. Nanogenerator as an Active Sensor for Vortex Capture and Ambient Wind-Velocity Detection. *Energy Environ. Sci.* **2012**, *5*, 8528–8533.

(21) Wang, Z. L.; Song, J. Piezoelectric Nanogenerators Based on Zinc Oxide Nanowire

Arrays. *Science.* **2006**, *312*, 242–246.

(22) Hu, Y.; Yang, J.; Jing, Q.; Niu, S.; Wu, W.; Wang, Z. L. Triboelectric Nanogenerator Built on Suspended 3d Spiral Structure as Vibration and Positioning Sensor and Wave Energy Harvester. *ACS Nano* **2013**, *7*, 10424–10432.

(23) Yang, Y.; Guo, W.; Pradel, K. C.; Zhu, G.; Zhou, Y.; Zhang, Y.; Hu, Y.; Lin, L.; Wang, Z. L. Pyroelectric Nanogenerators for Harvesting Thermoelectric Energy. *Nano Lett.* **2012**, *12*, 2833–2838.

(24) Yang, J.; You, J.; Chen, C. C.; Hsu, W. C.; Tan, H. R.; Zhang, X. W.; Hong, Z.; Yang, Y. Plasmonic Polymer Tandem Solar Cell. *ACS Nano* **2011**, *5*, 6210–6217.

(25) 3. A.A. Marino, R.O. Becker. Piezoelectric Effect and Growth Control in Bone. *Nature* **1970**, *228*, 473–474.

(26) Katsouras, I.; Asadi, K.; Li, M.; Van Driel, T. B.; Kjær, K. S.; Zhao, D.; Lenz, T.; Gu, Y.; Blom, P. W. M.; Damjanovic, D.; Nielsen, M. M.; De Leeuw, D. M. The Negative Piezoelectric Effect of the Ferroelectric Polymer Poly(Vinylidene Fluoride). *Nat. Mater.* **2016**, *15*, 78–84.

(27) W. Forrester, R. H. Crystal Structure of Barium Titanate. *Nature* **1945**, *156*, 177.

(28) Jaffe, B.; Roth, R. S.; Marzullo, S. Piezoelectric Properties of Lead Ceramics. *J. Appl. Phys.* **1954**, *809*, 10–12.

(29) Nassau, K.; Levinstein, H. J.; Loiacono, G. M. Ferroelectric Lithium Niobate. 1. Growth, Domain Structure, Dislocations and Etching. *J. Phys. Chem. Solids* **1966**, *27*, 983–988.

(30) Wang, X. Song, J., Liu, J., Wang, Z. L. Direct-Current Nanogenerator. *Science (80-.).* **2007**, *316*, 102–105.

(31) Ahmad, A. S.; Usman, M. M.; Bello Abubakar, S.; Gidado, A. Y. Review on the Application of Piezoelectric Materials in the Development of Ultrasonic Motors. *J. Adv. Res. Appl. Mech. J. Adv. Res. Appl. Mech. J.* **2017**, *33*, 9–19.

(32) Srivastava, A. K.; Divya, P.; Praveenkumar, B.; Boomishankar, R. Potentially Ferroelectric {CuIIL2}n Based Two-Dimensional Framework Exhibiting High Polarization and Guest-Assisted Dielectric Anomaly. *Chem. Mater.* **2015**, *27*, 5222–5229.

(33) Srivastava, A. K.; Vijayakanth, T.; Divya, P.; Praveenkumar, B.; Steiner, A.; Boomishankar, R. Altering Polarization Attributes in Ferroelectric Metallo-Cavitands by Varying Hydrated Alkali-Metal Guest Cations. *J. Mater. Chem. C* **2017**, *5*, 7352–7359.

(34) Anant Kumar Srivastava, B. Praveenkumar, Indra Kumar Mahawar, Pillutla Divya, S. Shalini, and R. B. Anion Driven [CuIIL2]n Frameworks: Crystal Structures, Guest-Encapsulation, Dielectric, and Possible Ferroelectric Properties. *Chem. mater* **2014**, *12*, 3811–3817.

(35) Yadav, A.; Srivastava, A. K.; Kulkarni, P.; Divya, P.; Steiner, A.; Praveenkumar, B.; Boomishankar, R. Anion-Induced Ferroelectric Polarization in a Luminescent Metal-Organic Cage Compound. *J. Mater. Chem. C* **2017**, *5*, 10624–10629.

(36) Yadav, A.; Kulkarni, P.; Praveenkumar, B.; Steiner, A.; Boomishankar, R. Hierarchical Frameworks of Metal–Organic Cages with Axial Ferroelectric Anisotropy. *Chem. - A Eur. J.* **2018**, *24*, 14639–14643.

(37) Sheldrick GM. A short history of SHELX. *Acta Crystallogr A.* **2008**, *64*, 112-22.

(38) Spek, A. L. Single-Crystal Structure Validation with the Program PLATON. *J. Appl. Crystallogr.* **2003**, *36*, 7–13.

END of CHAPTER 3

CHAPTER 4

Synthesis of Pd_6L_8 discrete cages and their role in anticancer activities.

4.1 Introduction

Self-assembled multi-metallic metal-organic complexes (MOCs) can be well-defined as discrete two-dimensional (2D) macrocycles or three-dimensional (3D) supramolecular entities[1-4]. The 2D- macrocycles such as triangles, squares, and hexagons can be formed by the self-assembly reaction of ligands and directionally controlled single-metal acceptors[5-7]. 3D-MOCs can be synthesized by using metal-centres or metal-clusters and ligands with multiple donating sites. These systems can be organized into big and symmetrical discrete molecules such as tetrahedron, octahedron, cube, and icosidodecahedron in a spontaneous self-assembly process[8-11]. Depending upon their characteristics, the MOCs have shown multiple applications such as host-guest chemistry (guest encapsulation), catalysis, sensing, and optical emission [12-14]. Apart from these conventional applications, the idea of using supramolecular metal-organic complexes in the biomedical applications has recently emerged to address some of theproblems associated with conventional biomedical materials. Particularly, the ease with which these MOCs can be fine-tuned for their shapes, dimensions, structures and properties via the rational choice of metals, coordination geometry, and their ability to incorporate activefunctionalities by pre- or post- self-assembly modifications promises their application as potential biologically relevant substances[15-19]. However, the use and synthesis of metal-based drugs, especially multinuclear metal complexes in the biological field, have been limited overthe years ever since the report on activity of cisplatin[20-25]. Despite its wide applicability, the use of cisplatin is constrained because of the severe dose-limiting side effects[26]. Also, prolonged studies on Pt-based drugs revealed several issues related to neurotoxicity, hepatotoxicity, serious side effects, drug resistance, and limited activity[27-30]. It is also known that cis platin capably binds to serum proteins, especially human serum albumin (HsA), which has major content in plasma[31]. Therefore, several derivatives of cisplatin and mono- and polynuclear complexes of other metal ions have been synthesized and investigated for their anti-cancer activity[32]. However, most of the known inorganic anticancer drug molecules or complexes have active effects on both cancer and normal cells because of the strong resemblance of the mechanisms of growth regulation of normal cells as compared to their transformed counterpart. Recently, a few self-assembled MOCs have been used as selective anticancer drugs and drug carriers[33-35]. Notable examples of metallacages and macrocyles werebuilt using metal ions of such as Pt, Ru, Pd, Ir, and Rh have shown to exhibit excellent anticancer properties[36-40].

Infect, a few Pt and Ru-based MOCs were employed as anticancer drugs with good activities[41-43]. Spurred by these findings, MOCs with different and cost-effective metal ions were explored for their activity against cancer cells[44]. In this effort, we were interested in the construction of MOCs using pyridyl donor ligands built on amide linker backbones. Compared with the widely used less polar donor ligands, use of polar amide-based ligands was particularly advantageous due to their possible interactions with biomolecules like DNA that help in the internalization of these metallo-drugs[35]. One of the robust platforms to obtain cationic MOCs is the use of C_3 symmetric ligands with pyridine donor atoms. Hence, we envisioned that a combination of these tripodal ligands on the amide backbone will facilitate the MOCs to interact with a variety of enzymes and biological receptor systems [45]. Herein, we present the synthesis and anticancer studies of three octahedral $Pd_6L_8]^{+12}$ type metallocages 1, 2 and 3 starting from Pd(II) ions and the amide (or phosphoramide) derived ligands of tris(3-pyridinyl) phosphoramide (L1), tris (3-pyridinyl) benzene 1,3,5 tricarboxamide (L2), and tris (6-aminoquinonyl) benzene 1,3,5 tricarboxamide (L3) ligands, respectively[46-47]. Further, cytotoxicity experiments against human cancer cell lines have been performed for the 1, 2 and 3 and their efficacies were compared with their corresponding ligand motifs. Also, the activities of these MOCs and ligands were tested against the normal cell lines, which showed excellent selectivity for cage 3. The IC_{50} values of >20, 11.5 and 5 μm were observed for the compounds 1, 2 and 3, respectively.The Western blotting experiment suggested that 3 is responsible for damaging double- strand DNA that with the possible cell apoptosis.

4.2 General experimental section:

4.2.1 General remarks

All the chemicals employed in this work were purchased from commercially available sources and used as it without further purification except $POCl_3$, which was purified by distillation prior to use. Toluene solvent was dried freshly according to standard procedure. All NMR solvents were purchased from Sigma Aldrich including DMSO-d_6, and MeOH-d_4. NMR spectra were recorded on a Bruker 400 or a Joel 400 MHz spectrometers (^{1}H NMR, 400.13MHz; $^{13}C\{^1H\}$ NMR, 100.62 MHz and, $^{31}P\{^1H\}$ NMR, 161.97 MHZ) at room temperature using $SiMe_4$ (^{1}H, ^{13}C NMR) and 85% H_3PO_4 (^{31}P NMR). The MALDI-TOF and ESI-MS spectra were obtained on an Applied Biosystem MALDI-TOF/TOF and water Synapt G2 Q-TOF spectrometers, respectively. FT-IR spectra were recorded on a Perkin-Elmer

spectrophotometer in the ATR mode Melting points were analyzed using an Electrothermal melting point apparatus and were uncorrected. Elemental analyses were performed on a Vario-EL cube elemental analyzer.

4.2.2 Syntheses

L1: We followed a slightly modified procedure from the literature to synthesize the ligand L1 as given below.[45] To a stirred solution of 3-aminopyridine (1.48 gm, 15.7mmol, 3.1eq) and triethylamine (5.2ml, 5eq) in 100 ml of dry toluene, kept at 0° C in an oven-dried two-neck round bottom flask, phosphoryl trichloride(1 gm, 5.2 mmol, 1eq) in 10 ml dry toluene was added over a period of 10 minutes in the presence of nitrogen or argon. The reaction mixture was refluxed for 12 hours and was cooled back to room temperature. The resulting colourless precipitate was collected through filtration, washed several times with water and dried under vacuum. Yield: 1.45 g (85%) ^{1}H NMR: (400 MHz, DMSO-d_6) δ = 8.4 (d, NH, 3H), 8.42 (s, 3H), 8.08 (dd, 3H), 7.57 (m 3H), 7.24 (m, 3H). ^{31}P{1H} NMR: (242.95 MHz, DMSO-d_6) δ= -3.77 (s). MALDI-TOF m/z = 326.30. Anal. Calcd. for $C_{15}H_{15}N_6OP$: C, 55.21; H, 4.63; N, 25.76. Found: C, 55.50; H, 4.58; N, 25.81. FT-IR data (cm^{-1}): 3088, 1587, 1477, 1386, 1197, 1121, 1061, 938, 810, 699, and 514.

L2: Ligand L2 has been synthesized by modify the literature procedure.[46] To a stirredsolution of 3-aminopyridine (1.48 gm, 15.7 mmol, 3.1eq) and triethylamine (5.2 ml, 5eq) in 100 ml of dry THF, kept at 0° C in an oven-dried two-neck round bottom flask, 1,3,5-benzenetricarbonylchloride (1.35 gm, 5.2 mmol, 1eq) solution in 30 ml of dry THF was added dropwise over a period of 20 minutes in the presence of nitrogen or argon. The reaction mixture was refluxed for 12 hours and was then cooled back to room temperature. The resulting colorless precipitate was collected through filtration, washed several times with water and methanol, and dried under vacuum. Yield: 1.70 g (75%) ^{1}H NMR: (400 MHz, DMSO-d_6) δ = 10.91 (s, NH, 3H), 9.03 (s, 3H), 8.82 (s, 3H), 8.37 (dd, 3H), 8.29 (m, 3H), 7.47 (dd, 3H). MALDI- TOF m/z = 438.30. Anal. calcd. for $C_{24}H_{18}N_6O_3$: C, 65.75; H, 4.14; N, 19.17. Found: C, 65.55; H, 4.20; N, 19.24. FT-IR data (cm^{-1}): 3268, 2559, 1737, 1386, 1667, 1121, 828, and 717.

L3: Ligand L3 has been synthesized by modify the literature procedure.[47] To a stirredsolution of 3-aminoquinonile (2.25 gm, 15.7 mmol, 3.1eq) and triethylamine (5.2 ml, 5eq) in 100 ml of dry THF, kept at 0° C in an oven-dried two-neck round bottom flask, 1,3,5-

benzenetricarbonylchloride (1.35 gm, 5.2 mmol, 1eq) solution in 30 ml of dry THF was added dropwise over a period of 20 minutes in the presence of nitrogen or argon. The reaction mixture refluxed for 12 hours and was cooled back to room temperature. The resulting grey colored precipitate was collected through filtration, washed several times with water and methanol, and dried under vacuum. Yield: 2.35 g (76%) ^{1}H NMR: (400 MHz, DMSO-d_6) δ = 11.03 (s, NH, 3H), 8.84 (d, 3H), 8.61 (s, 3H), 8.38 (dd, 3H), 8.13 - 8.16 (m, 3H), 8.06-8.09 (m, 3H), 7.52 (dd, 3H). MALDI- TOF m/z = 588.30. Anal. Calcd. for $C_{36}H_{24}N_6O_3$: C, 73.46; H, 4.11; N, 14.28. Found: C, 73.55; H, 4.18; N, 14.03. FT-IR data (cm^{-1}): 3269, 2559, 1767, 1386, 1420, 1121, 828, and 702.

1: A solution of $Pd(CH_3CN)_4(BF_4)_2$ (22.2 mg, 0.05 mmol) in 0.5 ml DMSO was added toa solution of the ligand L1 (22.8 mg, 0.07 mmol) in DMSO (0.5 mL) and the mixture was stirred at 50 °C for 8 h. The resultant light orange-colored solution was cooled to room temperature and poured into a conical flask containing cold ethyl acetate (15 mL). The obtainedprecipitate was collected through filtration. The residue was washed with ethyl acetate and diethyl ether and dried under vacuum to yield the compound 1: Isolated yield: 150 mg (70%).^{1}H NMR (400 MHz, DMSO-d_6): δ = 8.40 (d, 24H, NH), 8.33 (s, 36H), 7.52 (d, 36H), 7.39 (dd, 36H), 7.08 (m, 36H). ^{31}P{^{1}H} NMR (242.95 MHz, DMSO-d_6): δ = -4.36 (s). ESI-MS calculated m/z= 476.3, 570.12, and 701.23 for $[Pd_6(L1)_8+5BF_4]^{7+}$, $[Pd_6(L1)_8+6BF_4]^{6+}$, $[Pd_6(L1)_8+7BF_4]^{5+}$, respectively. Anal. calcd. for $C_{120}H_{120}N_{48}O_8P_8B_{12}F_{48}Pd_6$: C, 33.59; H, 2.82; N, 15.67. Found: C, 33.80; H, 2.85; N, 15.30. FT-IR data (cm^{-1}): 3298, 1580, 1497, 1395, 1282, 1021, 935, 805, 759, 693, and 627.

2: A solution of $Pd(CH_3CN)_4(BF_4)_2$ (22.2 mg, 0.05 mmol) in 0.5 ml DMSO was added toa solution of the ligand L2 (30.6 mg, 0.07 mmol) in DMSO (1 mL) and the mixture was stirredat 50 °C for 1 h. The resultant light orange colored solution was cooled to room temperature and poured into a conical flask containing cold ethyl acetate (15 mL). The obtained precipitatewas collected through filtration. The residue was washed with ethyl acetate and diethyl ether and dried under vacuum to yield the compound 2: Isolated yield: 194 mg (75%). ^{1}H NMR (400MHz, DMSO-d_6): δ = 11.19 (s, 24H, NH), 9.52 (s, 24H), 8.75 (d, 24H), 8.44 (s, 24H), 8.03 (d,24H), 7.73 (dd, 24H). Anal. calcd. for $C_{192}H_{144}N_{48}O_{24}P_8B_{12}F_{48}Pd_6$: C, 44.45; H, 2.80; N, 12.96.Found: C, 43.99; H, 2.85; N, 12.56. FT-IR data (cm^{-1}): 3436, 2480, 1697, 1595, 1057, 803, and 730.

3: A solution of $Pd(CH_3CN)_4(BF_4)_2$ (22.2 mg, 0.05 mmol) in 0.5 ml was added to a solution of the ligand L3 (23.5 mg, 0.07 mmol) in DMSO (1.5 mL) and the mixture was stirredat 50 ^oC for 1 h. The resultant light orange colored solution was cooled to room temperature and poured into a conical flask containing cold ethyl acetate (15 mL). The obtained precipitatewas collected through filtration. The residue was washed with ethyl acetate and diethyl ether and dried under vacuum to yield the compound 3: Isolated yield: 223 mg (70%). ^1H NMR (400MHz, DMSO-d_6): δ = 10.92 (d, 24H, NH), 9.72 (s, 24H), 9.63 (d, 24H), 8.72 (dd, 36H), 8.46-8.40 (m, 48H) 7. 80 (m, 48H). Anal. Calcd. for $C_{288}H_{192}N_{48}O_{24}P_8B_{12}F_{48}Pd_6$: C, 54.14; H, 3.03; N, 10.52. Found: C, 53.97; H, 3.15; N, 10.47. FT-IR data (cm^{-1}): 3468, 2569, 1693, 1590, 1055, 819, and 720.

4.2.3 Preparation of stock solutions for cell viability assay

Stock solutions have been prepared in DMSO of 5 mg/mL of ligands (L1, L2, and L3) and MOCs (1,2, and 3) and stored at -20 ^oC.

4.2.4 Cancer cell growth inhibition assay.

MTT assay was performed to analyse the proliferation status of MCF-7, a breast cancer cell line and HEK 293, non-cancerous cell line. Both the cell lines were cultured in Dulbecco's modified Eagle's medium (DMEM) supplemented with 10% heat-inactivated fetal bovine serum (FBS) and 1 % penicillin-streptomycin. For MTT assay, $5x10^3$ cells supplemented with suspended 10% FBS containing DMEM were seeded in a 96-well plate. Cells were treated with different concentrations of the compounds and were grown for 48 hrs at 37°C. The media containing the compounds was aspirated and 0.5 mg/ml thiazolyl blue tetrazolium (MTT; Sigma-Aldrich, USA) was dissolved in DMEM and was further incubated for 4 hrs at 37°C. After 4 hrs, the MTT solution was aspirated, 100 µl of DMSO was added to each well to dissolve the formazan crystals. The absorbance was measured at 570 nm wavelength on Varioskan Flash spectral scanning multimode plate reader (Thermo Fisher Scientific, USA). The absorbance of cells was plotted as % viability against varying concentrations of the compounds after normalising DMSO and growth media controls.

4.3 Result and Discussion:

4.3.1 Syntheses

The ligands L1, L2, and L3 were synthesized using the previously reported procedures and were characterized by the mass and multiple NMR spectroscopy (Figure A1-A8, Appendix 4).[45-47] The angle between the tripodal arms of the ligand L1 is around 109° and those in L2 and L3 are 120°. Hong and co-workers have previously carried out the metallation studies of the ligand L1 with various metal ions in the presence of chloride and perchlorate anions resulting in the formation of $[M_6L_8]^{12+}$ cages. Interestingly, two unique conformations, syn and anti, were observed for L1 in these cages (Figure A9, Appendix 4). The orientation of the ligand was found to be syn for the complexes of lighter 3d metal ions, while an anti-conformation was observed for the cage built from the heavier Pd(II) ion. Similar ligand conformations have been noted for the ligands L2 and L3 in their corresponding MOCs. Since highly soluble complexes (in water or aqueous buffer solution) of compounds 1, 2 and 3 and non-interfering anions are desiredfor the cytotoxic studies, we newly synthesized these cages in the presence of non-coordinatingtetrafluoroborate (BF_4^-) anions by a modified synthetic procedure. Thus, treatment of the tetratopic Pd(II) precursor $Pd(CH_3CN)_4(BF_4)_2$ with the tripodal ligands L1, L2 and L3 have resulted in the formation of the octahedral cage complexes $[Pd_6(L1)_8.12BF_4]$ (1), $[Pd_6(L2)_8.12BF_4]$ (2) and $[Pd_6(L3)_8.12BF_4]$ (3), respectively (Figure A11, Appendix 4). In all the cases, the reaction completion was monitored by a visual colour change from yellow to orange. 1 was found to be soluble in a variety of solvents such as DMSO, DMF, MeCN and MeOH. The compounds 2 and 3 were soluble only in higher polar solvents like DSMO and DMF and slightly in MeOH and H_2O. Further, the formation of the compounds 1, 2, and3 was confirmed by ^1H-, and ^{31}P-NMR studies (Figure 4.1, A12-A16, Appendix 4). The ^1H- NMR profile for 1 showed four unique signature peaks originating from the metal-boundligand L1 with a marked change in the chemical shifts confirming the coordination of pyridineN-atom with the metal acceptors. The observed broadening in the proton peaks signify the formation of the bigger cage-like molecule. The Phosphorous NMR profile of 1 showed a single peak at -8.29 ppm with a change in chemical shift value of 4.68 ppm from that of L1 (-3.29, ppm), which confirms the formation of a single product. To further establish the structureof 1, the ESI-MS studies were performed on its MeCN solution, which showed the isotopic distribution of peaks with m/z values cantered at 476.3, 570.4, and 701 for the species

corresponding to $[Pd_6(L1)_8.5BF_4]^{+7}$, $[Pd_6(L1)_8.6BF_4]^{+6}$, $[Pd_6(L1)_8.5BF_4]^{+5}$, ions, respectively (Figure A11, Appendix 4).

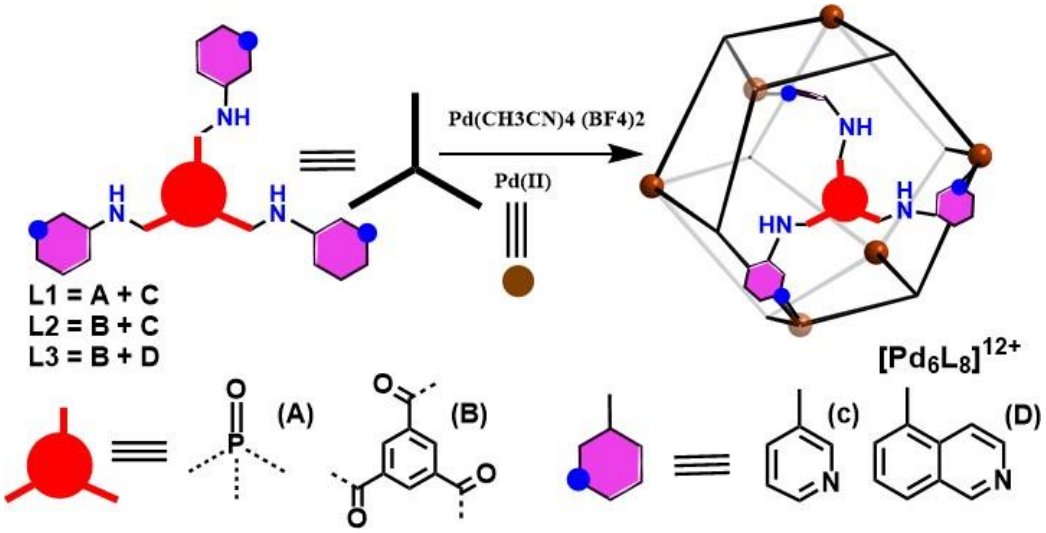

Scheme 4.1 *Schematic presentation of ligand L1, ligand L2 and ligand L3 and their respective metallocages 1, 2 and 3.*

The compound 2 showed six proton peaks due to the ligand L2 in DMSO-d6 solution. Of these six peaks, one originates from the amide NH-group, four peaks due to the pyridyl moity and one due to the central benzene ring. Maximum change in chemical shift was observed for the proton(Ha), which is positioned near to the metal-bound pyridine nitrogen (Figure 4.1b, A13 Appendix 4). These protons peaks match with the reported literature. CHN analysis showed weight percentage of elements present in the evacuated product, which again confirms the formation of expected cage $[Pd_6(L2)_8.12BF_4]$ (2). Proton NMR experiments on compound 3 in DMSO-d_6 solvent showed nine peaks due to the metal-bound ligand L3, with slight shift in their chemical shift values accompanied by notable peak broadening (Figure 4.1 C). This indicates the formation of a stable MOC assembly mediated by the coordination of N_{py} groups with the tetratopic Pd(II) acceptors. Of these nine peaks, one is attributed to the amide NH-group, one due to the central benzene ring and seven due to the quinolyl moieties. The observed ^{1}H-NMR signals match the iso-structural cages reported in the literature. (Figure A14, Appendix 4). Further, to confirm the composition of product 2 and 3, we tried to perform the ESI-MS and MALDI-TOF experiments. However, poor solubility of the MOCs in organic solvents except DMSO and DMF, we were unable to get good results which could have confirmed the composition of the product (Figure A15-16, Appendix 4).

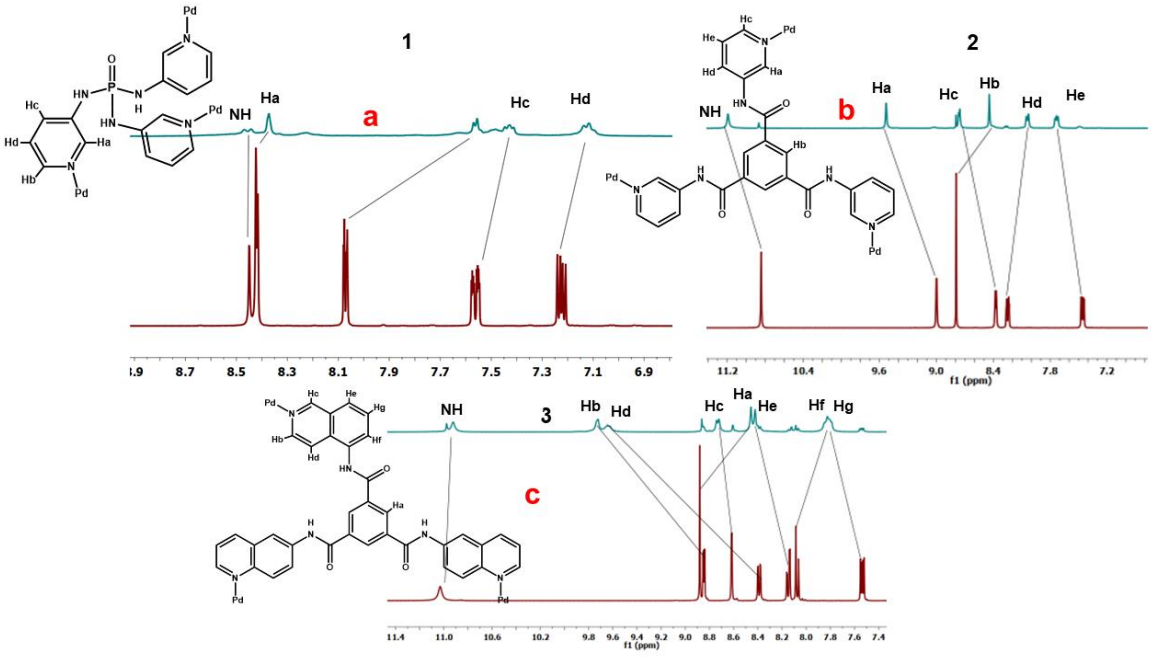

Figure 4.1 *(a) ^{1}H NMR of Ligand L1 (below) and 1 (above), (b) ^{1}H NMR of Ligand L2(below) and 2 (above), and (c) ^{1}H NMR of Ligand L1 (below) and 3.*

Our attempts to obtain crystals of the compounds 1, 2 and 3 suitable for single-crystal X-ray diffraction were not very successful. However, the core structures of these cages along with other counter anions were already established in the literature providing us with the necessary understanding of their complex structural architectures.

4.3.2 Anticancer Activity

All these self-assembled compounds 1, 2 and 3 are air and moisture stable in the solid-state, and they can be stored in air for more than two months without any noticeable decomposition. Hence their stability in solution will facilitate them for biological applications. Thus, we set out to investigate the influence of these MOCs along with these different pyridine-based ligands (L1, L2, and L3) for their cytotoxic activity. In vitro anticancer efficacies of self-assembled metal-organic complexes 1-3 were assessed by an MTT assay in human cancer cell line MCF-7 (breast). The free ligands (L1, L2, and L3) were tested as a control (Figure 4.2). These cells were exposed to various concentrations of the compounds including ligands and

the MOCs 1–3 for 24 h and the results are summarized. (Table 4.1, Appendix 4). Data suggested that all three ligands are inactive and hence unable to kill MCF-7 cells. However, self-assemblies 2 and 3 showed very good result, especially, the activity observed for 3 was very promising.

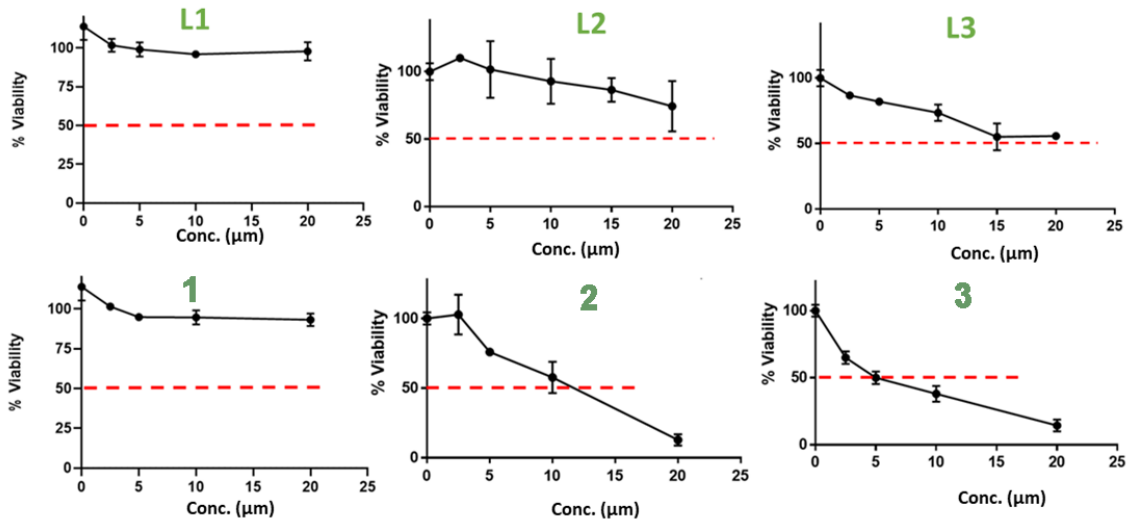

Figure 4.2 *Half-maximum inhibitory concentration (IC_{50}) plots for all three ligands and their respective metallocages 1, 2 and 3 against MCF-7 cancer cell lines.*

As seen from figure 4.2, the compound 3 showed excellent anticancer activity among these three compounds with the observed lowest IC_{50} value of 5 µM towards MCF-7 cancer cell line. In fact, both 2 and 3, the MOCs based on the planar amide backbone have showed better activity than cisplatin against MCF-7 cancer cells (Table 4.1, Appendix 4). The IC_{50} values ofall cell in figure 4.2 indicate that the free ligands L1–L3 have no anticancer ability. Results obtained by MTT experiments may be rationalized by the observation that the ligands themselves are neutral by charge and that make them inactive to diffuse inside the cell and perhaps they undergo cell uptake only by the formation of large self-assemblies with the cationic charge on each metal centre. However, 1 was found inactive towards cancer cells,suggesting that the shape/size of the assemblies also plays a major role for the cell uptake. Cancer cell selectivity is an important factor to examine for any drug. Cisplatin is an exampleof a drug with less cancer cell selectivity as they also kill the normal cells that induced many side effects in the human body. The cancer cell selectivity of the ligands L2-L3 and MOCs 1-3, on the cytotoxicity of cancer and normal cells were also investigated in human lung cancer

cell HEK29 as summarized (Figure 4.3, A17, Appendix 4). The cytotoxicity of the commonly used anticancer drugs, cisplatin, paclitaxel, and doxorubicin on normal HEK29 cell line were also put (Table 4.1, Appendix 4) for comparison.

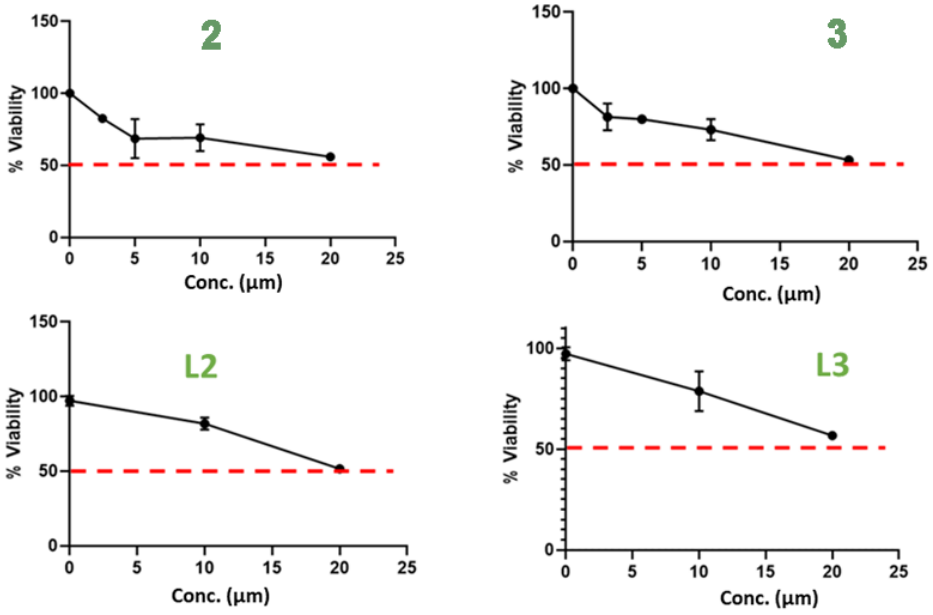

Figure 4.3 Half-maximum inhibitory concentration (*IC_{50}) plots for ligand L2 and L3 and their respective compounds 2 and 3 against HEK29 normal cell lines.*

The active MOCs showed good performance as they are less cytotoxic toward HEK29 normal cells (Figure 4.3, A17, Appendix 4). The IC_{50} value for compound 3 is lowest among other compounds which is 5 µM for breast cancer cell and the high value of IC_{50} for compound 3 towards normal kidney cell line. The selectivity index (SI) is defined as the ratio of IC_{50} value of normal cells and cancer cells. The SI ratio for 3 was calculated to be 4. This result indicates that the large self-assembled 3 is able to kill cancer cells more effectively and selectively than the well-known cisplatin.

It is known that DNA may be a potential target for Pt, Ru- based anticancer drugs, and many ruthenium compounds are known to have high selectivity for binding to DNA. The western blotting technique is used to identify the protein molecules based on their sizes. Here. this technique has helped us to understand the cell death of the MCF-7 cells. The summarized data based on the IC_{50} values suggests that 3 is a potent molecule with high selectivity and efficacy. To understand the mechanistic insights within the cells, treatment of cancer cells with3 and ligand L3 was undertaken for a period of 24 hours. A high activity level of γH2X marker suggested the damage of double strand DNA is higher for 3 than ligand L3.

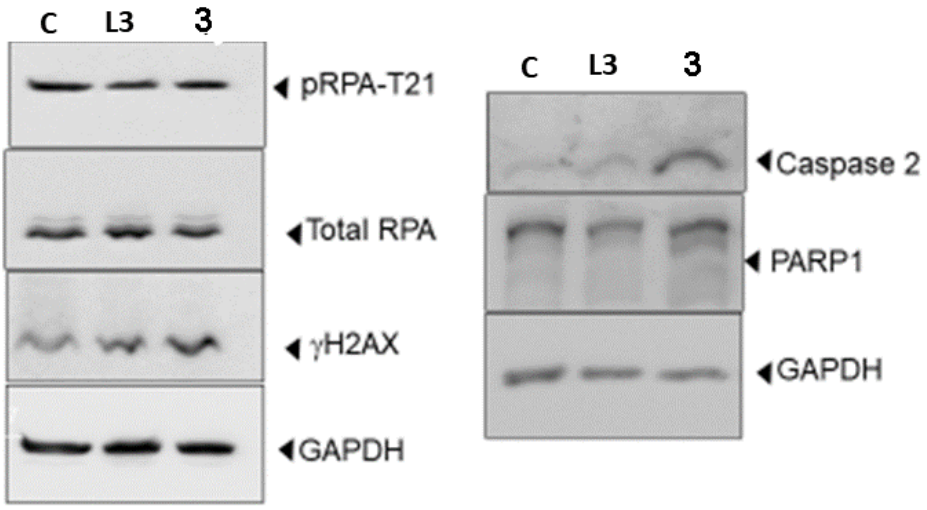

Figure 4.4 *Western blotting graph of control, ligand L3 and 3 and observed the activation levels.*

Whereas, the RPA marker did not show any such activity which suggests that only double-strand DNA break, while there was no damage happening for the single-strand DNA in the cells (Figure 4.4). PARP1 and Caspase 2 protein markers were used to confirm apoptosis, a program of cell death in the cell lines. High activity in these two markers has been recorded. However, no such activities were noticed for these two (PARP1 and Caspase 2) markers during the treatment of cells with the uncoordinated ligand L3 (Figure 4.4). Thus, the western blotting technique clearly established the high activity for 3 as compared to that of ligand L3.

Conclusion:

In summary, we report the synthesis of a series of $[Pd_6L_8]^{+12}$ based self-assembled metal-organic cages by the self-assembly reaction of phosphoramide and benzenecarboxamide based flexible tripodal ligands (L1, L2, L3) with $[Pd(CH_3CN(BF_4)_2]$ metal salt. The cytotoxicity of these complexes against breast cancer cell HCF-7 was evaluated. The obtained IC_{50} values for all three ligands and cage 1 are more than 20 μm that renders inactivity towards cancer cells. However, 2 and 3 exhibited good results as the IC_{50} values of 11.5 and 5 μm, respectively, against MCF-7, cancer cell lines were observed, which are better than that observed for cisplatin. Also, compounds 2 and 3 have good selectivity for the MCF-7 cancer cell lines in comparison with the normal HEK29 cell lines. All, these observations stimulate the research on the applications of MOCs with less-expensive metal ions for cytotoxic studies.

References:

(1) Sun, Y.; Chen, C.; J. Stang, P. Soft Materials with Diverse Suprastructures via the Self-Assembly of Metal–Organic Complexes. *Acc. Chem. Res.* **2019**, *52*, 802–817.

(2) Cook, T. R.; Stang, P. J. Recent Developments in the Preparation and Chemistry of Metallacycles and Metallacages via Coordination. *Chem. Rev.* **2015**, *115*, 7001–7045.

(3) Smulders, M. M. J.; Riddell, I. A.; Browne, C.; Nitschke, J. R. Building on Architectural Principles for Three-Dimensional Metallosupramolecular Construction. *Chem. Soc. Rev.* **2013**, *42*, 1728–1754.

(4) Chakrabarty, R.; Mukherjee, P. S.; Stang, P. J. Supramolecular Coordination: Self-Assembly of Finite Two- and Three-Dimensional Ensembles. *Chem. Rev.* **2011**, *111*, 6810–6918.

(5) Cook, T. R.; Zheng, Y. R.; Stang, P. J. Metal-Organic Frameworks and Self-Assembled Supramolecular Coordination Complexes: Comparing and Contrasting the Design, Synthesis, and Functionality of Metal-Organic Materials. *Chem. Rev.* **2013**, *113*, 734–777.

(6) Cotton, F. A.; Daniels, L. M.; Lin, C.; Murillo, C. A. Square and Triangular Arrays Based on Mo24+ and Rh24+ Units. *J. Am. Chem. Soc.* **1999**, *121*, 4538–4539.

(7) Li, S.; Huang, J.; Zhou, F.; Cook, T. R.; Yan, X.; Ye, Y.; Zhu, B.; Zheng, B.; Stang, P. J. Self-Assembly of Triangular and Hexagonal Molecular Necklaces. *J. Am. Chem. Soc.* **2014**, *136*, 5908–5911.

(8) L. Caulder, D.; Brückner, C.; E. Powers, R.; König, S.; N. Parac, T.; A. Leary, J.; N. Raymond, K. Design, Formation and Properties of Tetrahedral M4L4 and M4L6 Supramolecular Clusters1. *J. Am. Chem. Soc.* **2001**, *123*, 8923–8938.

(9) Komine, S.; Tateishi, T.; Kojima, T.; Nakagawa, H.; Hayashi, Y.; Takahashi, S.; Hiraoka, S. Self-Assembly Processes of Octahedron-Shaped Pd 6 L 12 Cages. *Dalt. Trans.* **2019**, *48*, 4139–4148.

(10) Suzuki, K.; Tominaga, M.; Kawano, M.; Fujita, M. Self-Assembly of an M6L12 Coordination Cube. *Chem. Commun.* **2009**, *13*, 1638–1640.

(11) Fujita, D.; Ueda, Y.; Sato, S.; Yokoyama, H.; Mizuno, N.; Kumasaka, T.; Fujita, M. Self-Assembly of M30L60 Icosidodecahedron. *Chem* **2016**, *1*, 91–101.

(12) Browne, C.; Brenet, S.; Clegg, J. K.; Nitschke, J. R. Solvent-Dependent Host-Guest Chemistry of an Fe8L12 Cubic Capsule. *Angew. Chemie. Int. Ed.* **2013**, *52*, 1944–1948.

(13) Ueda, Y.; Ito, H.; Fujita, D.; Fujita, M. Permeable Self-Assembled Molecular Containers for Catalyst Isolation Enabling Two-Step Cascade Reactions. *J. Am. Chem. Soc.* **2017**, *139*, 6090–6093.

(14) Zhao, J.; Zhou, Z.; Li, G.; Stang, P. J.; Yan, X. Light-Emitting Self-Assembled Metallacages. *Natl. Sci. Rev.* **2021**, *8*.

(15) Ward, M. D.; Hunter, C. A.; Williams, N. H. Coordination Cages Based on Bis(Pyrazolylpyridine) Ligands: Structures, Dynamic Behavior, Guest Binding, and Catalysis. *Acc. Chem. Res.* **2018**, *51*, 2073–2082.

(16) Zhang, D.; Ronson, T. K.; Nitschke, J. R. Functional Capsules via Subcomponent Self-Assembly. *Acc. Chem. Res.* **2018**, *51*, 2423–2436.

(17) Mari, C.; Pierroz, V.; Ferrari, S.; Gasser, G. Combination of Ru(II) Complexes and Light: New Frontiers in Cancer Therapy. *Chem. Sci.* **2015**, *6*, 2660–2686.

(18) Zarra, S.; Wood, D. M.; Roberts, D. A.; Nitschke, J. R. Molecular Containers in Complex Chemical Systems. *Chem. Soc. Rev.* **2015**, *44*, 419–432.

(19) Chen, L. J.; Yang, H. B.; Shionoya, M. Chiral Metallosupramolecular Architectures. *Chem. Soc. Rev.* **2017**, *46*, 2555–2576.

(20) Cook, T. R.; Vajpayee, V.; Lee, M. H.; Stang, P. J.; Chi, K. W. Biomedical and Biochemical Applications of Self-Assembled Metallacycles and Metallacages. *Acc. Chem. Res.* **2013**, *46*, 2464–2474.

(21) Ahmedova, A. Biomedical Applications of Metallosupramolecular Assemblies-Structural Aspects of the Anticancer Activity. *Front. Chem.* **2018**, *6*.

(22) Zhou, J.; Zhang, Y.; Yu, G.; Crawley, M. R.; Fulong, C. R. P.; Friedman, A. E.; Sengupta, S.; Sun, J.; Li, Q.; Huang, F.; Cook, T. R. Highly Emissive Self-Assembled BODIPY-Platinum Supramolecular Triangles. *J. Am. Chem. Soc.* **2018**, *140*, 7730–7736.

(23) Jana, A.; Bhowmick, S.; Kumar, S.; Singh, K.; Garg, P.; Das, N. Self-Assembly of Pt(II) Based Nanoscalar Ionic Hexagons and Their Anticancer Potencies. *Inorganica Chim. Acta* **2019**, *484*, 19–26.

(24) Zhou, Z.; Liu, J.; Rees, T. W.; Wang, H.; Li, X.; Chao, H.; Stang, P. J. Heterometallic Ru–Pt Metallacycle for Two-Photon Photodynamic Therapy. *Proc. Natl. Acad. Sci. U. S. A.* **2018**, *115*, 5664–5669.

(25) Yu, G.; Cook, T. R.; Li, Y.; Yan, X.; Wu, D.; Shao, L.; Shen, J.; Tang, G.; Huang, F.; Chen, X.; Stang, P. J. Tetraphenylethene-Based Highly Emissive Metallacage as a Component of Theranostic Supramolecular Nanoparticles. *Proc. Natl. Acad. Sci. U. S. A.* **2016**, *113*, 13720–13725.

(26) Siddik, Z. H. Cisplatin: Mode of Cytotoxic Action and Molecular Basis of Resistance. *Oncogene* **2003**, *22*, 7265–7279.

(27) Wong, E.; Giandornenico, C. M. Current Status of Platinum-Based Antitumor Drugs. *Chem. Rev.* **1999**, *99*, 2451–2466.

(28) Lazarević, T.; Rilak, A.; Bugarčić, Ž. D. Platinum, Palladium, Gold and Ruthenium Complexes as Anticancer Agents: Current Clinical Uses, Cytotoxicity Studies and Future Perspectives. *Eur. J. Med. Chem.* **2017**, *142*, 8–31.

(29) Coskun, M. D.; Ari, F.; Oral, A. Y.; Sarimahmut, M.; Kutlu, H. M.; Yilmaz, V. T.; Ulukaya, E. Promising Anti-Growth Effects of Palladium(II) Saccharinate Complex of Terpyridine by Inducing Apoptosis on Transformed Fibroblasts in Vitro. *Bioorganic Med. Chem.* **2013**, *21*, 4698–4705.

(30) Xu, W. Q.; Fan, Y. Z.; Wang, H. P.; Teng, J.; Li, Y. H.; Chen, C. X.; Fenske, D.; Jiang, J. J.; Su, C. Y. Investigation of Binding Behavior between Drug Molecule 5-Fluoracil and M4L4-Type Tetrahedral Cages: Selectivity, Capture, and Release. *Chem. - A Eur. J.* **2017**, *23* , 3542–3547.

(31) Ferraro, G.; Massai, L.; Messori, L.; Merlino, A. Cisplatin Binding to Human Serum Albumin: A Structural Study. *Chem. Commun.* **2015**, *51*, 9436–9439.

(32) Furrer, M. A.; Schmitt, F.; Wiederkehr, M.; Juillerat-Jeanneret, L.; Therrien, B. Cellular Delivery of Pyrenyl-Arene Ruthenium Complexes by a Water-Soluble Arene Ruthenium Metalla-Cage. *Dalt. Trans.* **2012**, *41*, 7201–7211.

(33) Han, J.; Räder, A. F. B.; Reichart, F.; Aikman, B.; Wenzel, M. N.; Woods, B.; Weinmüller, M.; Ludwig, B. S.; Stürup, S.; Groothuis, G. M. M.; Permentier, H. P.; Bischoff, R.; Kessler, H.; Horvatovich, P.; Casini, A. Bioconjugation of Supramolecular Metallacages to Integrin Ligands for Targeted Delivery of Cisplatin. *Bioconjug. Chem.* **2018**, *29*, 3856–3865.

(34) Yue, Z.; Wang, H.; Bowers, D. J.; Gao, M.; Stilgenbauer, M.; Nielsen, F.; Shelley, J. T.; Zheng, Y. R. Nanoparticles of Metal-Organic Cages Designed to Encapsulate Platinum-Based Anticancer Agents. *Dalt. Trans.* **2018**, *47*, 670–674.

(35) Zheng, Y. R.; Suntharalingam, K.; Johnstone, T. C.; Lippard, S. J. Encapsulation of Pt(IV) Prodrugs within a Pt(II) Cage for Drug Delivery. *Chem. Sci.* **2015**, *6*, 1189–1193.

(36) Therrien, B.; Furrer, J. The Biological Side of Water-Soluble Arene Ruthenium Assemblies. *Adv. Chem.* **2014**, *2014*, 1–20.

(37) Casini, A.; Woods, B.; Wenzel, M. The Promise of Self-Assembled 3D Supramolecular Coordination Complexes for Biomedical Applications. *Inorg. Chem.* **2017**, *56* , 14715–14729.

(38) Schmitt, F.; Freudenreich, J.; Barry, N. P. E.; Juillerat-Jeanneret, L.; Süss-Fink, G.; Therrien, B. Organometallic Cages as Vehicles for Intracellular Release of Photosensitizers. *J. Am. Chem. Soc.* **2012**, *134*, 754–757.

(39) Paul, L. E. H.; Therrien, B.; Furrer, J. Investigation of the Reactivity between a Ruthenium Hexacationic Prism and Biological Ligands. *Inorg. Chem.* **2012**, *51*, 1057–1067.

(40) Hearn, J. M.; Romero-Canelón, I.; Qamar, B.; Liu, Z.; Hands-Portman, I.; Sadler, P. J. Organometallic Iridium(III) Anticancer Complexes with New Mechanisms of Action: NCI-60 Screening, Mitochondrial Targeting, and Apoptosis. *ACS Chem. Biol.* **2013**, *8*, 1335–1343.

(41) Ahmad, N.; Younus, H. A.; Chughtai, A. H.; Verpoort, F. Metal-Organic Molecular Cages: Applications of Biochemical Implications. *Chem. Soc. Rev.* **2015**, *44*, 9–25.

(42) Mari, C.; Pierroz, V.; Ferrari, S.; Gasser, G. Combination of Ru(II) Complexes and Light: New Frontiers in Cancer Therapy. *Chem. Sci.* **2015**, *6*, 2660–2686.

(43) Zhang, M.; Li, S.; Yan, X.; Zhou, Z.; Lal Saha, M.; Wang, Y. C.; Stang, P. J. Fluorescent Metallacycle-Cored Polymers via Covalent Linkage and Their Use as Contrast Agents for Cell Imaging. *Proc. Natl. Acad. Sci. U. S. A.* **2016**, *113*, 11100–11105.

(44) Paul, L. E. H.; Therrien, B.; Furrer, J. Interactions of Arene Ruthenium Metallaprisms with Human Proteins. *Org. Biomol. Chem.* **2015**, *13*, 946–953.

(45) Li, X. J.; Jiang, F. L.; Wu, M. Y.; Zhang, S. Q.; Zhou, Y. F.; Hong, M. C. Self-Assembly of Discrete M 6L 8 Coordination Cages Based on a Conformationally Flexible Tripodal Phosphoric Triamide Ligand. *Inorg. Chem.* **2012**, *51*, 4116–4122.

(46) Moon, D.; Kang, S.; Park, J.; Lee, K.; John, R. P.; Won, H.; Seong, G. H.; Kim, Y. S.; Kim, G. H.; Rhee, H.; Lah, M. S. Face-Driven Corner-Linked Octahedral Nanocages: M_6L_8 Cages Formed by C3-Symmetric Triangular Facial Ligands Linked via C4-Symmetric Square Tetratopic PdII Ions at Truncated Octahedron Corners. *J. Am. Chem. Soc.* **2006**, *128*, 3530–3531.

(47) Noh, T. H.; Hong, W.; Lee, H.; Jung, O. Indistinguishability and Distinguishability between Amide and Ester Moieties in the Construction and Properties of M_6L_8 Octahedron Nanocages. **2015**, *44*, 787-794.

END of CHAPTER 4

Thesis Conclusion and Future Perspectives

In summary, this thesis demonstrated the use of di- and tripodal pyridyl phosphoramide ligands and other similarly functionalized multidentate ligands for the construction of various metal-ligands cages, which exhibited interesting structural chemistry and showed applications as piezoelectric materials and biological targets. In chapter 2, reactions of ditopic pyridyl donor ligands based on phosphoramide backbone and tetratopic metal ion acceptors have shown to result in the formation of several metallomacrocyles. Among these macrocyclic structures, the most prevalent ones are typically the self-assembled supramolecular squares. However, it has been proved that supramolecular trimers are feasible in solution if the ligand's backbone is flexible in nature, as they are entropically favoured compared to enthalpically favoured supramolecular tetramer. Yet, the kinetically labile metal-ligand coordination bonds provided the freedom to the metal-ligand self-assembled structures to self-correct themselves and form thermodynamically stable tetrameric products in the solution. Thus, molecular trimers are less common in the literature, mainly because of the strain created in their structures. Factors such as solvents, temperature, and concentration can tune the possibility of the formation of either trimeric or tetrameric structures in the solution. Here, using the 3-pyridyl functionalized phenyl phosphoric diamide ligands and tetrtopic Pd(II) acceptors, we have observed the preferential formation of entropically favoured supramolecular trimer from the mixture of both supramolecular trimer and tetramer in solution. In contrast, the use of a similarly functionalized 4-pyridyl substituted ligand yields a polymeric assembly. Chapter 3 describes the materials application of the crystalline supramolecular coordination complexes (SCCs) as piezoelectric nanogenerators. Recently, cationic cages of octahedral M_6L_8 structure were shown to exhibit ferroelectricity owing to their charge-separated structures, in which the toggling of the anions and their H-bonding interactions with the cage framework were responsible for their polarization. In this chapter, we have described new examples of discrete charge-separated octahedral $[M_6L_8]^{12+}$ cages starting from $Ni(NO_3)_2$ and, $Zn(NO_3)_2$ and the P (V) based tripodal ligand containing 3-pyridyl functionalities and explored their dielectric and piezoelectric properties. Polymer composites of these cages were prepared in combination with PDMS polymer and utilized for the piezoelectric energy harvesting applications. The peak-to-peak output voltage obtained for best performing 10wt % composite of the Zn-Cage in PDMS is 11.3 V. The output voltage obtained from this device has also been utilized for charging a of 10 μF capacitor. In chapter 4, three discrete octahedral $[Pd_6L_8]^{12+}$ cage assemblies were

synthesized based on various tripodal ligands and their cytotoxic studies were performed. The self-assembly reaction of $Pd(BF_4)_2$ with three tripodal ligands (L1, L2 and L3) produced the three discrete self-assemblies architectures **1**, **2** and **3**. The cytotoxicity of these complexes against breast cancer cell HCF-7 was examined. The obtained IC_{50} values from the MTT experiments for all three ligands and cage **1** are more than 20 μm, which renders inactivity towards cancer cells. However, the efficacies of **2** and **3** towards cancer cells were found to be better than cisplatin as the IC_{50} values of these cages were found to be 11.5 and 5 μm, respectively. Also, complexes **2** and **3** have shown good selectivity for the MCF-7 cancer cell lines in comparison with the normal HEK 29 cell lines. To understand the cause of the cancer cell deaths, the western blotting method has been used. In this way, treatment of cancer cells with cage **3**, ligand L3 and control C were undertaken for a period of 24 hours. A high activity level of γH2X marker is observed for cage **3** suggesting the damage of double-strand DNA. PARP1 and Caspase 2 protein markers were used to confirm apoptosis. High activity in these two markers has been recorded for cage **3** in comparison to ligand L3 and control C. This probed the apoptosis happened for the cancer cells in presence of cage **3**.

This thesis thus highlights the role of ligand design that not only provides a rich structural control but also demonstrates the potential of discrete metal-ligand self-assemblies in materials applications and biological activity. Such findings demonstrate the potential of supramolecular coordination assemblies in several research frontiers in the years to come.

Appendix

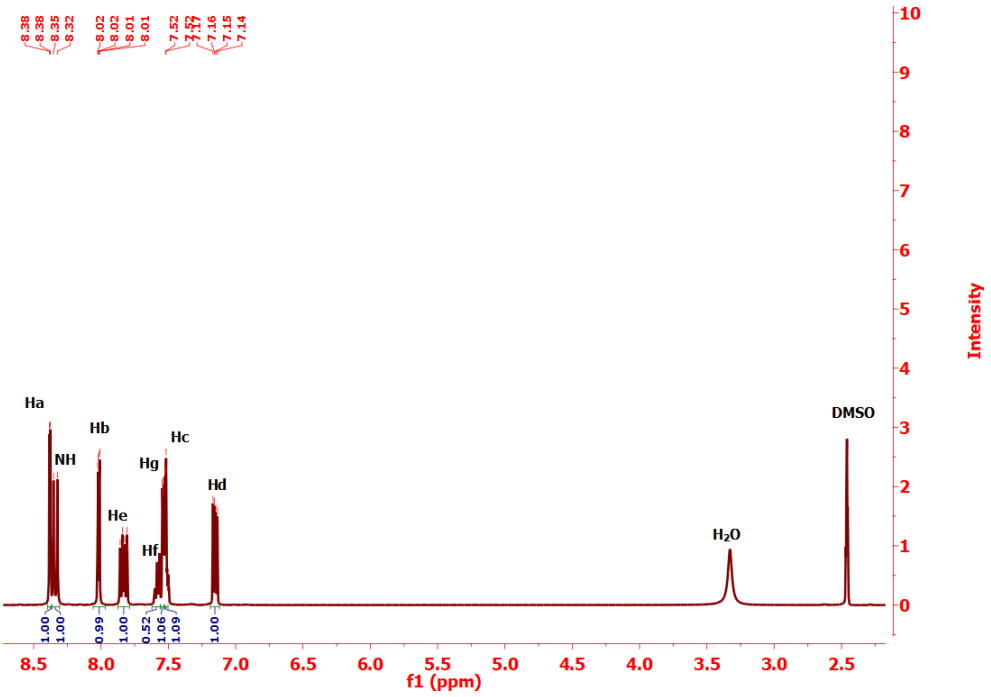

Figure A1: ^{1}H NMR of ligand **L**^{1} in DMSO-d_6 sovlent at 600 MHz.

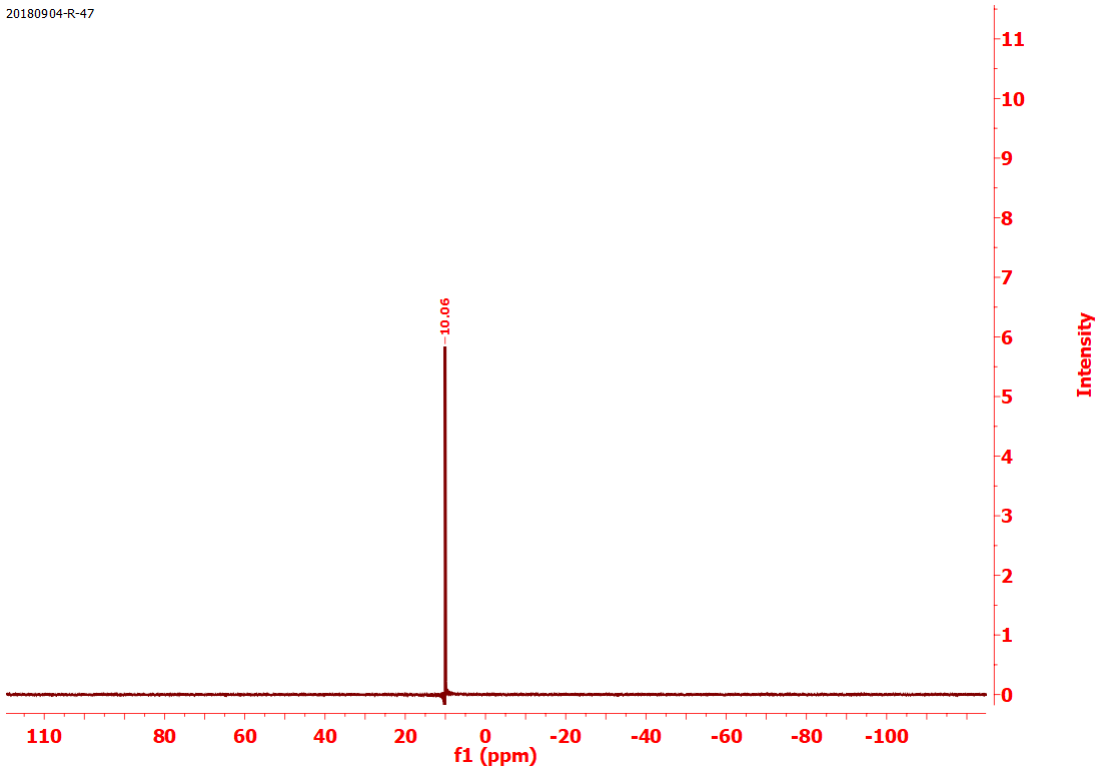

Figure A2: ^{31}P NMR of ligand **L**^{1} in DMSO-d_6 sovlent at 600 MHz.

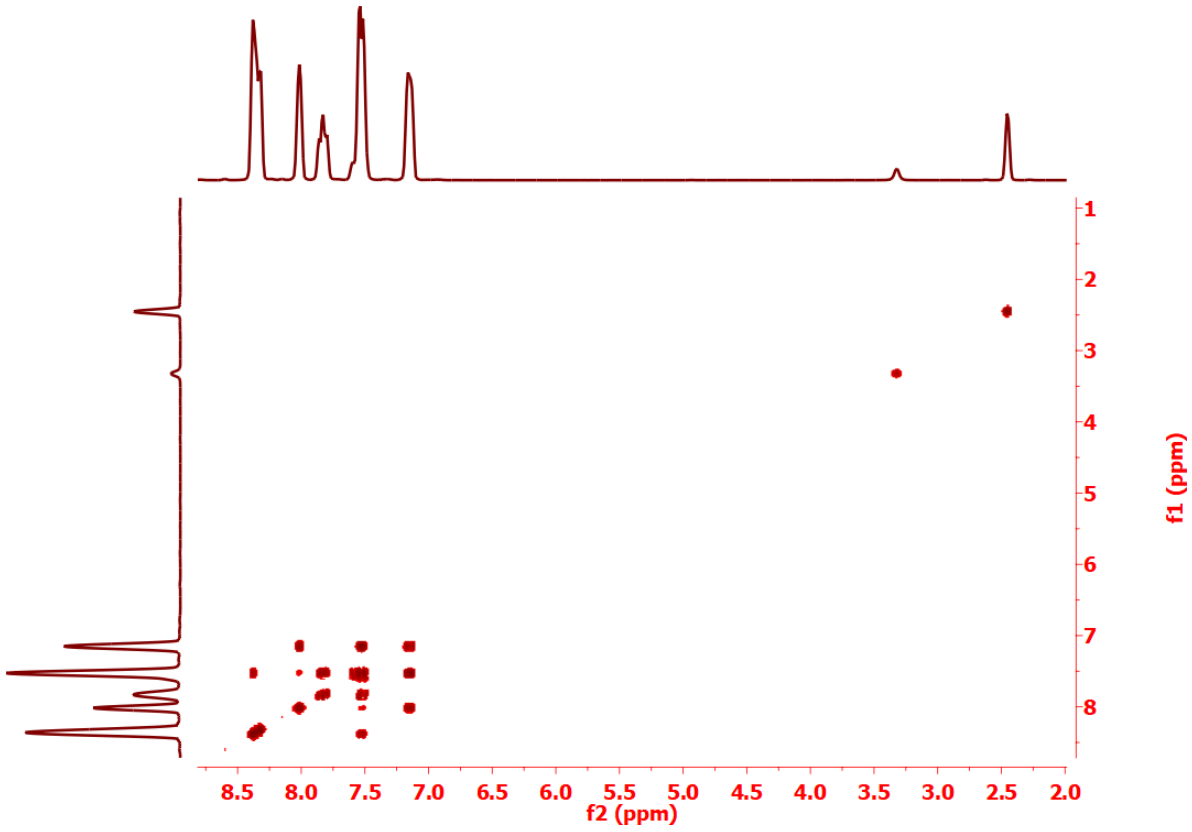

Figure A3: ^{1}H-^{1}H 2D-COSY of the ligand $\mathbf{L^1}$ in DMSO-d_6 at 600 MHz.

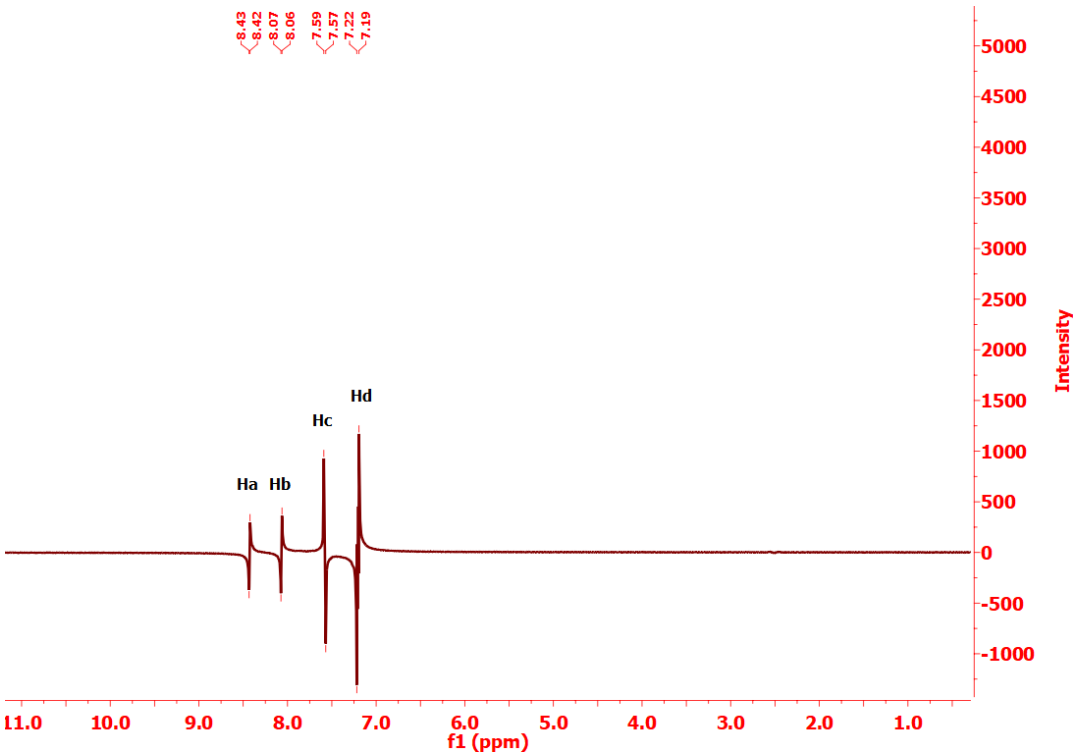

Figure A4: ^{1}H-^{1}H selective 1D-TOCSY of the ligand $\mathbf{L^1}$ in DMSO-d_6 at 600 MHz.

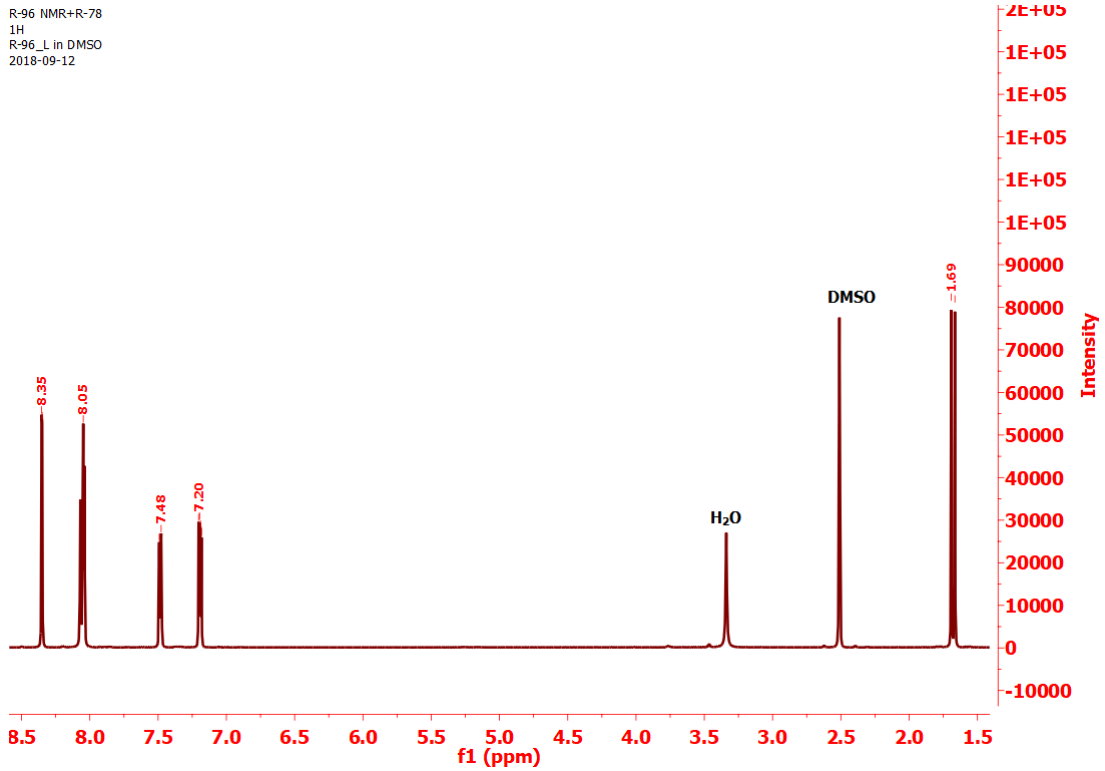

Figure A5: ^{1}H NMR of ligand $\mathbf{L^2}$ in DMSO-d_6 at 400 MHz.

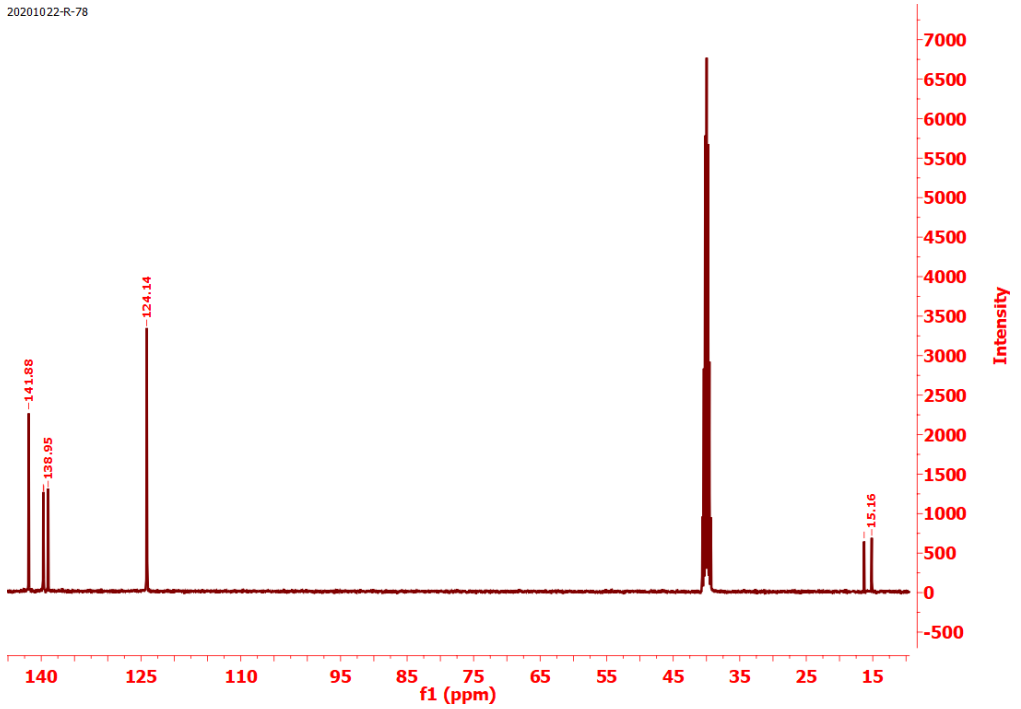

Figure A6: ^{13}C NMR of ligand $\mathbf{L^2}$ in DMSO-d_6 at 400 MHz.

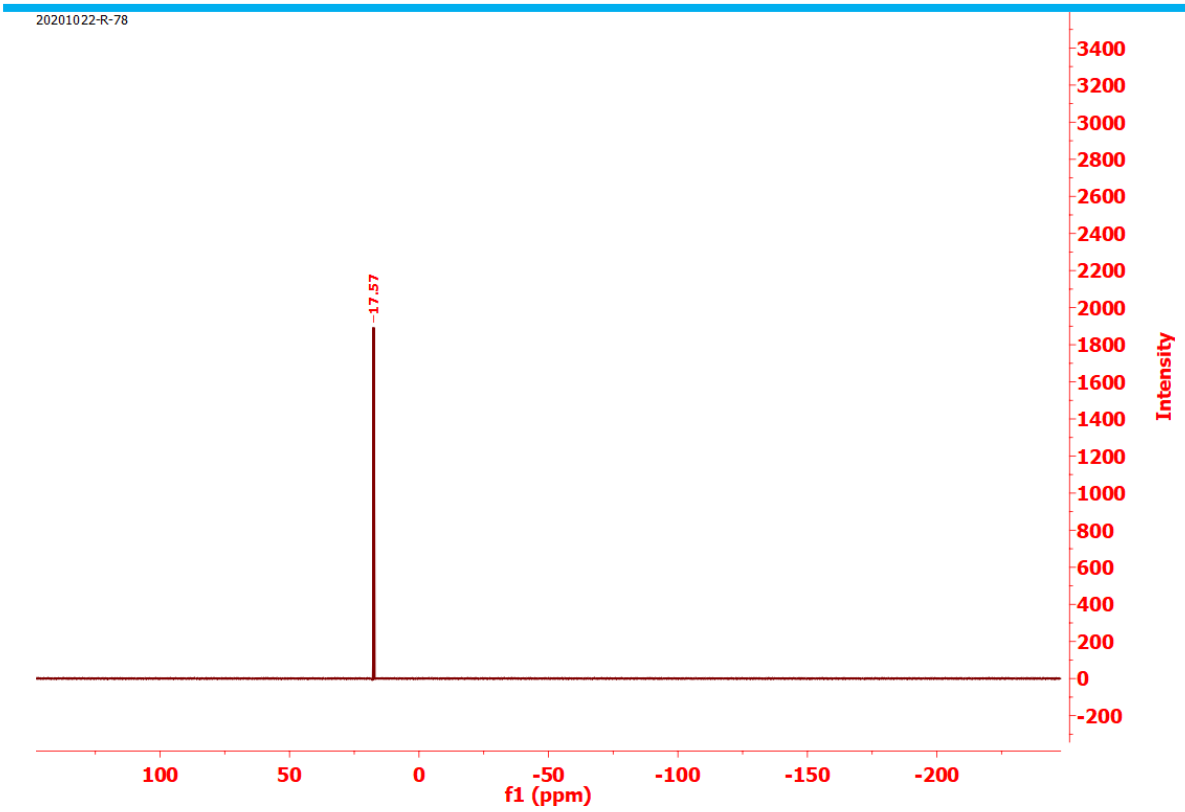

Figure A7: ^{31}P NMR of ligand $\mathbf{L^2}$ in DMSO-d_6 at 400 MHz.

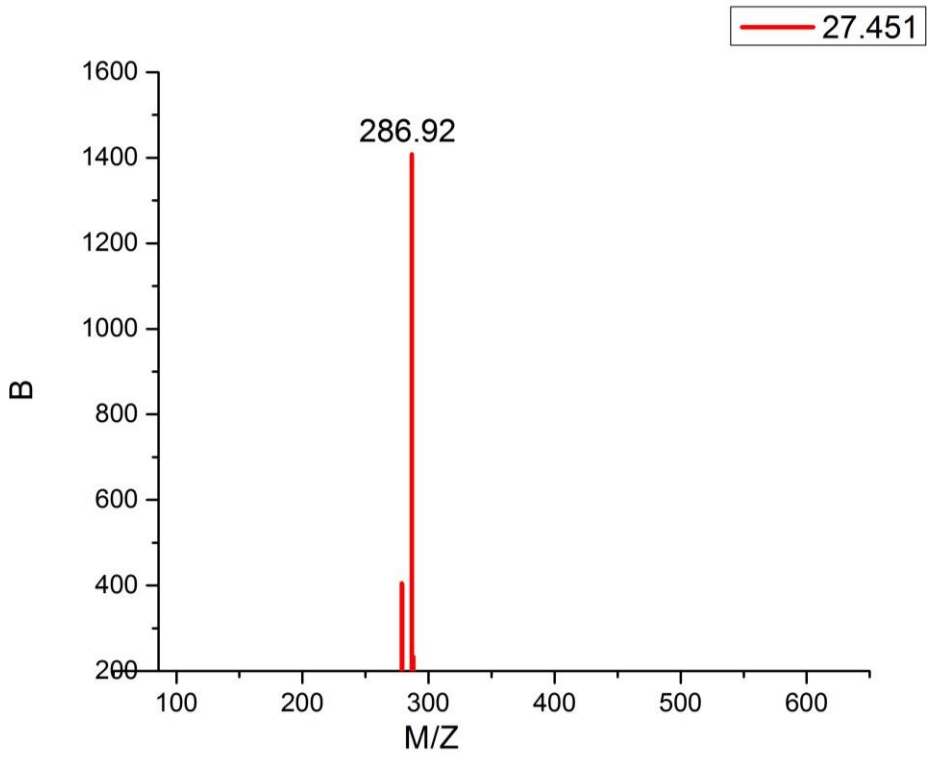

Figure S8: MALDI-TOF of ligand $\mathbf{L^2}$ in water showing the peaks for the species M+K^+= 286.92 m/z.

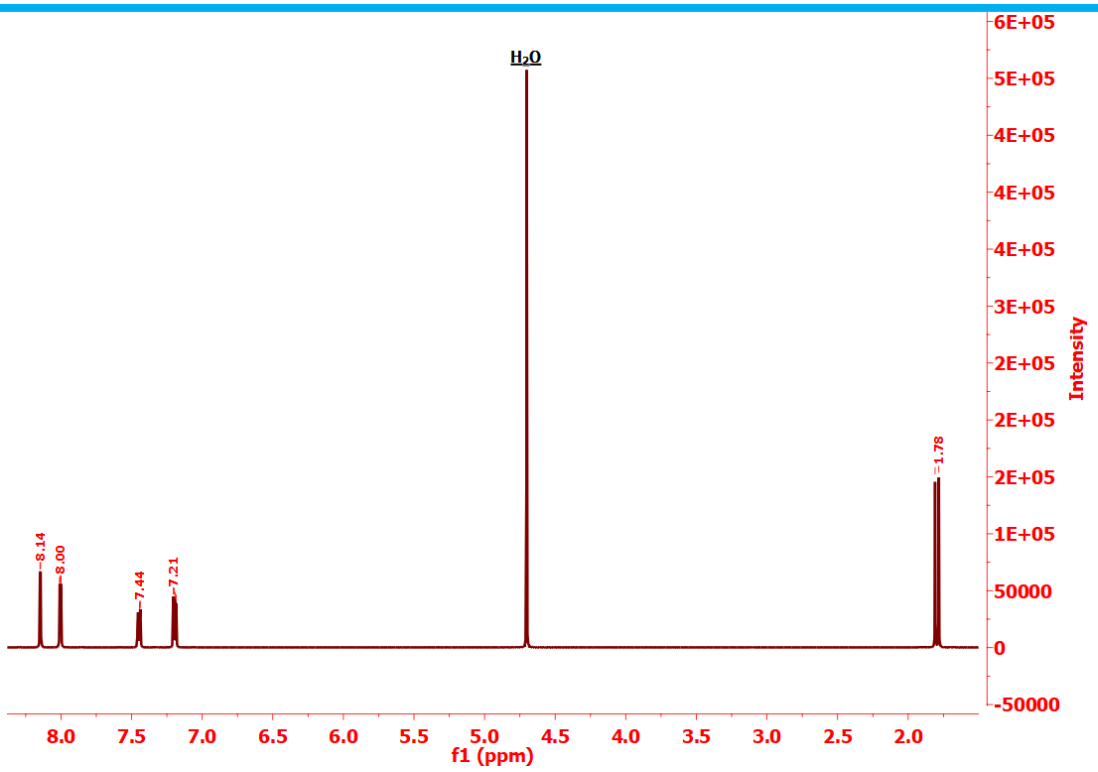

Figure A9: ^{1}H NMR of ligand $\mathbf{L^2}$ in D_2O at 400 MHz.

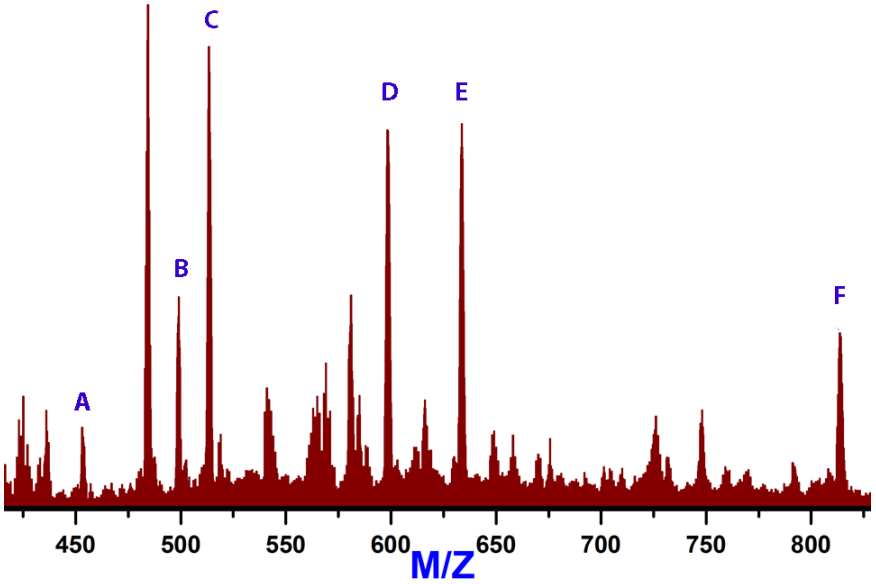

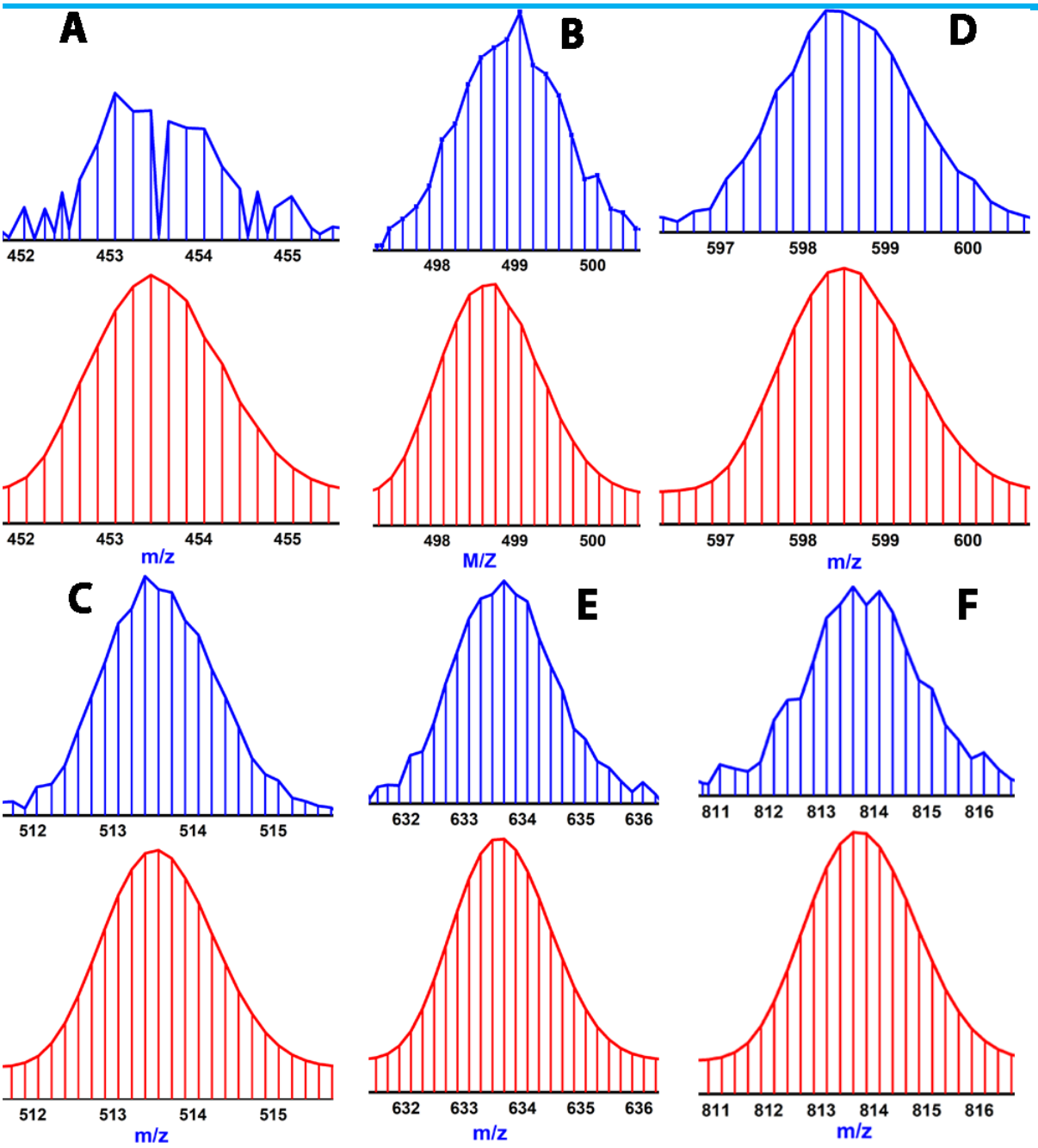

Figure A10: ESI-MS spectrum of of **1** in DMSO/MeCN. The peak patterns for A, B, D corresponds to the experimental (blue) and simulated (red) isotopic distribution of peaks for the trimeric fragments $[Pd_3(\mathbf{L^1})_6+BF_4]^{+5}$, $[Pd_3(\mathbf{L^1})_6+9DMSO+6H_2O]^{+6}$ and, $[Pd_3(\mathbf{L^1})_6+BF_4+7DMSO+10H_2O]^{+5}$, respectively. Similarly, the peak patterns for C, E and F corresponds to the experimental (blue) and simulated (red) isotopic distribution of peaks for the tetrameric fragments $[Pd_4(\mathbf{L^1})_8+2BF_4]^{+6}$, $[Pd_4(\mathbf{L^1})_8+3BF_4]^{+5}$ and $[Pd_4(\mathbf{L^1})_8+2BF_4]^{+4}$, respectively.

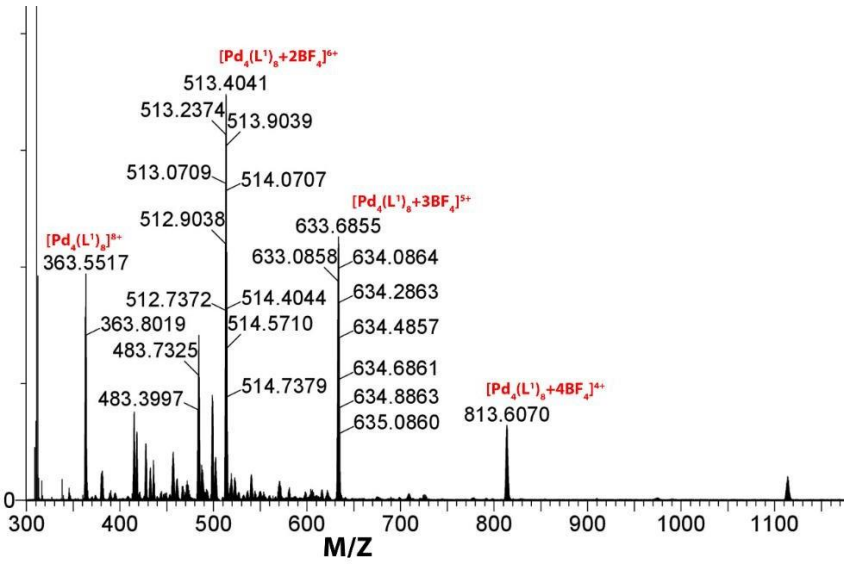

Figure A11: ESI-MS of product **1** in MeCN/DMSO solvent where most of the peaks belong to molecular tetramer (**1b**).

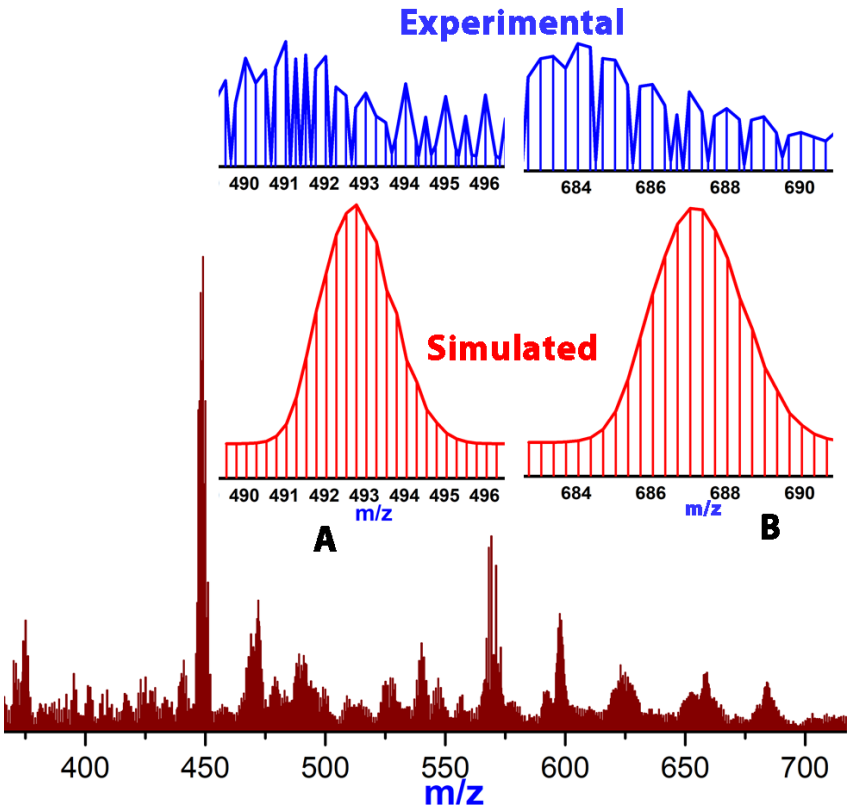

Figure A12: ESI-MS spectrum of **2** in DMSO/MeCN solvent. The experimental (blue) and simulated (red) isotopic distribution of peaks for fragements $[Pd_3(\mathbf{L^2})_6+2BF_4]^{+4}$ and $[Pd_3(\mathbf{L^2})_6+3BF_4]^{+3}$ are given as insets A and B, respectively.

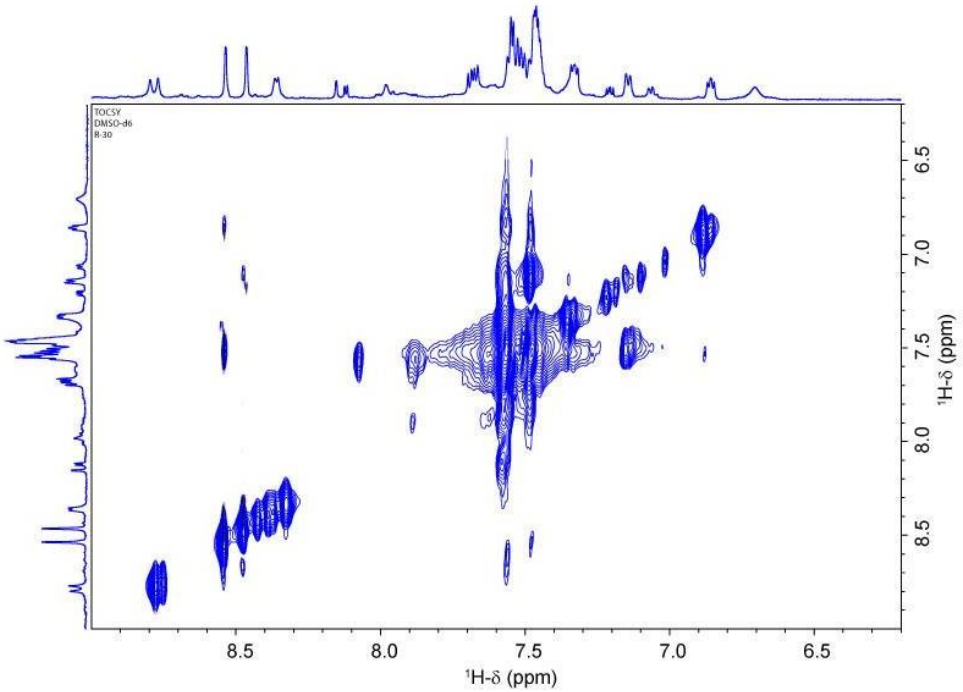

Figure A13: ^{1}H-^{1}H 2D-TOCSY NMR of **1** in DMSO-d_6 solvent at 600 MHz.

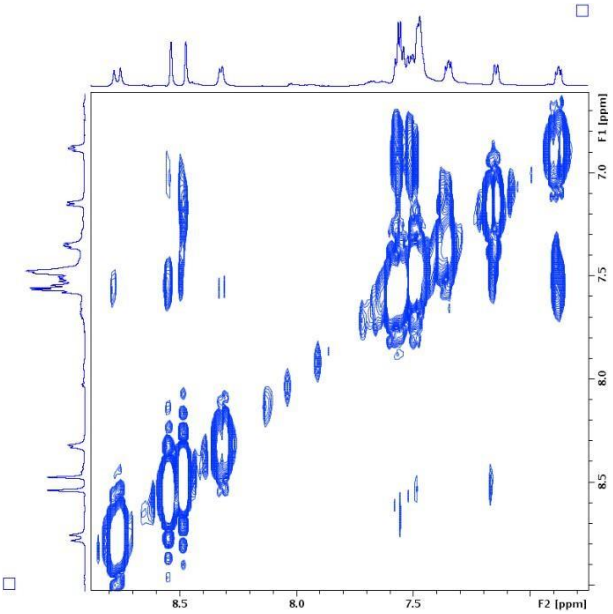

Figure A14: ^{1}H-^{1}H 2D-COSY NMR of **1** in DMSO-d_6 solvent at 600 MHz.

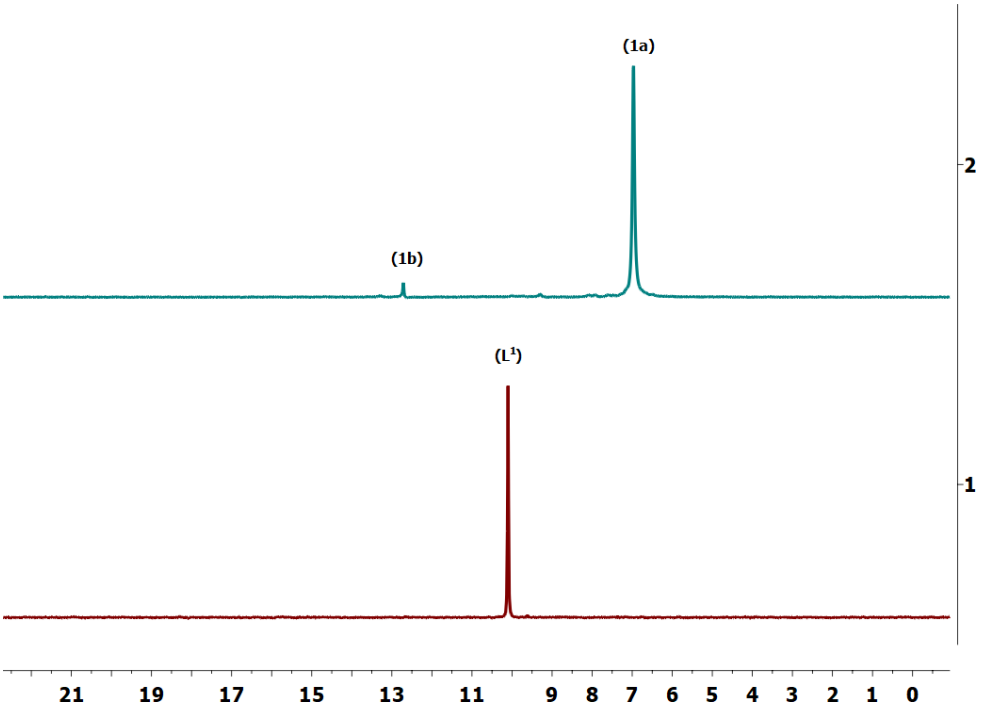

Figure A15: Stacked ^{31}P NMR of Ligand **L^1** (below) and product **1** (above).

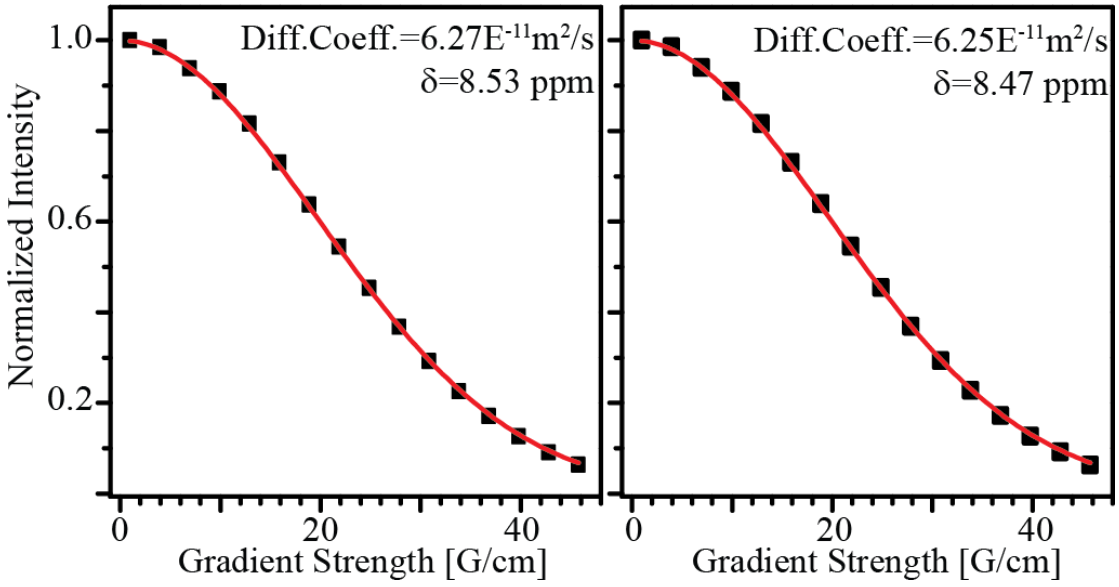

Figure A16: ^{1}H-DOSY NMR derived decay profiles of (left) Ha' ($\delta(^1H)$ = 8.53 ppm) and (right) Ha ($\delta(^1H)$ = 8.47 ppm).

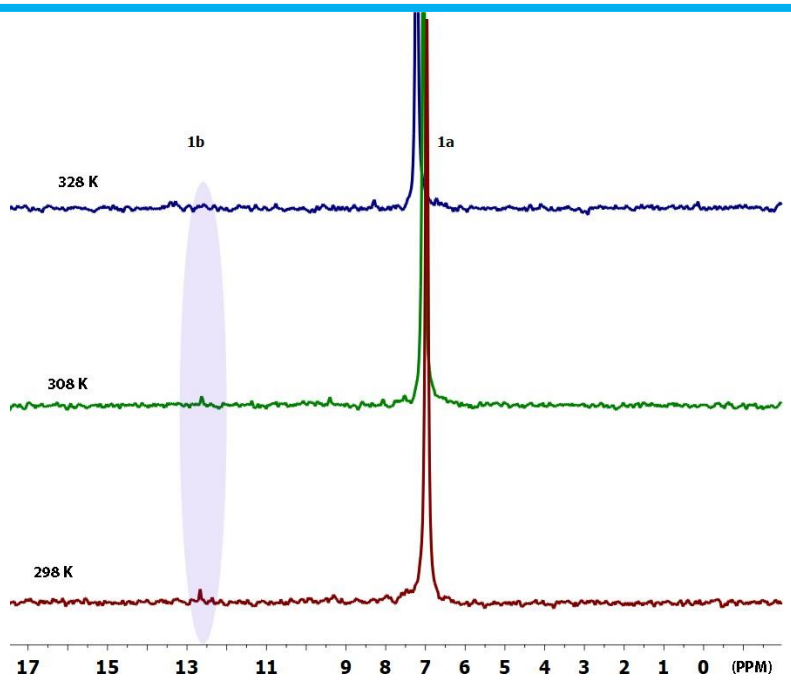

Figure A17: Temperature (from 298 K to 328 K) dependent ^{31}P NMR of **1** in DMSO-d_6 solvent.

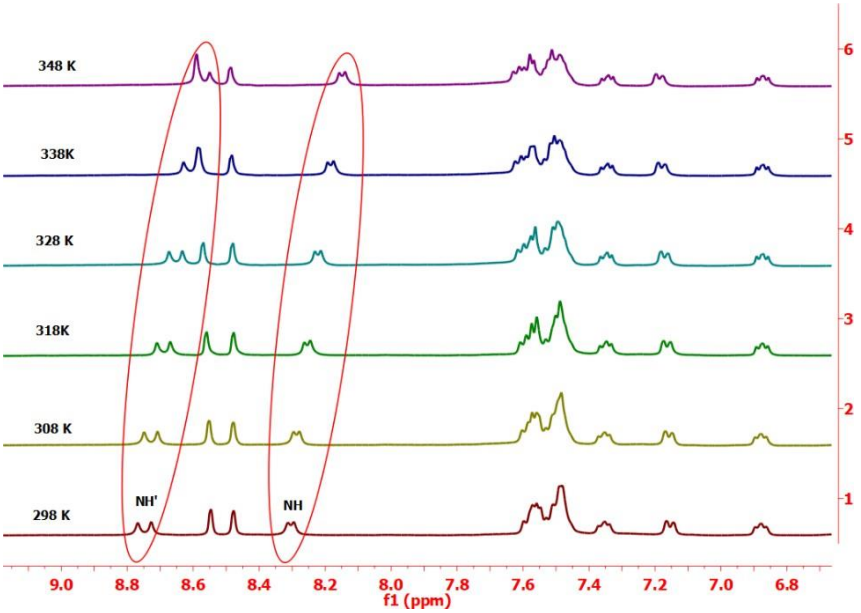

Figure A18: Temperature (from 298 K to 348 K) dependent ^{1}H NMR of **1** in DMSO-d_6 solvent.

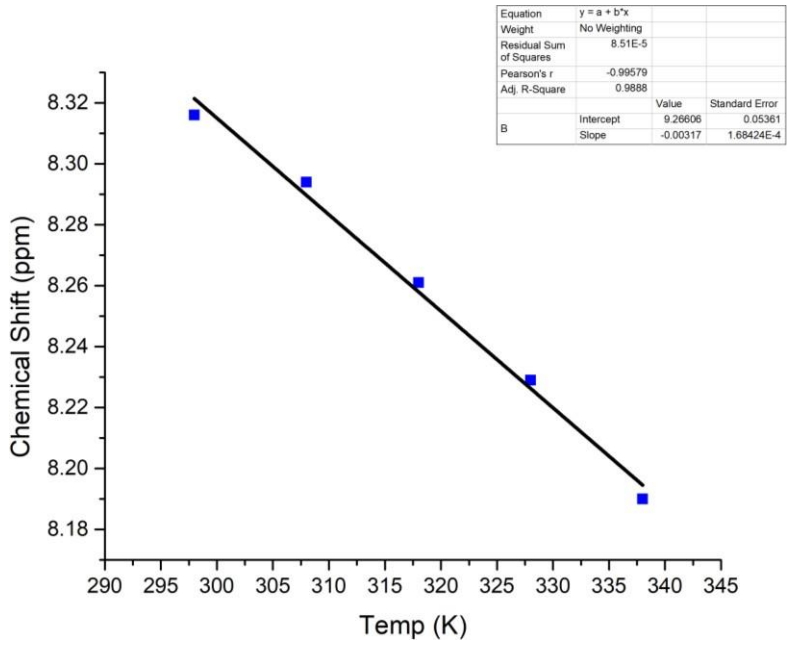

Figure A19: The linear fitting of NH proton of the product (**1**) between Temperature (from 298 K to 348 K) and chemical shift in DMSO-d_6 solvent. The calculated temperature coefficient value is -3.2 ppb/K.

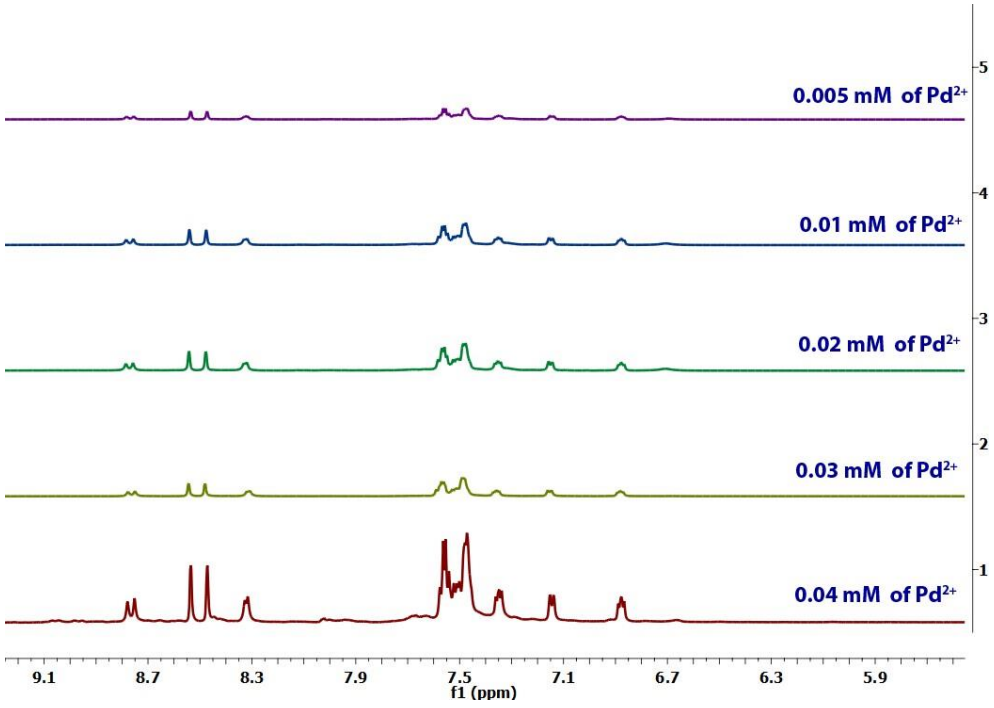

Figure A20: Concentration (0.04 to 0.005 mM, from below to above spectra respectively) dependent ^{1}H NMR of **1** in DMSO-d_6 solvent.

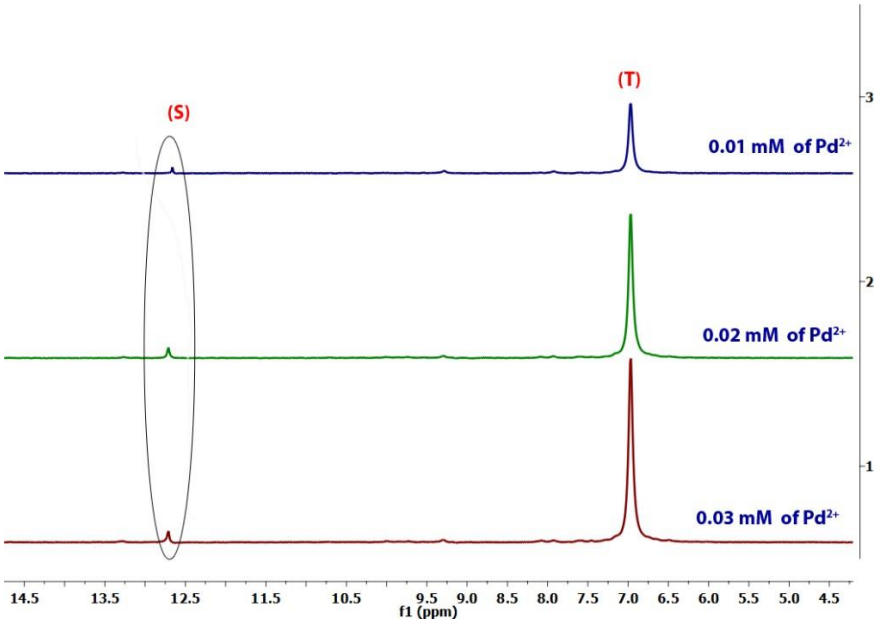

Figure A21: Concentration (0.03 to 0.01 mM, from below to above spectra respectively) dependent ^{31}P NMR of product **1** in DMSO-d_6 sovlent.

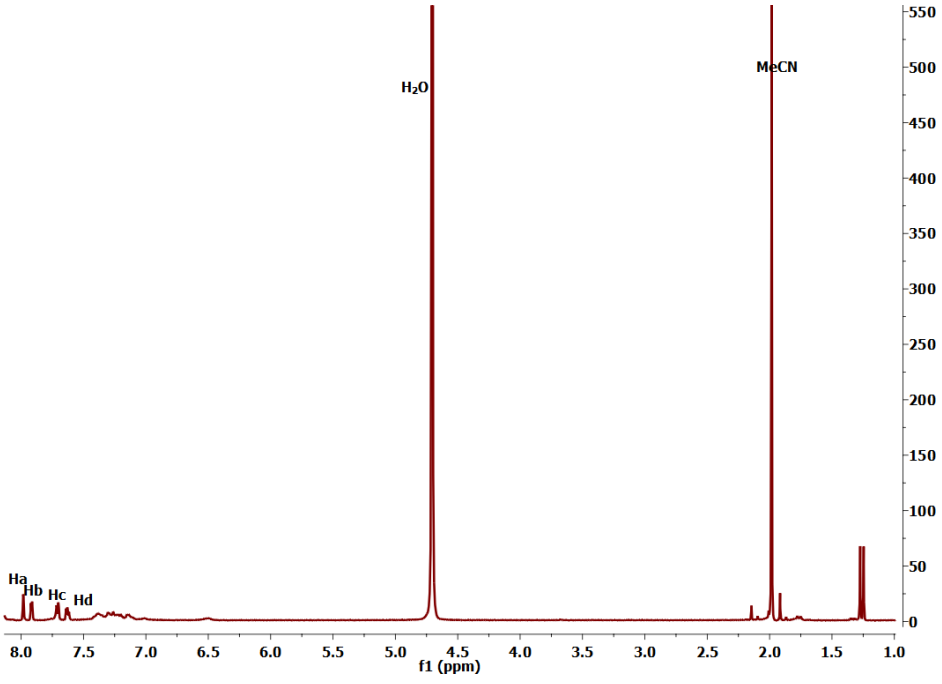

Figure A22: ^{1}H NMR of **2** in D_2O at 600 MHz. Product **2** has poor solubility in water.

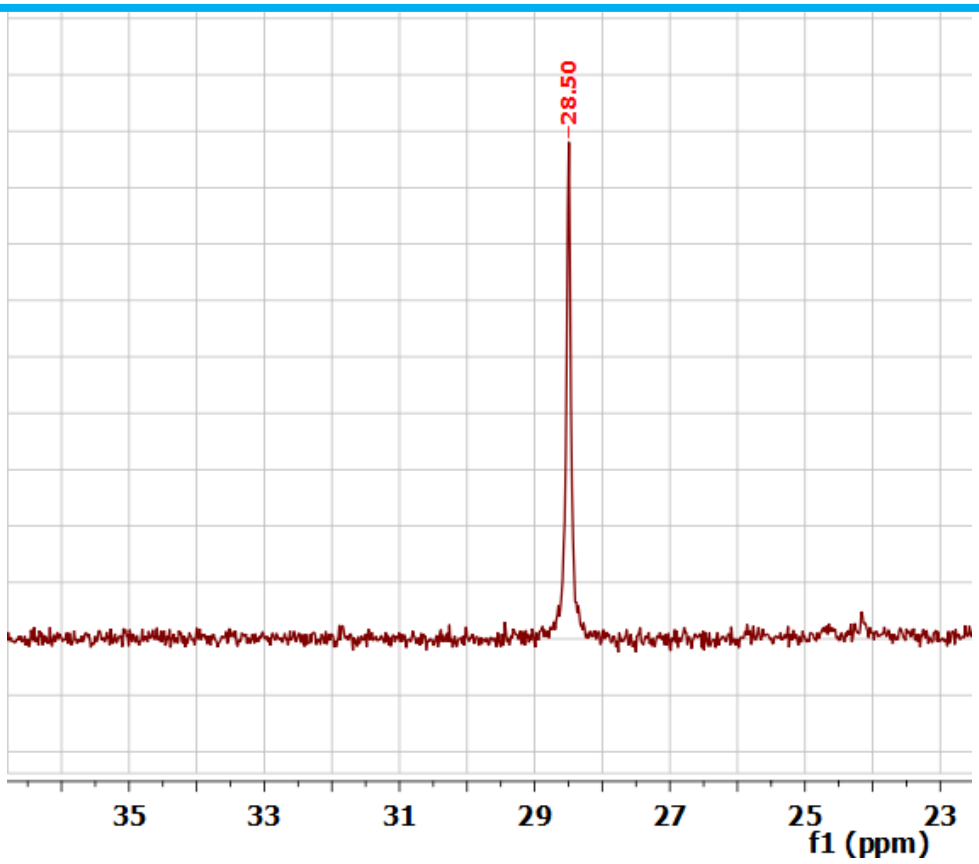

Figure A23: ^{31}P NMR of **2** in D_2O at 600 MHz.

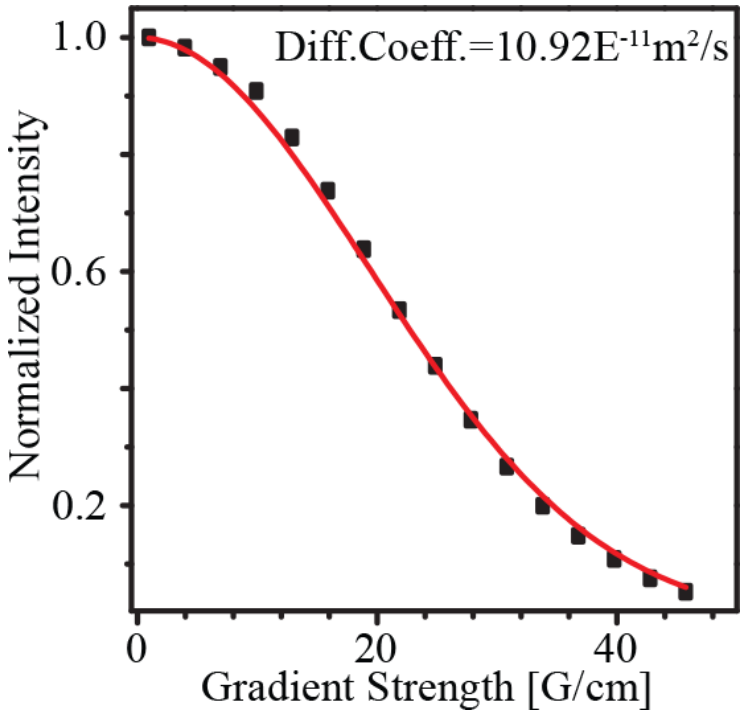

Figure A24: ^{1}H-DOSY NMR of cage **2** in DMSO-d_6 at 600 MHz.

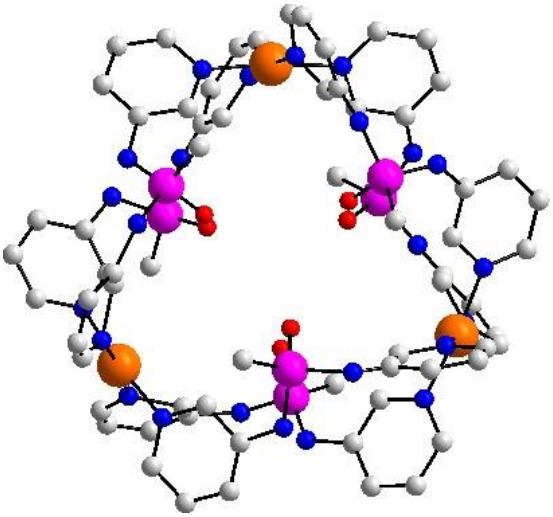

Figure A25: Energy-optimized structure of [**2**]$^{6+}$. Anions and solvates have been omitted from the calculation. The H-atoms are not shown in the diagram for clarity

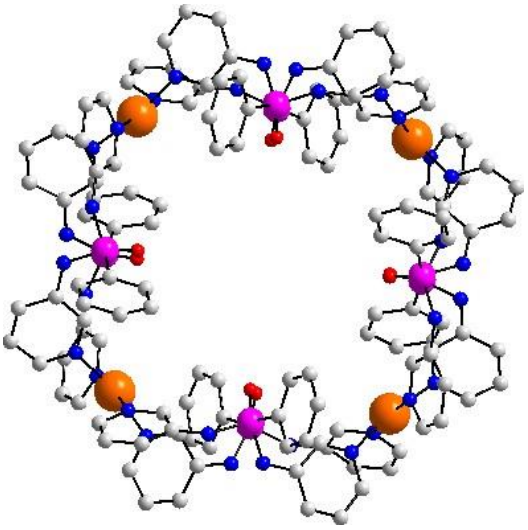

Figure S26: Energy-optimized structure of [**1b**]$^{8+}$. Anions and solvates have been omitted from the calculation. The H-atoms are not shown in the diagram for clarity.

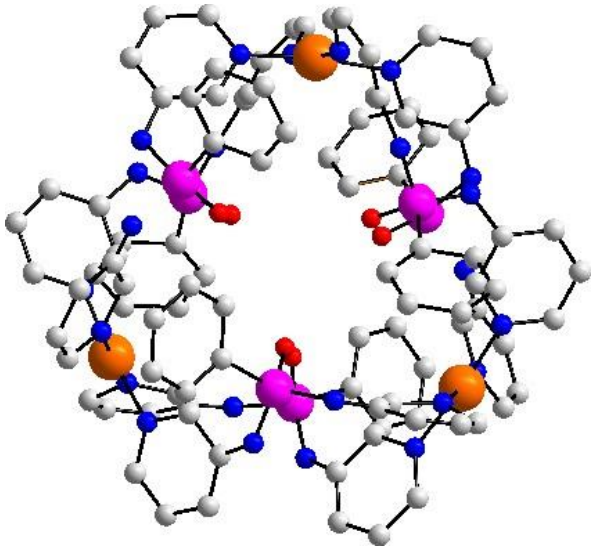

Figure A27: Energy-optimized structure of [**1a**]$^{6+}$. Anions and solvates have been omitted from the calculation. The H-atoms are not shown in the diagram for clarity.

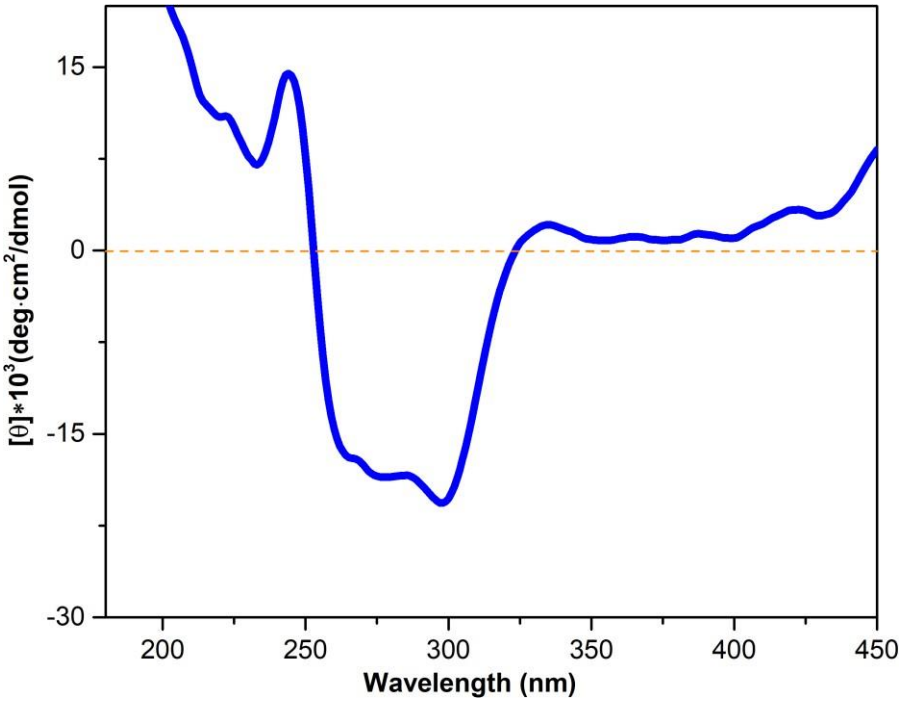

Figure A28: CD (circular dichroism) experiment of Product **1** in DMSO (1mg/ 1ml) solvent.

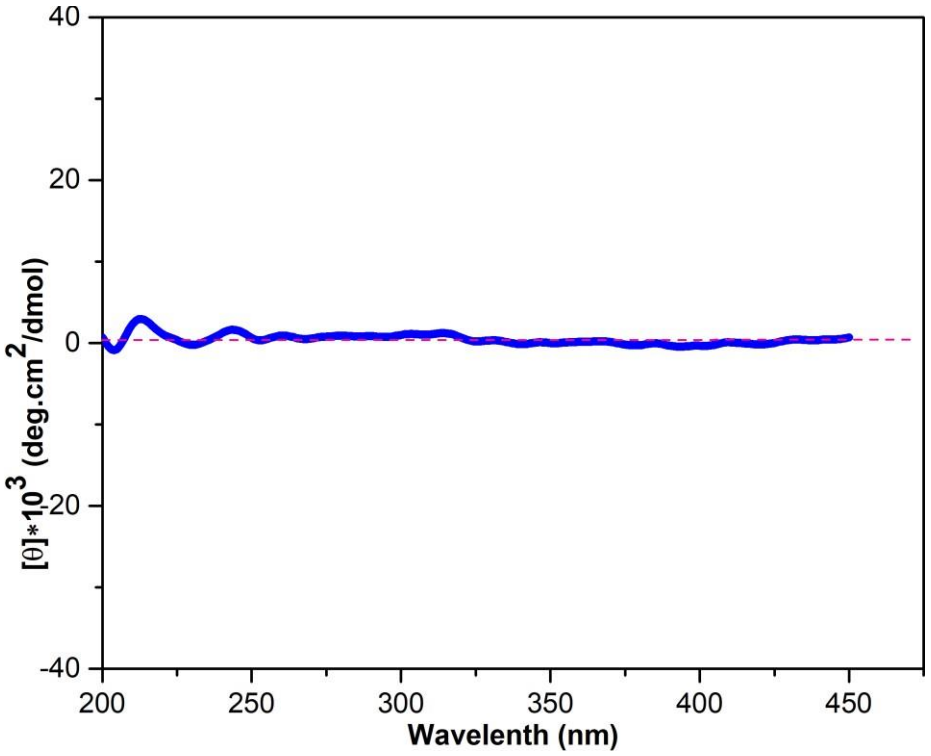

Figure A29: CD (circular dichroism) experiment of Product **2** in DMSO (1mg/ 1ml) solvent.

Table A2.1 Selected bond lengths (Å) and bond angles (˚) for compound **1a**

1a	**Bond lenths**	**Bond Angles**
	Pd(1)-N(33) 1.985(11)	N(33)-Pd(1)-N(63)#1 90(2)
	Pd(1)-N(63)#1 2.00(6)	N(33)-Pd(1)-N(13) 89.1(7)
	Pd(1)-N(13) 1.999(12)	N(63)#1-Pd(1)-N(13) 174.7(14)
	Pd(1)-N(53) 2.021(13)	N(33)-Pd(1)-N(53) 177.8(6)
	Pd(2)-N(43) 1.990(15)	N(63)#1-Pd(1)-N(53) 90(2)
	Pd(2)-N(43)#1 1.990(15)	N(13)-Pd(1)-N(53) 91.3(7)

Pd(2)-N(23)#1	2.014(13)	N(43)-Pd(2)-N(43)#1	175(2)
Pd(2)-N(23)	2.014(12)	N(43)-Pd(2)-N(23)#1	91.9(17)
P(1)-O(1)	1.482(19)	N(43)#1-Pd(2)-N(23)#1	88(2)
P(1)-N(1)	1.59(2)	N(43)-Pd(2)-N(23)	88.2(7)
P(1)-N(2)	1.66(2)	N(43)#1-Pd(2)-N(23)	92(2)
P(2)-O(2)	1.48(2)	N(23)#1-Pd(2)-N(23)	177.7(19)
P(2)-N(3)	1.62(2)	O(1)-P(1)-N(1)	115.1(12)
P(2)-N(4)	1.63(3)	O(1)-P(1)-N(2)	114.8(12)
P(2)-C(21P)	1.782(14)	N(1)-P(1)-N(2)	102.8(12)
P(3)-O(3)	1.466(19)	O(1)-P(1)-C(11P)	115.9(12)
P(3)-N(5)	1.59(2)	N(1)-P(1)-C(11P)	104.0(13)
P(3)-N(6)	1.60(2)	N(2)-P(1)-C(11P)	102.4(11)
B(1)-F(2)	1.30(3)	O(2)-P(2)-N(3)	114.3(12)
B(1)-F(1)	1.36(3)	O(2)-P(2)-N(4)	110.9(13)
B(1)-F(3)	1.37(3)	N(3)-P(2)-N(4)	103.8(12)
B(1)-F(4)	1.38(3)	O(2)-P(2)-C(21P)	113.6(11)
B(2)-F(6)	1.29(4)	N(3)-P(2)-C(21P)	104.0(10)
B(2)-F(5)	1.37(4)	N(4)-P(2)-C(21P)	109.6(12)
B(2)-F(7)	1.38(4)	O(3)-P(3)-N(5)	114.0(12)
B(2)-F(8)	1.39(4)	O(3)-P(3)-N(6)	112.0(13)
B(2')-F(6')	1.29(4)	N(5)-P(3)-N(6)	105.6(13)
B(2')-F(5')	1.37(4)	O(3)-P(3)-C(31P)	109.5(11)
B(2')-F(7')	1.38(4)	N(5)-P(3)-C(31P)	103.2(11)

	B(2')-F(8') 1.39(4) B(3)-F(10) 1.29(4) B(3)-F(9) 1.37(3) B(3)-F(11) 1.37(3) B(3)-F(12) 1.38(4) B(4)-F(14) 1.29(4) B(4)-F(13) 1.36(3) B(4)-F(16) 1.38(4) B(4)-F(15) 1.39(3) B(4')-F(14') 1.29(4) B(4')-F(13') 1.37(4) B(4')-F(15') 1.38(4) B(4')-F(16') 1.39(4)	N(6)-P(3)-C(31P) 112.3(13) F(2)-B(1)-F(1)106(2) F(2)-B(1)-F(3)116(2) F(1)-B(1)-F(3)112(2) F(2)-B(1)-F(4)112(2) F(1)-B(1)-F(4)108(2) F(3)-B(1)-F(4)103(2) F(6)-B(2)-F(5)108(4) F(6)-B(2)-F(7)122(4) F(5)-B(2)-F(7)108(4) F(6)-B(2)-F(8)111(4) F(5)-B(2)-F(8)107(4) F(7)-B(2)-F(8)101(3) F(6')-B(2')-F(5') 108(4) F(6')-B(2')-F(7') 125(4) F(5')-B(2')-F(7') 105(3) F(6')-B(2')-F(8') 107(4) F(5')-B(2')-F(8') 109(4) F(7')-B(2')-F(8') 102(3) F(10)-B(3)-F(9) 110(3) F(10)-B(3)-F(11) 117(4) F(9)-B(3)-F(11) 107(3) F(10)-B(3)-F(12) 109(3)

		F(9)-B(3)-F(12)	107(3)
		F(11)-B(3)-F(12)	106(3)
		F(14)-B(4)-F(13)	109(3)
		F(14)-B(4)-F(16)	109(4)
		F(13)-B(4)-F(16)	107(4)
		F(14)-B(4)-F(15)	120(4)
		F(13)-B(4)-F(15)	110(3)
		F(16)-B(4)-F(15)	102(3)
		F(14')-B(4')-F(13')	108(4)
		F(14')-B(4')-F(15')	120(4)
		F(13')-B(4')-F(15')	107(4)
		F(14')-B(4')-F(16')	110(4)
		F(13')-B(4')-F(16')	105(4)
		F(15')-B(4')-F(16')	105(3)

Table A2.1: Hydrogen bonding table of compound **1a.**

D-H...A	d(D-H)	d(H...A)	d(D...A)	<(DHA)
N(1)-H(1)...F(7)#1	0.88	1.95	2.81(6)	166.5
N(1)-H(1)...F(7')#1	0.88	2.04	2.82(5)	147.2
N(2)-H(2)...F(5)#1	0.88	2.60	3.08(7)	114.9
N(2)-H(2)...F(5')#1	0.88	2.61	3.17(6)	122.8

N(2)-H(2)...F(16)#2	0.88	1.96	2.81(5)	163.9
N(2)-H(2)...F(15')#2	0.88	2.06	2.88(5)	154.6
N(3)-H(3)...O(4G)	0.88	1.92	2.80(5)	176.0
N(4)-H(4)...F(13)	0.88	2.20	3.06(5)	165.8
N(4)-H(4)...F(13')	0.88	2.24	2.97(8)	140.2
N(4)-H(4)...F(14')	0.88	2.37	3.16(9)	149.9
N(4)-H(4)...F(16')	0.88	2.54	2.96(5)	110.2
N(5)-H(5)...F(1)	0.88	2.50	3.20(3)	137.4
N(5)-H(5)...F(2)	0.88	2.15	3.00(3)	163.3
N(6)-H(6)...F(8)	0.88	1.93	2.79(5)	164.9
N(6)-H(6)...F(8')	0.88	1.89	2.76(4)	169.5

Appendix 3

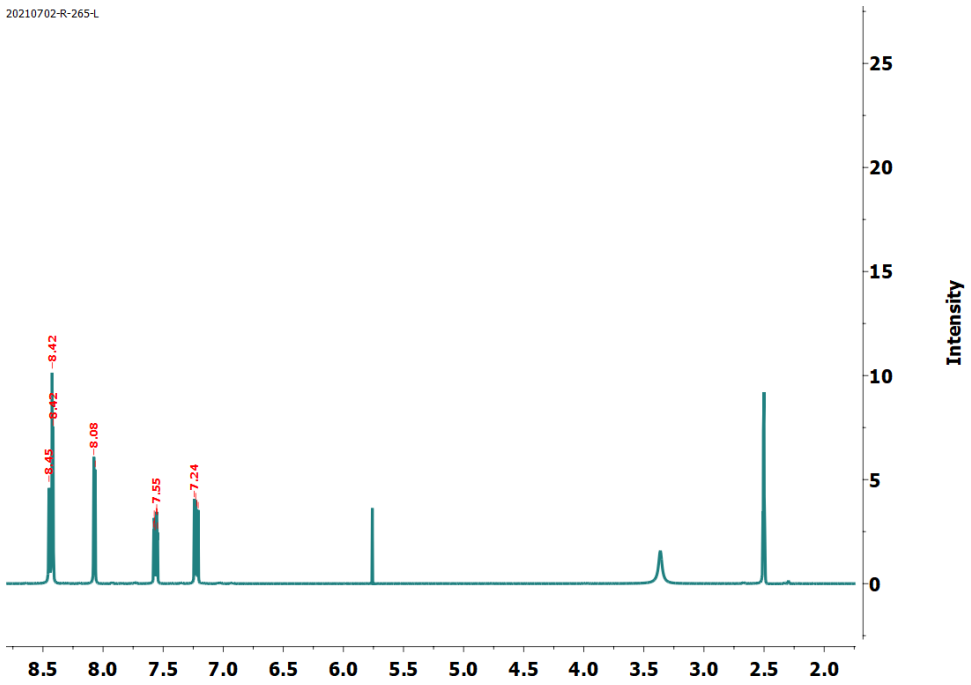

Figure A1: ^{1}H NMR of ligand L in DMSO-d_6 at 400 MHz

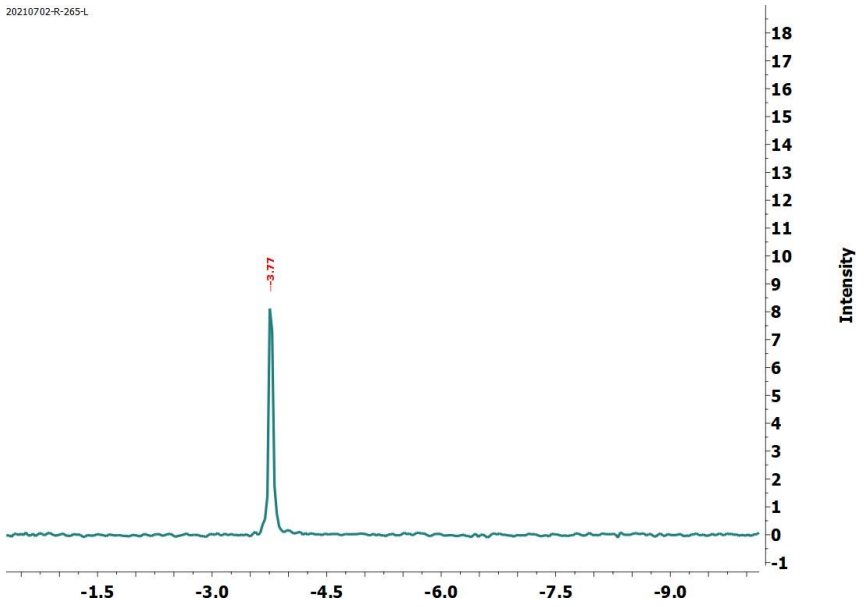

Figure A2: ^{31}P NMR of ligand L in DMSO-d_6 at 400 MHz

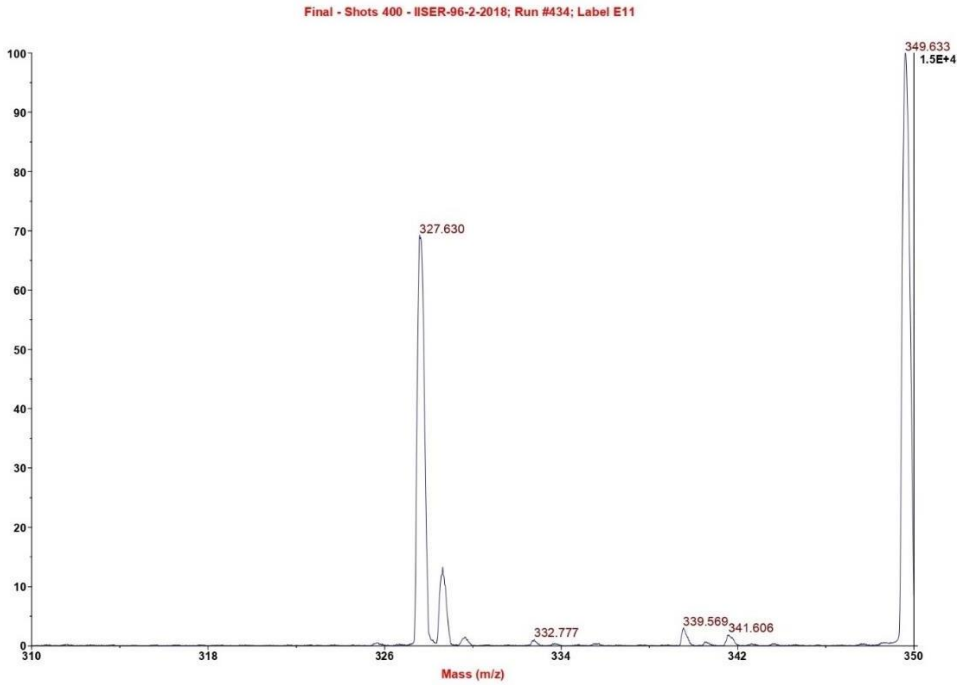

Figure A3: MALDI-TOF plot of ligand L in MeOH

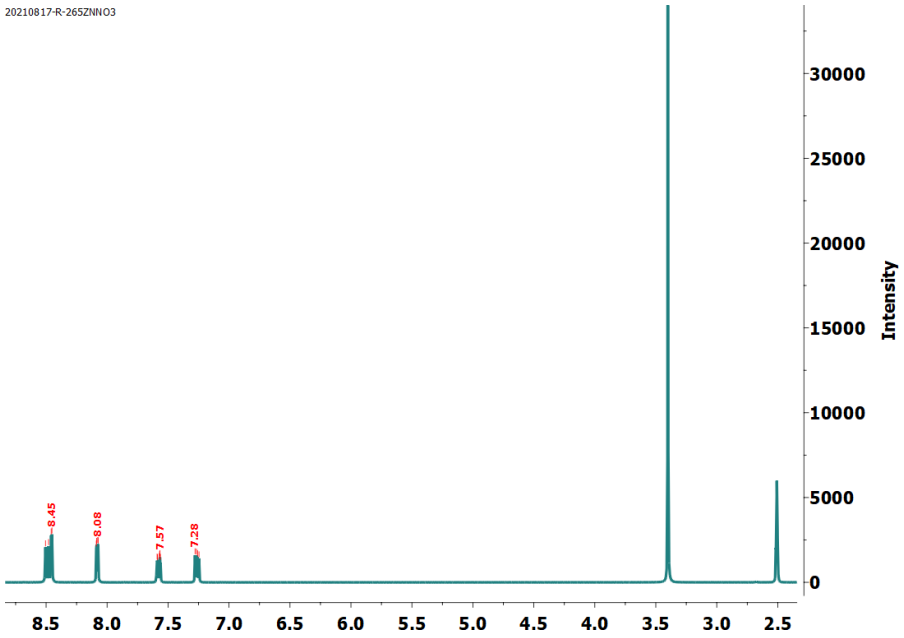

Figure A4: ^{1}H NMR of ligand Cage2 in DMSO-d_6 at 400 MHz.

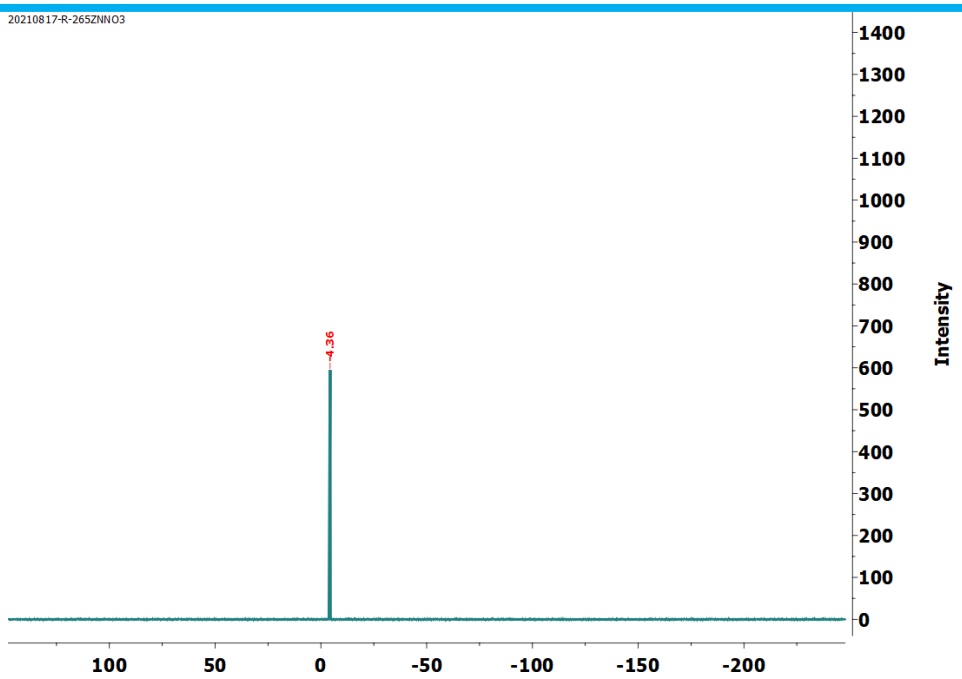

Figure A5: ^{31}P NMR of cage2 in DMSO-d_6 at 400 MHz

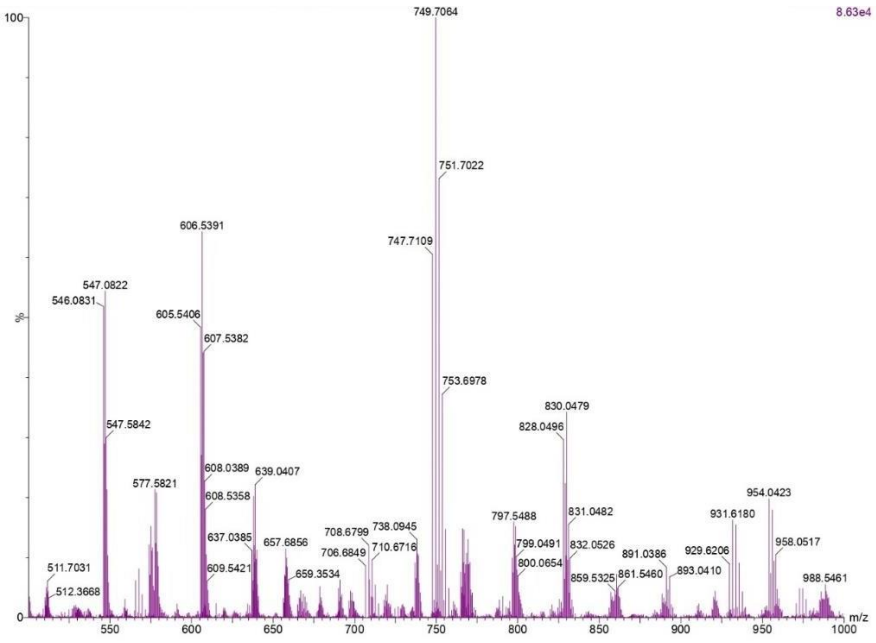

Figure A6: ESI-MS plot of cage1 in MeOH/H_2O

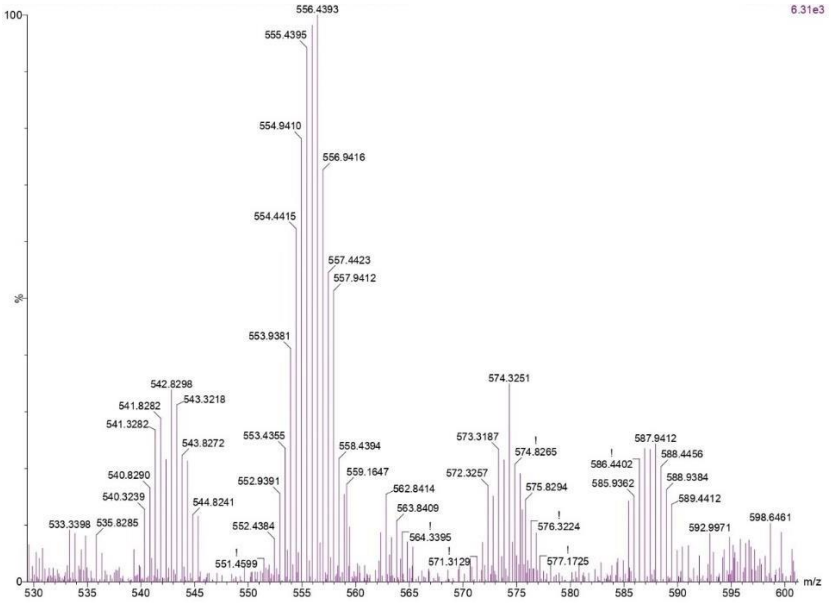

Figure A7: ESI-MS plot of cage2 in MeOH/H_2O

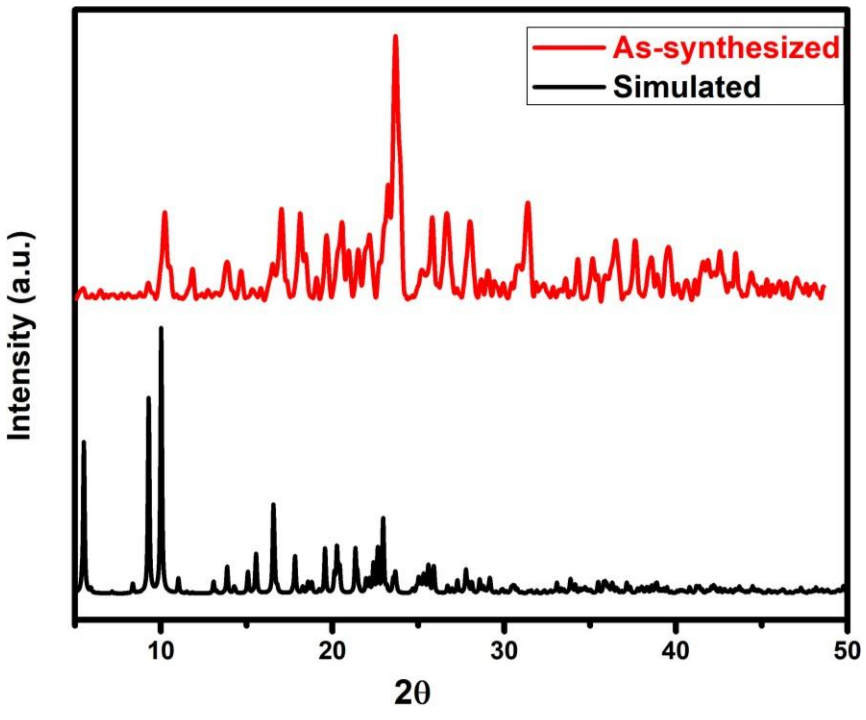

Figure A8: stacked PXRD profiles of simulated (below) and as-synthesized of cage1.

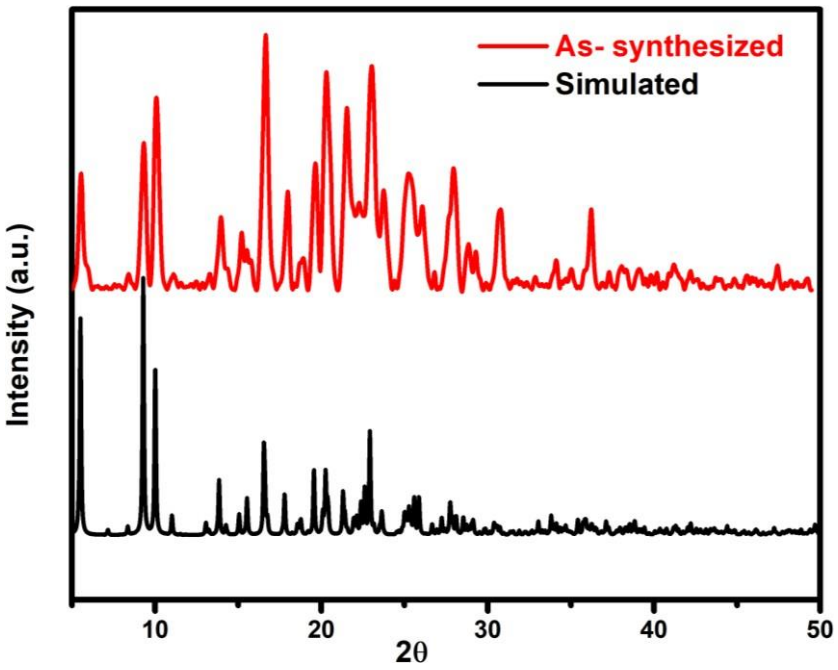

Figure A9 : stacked PXRD profiles of simulated (below) and as-synthesized of cage2.

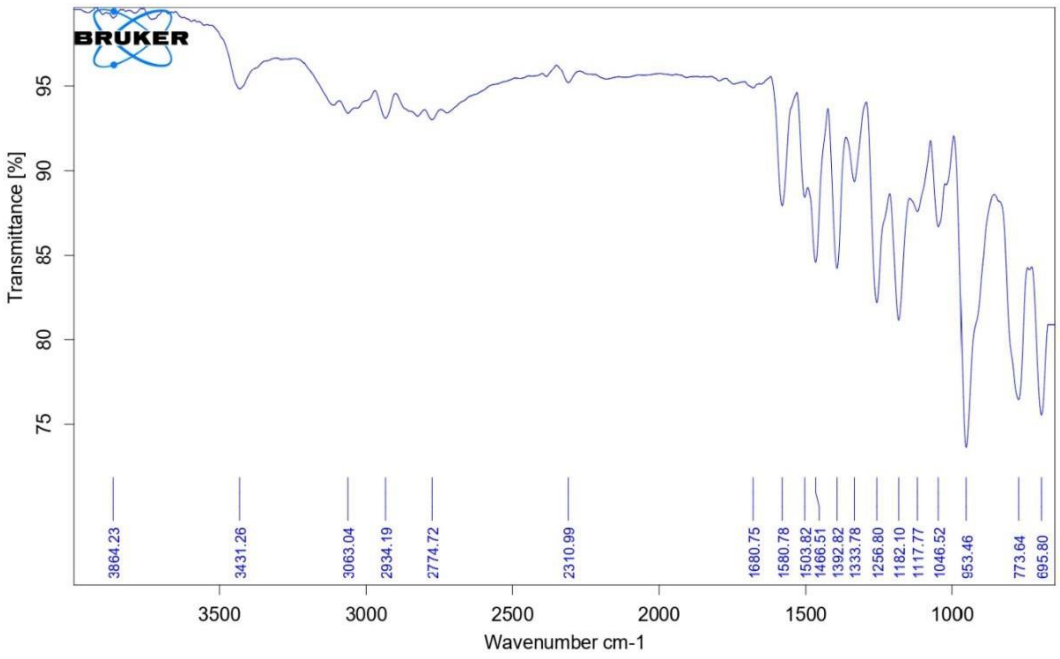

Figure A10: FTIR plot of ligand L1 in solid state.

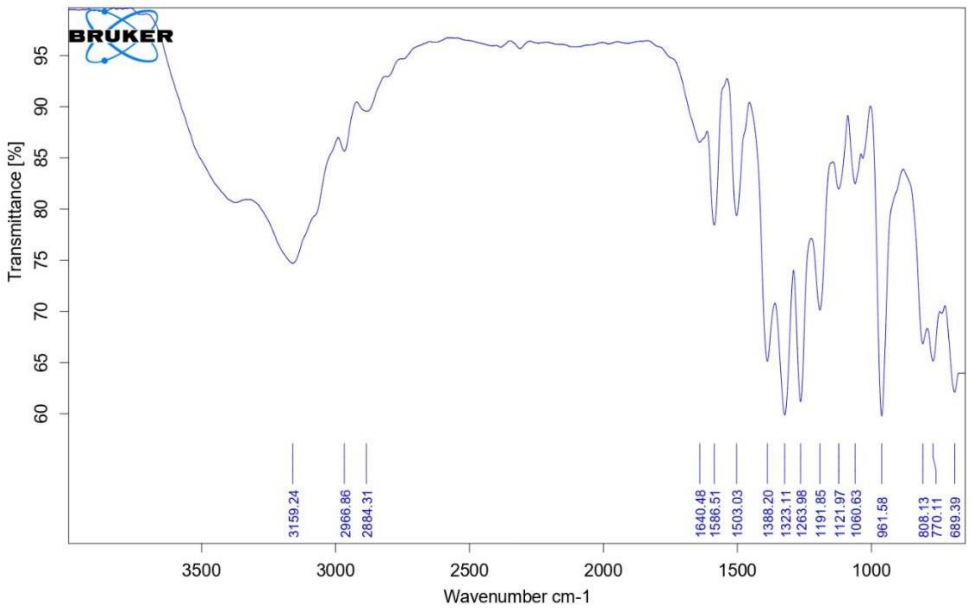

Figure A11: FTIR plot of cage1 in solid state.

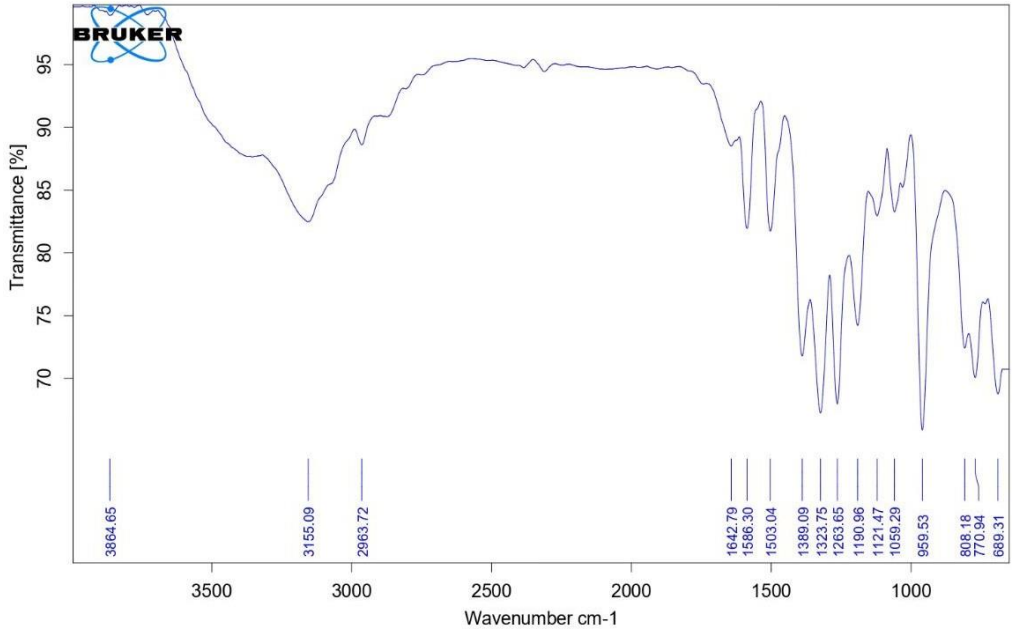

Figure A12: FTIR plot of cage1 in solid state.

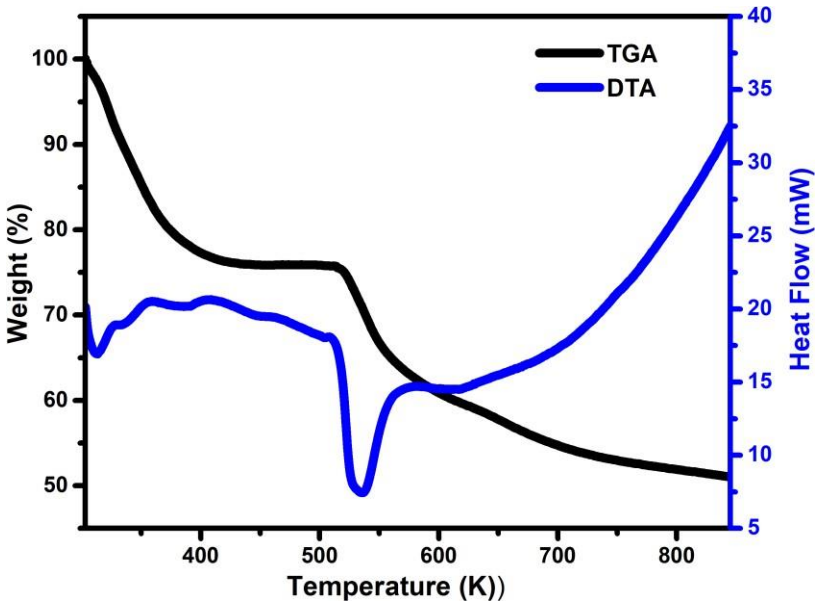

Figure A13: TGA and DTA plot of cage1.

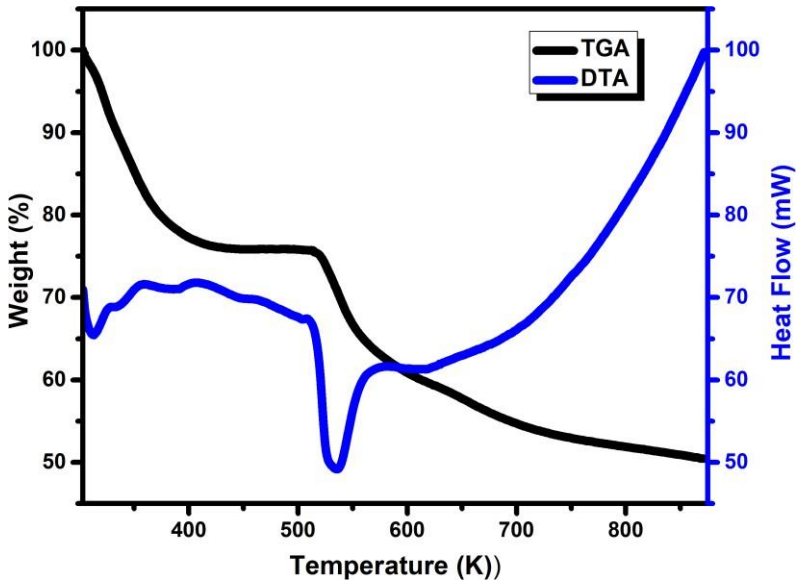

Figure A14: TGA and DTA plot of cage2.

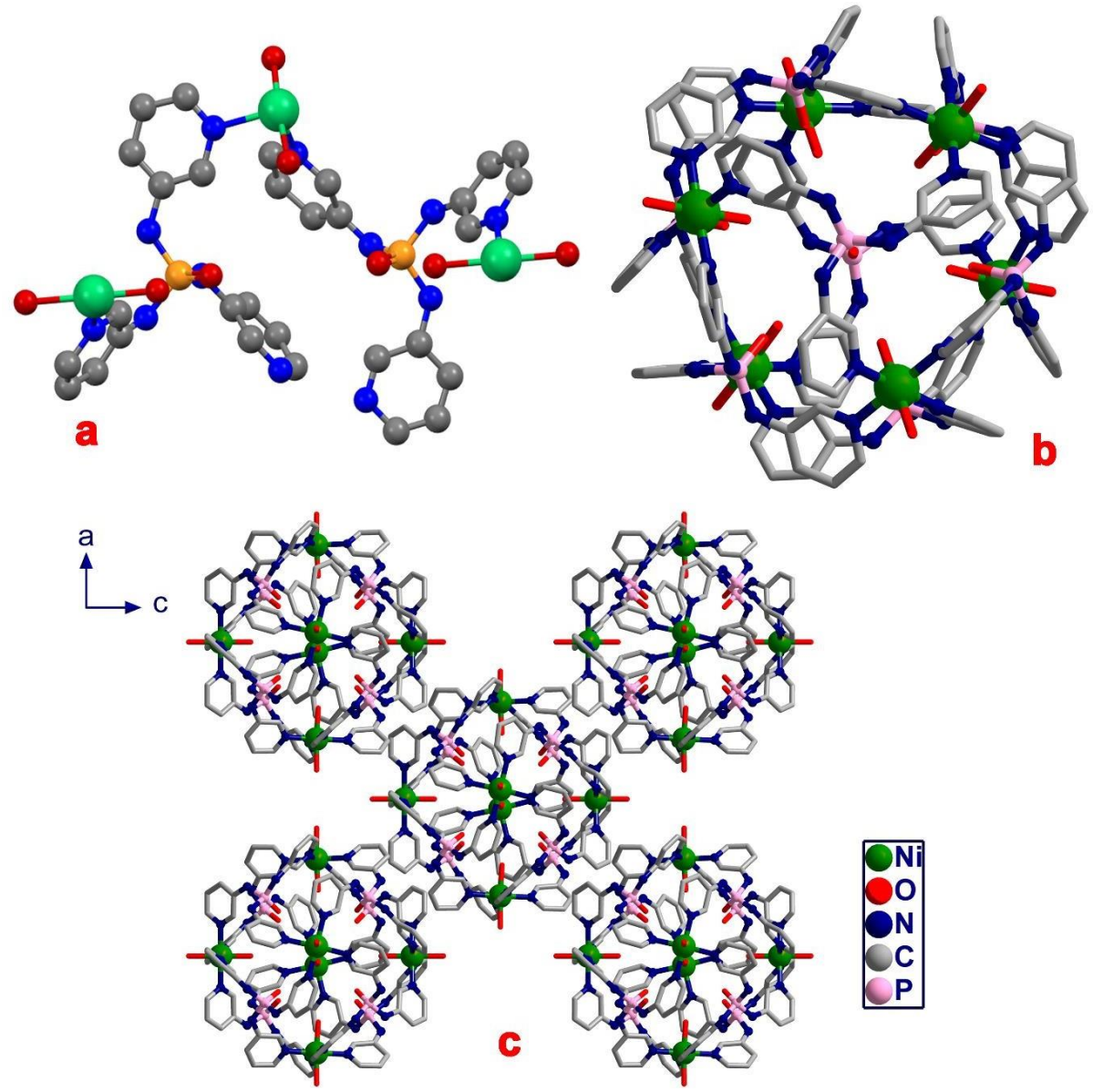

Figure 15: (a) Asymmetric unit of cage1, (b) view along C3 symmetry of cage1 and (c) packing diagram of cage 1 along b-axis.

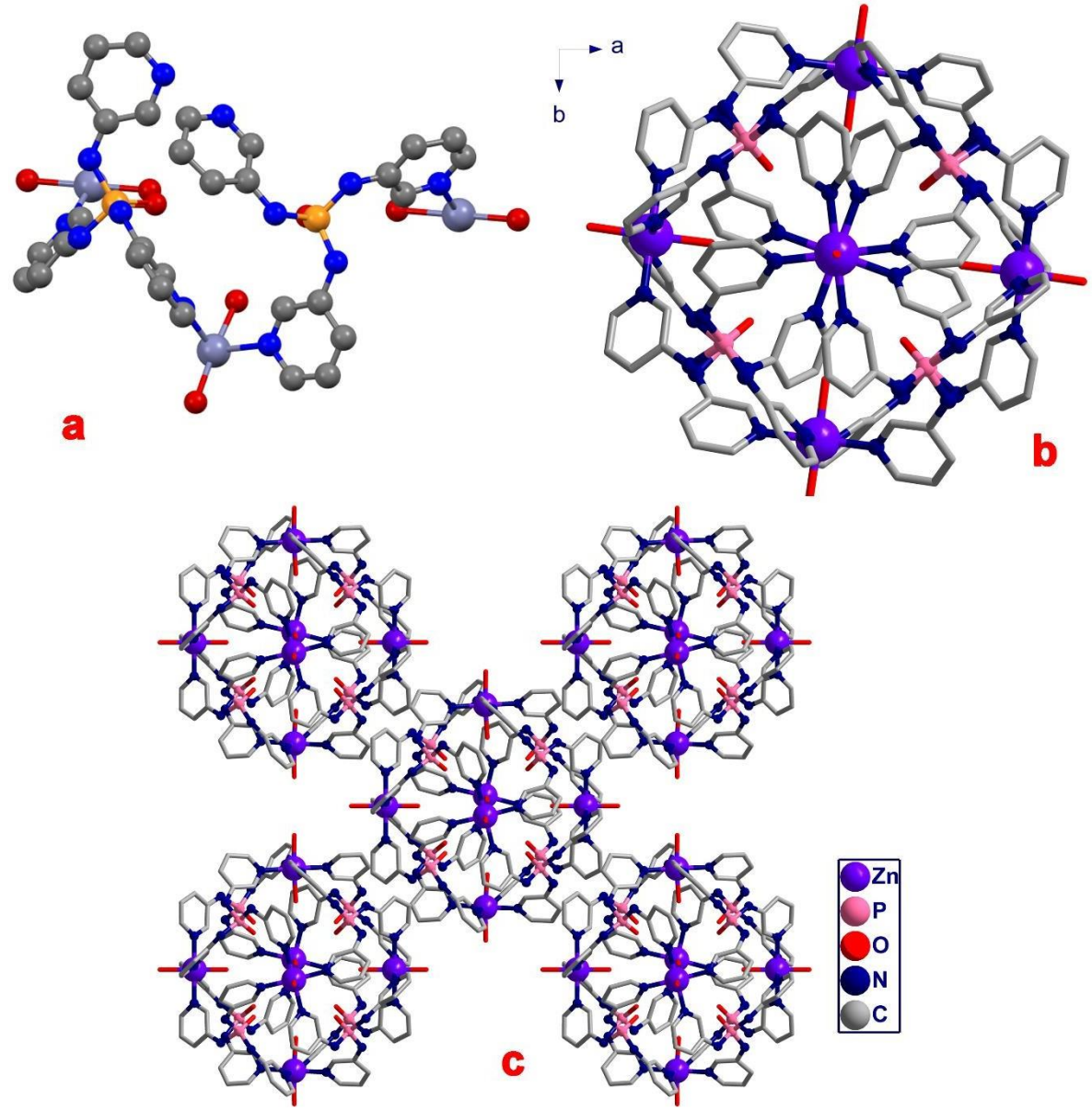

Figure A16: (a) Asymmetric unit of cage2, (b) view along C-axis of cage2 and (c) packing diagram of cage 1 along c-axis.

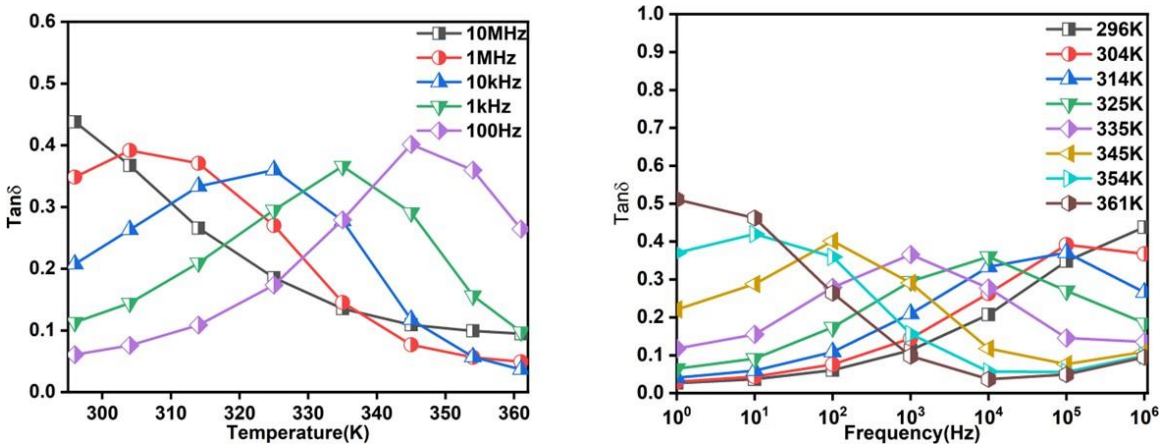

Figure A17: Temperature and frequency dependent dielectric loss (tanδ) of cage1

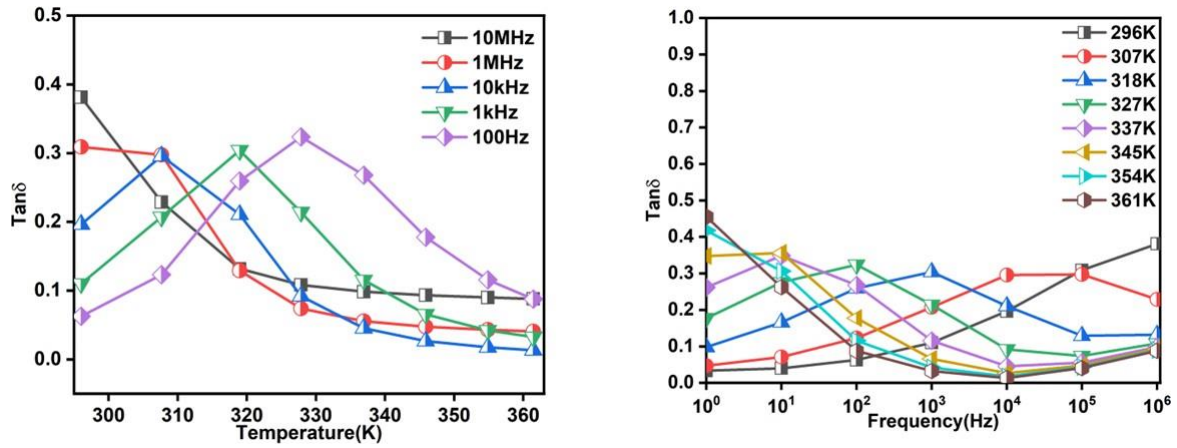

Figure A18: Temperature and frequency dependent dielectric loss (tanδ) of cage2

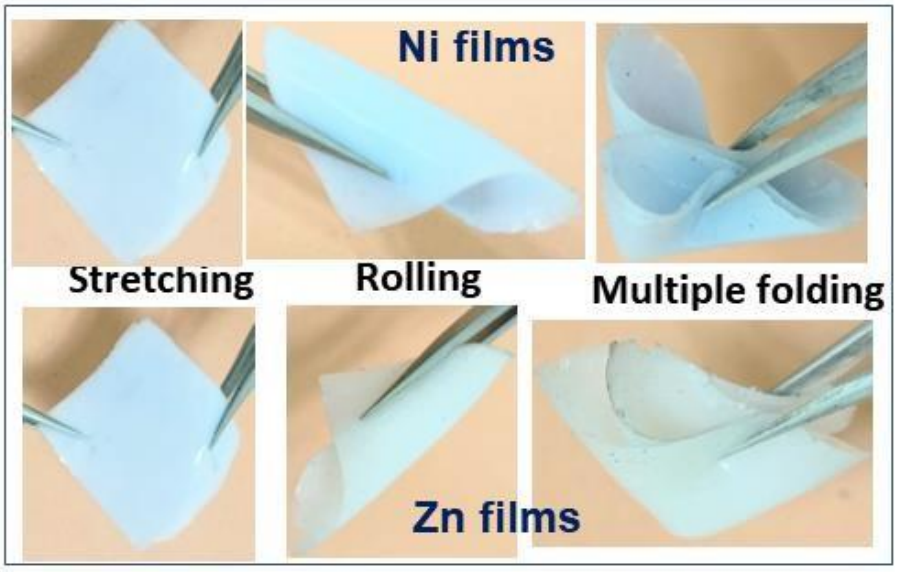

Figure A19: Stretching, rolling and multiple folding of films images of cage1 (above) and cage2 (below).

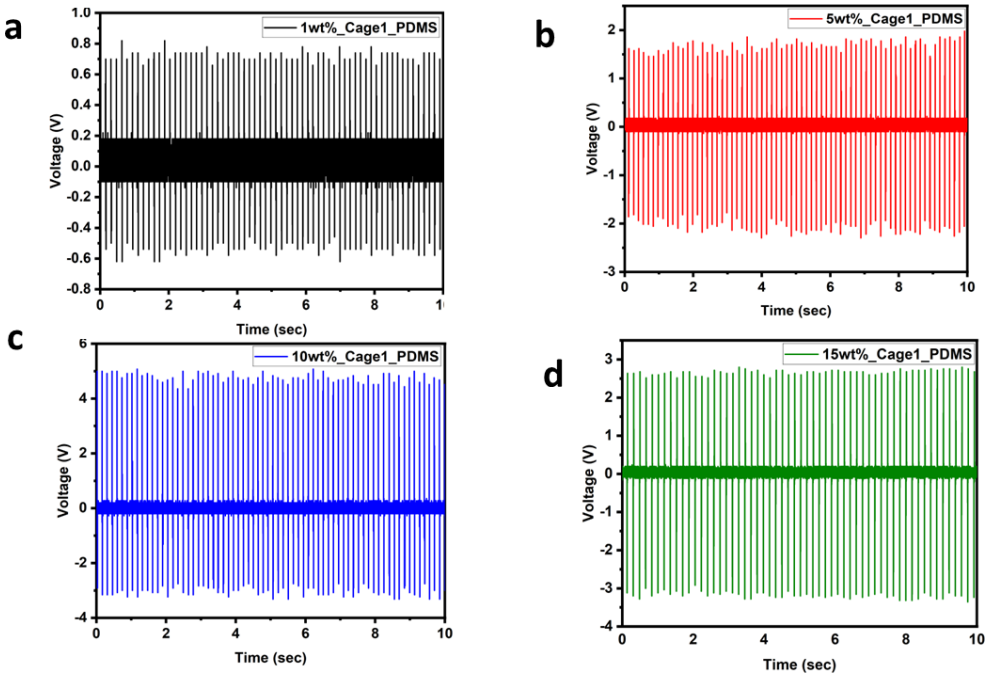

Figure 20: Peak-to-peak output voltage (V_{OC}) of composite devices of cage1 with different weight load (1, 5, 10 and 15wt %)

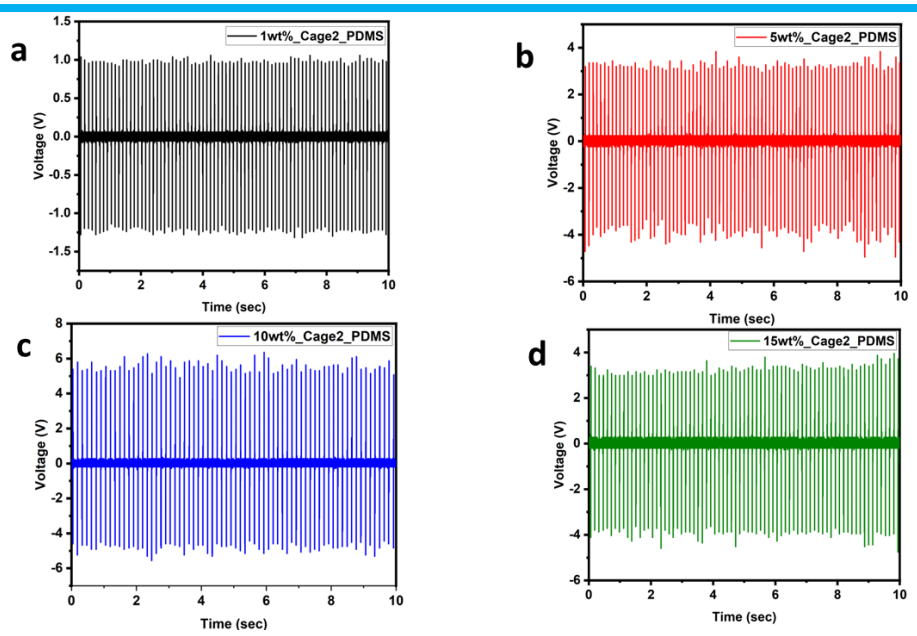

Figure 21: Peak-to-peak output voltage (V_{OC}) of composite devices of cage2 with different weight load (1, 5, 10 and 15wt %)

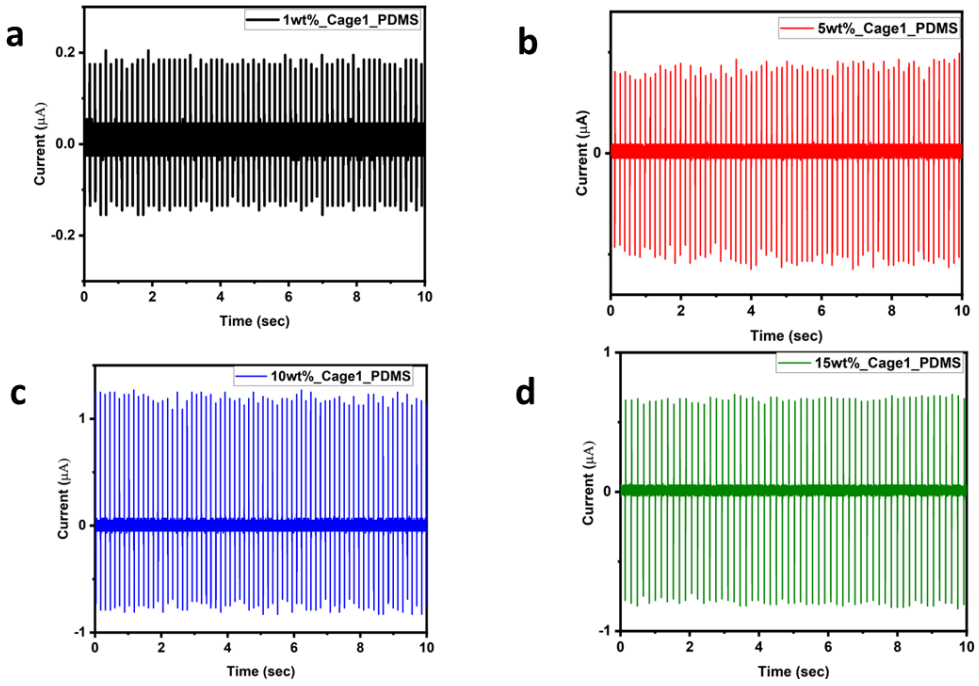

Figure 22: Peak-to-peak output current (I_{OC}) of composite devices of cage1 with different weight load (1, 5, 10 and 15wt %)

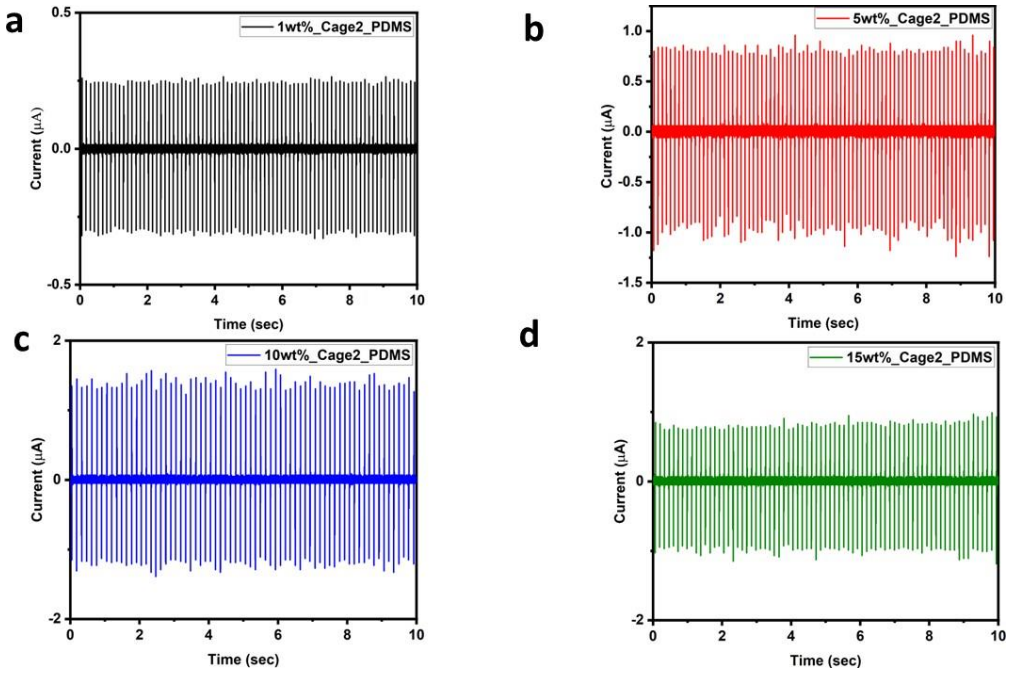

Figure 23: Peak-to-peak output current (I_{OC}) of composite devices of cage2 with different weight load (1, 5, 10 and 15wt %)

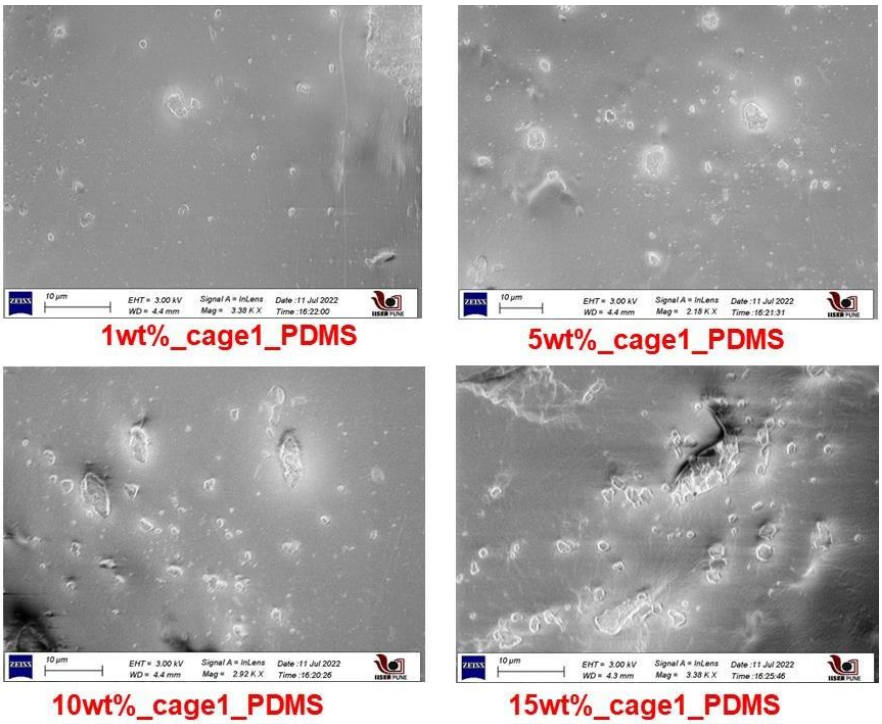

Figure 24: FFSEM images of composite films in PDMS of cage1 with different wight percentages.

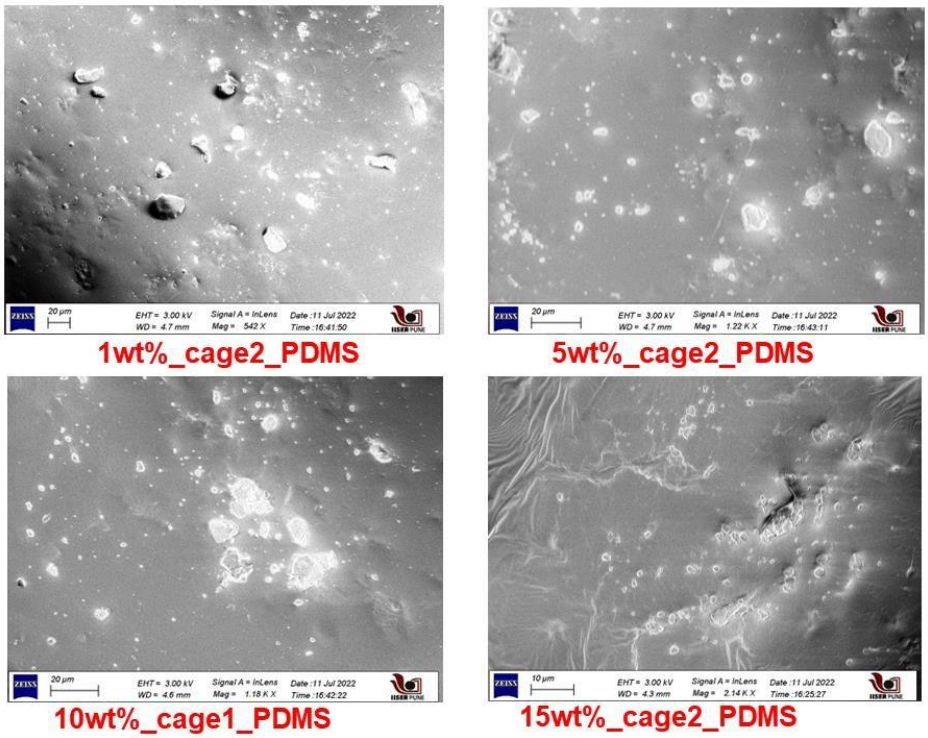

Figure 25: FFSEM images of composite films in PDMS of cage2 with different wight percentages.

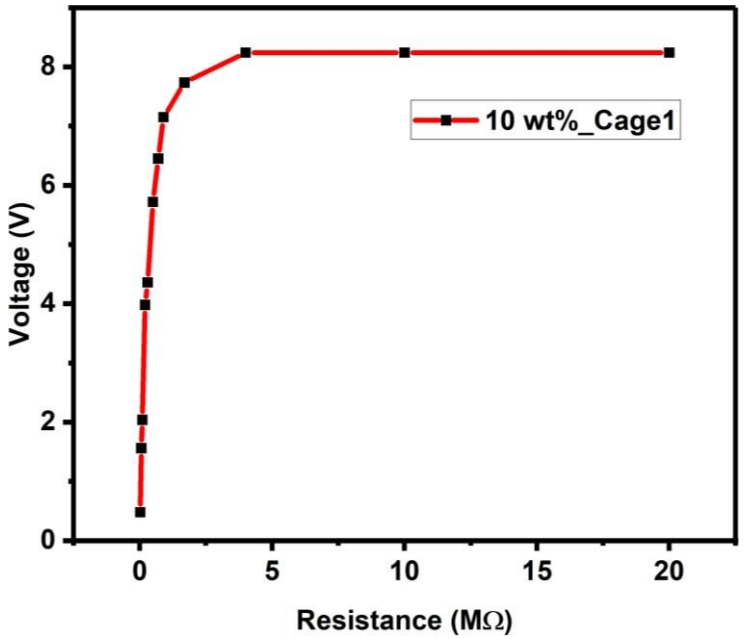

Figure A26: Resistance dependent output voltages of 10wt%_cage1_PDMS device.

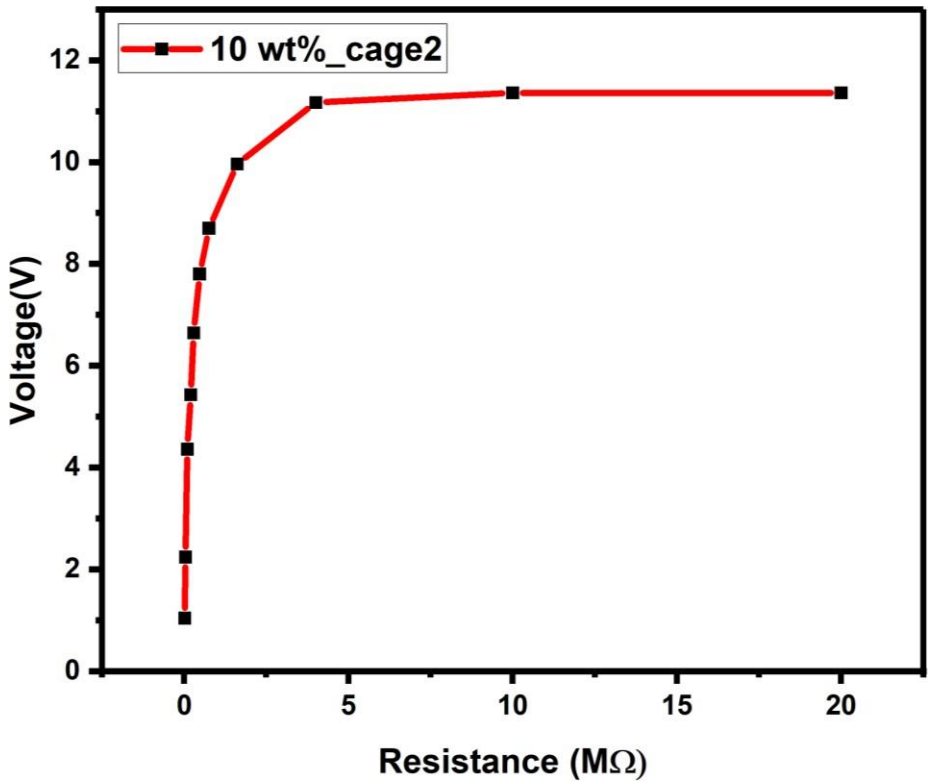

Figure A27: Resistance dependent output voltages of 10wt%_cage2_PDMS device.

Table A3.1 Selected bond lengths (Å) and bond angles (˚) for cage1 and cage2.

cage1	Bond lengths and bond angle	cage2	Bond lengths and bond angle
Ni(1)-O(4)	2.093(19)	Zn(2)-O(3MW)	2.131(6)
Ni(1)-O(3)	2.098(13)	Zn(2)-N(5CM)	2.134(8)
Ni(1)-N(12)#1	2.121(10)	Zn(2)-N(2CM)#1	2.141(9)
Ni(1)-N(12)#2	2.121(10)	Zn(2)-O(4MW)	2.161(6)
Ni(1)-N(12)#3	2.121(10)	Zn(2)-N(1CM)	2.166(10)
Ni(1)-N(12)	2.121(10)	Zn(2)-N(6CM)#1	2.179(9)
O(1)-Ni(3)	2.149(13)	Zn(3)-O(5MW)	2.063(17)
N(1)-C(1)	1.316(12)	Zn(3)-N(4CM)	2.184(11)
N(1)-C(5)	1.365(14)	Zn(3)-N(4CM)#2	2.184(11)
N(1)-Ni(3)	2.136(8)	Zn(3)-N(4CM)#1	2.184(11)

C(1)-C(2)	1.432(13)	Zn(3)-N(4CM)#3	2.184(11)
C(1)-H(1)	0.93	Zn(3)-O(6MW)	2.218(14)
C(4)-C(5)	1.347(16)	Zn(1)-O(1MW)	2.07(2)
C(4)-C(3)	1.413(16)	Zn(1)-O(2MW)	2.162(16)
C(4)-H(4)	0.93	Zn(1)-N(3CM)#2	2.214(12)
Ni(3)-O(2)	2.013(14)	Zn(1)-N(3CM)#1	2.214(12)
C(3)-C(2)	1.367(14)	Zn(1)-N(3CM)#3	2.214(12)
C(3)-H(3)	0.93	Zn(1)-N(3CM)	2.214(12)
Ni(2)-N(7)#3	2.075(8)	P(1)-O(00A)	1.464(9)
Ni(2)-O(5)	2.093(5)	P(1)-N(2)	1.600(11)
Ni(2)-O(6)	2.097(5)	P(1)-N(1)	1.644(12)
Ni(2)-N(6)	2.111(7)	P(1)-N(3)	1.669(13)
Ni(2)-N(5)	2.127(8)	P(2)-O(00C)	1.505(8)
Ni(2)-N(9)#3	2.135(9)	P(2)-N(6)	1.620(12)
C(2)-N(11N)	1.391(12)	P(2)-N(4)	1.665(10)
N(5)-C(14)	1.285(13)	P(2)-N(5)	1.691(12)
N(5)-C(15)	1.382(12)	N(4)-C(16)	1.380(15)
C(5)-H(5)	0.93	N(3)-C(11)	1.417(15)
C(6)-N(7)	1.365(12)	N(5)-C(21)	1.338(17)
C(6)-C(5A)	1.379(13)	N(1CM)-C(10)	1.301(15)
C(6)-H(6)	0.93	N(1CM)-C(9)	1.378(15)
O(8)-P(2N)	1.442(7)	N(5CM)-C(30)	1.353(13)
C(8)-N(7)	1.366(11)	N(5CM)-C(29)	1.390(13)
C(8)-C(7)	1.396(13)	N(6CM)-C(19)	1.285(15)
C(8)-H(8)	0.93	N(6CM)-C(20)	1.382(15)
C(7)-C(10)	1.375(14)	N(6CM)-Zn(2)#2	2.179(9)
O(7)-P(1N)	1.513(7)	N(2CM)-C(15)	1.330(14)
N(9)-C(25)	1.278(12)	N(2CM)-C(14)	1.387(14)
N(9)-C(24)	1.353(13)	N(2CM)-Zn(2)#2	2.141(9)
C(10)-C(5A)	1.358(13)	C(30)-C(26)	1.350(15)
C(10)-H(10)	0.93	C(30)-H(30)	0.95
C(11)-C(12)	1.352(13)	C(10)-C(6)	1.363(16)
C(11)-C(15)	1.354(13)	C(10)-H(10)	0.95
C(11)-N(12N)	1.427(12)	N(2)-C(6)	1.438(15)
N(11N)-P(1N)	1.641(9)	C(19)-C(18)	1.348(19)
N(11N)-H(11N)	0.86	C(19)-H(19)	0.95
C(13)-C(12)	1.396(14)	N(6)-C(26)	1.496(17)
C(13)-C(14)	1.410(16)	N(3CM)-C(4)	1.316(19)
C(13)-H(13)	0.93	N(3CM)-C(5)	1.323(16)
N(13N)-C(5A)	1.455(13)	N(1)-C(1)	1.371(17)

N(13N)-P(1N)	1.608(9)	C(26)-C(27)	1.426(16)
N(13N)-H(13N)	0.86	C(24)-C(23)	1.32(2)
C(12)-H(12)	0.93	C(24)-N(4CM)	1.333(17)
N(12N)-P(1N)	1.631(8)	C(24)-H(24)	0.95
N(12N)-H(12N)	0.86	C(11)-C(12)	1.376(15)
N(12)-C(27)	1.327(14)	C(11)-C(15)	1.395(15)
N(12)-C(28)	1.334(19)	N(4CM)-C(25)	1.296(16)
C(15)-H(15)	0.93	C(25)-C(21)	1.474(17)
C(14)-H(14)	0.93	C(25)-H(25)	0.95
N(6)-C(16)	1.325(12)	C(21)-C(22)	1.369(17)
N(6)-C(20)	1.344(12)	C(27)-C(28)	1.377(16)
C(16)-C(17)	1.435(13)	C(27)-H(27)	0.95
C(16)-H(16)	0.93	C(15)-H(15)	0.95
C(17)-N(21N)	1.342(13)	C(6)-C(7)	1.432(16)
C(17)-C(18)	1.387(13)	C(18)-C(17)	1.432(17)
C(18)-C(19)	1.446(14)	C(18)-H(18)	0.95
C(18)-H(18)	0.93	C(7)-C(8)	1.368(17)
C(19)-C(20)	1.371(12)	C(7)-H(7)	0.95
C(19)-H(19)	0.93	C(16)-C(20)	1.387(16)
C(20)-H(20)	0.93	C(16)-C(17)	1.395(16)
C(21)-C(25)	1.402(14)	C(14)-C(13)	1.345(15)
C(21)-N(23N)	1.406(13)	C(14)-H(14)	0.95
C(21)-C(22)	1.407(13)	C(8)-C(9)	1.343(18)
N(21N)-P(2N)	1.657(10)	C(8)-H(8)	0.95
N(21N)-H(21N)	0.86	C(12)-C(13)	1.409(18)
C(22)-C(23)	1.329(15)	C(12)-H(12)	0.95
C(22)-H(22)	0.93	C(23)-C(22)	1.339(18)
N(22N)-C(26)	1.420(13)	C(23)-H(23)	0.95
N(22N)-P(2N)	1.634(9)	C(5)-C(1)	1.428(19)
N(22N)-H(22N)	0.86	C(5)-H(5)	0.95
C(23)-C(24)	1.367(16)	C(1)-C(2)	1.366(18)
C(23)-H(23)	0.93	C(20)-H(20)	0.95
N(23N)-P(2N)	1.639(9)	C(13)-H(13)	0.95
N(23N)-H(23N)	0.86	C(28)-C(29)	1.381(15)
C(24)-H(24)	0.93	C(28)-H(28)	0.95
C(25)-H(25)	0.93	C(17)-H(17)	0.95

C(26)-C(27)	1.390(15)	C(29)-H(29)	0.95
C(26)-C(30)	1.390(15)	C(9)-H(9)	0.95
C(27)-H(27)	0.93	C(22)-H(22)	0.95
C(28)-C(29)	1.37(2)	C(2)-C(3)	1.46(2)
C(28)-H(28)	0.93	C(2)-H(2)	0.95
C(29)-C(30)	1.299(19)	C(3)-C(4)	1.25(2)
C(29)-H(29)	0.93	C(3)-H(3)	0.95
C(30)-H(30)	0.93	C(4)-H(4)	0.95
O(4)-Ni(1)-O(3)	180	O(3MW)-Zn(2)-N(5CM)	91.0(3)
O(4)-Ni(1)-N(12)#1	89.6(3)	O(3MW)-Zn(2)-N(2CM)#1	89.2(3)
O(3)-Ni(1)-N(12)#1	90.4(3)	N(5CM)-Zn(2)-N(2CM)#1	178.7(4)
O(4)-Ni(1)-N(12)#2	89.6(3)	O(3MW)-Zn(2)-O(4MW)	175.6(4)
O(3)-Ni(1)-N(12)#2	90.4(3)	N(5CM)-Zn(2)-O(4MW)	91.1(3)
N(12)#1-Ni(1)-N(12)#2	89.997(5)	N(2CM)#1-Zn(2)-O(4MW)	88.8(3)
O(4)-Ni(1)-N(12)#3	89.6(3)	O(3MW)-Zn(2)-N(1CM)	86.9(3)
O(3)-Ni(1)-N(12)#3	90.4(3)	N(5CM)-Zn(2)-N(1CM)	89.6(3)
N(12)#1-Ni(1)-N(12)#3	89.997(6)	N(2CM)#1-Zn(2)-N(1CM)	91.7(4)
N(12)#2-Ni(1)-N(12)#3	179.2(5)	O(4MW)-Zn(2)-N(1CM)	89.2(4)
O(4)-Ni(1)-N(12)	89.6(3)	O(3MW)-Zn(2)-N(6CM)#1	91.1(3)
O(3)-Ni(1)-N(12)	90.4(3)	N(5CM)-Zn(2)-N(6CM)#1	88.6(3)
N(12)#1-Ni(1)-N(12)	179.1(5)	N(2CM)#1-Zn(2)-N(6CM)#1	90.1(4)
N(12)#2-Ni(1)-N(12)	89.997(7)	O(4MW)-Zn(2)-N(6CM)#1	92.7(4)
N(12)#3-Ni(1)-N(12)	89.997(5)	N(1CM)-Zn(2)-N(6CM)#1	177.4(4)
C(1)-N(1)-C(5)	120.0(9)	O(5MW)-Zn(3)-N(4CM)	90.3(3)
C(1)-N(1)-Ni(3)	120.2(6)	O(5MW)-Zn(3)-N(4CM)#2	90.3(3)
C(5)-N(1)-Ni(3)	119.8(8)	N(4CM)-Zn(3)-N(4CM)#2	89.999(4)
N(1)-C(1)-C(2)	122.5(8)	O(5MW)-Zn(3)-N(4CM)#1	90.3(3)
N(1)-C(1)-H(1)	118.7	N(4CM)-Zn(3)-N(4CM)#1	89.998(4)
C(2)-C(1)-H(1)	118.7	N(4CM)#2-Zn(3)-N(4CM)#1	179.4(6)

C(5)-C(4)-C(3)	119.6(11)	O(5MW)-Zn(3)-N(4CM)#3	90.3(3)
C(5)-C(4)-H(4)	120.2	N(4CM)-Zn(3)-N(4CM)#3	179.4(6)
C(3)-C(4)-H(4)	120.2	N(4CM)#2-Zn(3)-N(4CM)#3	89.999(4)
O(2)-Ni(3)-N(1)#1	90.2(2)	N(4CM)#1-Zn(3)-N(4CM)#3	89.999(4)
O(2)-Ni(3)-N(1)#2	90.2(2)	O(5MW)-Zn(3)-O(6MW)	180
N(1)#1-Ni(3)-N(1)#2	89.999(3)	N(4CM)-Zn(3)-O(6MW)	89.7(3)
O(2)-Ni(3)-N(1)#3	90.2(2)	N(4CM)#2-Zn(3)-O(6MW)	89.7(3)
N(1)#1-Ni(3)-N(1)#3	89.999(2)	N(4CM)#1-Zn(3)-O(6MW)	89.7(3)
N(1)#2-Ni(3)-N(1)#3	179.6(4)	N(4CM)#3-Zn(3)-O(6MW)	89.7(3)
O(2)-Ni(3)-N(1)	90.2(2)	O(1MW)-Zn(1)-O(2MW)	180
N(1)#1-Ni(3)-N(1)	179.6(4)	O(1MW)-Zn(1)-N(3CM)#2	89.5(3)
N(1)#2-Ni(3)-N(1)	90.001(3)	O(2MW)-Zn(1)-N(3CM)#2	90.5(3)
N(1)#3-Ni(3)-N(1)	89.998(3)	O(1MW)-Zn(1)-N(3CM)#1	89.5(3)
O(2)-Ni(3)-O(1)	180	O(2MW)-Zn(1)-N(3CM)#1	90.5(3)
N(1)#1-Ni(3)-O(1)	89.8(2)	N(3CM)#2-Zn(1)-N(3CM)#1	179.0(6)
N(1)#2-Ni(3)-O(1)	89.8(2)	O(1MW)-Zn(1)-N(3CM)#3	89.5(3)
N(1)#3-Ni(3)-O(1)	89.8(2)	O(2MW)-Zn(1)-N(3CM)#3	90.5(3)
N(1)-Ni(3)-O(1)	89.8(2)	N(3CM)#2-Zn(1)-N(3CM)#3	89.995(7)
C(2)-C(3)-C(4)	120.3(11)	N(3CM)#1-Zn(1)-N(3CM)#3	89.995(8)
C(2)-C(3)-H(3)	119.9	O(1MW)-Zn(1)-N(3CM)	89.5(3)
C(4)-C(3)-H(3)	119.9	O(2MW)-Zn(1)-N(3CM)	90.5(3)
N(7)#3-Ni(2)-O(5)	91.2(2)	N(3CM)#2-Zn(1)-N(3CM)	89.997(8)
N(7)#3-Ni(2)-O(6)	91.0(2)	N(3CM)#1-Zn(1)-N(3CM)	89.994(7)
O(5)-Ni(2)-O(6)	175.8(3)	N(3CM)#3-Zn(1)-N(3CM)	179.0(6)
N(7)#3-Ni(2)-N(6)	179.0(3)	O(00A)-P(1)-N(2)	112.6(6)
O(5)-Ni(2)-N(6)	89.6(2)	O(00A)-P(1)-N(1)	111.4(6)
O(6)-Ni(2)-N(6)	88.3(2)	N(2)-P(1)-N(1)	105.9(6)
N(7)#3-Ni(2)-N(5)	88.3(3)	O(00A)-P(1)-N(3)	113.6(6)

O(5)-Ni(2)-N(5)	91.3(3)	N(2)-P(1)-N(3)	104.5(6)
O(6)-Ni(2)-N(5)	92.4(3)	N(1)-P(1)-N(3)	108.3(6)
N(6)-Ni(2)-N(5)	91.0(3)	O(00C)-P(2)-N(6)	114.0(5)
N(7)#3-Ni(2)-N(9)#3	89.6(3)	O(00C)-P(2)-N(4)	114.4(5)
O(5)-Ni(2)-N(9)#3	87.2(3)	N(6)-P(2)-N(4)	104.0(6)
O(6)-Ni(2)-N(9)#3	89.1(3)	O(00C)-P(2)-N(5)	114.9(5)
N(6)-Ni(2)-N(9)#3	91.2(3)	N(6)-P(2)-N(5)	106.1(6)
N(5)-Ni(2)-N(9)#3	177.4(3)	N(4)-P(2)-N(5)	102.1(5)
C(3)-C(2)-N(11N)	122.1(9)	C(16)-N(4)-P(2)	124.8(8)
C(3)-C(2)-C(1)	116.4(9)	C(11)-N(3)-P(1)	124.1(9)
N(11N)-C(2)-C(1)	121.5(8)	C(21)-N(5)-P(2)	128.7(9)
C(14)-N(5)-C(15)	120.3(9)	C(10)-N(1CM)-C(9)	115.1(11)
C(14)-N(5)-Ni(2)	119.1(7)	C(10)-N(1CM)-Zn(2)	122.5(8)
C(15)-N(5)-Ni(2)	120.2(6)	C(9)-N(1CM)-Zn(2)	122.4(9)
C(4)-C(5)-N(1)	121.1(12)	C(30)-N(5CM)-C(29)	117.9(9)
C(4)-C(5)-H(5)	119.5	C(30)-N(5CM)-Zn(2)	120.3(7)
N(1)-C(5)-H(5)	119.5	C(29)-N(5CM)-Zn(2)	121.8(7)
N(7)-C(6)-C(5A)	124.3(9)	C(19)-N(6CM)-C(20)	117.0(11)
N(7)-C(6)-H(6)	117.9	C(19)-N(6CM)-Zn(2)#2	121.3(9)
C(5A)-C(6)-H(6)	117.9	C(20)-N(6CM)-Zn(2)#2	121.4(7)
N(7)-C(8)-C(7)	122.2(10)	C(15)-N(2CM)-C(14)	118.6(9)
N(7)-C(8)-H(8)	118.9	C(15)-N(2CM)-Zn(2)#2	122.0(8)
C(7)-C(8)-H(8)	118.9	C(14)-N(2CM)-Zn(2)#2	119.2(8)
C(6)-N(7)-C(8)	115.5(8)	C(26)-C(30)-N(5CM)	122.3(11)
C(6)-N(7)-Ni(2)#2	121.6(6)	C(26)-C(30)-H(30)	118.9
C(8)-N(7)-Ni(2)#2	122.9(6)	N(5CM)-C(30)-H(30)	118.9
C(10)-C(7)-C(8)	119.6(9)	N(1CM)-C(10)-C(6)	126.3(11)
C(25)-N(9)-C(24)	117.5(10)	N(1CM)-C(10)-H(10)	116.9

C(25)-N(9)-Ni(2)#2	121.0(6)	C(6)-C(10)-H(10)	116.9
C(24)-N(9)-Ni(2)#2	121.5(7)	C(6)-N(2)-P(1)	126.9(8)
C(5A)-C(10)-C(7)	119.5(9)	N(6CM)-C(19)-C(18)	126.5(14)
C(5A)-C(10)-H(10)	120.2	N(6CM)-C(19)-H(19)	116.8
C(7)-C(10)-H(10)	120.2	C(18)-C(19)-H(19)	116.8
C(12)-C(11)-C(15)	117.9(8)	C(26)-N(6)-P(2)	122.5(8)
C(12)-C(11)-N(12N)	118.9(8)	C(4)-N(3CM)-C(5)	121.4(14)
C(15)-C(11)-N(12N)	123.2(8)	C(4)-N(3CM)-Zn(1)	121.1(11)
C(2)-N(11N)-P(1N)	129.1(7)	C(5)-N(3CM)-Zn(1)	117.4(10)
C(2)-N(11N)-H(11N)	115.5	C(1)-N(1)-P(1)	130.0(10)
P(1N)-N(11N)-H(11N)	115.5	C(30)-C(26)-C(27)	121.4(11)
C(12)-C(13)-C(14)	117.8(10)	C(30)-C(26)-N(6)	122.8(10)
C(12)-C(13)-H(13)	121.1	C(27)-C(26)-N(6)	115.7(10)
C(14)-C(13)-H(13)	121.1	C(23)-C(24)-N(4CM)	125.9(15)
C(5A)-N(13N)-P(1N)	127.6(7)	C(23)-C(24)-H(24)	117.1
C(5A)-N(13N)-H(13N)	116.2	N(4CM)-C(24)-H(24)	117.1
P(1N)-N(13N)-H(13N)	116.2	C(12)-C(11)-C(15)	116.5(10)
C(11)-C(12)-C(13)	121.0(10)	C(12)-C(11)-N(3)	117.4(10)
C(11)-C(12)-H(12)	119.5	C(15)-C(11)-N(3)	126.1(10)
C(13)-C(12)-H(12)	119.5	C(25)-N(4CM)-C(24)	115.7(13)
C(11)-N(12N)-P(1N)	127.1(7)	C(25)-N(4CM)-Zn(3)	119.8(8)
C(11)-N(12N)-H(12N)	116.4	C(24)-N(4CM)-Zn(3)	124.5(11)
P(1N)-N(12N)-H(12N)	116.4	N(4CM)-C(25)-C(21)	123.6(12)
C(27)-N(12)-C(28)	117.2(11)	N(4CM)-C(25)-H(25)	118.2

C(27)-N(12)-Ni(1)	120.7(8)	C(21)-C(25)-H(25)	118.2
C(28)-N(12)-Ni(1)	122.0(9)	N(5)-C(21)-C(22)	122.9(12)
C(11)-C(15)-N(5)	122.1(8)	N(5)-C(21)-C(25)	122.5(11)
C(11)-C(15)-H(15)	118.9	C(22)-C(21)-C(25)	114.5(14)
N(5)-C(15)-H(15)	118.9	C(28)-C(27)-C(26)	115.7(10)
N(5)-C(14)-C(13)	120.9(11)	C(28)-C(27)-H(27)	122.1
N(5)-C(14)-H(14)	119.6	C(26)-C(27)-H(27)	122.1
C(13)-C(14)-H(14)	119.6	N(2CM)-C(15)-C(11)	123.2(10)
C(16)-N(6)-C(20)	118.9(8)	N(2CM)-C(15)-H(15)	118.4
C(16)-N(6)-Ni(2)	121.9(6)	C(11)-C(15)-H(15)	118.4
C(20)-N(6)-Ni(2)	119.0(6)	C(10)-C(6)-C(7)	117.1(12)
N(6)-C(16)-C(17)	124.1(9)	C(10)-C(6)-N(2)	124.1(10)
N(6)-C(16)-H(16)	117.9	C(7)-C(6)-N(2)	118.7(11)
C(17)-C(16)-H(16)	117.9	C(19)-C(18)-C(17)	116.2(12)
N(21N)-C(17)-C(18)	119.4(9)	C(19)-C(18)-H(18)	121.9
N(21N)-C(17)-C(16)	124.7(9)	C(17)-C(18)-H(18)	121.9
C(18)-C(17)-C(16)	115.6(9)	C(8)-C(7)-C(6)	117.5(12)
C(17)-C(18)-C(19)	120.3(8)	C(8)-C(7)-H(7)	121.3
C(17)-C(18)-H(18)	119.8	C(6)-C(7)-H(7)	121.3
C(19)-C(18)-H(18)	119.8	N(4)-C(16)-C(20)	125.7(10)
C(20)-C(19)-C(18)	117.5(9)	N(4)-C(16)-C(17)	119.3(10)
C(20)-C(19)-H(19)	121.2	C(20)-C(16)-C(17)	114.9(11)
C(18)-C(19)-H(19)	121.2	C(13)-C(14)-N(2CM)	122.0(12)
N(6)-C(20)-C(19)	123.4(9)	C(13)-C(14)-H(14)	119
N(6)-C(20)-H(20)	118.3	N(2CM)-C(14)-H(14)	119
C(19)-C(20)-H(20)	118.3	C(9)-C(8)-C(7)	119.7(13)
O(7)-P(1N)-N(13N)	113.0(4)	C(9)-C(8)-H(8)	120.2
O(7)-P(1N)-N(12N)	113.1(4)	C(7)-C(8)-H(8)	120.2

N(13N)-P(1N)-N(12N)	105.4(4)	C(11)-C(12)-C(13)	121.6(10)
O(7)-P(1N)-N(11N)	115.7(4)	C(11)-C(12)-H(12)	119.2
N(13N)-P(1N)-N(11N)	104.7(4)	C(13)-C(12)-H(12)	119.2
N(12N)-P(1N)-N(11N)	103.9(4)	C(24)-C(23)-C(22)	119.4(13)
C(25)-C(21)-N(23N)	122.8(8)	C(24)-C(23)-H(23)	120.3
C(25)-C(21)-C(22)	117.4(9)	C(22)-C(23)-H(23)	120.3
N(23N)-C(21)-C(22)	119.4(9)	N(3CM)-C(5)-C(1)	120.2(12)
C(17)-N(21N)-P(2N)	128.3(7)	N(3CM)-C(5)-H(5)	119.9
C(17)-N(21N)-H(21N)	115.8	C(1)-C(5)-H(5)	119.9
P(2N)-N(21N)-H(21N)	115.8	C(2)-C(1)-N(1)	120.8(13)
C(23)-C(22)-C(21)	116.6(10)	C(2)-C(1)-C(5)	117.1(13)
C(23)-C(22)-H(22)	121.7	N(1)-C(1)-C(5)	122.0(11)
C(21)-C(22)-H(22)	121.7	N(6CM)-C(20)-C(16)	124.3(10)
C(26)-N(22N)-P(2N)	129.5(7)	N(6CM)-C(20)-H(20)	117.9
C(26)-N(22N)-H(22N)	115.2	C(16)-C(20)-H(20)	117.9
P(2N)-N(22N)-H(22N)	115.2	C(14)-C(13)-C(12)	117.8(12)
C(22)-C(23)-C(24)	122.5(10)	C(14)-C(13)-H(13)	121.1
C(22)-C(23)-H(23)	118.7	C(12)-C(13)-H(13)	121.1
C(24)-C(23)-H(23)	118.7	C(27)-C(28)-C(29)	121.7(11)
C(21)-N(23N)-P(2N)	128.4(7)	C(27)-C(28)-H(28)	119.1
C(21)-N(23N)-H(23N)	115.8	C(29)-C(28)-H(28)	119.1
P(2N)-N(23N)-H(23N)	115.8	C(16)-C(17)-C(18)	121.1(12)

N(9)-C(24)-C(23)	121.2(11)	C(16)-C(17)-H(17)	119.5
N(9)-C(24)-H(24)	119.4	C(18)-C(17)-H(17)	119.5
C(23)-C(24)-H(24)	119.4	C(28)-C(29)-N(5CM)	120.8(11)
N(9)-C(25)-C(21)	124.3(9)	C(28)-C(29)-H(29)	119.6
N(9)-C(25)-H(25)	117.8	N(5CM)-C(29)-H(29)	119.6
C(21)-C(25)-H(25)	117.8	C(8)-C(9)-N(1CM)	124.2(13)
C(27)-C(26)-C(30)	117.6(9)	C(8)-C(9)-H(9)	117.9
C(27)-C(26)-N(22N)	122.1(9)	N(1CM)-C(9)-H(9)	117.9
C(30)-C(26)-N(22N)	120.3(9)	C(23)-C(22)-C(21)	120.7(14)
N(12)-C(27)-C(26)	122.7(10)	C(23)-C(22)-H(22)	119.7
N(12)-C(27)-H(27)	118.7	C(21)-C(22)-H(22)	119.7
C(26)-C(27)-H(27)	118.7	C(1)-C(2)-C(3)	117.3(14)
N(12)-C(28)-C(29)	121.9(14)	C(1)-C(2)-H(2)	121.4
N(12)-C(28)-H(28)	119	C(3)-C(2)-H(2)	121.4
C(29)-C(28)-H(28)	119	C(4)-C(3)-C(2)	121.0(15)
C(30)-C(29)-C(28)	121.5(14)	C(4)-C(3)-H(3)	119.5
C(30)-C(29)-H(29)	119.3	C(2)-C(3)-H(3)	119.5
C(28)-C(29)-H(29)	119.3	C(3)-C(4)-N(3CM)	122.8(17)
C(29)-C(30)-C(26)	118.8(12)	C(3)-C(4)-H(4)	118.6
C(29)-C(30)-H(30)	120.6	N(3CM)-C(4)-H(4)	118.6
C(26)-C(30)-H(30)	120.6		
O(8)-P(2N)-N(22N)	111.7(5)		
O(8)-P(2N)-N(23N)	111.8(5)		
N(22N)-P(2N)-N(23N)	107.3(5)		
O(8)-P(2N)-N(21N)	114.6(5)		
N(22N)-P(2N)-N(21N)	106.2(5)		
N(23N)-P(2N)-N(21N)	104.7(5)		

C(10)-C(5A)-C(6)	118.8(9)		
C(10)-C(5A)-N(13N)	120.8(9)		
C(6)-C(5A)-N(13N)	120.4(8)		

Appendix 4

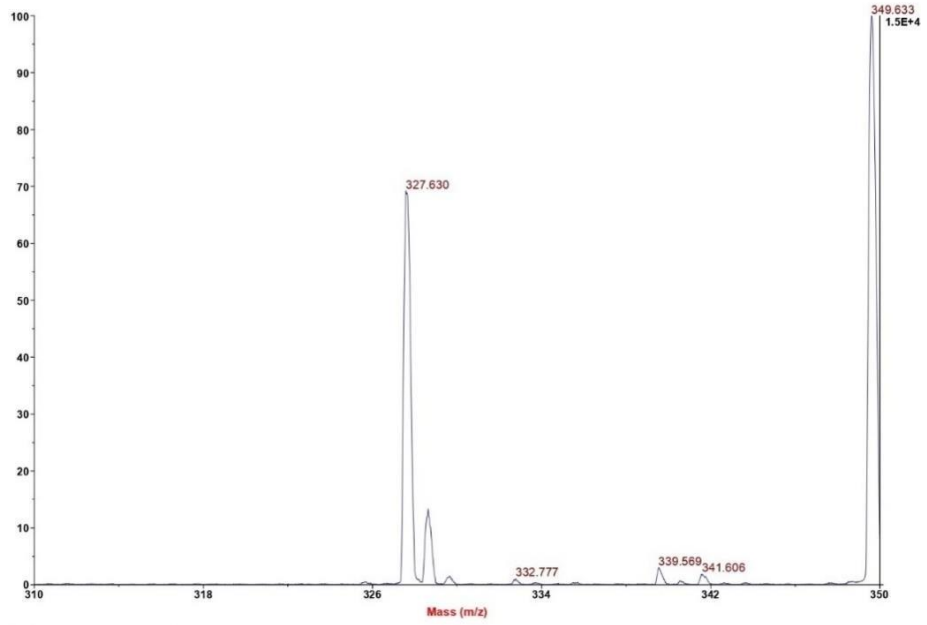

Figure A1: MALDI-TOF of ligand L1 in MeOH.

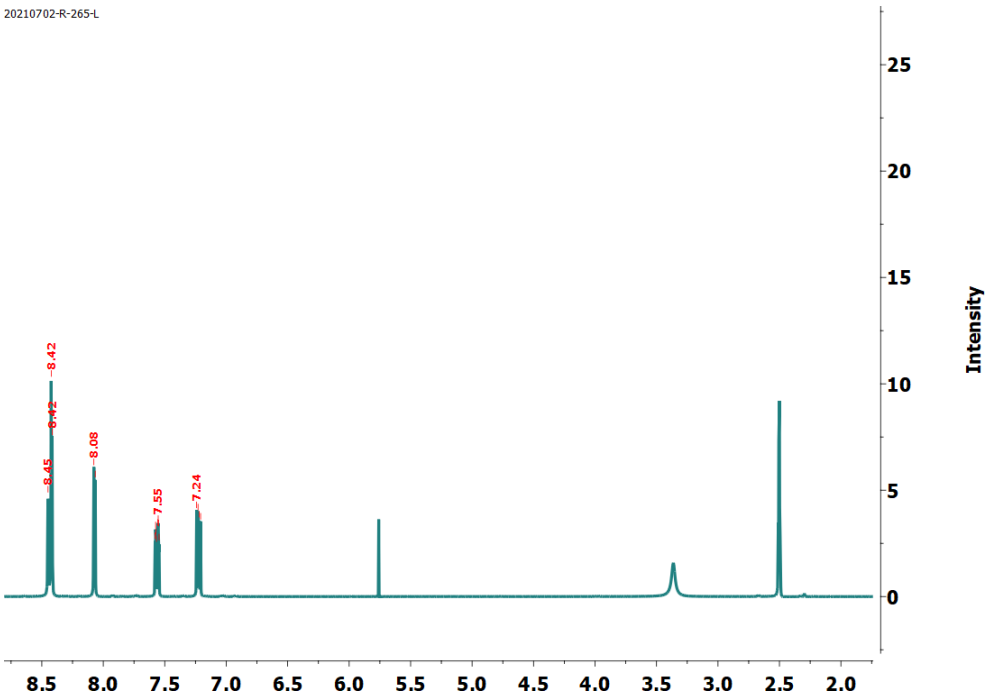

Figure A2: ^{1}H NMR of Ligand L1 in DMSO-d_6

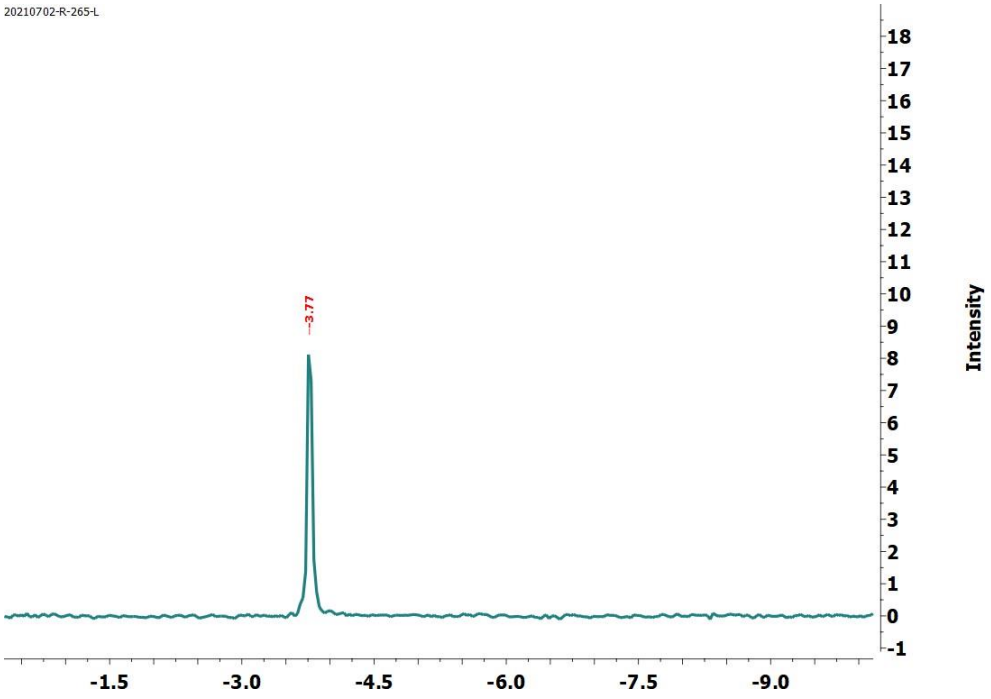

Figure A3: ^{31}P NMR of Ligand L1 in DMSO-d_6

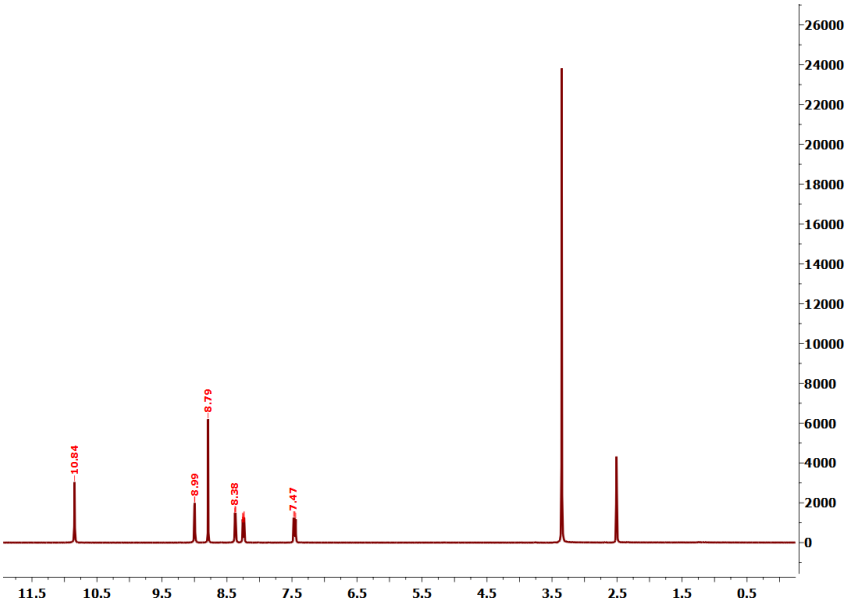

Figure A4: ^{1}H NMR of Ligand L2 in DMSO-d_6

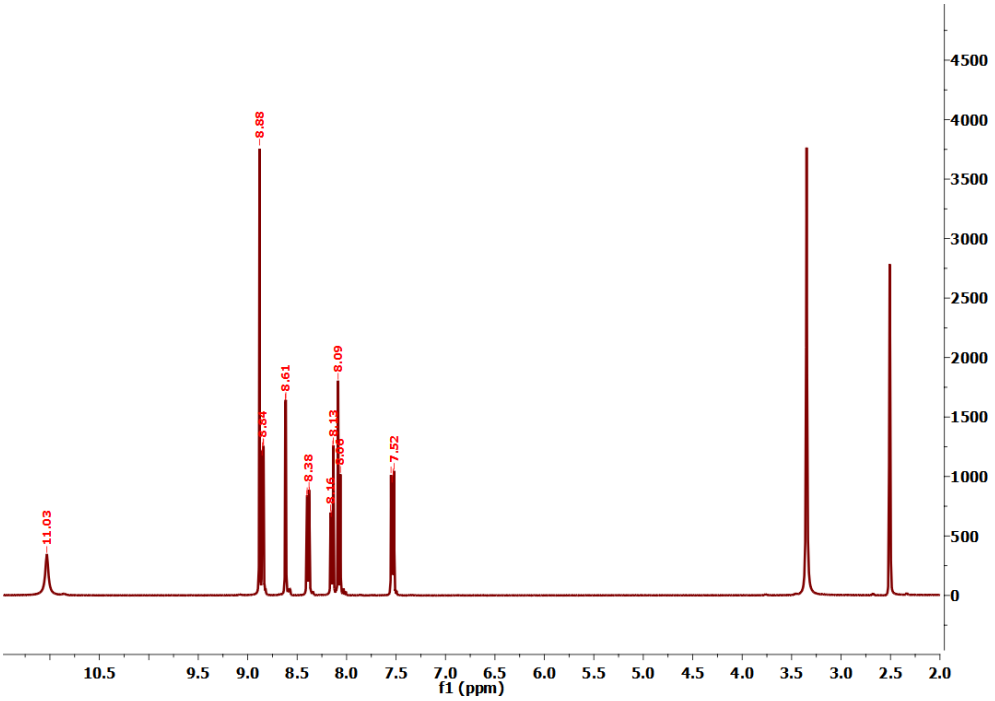

Figure A5: ^{1}H NMR of Ligand L3 in DMSO-d_6

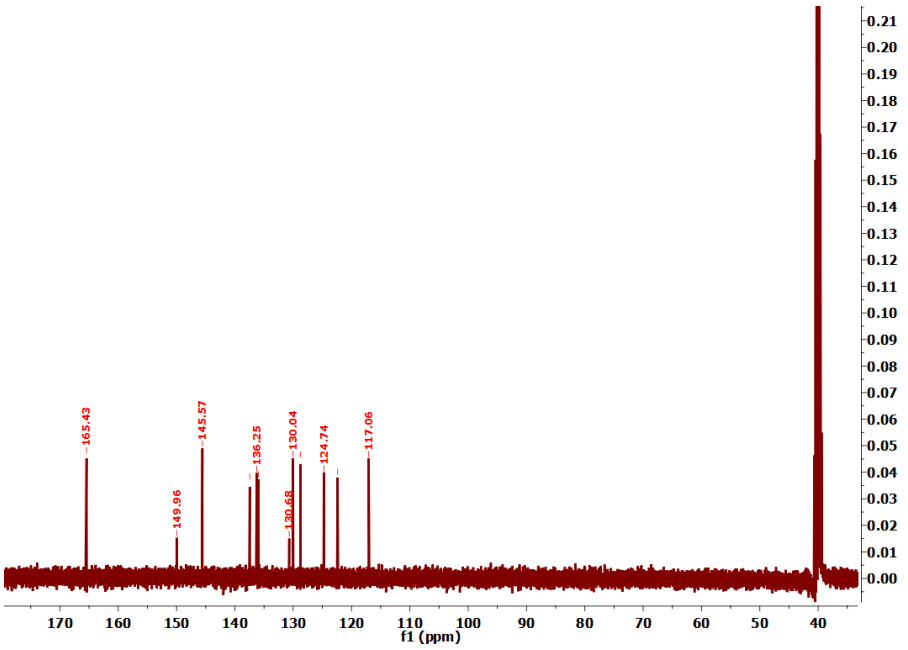

Figure A6: ^{13}C NMR of Ligand L3 in DMSO-d_6

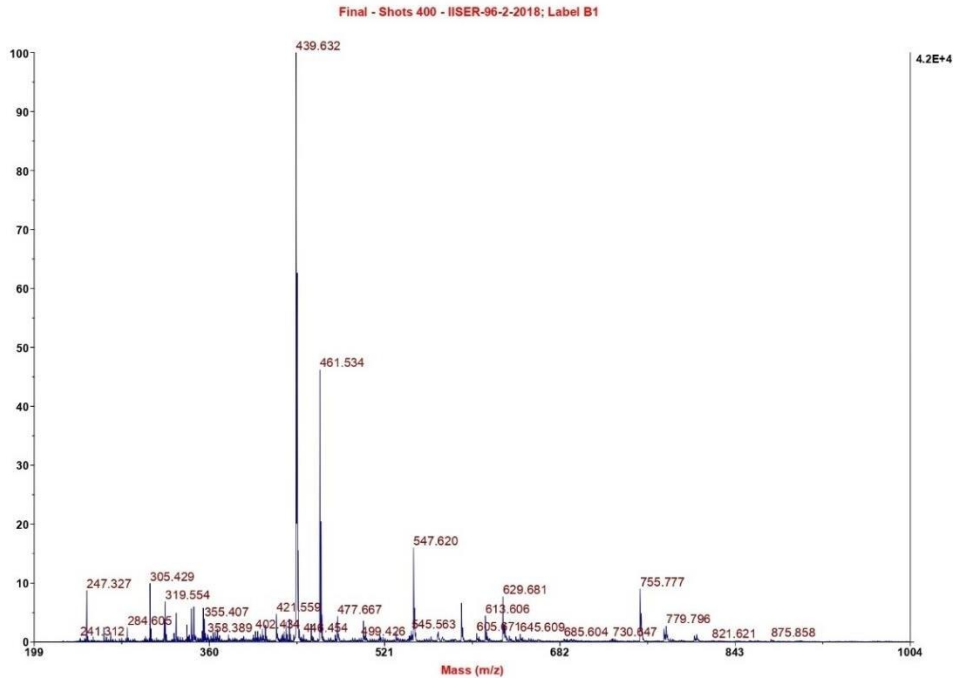

Figure A7: MALDI-TOF of ligand L2 in DMSO/MeOH solvent mixture.

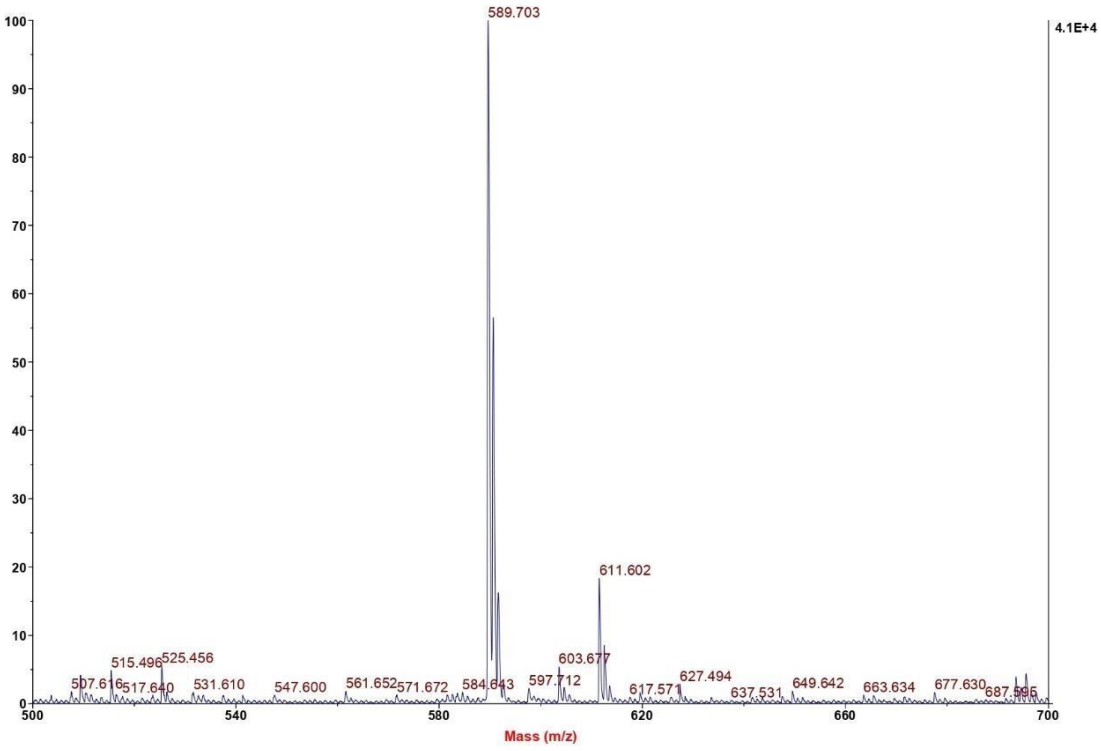

Figure A8: MALDI-TOF of ligand L3 in DMSO/MeOH solvent mixture.

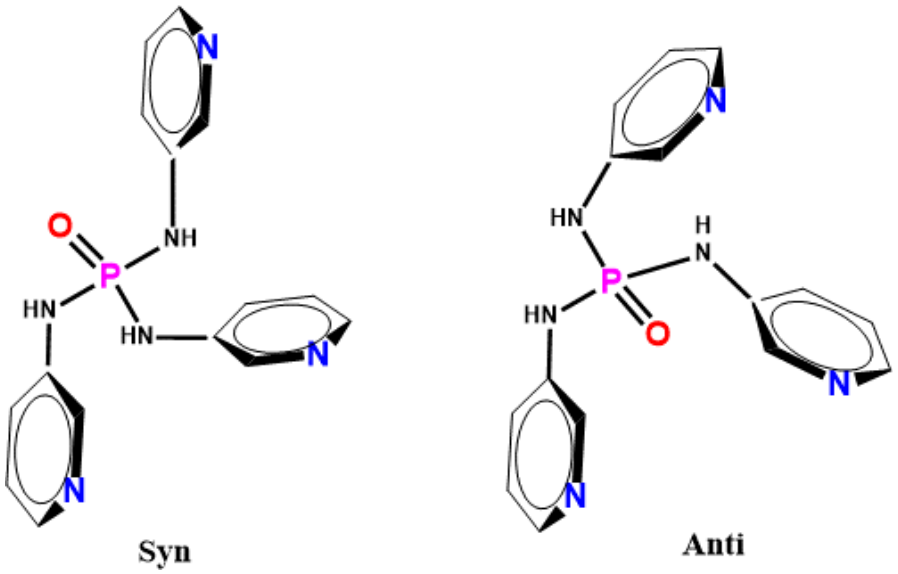

Figure A9: Syn and Anti conformers of ligand L1.

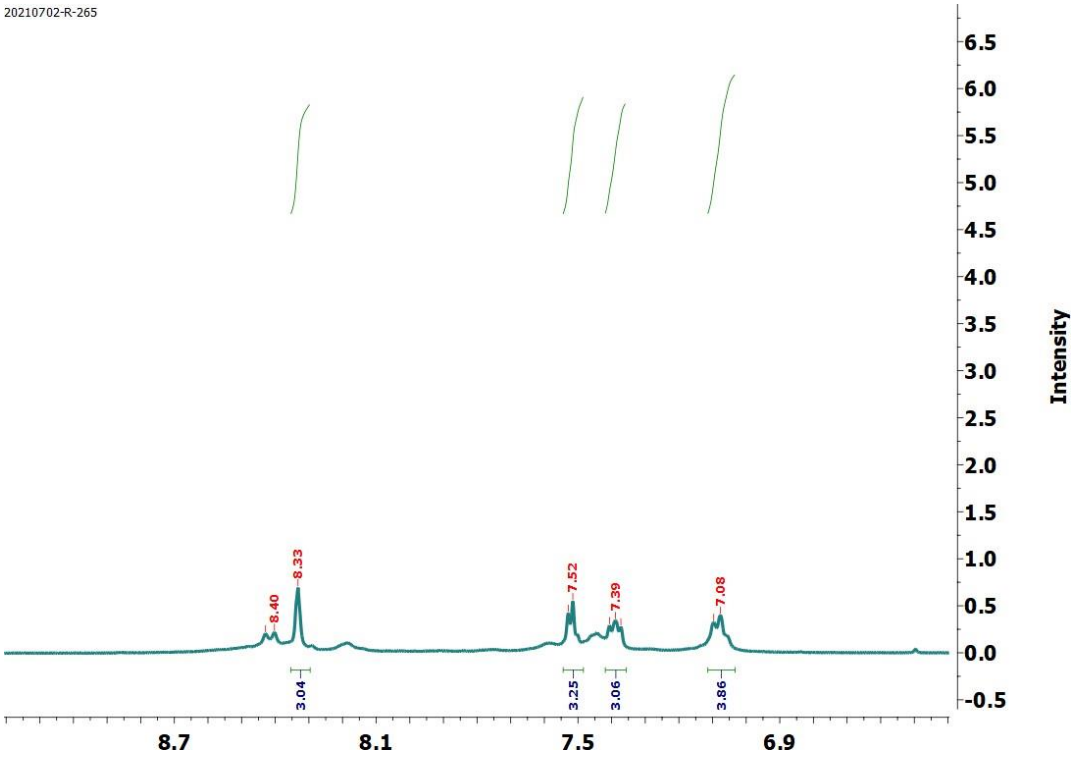

Figure A10: ^{1}H NMR of cage 1 in DMSO-d_6

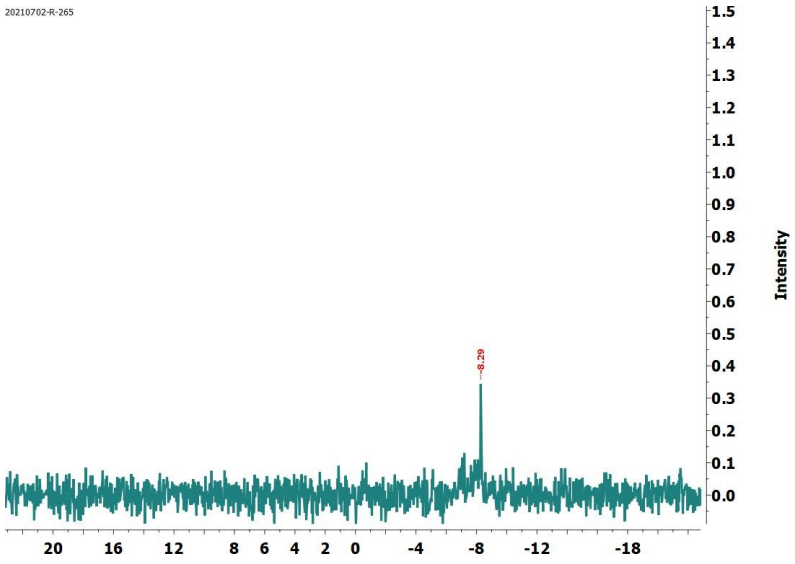

Figure A11: ^{31}P NMR of cage 1 in DMSO-d_6

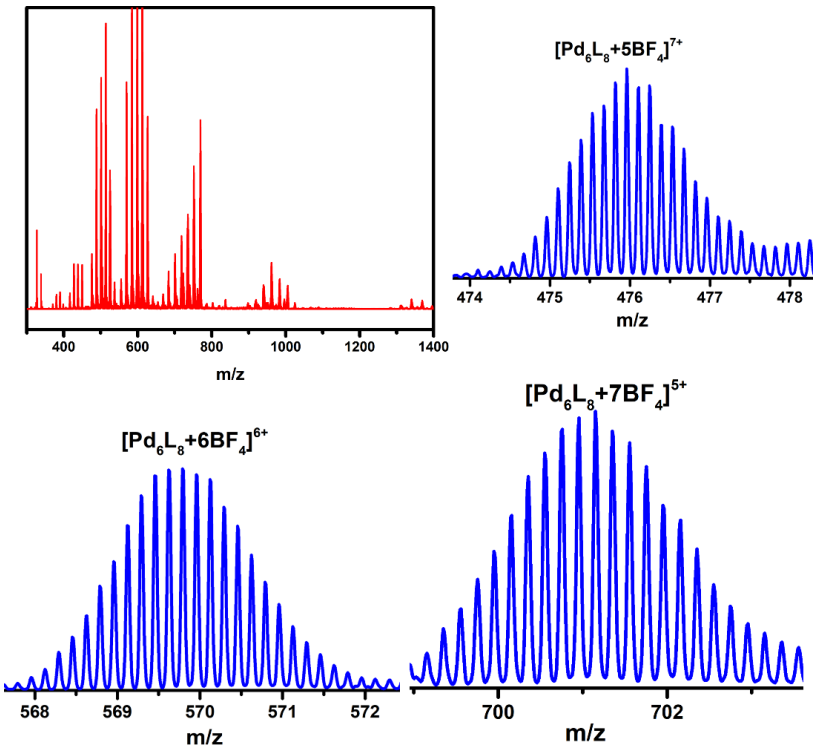

Figure A12: ESI-MS of cage 1 in Acetonitrile with zoomed isotopic peaks with different composition of anions.

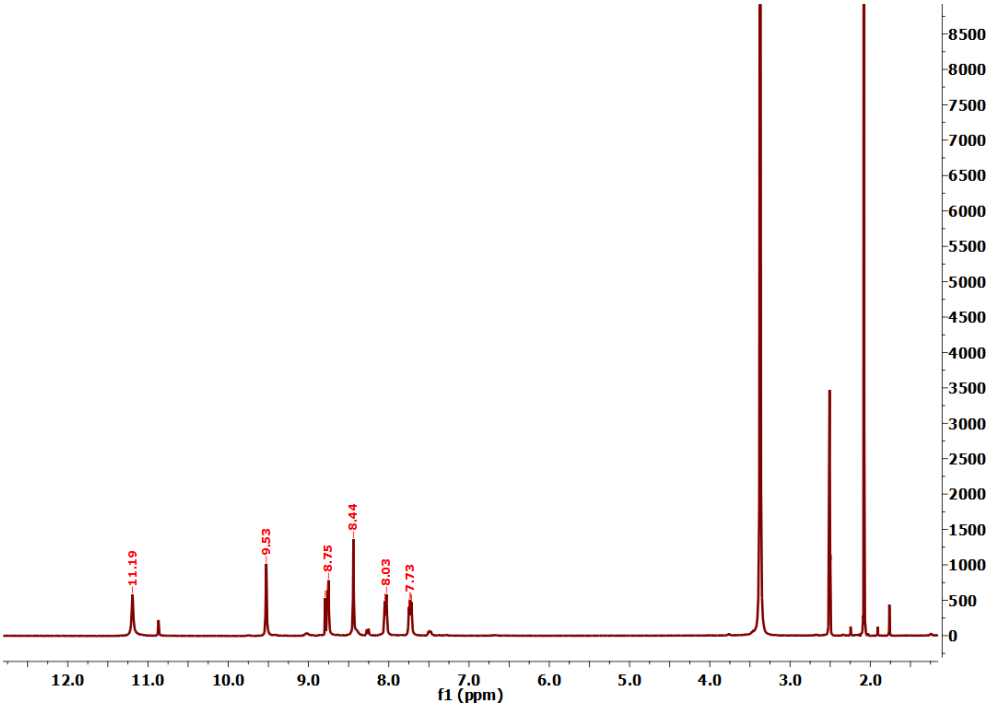

Figure A13: ^{1}H NMR of cage 2 in DMSO-d_6

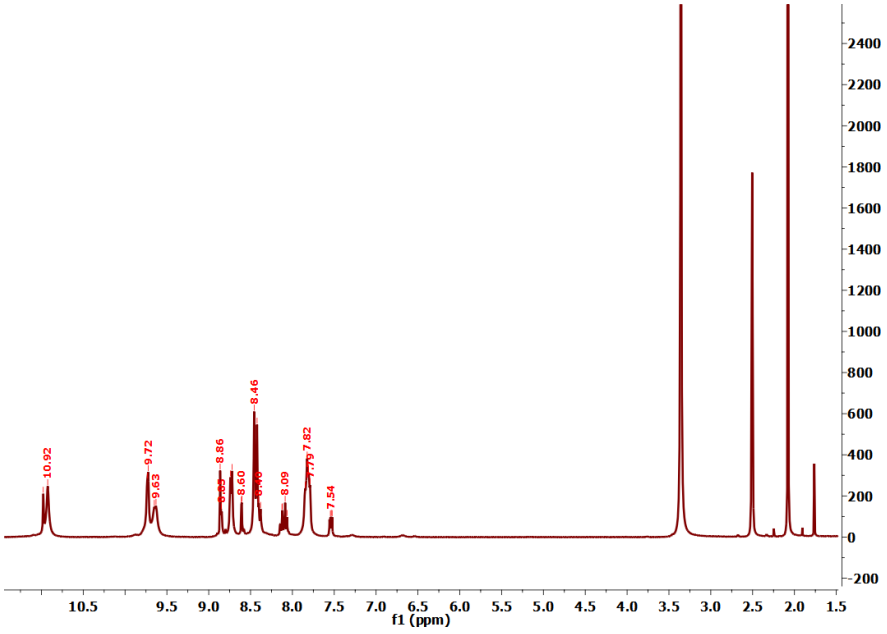

Figure A14: ^{1}H NMR of cage 3 in DMSO-d_6

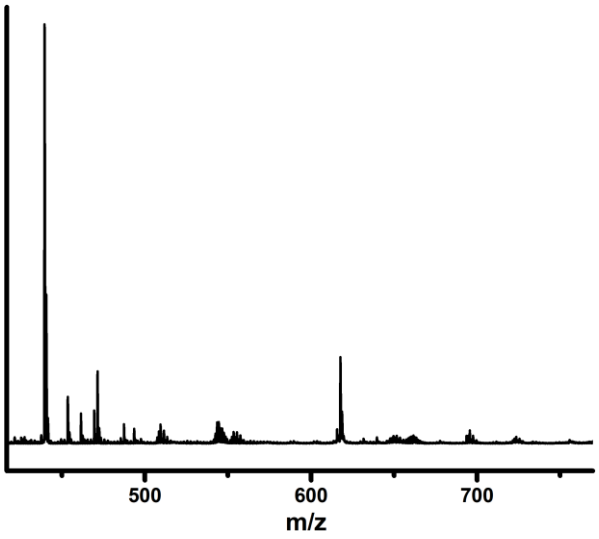

Figure A15: MALDI-TOF of broken Cage 2 with fragmented peaks.

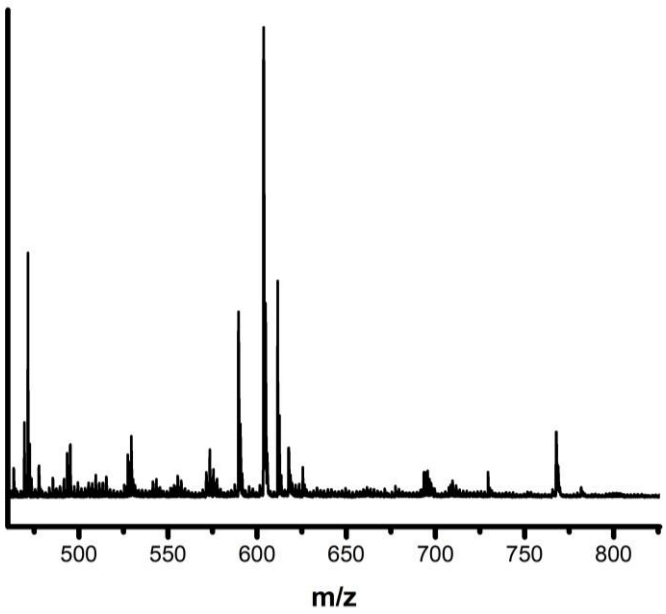

Figure A16: MALDI-TOF of broken Cage 3 with fragmented peaks.

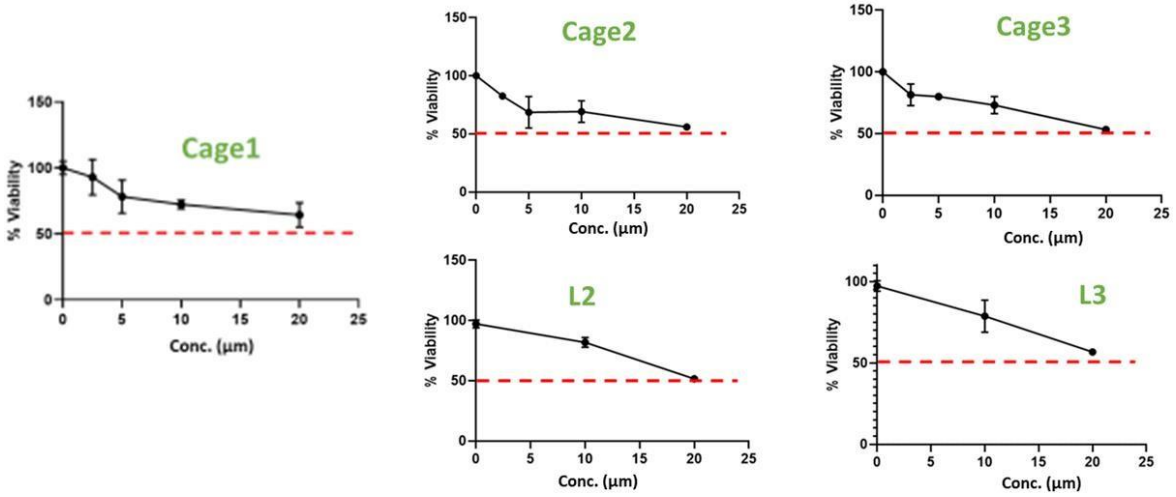

Figure A17: Efficacy towards normal cell lines HEK29 of L2 and L3 and their self-assembled metallocages 1, 2 and 3.

Efficacy and Selectivity

	IC_{50} (µM)	
	MCF-7 (Cancer cell)	HEK293 (Normal cell)
L1	> 20	-
L2	> 20	20
L3	> 15	>20
cage1	> 20	>20
cage2	11.5	>20
Cage3	**5**	20
Published data		
1 (Hexanuclear complex)	23	30
1-$[(acac)_2Pd]^{6+}$	1	3
1-$[(acac)_2Pt]^{6+}$	12	23
Cisplatin	> 50	77
Doxorubicin	0.29	-

Table 4.1: Efficacy towards cancer cell HCF-7 and normal cell lines HEK29 of L1, L2 and L3 and their self-assembled metallocages 1, 2 and 3.

Chapter 5

A Flexible Energy Harvester from an Organic Ferroelectric Ammonium Salt

5.1 Introduction

Materials that find applications in the energy, environment and healthcare sectors havegarnered much attention in recent years.[1-3] A common requirement for state-of-the-art materialsis the need to achieve energetic self-sufficiency. Hence, substances that produce electric responses to the external stimuli such as light, heat and mechanical force are much sought afterfor energy harvesting applications through the photovoltaic, thermoelectric and piezoelectric effects, respectively.[1,4-8] Multifunctionality of such materials typically extends to the other areas, i.e. dielectric, second-order nonlinear optical (NLO) and particularly ferroelectric properties. Coexistence of these with energy harvesting functionality, makes possible cross- integration of these phenomena in memory, NLO switching, and sensor devices.[9-11] Ferroelectric materials have recently been employed as nanogenerators in which electrical energy can be harvested by the application of external mechanical forces.[12-15] The uniquenessof ferroelectric materials lies in their ability to switch their polarization upon reversal of an external electric field.[16-17] Accordingly, the use of ferroelectric substances for piezoelectric energy harvesting is advantageous since the piezoelectric coefficient is directly proportional to the remnant polarization of the material.[18-19] Over the years, several oxide materials such as barium titanate, lithium niobate, lead zirconate titanate and zinc oxide were explored as piezoelectric nanogenerators.[20-23] Despite their exceptional performances, these materialsexhibit certain disadvantages due to their high processing temperatures, toxic metal content and poor mechanical flexibility, all limiting their utility in microelectronics.[13,24-26] In the field of purely organic nanogenerators, polyvinylidene fluoride (PVDF) and its co-polymers were found to exhibit excellent energy harvesting properties owing to their high piezoelectric response.[27-28] However, there are some intrinsic limitations of them, the most important of which are the requirement for external additives and the need of a high-voltage poling processto enhance their polarization properties.[29]

In this context, employing composites of ferroelectric materials with polymers is an attractive approach towards the fabrication of flexible nanogenerators.[7,30-33] Several composites made up of hybrid perovskites with both piezoelectric and non-piezoelectric macromolecules have been examined for these applications.[34-37] Our group has been developing composites of organic and hybrid organic-inorganic ferroelectric materials supported by ammonium and phosphonium cations[38-39]. One of the key advantages of employing phosphonium cations over typical ammonium cations is the stability of their organic salts in the ferroelectric phase for a wide

range of temperatures, attributed to the larger size of the phosphonium ions. In several instances, the transition temperature (T_c) from ferroelectric to paraelectric phase were absent until their melting points.[40-41] Thus, we reasoned that by judiciously introducing bulky and structurally in-equivalent substituents on to the ammonium cation, robust high-T_c organic salts with ferroelectric properties can be realized.

Herein, we report the synthesis of a two-component ferroelectric compound [Bn(4-Br-Bn)NMe_2]·BF_4 (Bn= Benzyl and 4-BrBn = 4-Bromobenzyl), (**2**), consisting of benzyl-4-bromobenzyldimethylammonium cation and tetrafluoroborate anion that crystallized in the ferroelectrically active polar orthorhombic *Pna2₁* space group. The polarization (*P*) vs. electric field (*E*) hysteresis loop measurements on **2** showed a sizable remnant polarization (P_r) of 14.4 μC/cm^2 at room temperature. The dielectric permittivity measurements showed no phase transition for this compound until its melting point (405 K). Subsequently, all-organic composite films consisting of thermoplastic polyurethane (TPU) and different (5, 10, 15 & 20) weight percentages (wt %) of **2** were prepared and studied for mechanical energy harvesting applications. A maximum open-circuit output voltage of 20 V, short-circuit current of 4 μA, current density of 1.1 μA cm^{-2} and a power density of 21.1 μW cm^{-2} was recorded for the 15 wt % **2**-TPU composite device. The energy storage capability of the 15 wt % **2**-TPU composite was demonstrated by charging a 100 μF capacitor within 30 s. To the best of our knowledge, the observed current and power densities are the highest among the all-organic piezoelectric energy harvesters reported so far.

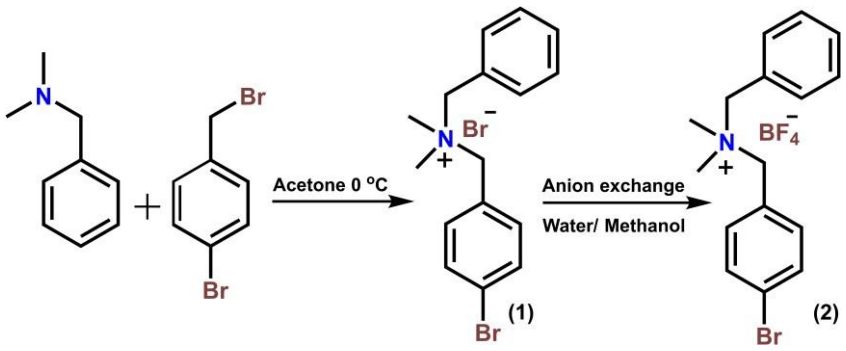

Scheme 1. Schematic showing the preparation of the ammonium salts **1** and **2**.

5.2 Experimental Section

5.2.1 Materials and Characterizations: All starting materials were purchased from Sigma-Aldrich and were used as bought without further purification. Thermoplastic polyurethane (TPU) was purchased from BASF and used as received. The NMR data for the ammonium compounds were recorded on a Bruker 400 or a Jeol 400 MHz spectrometer of (^{1}H NMR, 400.13 MHz; ^{13}C {^{1}H} NMR, 100.62 MHz). Electrospray Ionization (ESI) spectra andMALDI-TOF spectra were obtained using a Water Synapt G2 and Applied Biosystem MALDI-TOF/TOF spectrometer, respectively. The PerkinElmer STA-6000 analyzer with a heating rate of 10 ˚C/min in a nitrogen atmosphere was used for the thermogravimetric analysis. Melting point analyses were done using a Buchi M-560 melting point apparatus and were uncorrected.The variable temperature powder X-ray diffraction (VT-PXRD) data were measured in the 2- theta range of 5 to 50˚ on a Bruker-D8 Advance X-ray diffractometer. The FE-SEM analysis of all the piezo and ferroelectric crystallites and their composite films (all different wt%) were performed by using Zeiss ultra plus FE-SEM instrument with a minimum spatial resolution of 2 μm. The 3D X-Ray microtomography analyses were performed by using a Carl Zeiss Versa 510 microscope with an applied X-ray energy of 50 kV. The stress-strain measurements on pure TPU and the polymeric composite films were performed on a Instron 5943 model Universal Testing Machine (UTM) using rectangular film strips (0.2 mm thickness, 0.5 mm width and 10 mm gauge length) at 20 mm/min strain rate.

Synthesis of 1: To a stirred solution of 4-bromobenzyl bromide (4 mmol, 1 g) in acetone, *N*,*N*'-dimethylbenzyl amine (4 mmol, 0.6 ml) was added at 0 ˚C, the mixture was further stirred for 5-10 mins to get a white crystalline precipitate. The obtained precipitate was collected and washed with hexane. Single-crystals suitable for X-ray diffraction were obtained by the slow-evaporation of its solution in acetone. Yield: 1.43 g (94%). M.P.: 215-220 °C. ^{1}H NMR ($CDCl_3$): 7.65 (m, 4H), 7.53 (dd, 2H), 7.46 (t, 1H), 7.40 (dt, 2H,), 5.28 (s, 2H), 5.16 (s, 2H). 3.13 (s, 6H).^{13}C {^{1}H} NMR ($CDCl_3$): 135.02, 133.35, 132.23, 130.78, 129.23, 127.17, 126.26, 135.54, 67.46, 66.56, 48.08. MALDI-TOF: 304.06 $(M)^+$, 305.07 $(M + H)^+$ Anal. Calcd. for $C_{16}H_{19}NBr_2$: C, 49.90; H, 4.97; N, 3.64. Found: C, 49.38; H, 4.56; N, 3.74.

Synthesis of 2: To a solution of **1** (1 mmol, 382.9 mg) in methanol / water (1mL / 1 mL), one equivalent of $NaBF_4$ (1 mmol, 109.7 mg)) was added and the mixture was stirred for 1 h to get

clear solution and kept for crystallization. After 1 weak, colorless plate-crystals of **2** were obtained. Yield: 316 mg (81%). M.P.: 160-165 °C. ^{1}H NMR ($CDCl_3$): 7.65 (m, 4H), 7.52 (dd, 2H), 7.46 (t, 1H), 7.40 (dt, 2H,), 5.28 (s, 2H), 5.16 (s, 2H). 3.13 (s, 6H).^{13}C {^{1}H} NMR ($CDCl_3$): 135.02, 133.35, 132.23, 130.78, 129.23, 127.17, 126.26, 135.54, 67.46, 66.56, 48.08. MALDI-TOF: 304.06 $(M)^+$, 305.07 $(M + H)^+$ Anal. Calcd. for $C_{16}H_{19}BNF_4Br$: C, 49.02; H, 4.89; N, 3.57. Found: C, 48.88; H, 4.72; N, 3.52.

5.2.2 Method of preparation of the polymer composite films: The composite films with various (5, 10. 15 and 20) wt % of **2** were prepared by adding appropriate quantities of **2** to a homogeneous solution containing TPU in dimethylformamide (DMF). The mixture was further heated for 15 minutes at 70 ˚C followed by vortex mixing for 15 minutes. The homogeneous solutions of the composite mixtures were subsequently poured onto a petri dish and then were kept undisturbed in an oven at 70 ˚C for 5 hours. The dried free-standing composite films of various weight percentages wt % of **2** were subsequently peeled off from the glass Petri dish. To complete the device architecture copper adhesive tapes attached to lead Cu-wires were placed on either side of the composite films and covered with 3.5 mm thick PDMS polymer.

5.2.3 Single Crystal X-ray Diffraction Analysis: The single crystal X-ray diffraction data on the crystals of **1** and **2** were obtained on a Bruker Smart Apex Duo diffractometer by using Mo Kα radiation (λ=0.71073Å). The crystal structures were solved using the direct method and then refined by full-matrix least squares against F^2 using SHELXL-2014/7 built in the Apex 3 program. All the nonhydrogen atoms were refined anisotropically and the hydrogen atoms were fixed on the parent atoms using a riding model.[49-50]

5.2.4 Nonlinear optical Measurements: Nonlinear optical studies were performed using a Coherent Astrella Ti:Sapphire regenerative amplifier providing 800 nm pulses (75 fs pulse duration, 1 kHz repetition rate). Kurtz-Perry test has been performed at 293 K on size-graded samples of **2** and potassium dihydrogen phosphate (KDP), which was used as a SHG reference. The crushed single crystals of **2** and KDP were sieved through a mini-sieve set (Aldrich) and microcrystals of size 250-177 μm were collected. A tight layer of the size graded samples were formed by placing them in between microscope glass slides, which was sealed and then mounted to the sample holder. Average power of 800 nm beam used for Kurtz-Perry study was equal to 245 mW, spot area of 0.5 cm^2. The laser beam was directed onto sample at 45 degrees and was unfocused. Signal-collecting optics, mounted to the glass optical fiber, was placed

perpendicularly to the plane of sample (backscattering geometry) which was placed on a horizontally aligned holder. Scattered pumping radiation was suppressed with the use of 750 nm shortpass dielectric filter (FESH0750, Thorlabs).

5.2.5 Ferroelectric, Dielectric and Piezoelectric Measurements: The ferroelectric polarization (*P*) versus Electric Field (*E*) hysteresis loop measurements were performed on aixACCT TF-2000E model hysteresis loop analyzer. A sizable single crystal of approximate 1.2 mm thickness and 4.5 mm^2 area was chosen and was electroded with adhesive copper tapes as top and bottom electrodes. Leakage currents (and the current densities) were measured concomitantly as a function of the applied voltage during the hysteresis loop measurements.

The dielectric permittivity measurements were performed on the pressed powder pellet of **2**. The measurements were performed by using the Solartron Analytical 1260 model Impedance Analyzer coupled with a Dielectric Interface 1296A operating with Janis 129610A cryostat sample holder and a Lakeshore 336 model temperature controller. The piezoelectric energy harvesting properties of flexible **2**-TPU devices were examined on a custom-built periodic impact instrument. The output voltages and currents were measured using a Tektronix 2024 Mixed Signal Oscilloscope operating at an input impedance of 1 MΩ. The thickness and the active area of the devices under test were ~2.5 mm and 1750 mm^2, respectively.

5.3 Results and Discussion

5.3.1 Synthesis and Structure:

The reaction of 4-bromobenzyl bromide with N,N'-dimethylbenzyl amine yields the bromide salt **1**, [Bn(4-BrBn)NMe_2]·Br. Treatment of **1** with $NaBF_4$ results in an anion exchange leading to the formation of **2** (Scheme 1). The compounds **1** and **2** were characterized by NMR, mass-spectra and single-crystal X-ray diffraction analysis (Figures A1-A3). The single-crystal X-ray diffraction analysis reveals that the compound **2** crystallized in the polar orthorhombic space group $Pna2_1$ at 120 K (Table A5.1). However, the bromide salt **1** crystallized in the orthorhombic centrosymmetric space group *Pnma*, and therefore is not investigated for ferroelectric properties (Figure A4). Extracting the unit cell parameters of **2** at various temperatures indicates the absence of any structure phase transitions in **2** in the temperature range of 120-380 K (Figure A5). The thermogravimetric analysis 2 reveals that the compound

is stable up to 550 °C (Figure A6a). The bulk-phase purity of **2** was further established by powder X-ray diffraction analysis (figure A6b).

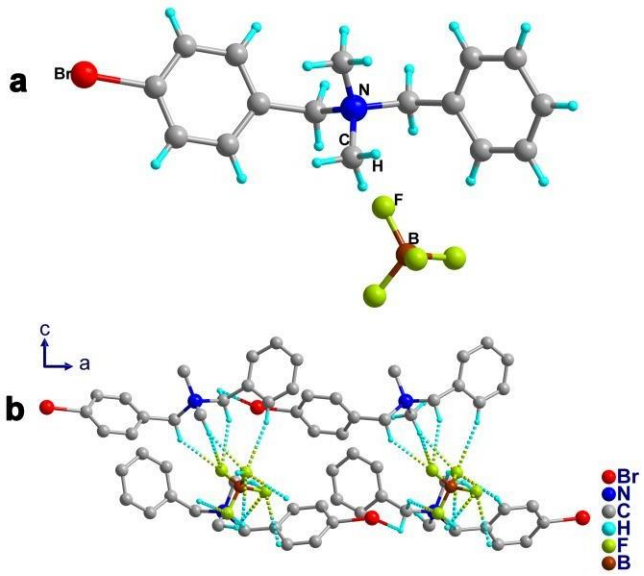

Figure 5.1 *(a) The molecular structure of **2**. (b) View of the C-H···F and C-H···Br hydrogen bonding interactions in **2** along the b-axis.*

The asymmetric unit of **2** contains one $[[Bn(4\text{-}Br\text{-}Bn)NMe_2]^+$ cation and one $(BF_4)^-$ ion (Figure 1a). The nitrogen center of the cation exhibits a distorted tetrahedral geometry. The C-N-C angles in the cation ranges from 105.8° to 110.2°. These angles are in close agreement with those found in the precursor bromide salt **1** (Tables A5.2-A5.3). The anionic BF_4 unit exhibits a nearly ideal tetrahedral angles for the F-B-F fragments that range between 108.14° and 109.92°. The asymmetry of the system may be attributed to the cumulative effects of the bulkier benzyl and the bromobenzyl groups on the ammonium cation and the noncentrosymmetric structure of $(BF_4)^-$ anion. The packing diagram indicates the presence of four cationic and four anionic units in the structure of **2** (Figure A7).

A closer view at the crystal structure of **2** revealed the presence of non-classical C-H···F and C-H···Br interactions in the molecule, in which the $(BF_4)^-$ unit was found to interact with four ammonium cations (Figures 5.1b and A8 and Table A5.4). Thirteen distinct C-H···F intermolecular contacts are experienced by the molecule. The d_{norm}-mapped Hirshfeld surfaces

indicate presence of various interactions, such as H···F/F···H (41.2 %), H···Br/Br···H (10.8 %), C···H/H···C (16.3 %), C···F/F···C (0.1 %), H···H (29.3%), C···C (0.8 %) and C···Br/Br···C (1.3 %) in the molecule (Figures 5.2 and A9). It is apparent that the H···F/F···H and H···Br/Br···H contacts display significant contributions of 41.2 and 10.8 % to the total Hirshfeld surface, respectively, accounting for the strong long-range order (Figures 5.2 and A10-A11). Because of the high fluorine content, the adjacent C-H groups to fluorine substituent attain increased acidic character and thereby strengthening the C-H···F interactions.[42] Although the dispersion and van der Waals contacts present in the molecule account for a larger percentage (30.1 %) of the overall interactions, they contribute to the short-range order with a low stabilization energy of 0.4-4 kJ/mol.

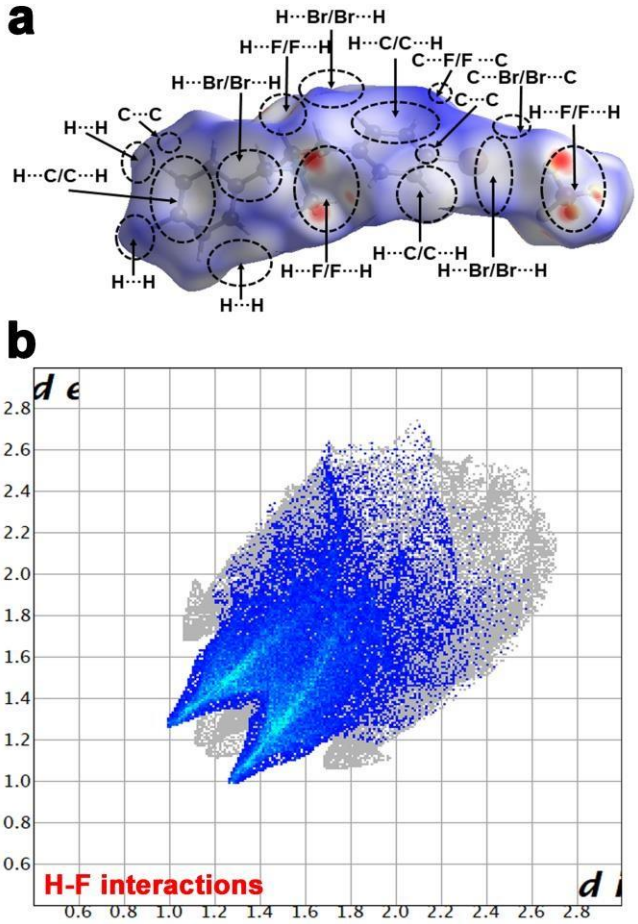

Figure 5.2 *(a) Hirshfeld Surface view of **2** showing all interactions present in the molecule. (b) 2D fingerprint plot of showing the H···F hydrogen bonding interactions in **2**.*

5.3.2 SHG, Ferroelectric, Dielectric, and Piezoelectric Studies: The Second Harmonic Generation (SHG) analysis of **2** was probed by a Kurtz-Perry type measurement at room temperature on sieved powder into 250 – 177 μm particle size range. Collected SHG signals show that relative efficiency of SHG is 0.11 versus KDP standard of the same particle size distribution. Accordingly, the observation of the distinct SHG response conclusively confirms the acentric structure of **2** (Figure A12).

The point group symmetry of **2** is C_{2V}, which is one of the ten polar point groups suitable for ferroelectric behaviour. The ferroelectric measurements of **2** were performed on its single crystal along its polar *c*-axis using a Sawyer-Tower circuit setup (Figure A13). The measurement resulted in a rectangular hysteresis loop for **2** at room temperature with a remnant polarization (P_r) 14.44 μC cm^{-2} at a coercive field (E_c) of 0.6 kV cm^{-1} (frequency 0.01 Hz) (Figure 3a). Furthermore, two opposite peaks at the switching coercive fields (E_c) were observed in the plot of current density (J) vs. electric field (E), which indicates the two stable states of opposite polarity. The high remnant polarization (P_r) value obtained for **2** is attributed to its charge separated two-component structure and a large number of non-classical H···F interactions present between them.

To further investigate the polarization attributes of **2**, dielectric permittivity measurements were performed on its powder pressed pellet. The real part of dielectric permittivity (ε′) was found to gradually increase upon sweeping the temperature from 298 to 360 K, beyond whichan abrupt raise in ε′ was observed. This can be attributed to the presence of a maximum numberof polarizable dipoles at higher temperatures near to its melting point. Furthermore, the ε′ vs. T profile shows no Curie point across all the measured temperatures confirming the absence of phase transition in this material up to 405 K (Figure 5.3b). The dielectric loss, the measure of the dissipation of electrical energy (in the form of heat), in **2** was extracted from the (tan δ) vs. T profile (Figure A14). It follows a similar trend as that of its ε′ vs. T profile and shows a low dielectric loss factor for **2**. The frequency (F) dependence of dielectric permittivity measurements also show a similar trend. Notably, the ε′ values were found to increase upon lowering the frequency, which indicates the presence of all four polarization mechanisms in **2** (Figure A15).[43] Also, an ε′ value of 6.65 at 100 kHz at 298 K was observed from the ε′ vs. T plots.

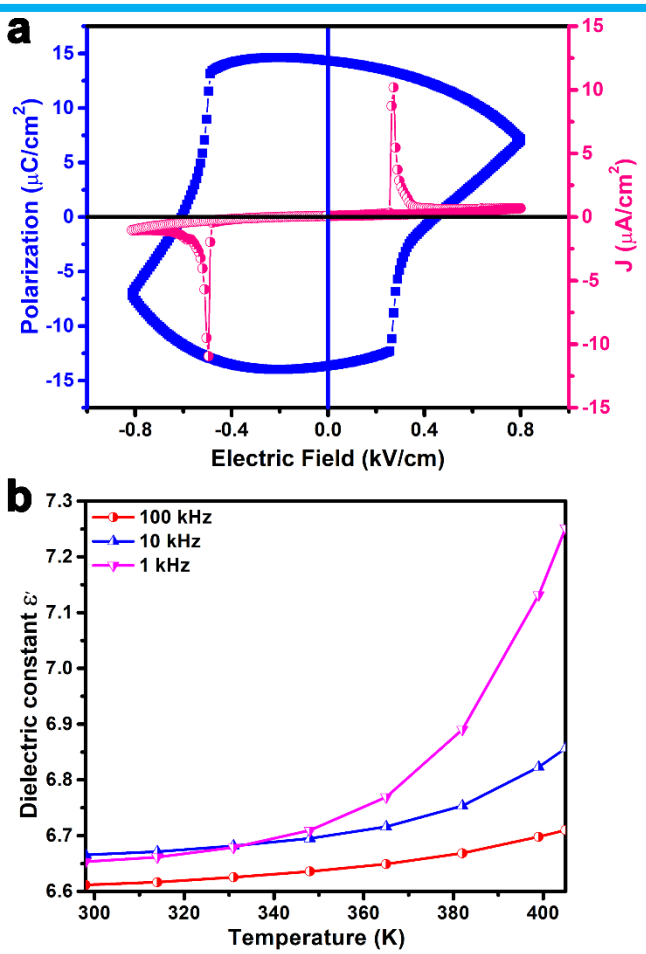

Figure 5.3 *(a) P-E hysteresis loop and the corresponding leakage current plots of* ***2****. (b) Temperature (T) dependent dielectric permittivity (ε') profile of* ***2****.*

The powder pressed pellet of **2** was further used to record the direct piezoelectric response (d_{33}) using "Berlincourt" method. The d_{33} value was found to be 2.16 pC N^{-1} at an operating frequency of 110 Hz and with an applied mechanical stress of 0.25 N (Figure S16). Additionally, the piezoelectric voltage coefficient (g_{33}) of **2** was calculated using the formula ($g_{33} = d_{33}/\varepsilon_{33}$). The observed maximum piezoelectric voltage coefficient (g_{33}) was found to be 37 □ 10^{-3} V m N^{-1}.[44]

5.3.3 Preparation and characterizations of 2-TPU devices:

Encouraged by the robust ferroelectric, dielectric and piezoelectric polarization behavior of **2**, we proceeded to study of its piezoelectric energy harvesting properties. For this purpose, composite materials with various (5, 10, 15 and 20) weight percentages (wt %) of **2** in

thermoplastic polyurethane (TPU) were prepared (Table A5). The preparation of the composite films involves the addition of the appropriate quantities of **2** into a homogeneous solution of TPU in DMF and subjecting them to a series of procedures depicted in Figure 5.4a. The composite material preparation details have been described in the experimental section. In this way, free standing composite films of **2**-TPU (5, 10, 15 and 20 wt %) were obtained. The flexibility of these films was further verified by subjecting them to mechanical stretching, bending, two-fold bending and rolling operations (Figure A17). A neat TPU film was also prepared by the analogous procedure for a performance comparison.

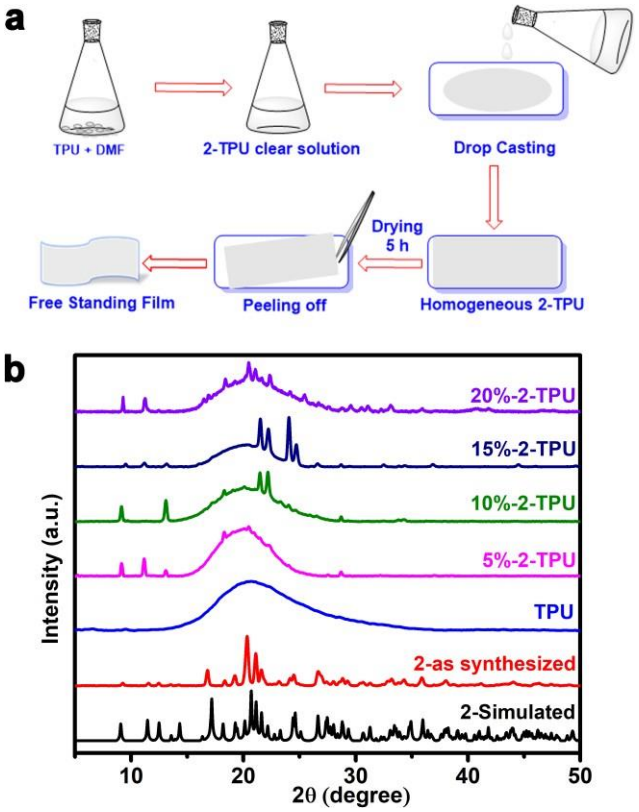

Figure 5.4 *(a) Schematic diagram for the preparation of **2**-TPU composite films. (b)The stacked PXRD profiles of all the **2**-TPU composite films, neat TPU, and experimental and theoretical PXRD profiles for **2**.*

The powder X-ray diffraction profiles of all the composite films exhibit the characteristic peaks present in the bulk phase of **2**. This indicates the crystallinity and phase purity of the embedded organic particles in the composite films (Figure 5.4b). However, to prevalent direction of the particles in the 15 wt % **2**-TPU composite film has been visualized by indexing the *hkl* peaks

and compared with those of pristine **2**. **(**Figure A18**)**. The FE-SEM and X-ray 3D-microtomography measurements were performed to gain insights into the structural morphology of the crystallites in the polymer matrix (Figure 5.5a and A19). These analyses indicate the uniform distribution of the particles in the composite films and crystalline nature of the embedded particles in the **2**-TPU composites. From the tomography images, agglomeration of the crystallites of **2** is seen at higher 20 wt % composite (Figure A20).

Using a Universal Testing Machine, the stress-strain relationships for all the **2**-TPU composite devices were examined. From figure 5.5b it is evident that the composite films are stretchable up to 50% strain without rupture. The stress at 50% strain was measured to be 3.58, 3.88, 4.21, 3.94 and 3.65 MPa for the neat TPU and 5, 10, 15 and 20 wt % **2**-TPU devices, respectively (Figure 5b). Also, all **2**-TPU composite films were found to yield higher stress values as compared to that of neat TPU. This observation confirms the efficient reinforcement of the ferroelectric particles in TPU matrix that helps in stabilizing the structural and interfacial interactions between the particles of **2** and TPU. Such high content (15-20 wt%) of crystalline particles in a polymer would typically compromise its flexibility significantly. This highlights one of the major advantages of all organic ferroelectric composites. Furthermore, the direct piezoelectric response (d_{33}) of all weight percentages (5, 10, 15 and 20 wt %) of **2**-TPU composite films were measured and the values are 0.24, 0.30, 0.50 and 1.0 pC N^{-1} respectively.

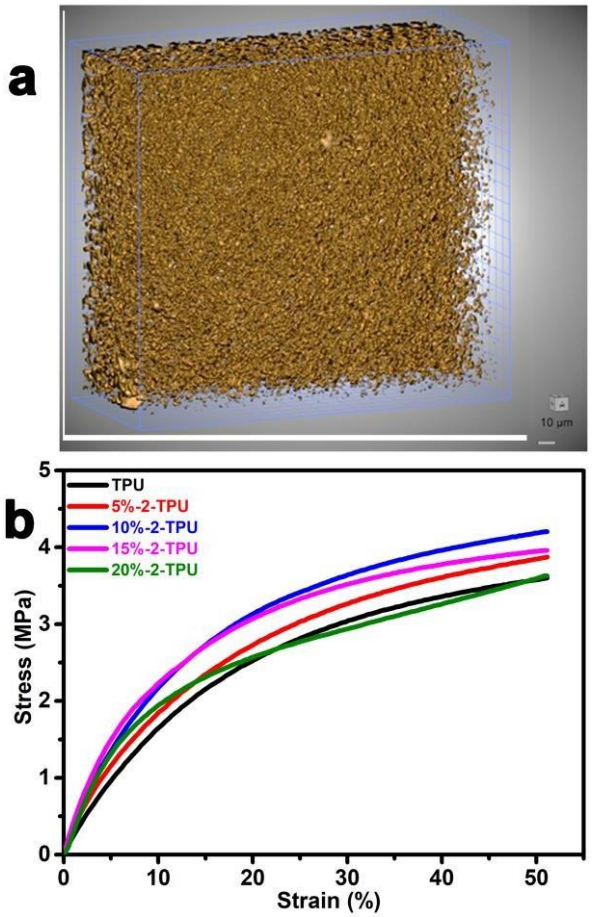

Figure 5.5 *(a) X-ray 3D-microtomography image of the 15 wt % **2**-TPU composite film. (b) Stress vs. Strain profile of neat TPU and all the **2**-TPU composite devices.*

5.3.4 Mechanical energy harvesting outputs of 2-TPU composite devices:

After establishing their structural integrity, their utility for the piezoelectric energy harvesting applications was probed. The device structures for these measurements were fabricated by placing Cu-adhesive tapes on either sides of the films and attaching Cu-wires on to their metal contacts. A final layer of polydimethylsiloxane (PDMS) was provided to complete the device architecture. The PDMS serves as a protecting layer to minimize the disturbances developed by the static charges during the measurement process. The output piezoelectric performances were obtained using a custom-made impact machine and the signals were collected using an oscilloscope. The peak-to-peak open circuit voltage (V_{PP}) for all the devices were recorded at a frequency of 9 Hz with an external load of 14.15 N. The V_{PP} values of 5.8, 15.4, 20.0, and 7.6 V were measured for the 5, 10, 15, and 20 wt % **2**-TPU composite devices, respectively

(Figure 5.6a and A21). The device made up of neat TPU was found to show a lower output voltage (V_{PP}) of only 200 mV, indicating the observed voltage output characteristics are clearly due to the embedded ferroelectric crystallites (of **2**) in the TPU matrix. The observed V_{PP} of 20 V for the 15 wt % **2**-TPU device is on the higher side of the values reported for polymer-organic salt composites.[40-41] Furthermore, the output peak-to-peak currents (I_{PP}) were calculated by attaching a 4.7 MΩ resistor across the devices and measuring the voltage drop. The calculated I_{PP} were found to be 0.9, 2.8, 4.0 and 1.4 µA for 5, 10, 15, and 20 wt % **2**-TPU composite devices, respectively (Figures A22-A23).

Both the V_{PP} and I_{PP} profiles show an increasing trend with an increase in the content of **2** up to 15 wt %. A further rise in the loading to 20 wt % results in the reduction of the V_{PP} and I_{PP} values (Figure A24). This can be attributed to the higher agglomeration of particles in the polymer matrix at the 20 wt % **2**-TPU film as observed from the tomography images.[45-46] A maximum current density of 1.1 µA cm^{-2} was computed for the 15 wt % **2**-TPU composite device (Figure 6.6b). The power density of the 15 wt % **2**-TPU composite device was calculated as a function of four (12.09, 12.73, 13.37 and 14. 15 N) different external loads and the maximum power density was found to be 21.1 µW cm^{-2} with 14.15 N external force (Figure6.6b and A25). To the best of our knowledge, the observed current, current density and powerdensity values are the highest among the organic composite energy harvesters known so far (Table A5.6). To check the feasibility of these devices for practical use, their output voltages were examined under different external resistances.[47] For each device, the voltage drop was measured across different load resistances starting from 0.1 MΩ to 44 MΩ. The output voltages were found to approach the open circuit V_{PP} with the increase in load resistance up to 10 MΩ and attains saturation for higher load-resistance values (Figure A26). Subsequently, the voltages generated from the best performing 15 wt % **2**-TPU composite device was utilized for charging a capacitor after rectification, using a four-diode full-wave rectifier circuit (Figure 7.7a). The voltages generated, by applying an external force of 14.2 N and a frequency of 9 Hz, were employed to charge a 100 µF capacitor. The maximum charging point of the capacitorwas reached within 30 s with a stored voltage of 1.56 V (Figure A27). The apparent differencein the voltage stored in the capacitor and the observed V_{PP} could presumably be due to the voltage lost in rectifying the diodes and leakage of the energy stored in the capacitor. The maximum stored energy (E) and calculated charge (Q) in the 100 µF.

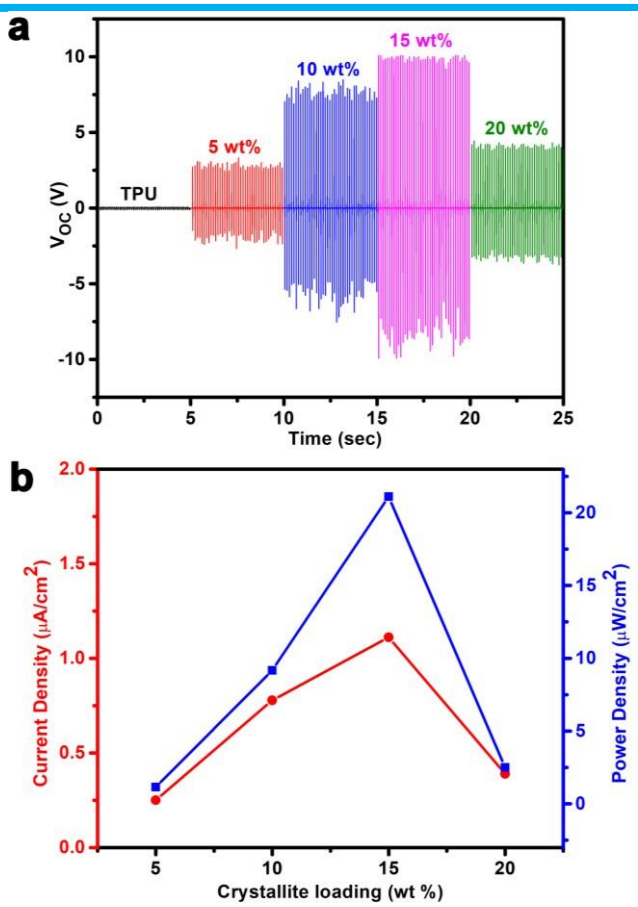

Figure 6.6 *(a) Measured V_{PP} profile for neat TPU and all the **2**-TPU composite devices. (b) Comparative current density (CD) and power density (PD) values of **2**-TPU composite devices. The solid curves tracing the points are guide to the eye.*

capacitor was found to be 121.6 µJ and 156 µC, respectively (Figure 7.7b). The energy conversion efficiency is the ratio of output electrical energy and the input mechanical energy.[48] The calculated energy conversion efficiency ($E_{\%}$) for compound **2** is 0.23% using the energy conversion efficiency equation and detailed calculation is given in the supporting information.

(Energy conversion efficiency, $E_{\%} = \frac{E_e}{E_m} \times 100$).

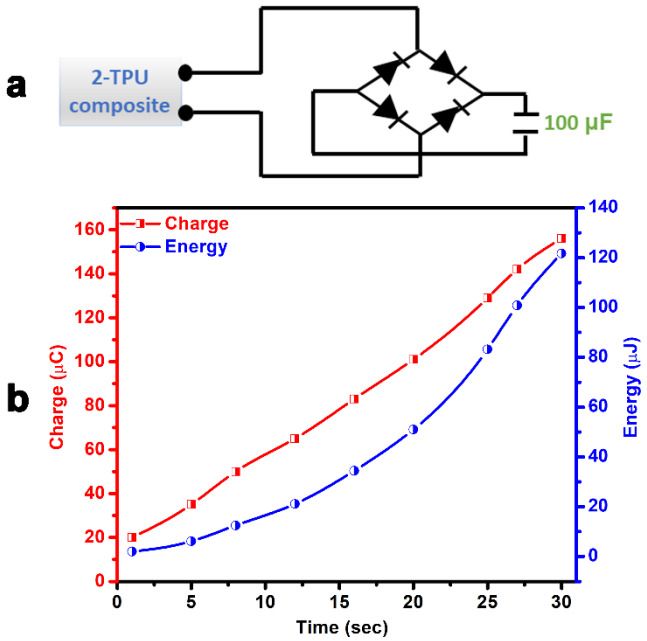

Figure 7.7: *(a) The diagram depicting the four-diode full-wave rectifier circuit. (b) Charge and energy accumulated in a 100 µF capacitor using the 15 wt % **2**-TPU composite device in 30 seconds. The solid curves tracing the points are guide to the eye.*

5.4 Conclusion

In summary, a two-component ammonium salt, **2**, containing bulky benzyl groups and BF_4^- anions has been prepared and studied for its ferroelectric properties. The asymmetry in its crystal structure originates from the combination heteroleptic mixed benzyl substituents within ammonium cation and the tetrahedral anions. The *P-E* hysteresis loop measurements on **2** gave a P_r value of 14.44 µC cm^{-2}. The high polarization value in **2** is attributed to its stable charge-separated structure and their long-range order assisted by the non-classical C-H···F and C-H···Br interactions. Furthermore, polymer composites comprising TPU and **2** in varied amounts (5, 10, 15, 20 wt %) were prepared and examined for piezoelectric energy harvesting application. A high output peak to peak voltage of 20 V was recorded for the champion device containing 15 wt % **2**-TPU. The calculated current, current density and power density values of the 15 wt % **2**-TPU composite were the highest reported for any polymer-organic composite mechanical energy harvester device. The practical utility of this device was tested by charging a 100 µF capacitor, which attains its maximum charging point within 30 s. These outcomes serve as a significant milestone in the development less-toxic all-organic composite materials for wearable electronics.

References

[1] O. Ellabban, H. Abu-Rub, F. Blaabjerg, *Renewable Sustainable Energy Rev.* **2011**, *15*, 1513-1524.

[2] T. R. Ray, J. Choi, A. J. Bandodkar, S. Krishnan, P. Gutruf, L. Tian, R. Ghaffari, J. A. Rogers, *Chem. reviews* **2019**, *119*, 5461-5533.

[3] Owusu, P. A.; Asumadu-Sarkodie, S. *Cogent Eng.* **2016**, *3*

[4] C. Bowen, H. Kim, P. Weaver, S. Dunn, *Energy Environ Sci.* **2014**, *7*, 25-44.

[5] F. Invernizzi, S. Dulio, M. Patrini, G. Guizzetti, P. Mustarelli, *Chem. Soc. Reviews* **2016**, *45*, 5455-5473.

[6] X. Yin, T. Wan, X. Deng, Y. Xie, C. Gao, C. Zhong, Z. Xu, C. Pan, G. Chen, W.-Y. Wong, *Chem. Eng. J.* **2021**, *405*, 126692.

[7] V. Jella, S. Ippili, J.-H. Eom, S. Pammi, J.-S. Jung, V.-D. Tran, V. H. Nguyen, A. Kirakosyan, S. Yun, D. Kim, *Nano Energy* **2019**, *57*, 74-93.

[8] W. Li, Z. Wang, F. Deschler, S. Gao, R. H. Friend, A. K. Cheetham, *Nature Reviews Mater.* **2017**, *2*, 1-18.

[9] S. Das, J. Appenzeller, *Nano lett.* **2011**, *11*, 4003-4007.

[10] Scott, J. F. *Science.* **2007**, *315*, 954–959.

[11] Li, H.; Bowen, C. R.; Yang, Y. *Adv. Funct. Mater.* **2021**, *31*, 1–23.[12] L. Huang, S. Lin, Z. Xu, H. Zhou, J. Duan, B. Hu, J. Zhou, *Adv. Mater.* **2020**, *32*, 1902034.

[13] Y. Zhang, W. Jie, P. Chen, W. Liu, J. Hao, *Adv. Mater.* **2018**, *30*, 1707007.

[14] J.-H. Lee, J. Kim, T. Y. Kim, M. S. Al Hossain, S.-W. Kim, J. H. Kim, *J. Mater. Chem. A* **2016**, *4*, 7983-7999.

[15] Y. M. You, W. Q. Liao, D. Zhao, H. Y. Ye, Y. Zhang, Q. Zhou, X. Niu, J. Wang, P. F. Li, D. W. Fu, Z. Wang, S. Gao, K. Yang, J. M. Liu, J. Li, Y. Yan, R. G. Xiong, *Science.* **2017**, *357*, 306–309.

[16] W. Zhang, R.-G. Xiong, *Chem. Rev.* **2012**, *112*, 1163-1195.

[17] T. Hang, W. Zhang, H.-Y. Ye, R.-G. Xiong, *Chem. Soc. Rev.* **2011**, *40*, 3577-3598.

[18] X. Ren, H. Fan, Y. Zhao, Z. Liu, *ACS Appl. Mater. Interfaces* **2016**, *8*, 26190-26197.

[19] R. Ding, X. Zhang, G. Chen, H. Wang, R. Kishor, J. Xiao, F. Gao,K. Zeng, X. Chen, X. W. Sun, *Nano Energy* **2017**, *37*, 126-135.

[20] W. Forrester, R. Hinde, *Nature* **1945**, *156*, 177-177.

[21] B. Jaffe, R. Roth, S. Marzullo, *J. Appl. Phys.* **1954**, *25*, 809-810.

[22] K. Nassau, H. J. Levinstein, G. M. Loiacono, *J. Phys. Chem. Solids* **1966**, *27*, 983-988.

[23] X. Wang, J. Song, J. Liu, Z. L. Wang, *Science* **2007**, *316*, 102-105.

[24] R. Ding, H. Liu, X. Zhang, J. Xiao, R. Kishor, H. Sun, B. Zhu, G. Chen, F. Gao, X. Feng, *Adv. Func. Mater.* **2016**, *26*, 7708-7716.

[25] X. Lu, H. Qu, M. Skorobogatiy, *ACS nano* **2017**, *11*, 2103-2114.

[26] F. Ram, T. Ambone, A. Sharma, R. Murugesan, D. Kajale, V. Borkar, S. F. Ali, P. K. Balu, G. Kumaraswamy, K. Shanmuganathan, *J. Phys. Chem. C* **2018**, *122*, 16540-16549.

[27] S.-G. Yoon, I. Swathi, V. Jella, A.-M. Thomas, C. Yoon, J. S. Jung, *J. Mater. Chem. A* **2021**.

[28] S.-H. Park, H. B. Lee, S. M. Yeon, J. Park, N. K. Lee, *ACS Appl. Mater. Interfaces* **2016**, *8*, 24773-24781.

[29] R. A. Whiter, V. Narayan, S. Kar-Narayan, *Adv. Energy*

Mater. **2014**, *4*, 1400519.

[30] F. R. Fan, W. Tang, Z. L. Wang, *Adv. Mater.* **2016**, *28*, 4283-4305.

[31] C. Bowen, H. Kim, P. Weaver, S. Dunn, *Energy Environ. Sci.* **2014**, *7*, 25-44.

[32] R. A. Whiter, V. Narayan, S. Kar **–** Narayan, *Adv. Energy Mater.* **2014**, *4*, 1400519.

[33] R. Pandey, G. SB, S. Grover, S. K. Singh, A. Kadam, S. Ogale, U. V. Waghmare, V . R. Rao, D. Kabra, *ACS Energy Lett.* **2019**, *4*, 1004-1011.

[34] Z.-X. Zhang, H.-Y. Zhang, W. Zhang, X.-G. Chen, H. Wang, R.-G. Xiong, *J. Am. Chem. Soc.* **2020**, *142*, 17787-17794.

[35] H. Park, C. H, J.-H. Lee, *J. Mater. Chem. A* **2020**, *8*, 24353-24367.

[36] V. Jella, S. Ippili, S.-G. Yoon, *ACS Appl. Electron. Mater.* **2020**, *2*, 2579-2590.

[37] B. Saravanakumar, S. Soyoon, S.-J. Kim, *ACS Appl. Mater. Interfaces* **2014**, *6*, 13716-13723.

[38] S. Deswal, S. K. Singh, R. Pandey, P. Nasa, D. Kabra, B. Praveenkumar,S. Ogale, R. Boomishankar, *Chem. Mater.* **2020**, *32*, 8333-8341.

[39] S. Deswal, S. K. Singh, P. Rambabu, P. Kulkarni, G. Vaitheeswaran, B. Praveenkumar, S. Ogale, R. Boomishankar, *Chem. Mater.* **2019**, *31*, 4545-4552.

[40] T. Vijayakanth, A. K. Srivastava, F. Ram, P. Kulkarni, K. Shanmuganathan, B. Praveenkumar, R. Boomishankar, *Angew. Chem. Int. Ed.* **2018**, *130*, 9192-9196.

[41] T. Vijayakanth, F. Ram, B. Praveenkumar, K. Shanmuganathan, R. Boomishankar, *Chem. Mater.* **2019**, *31*, 5964-5972.

[42] C. Jelsch, K. Ejsmont, L. Huder, *IUCrJ* **2014**, *1*, 119-128.

[43] M. E. Lines, A. M. Glass, *Principles and applications of ferroelectrics and related materials*, Oxford university press, **2001**.

[44] Y. Yan, J. E. Zhou, D. Maurya, Y. U. Wang, S. Priya, *Nat. Commun.* **2016**, *7*, 1–10.

[45] R. Ding, H. Liu, X. Zhang, J. Xiao, R. Kishor, H. Sun, B. Zhu, G. Chen, F. Gao, X. Feng, *Adv. Funct. Mater.* **2016**, *26*, 7708-7716.

[46] S. Siddiqui, D.-I. Kim, E. Roh, T. Q. Trung, M. T. Nguyen, N.-E. Lee, *Nano Energy* **2016**, *30*, 434-442.

[47] Y. Su, C. Dagdeviren, R. Li, *Adv. Funct. Mater.* **2015**, *25*, 5320-5325.

[48] C. Covaci, A. Gontean, *Sensors* **2020**, *20*, 1–37.

[49] G. M. Sheldrick, *Acta Crystallogr. Sect. A* **2008**, *64*, 112-122.

[50] A. L. Spek, *Acta Crystallogr. Sect. D* **2009**, *65*, 148-155.

Appendix 5

Appendix 5

Table A5.1. X-ray Crystallographic data for **1** and **2**.

Parameters	**1**	**2**
Chemical formula	$C_{16}H_{19}NBr_2$	$C_{16}H_{19}BNF_4Br$
Formula weight	385.12	392.04
Temperature	100(2) K	120(2) K
Crystal system	Orthorhombic	Orthorhombic
Space group	P n m a	P n a 2 1
a (Å), b (Å)	10.8819(14), 6.8476(9)	19.567(3), 8.4154(12)
c (Å)	21.412(3).	10.2687(16).
α (°), β (°), γ(°)	90, 90, 90	90, 90, 90
V (Å^3); Z	1595.5(4); 4	1690.9(4); 4
ρ (calc.) mg m^{-3}	1.603	1.540
μ(Mo Kα) mm^{-1}	5.068	2.467
2θ max (°)	28.371	27.523
R(int)	0.0523	0.1050
Completeness	100.0 %	99.9 %
Data/ restraints/ parameters	2153 / 0 / 101	3853 / 1 / 211
GOF	1.068	1.046
R1 (all data)	0.0311	0.0852
wR2 (all data)	0.0587	0.1091
max.peak/hole (e.Å^{-3})	0.770/-0.497	1.056/-0.920

Table A5.2. X-ray Crystallographic bond lengths and bond angles table for **1**.

Bond Lenths (Å)		Bond Angles (°)	
Br(2)-C(26)	1.899(3)	C(1)-N(1)-C(1)#1	109.57(19)
N(1)-C(1)	1.499(2)	C(1)-N(1)-C(21)	110.80(13)
N(1)-C(1)#1	1.499(2)	C(1)#1-N(1)-C(21)	110.80(13)
N(1)-C(21)	1.527(3)	C(1)-N(1)-C(11)	110.20(13)
N(1)-C(11)	1.533(3)	C(1)#1-N(1)-C(13)	110.20(13)
C(1)-H(1A)	0.9800	C(21)-N(1)-C(11)	105.19(18)
C(1)-H(1B)	0.9800	N(1)-C(1)-H(1A)	109.5
C(1)-H(1C)	0.9800	N(1)-C(1)-H(1B)	109.5
C(16)-H(16)	0.9500	H(1A)-C(1)-H(1B)	109.5
C(22)-C(23)	1.507(4)	H(1A)-C(1)-H(1C)	109.5
		H(1B)-C(1)-H(1C)	109.5

Table A5.3. X-ray Crystallographic bond lengths and bond angles table for **2**.

Bond Lenths (Å)		Bond Angles (°)	
Br(1)-C(25)	1.900(7)	F(1)-B(1)-F(4)	109.9(7)
B(1)-F(1)	1.379(10)	F(1)-B(1)-F(3)	109.5(6)
B(1)-F(4)	1.383(9)	F(4)-B(1)-F(3)	110.8(7)
B(1)-F(3)	1.390(11)	F(1)-B(1)-F(2)	109.3(7)
B(1)-F(2)	1.405(10)	F(4)-B(1)-F(2)	109.1(6)
N(1)-C(2)	1.484(9)	F(3)-B(1)-F(2)	108.2(7)
N(1)-C(1)	1.496(10)	C(2)-N(1)-C(1)	109.3(6)
N(1)-C(11)	1.529(9)	C(2)-N(1)-C(11)	109.4(6)
N(1)-C(21)	1.534(10)	C(1)-N(1)-C(11)	110.2(6)
C(1)-H(1A)	0.9600	C(2)-N(1)-C(21)	110.2(6)
C(1)-H(1B)	0.9600	C(1)-N(1)-C(21)	111.8(6)
C(1)-H(1C)	0.9600	N(1)-C(1)-H(1A)	109.5
C(2)-H(2A)	0.9600	N(1)-C(1)-H(1B)	109.5
C(2)-H(2B)	0.9600	N(1)-C(1)-H(1C)	109.5
C(2)-H(2C)	0.9600	N(1)-C(2)-H(2A)	109.5
C(10)-H(11A)	0.9700	N(1)-C(2)-H(2B)	109.5
C(10)-H(11B)	0.9700	N(1)-C(2)-H(2C)	109.5
C(15)-C(17)	1.395(12)	N(1)-C(11)-H(11A)	108.4
C(15)-H(16)	0.9300	N(1)-C(11)-H(11B)	108.4
		N(1)-C(21)-H(21B)	108.6

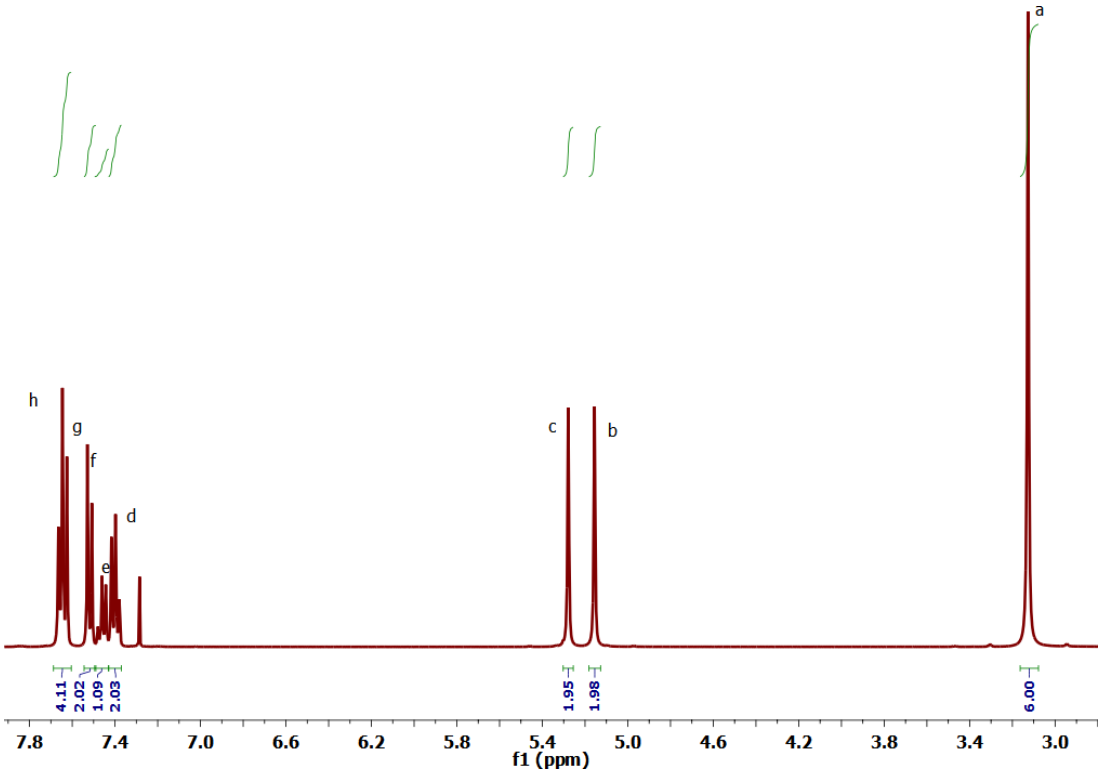

Figure A1*: ^{1}H NMR spectrum of **2** in $CDCl_3$ solvent. **1** and **2** showed same ^{1}H signals as the parent (ammonium) cation is same for both of them.*

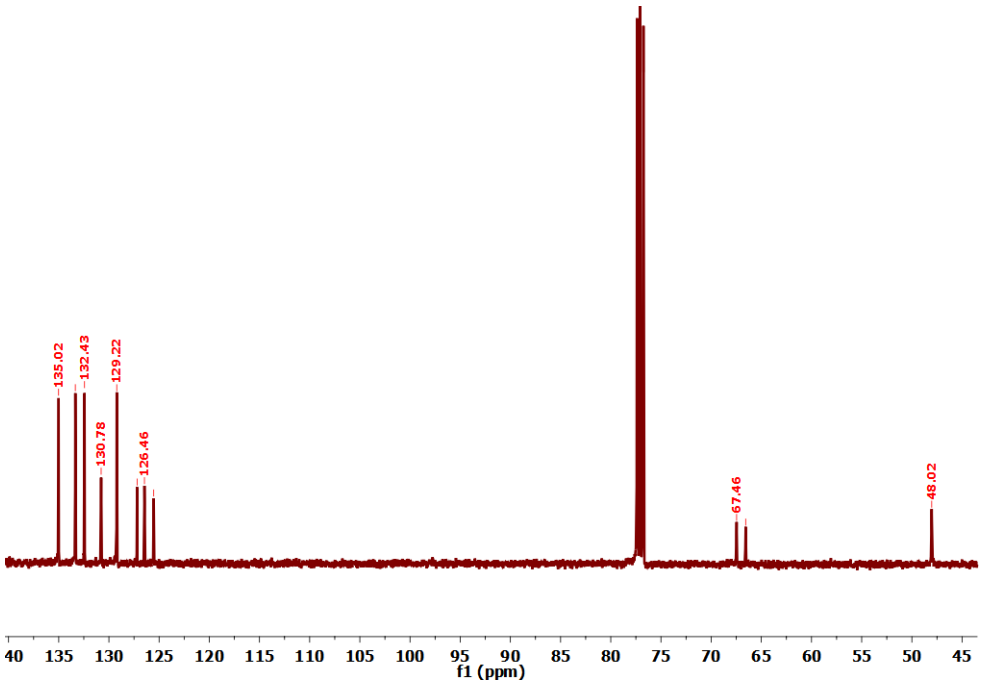

Figure A2: ^{13}C NMR spectrum of **2** in $CDCl_3$.

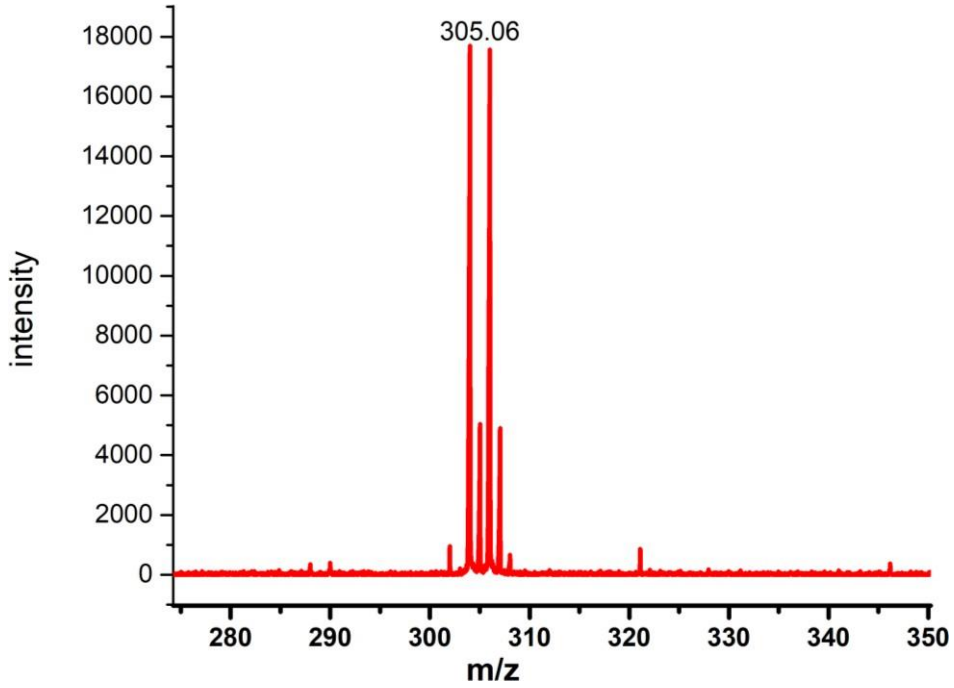

Figure A3: MALDI-TOF spectra of **2** in Methanol. **1** and **2** showed same m/z values as the parent (ammonium) cation is same for both of them.

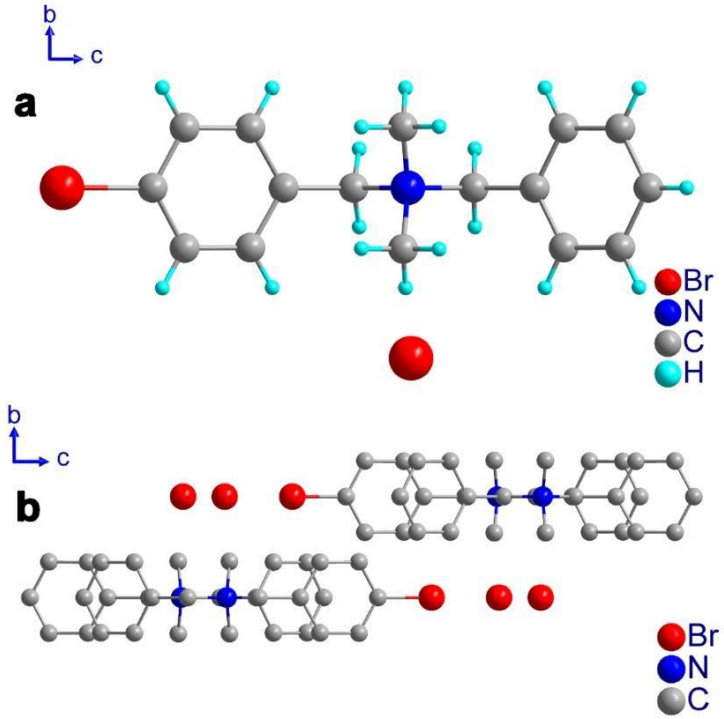

Figure A4: (a) Molecular structure of **1**. (b) Packing diagram of **1** along a-axis.

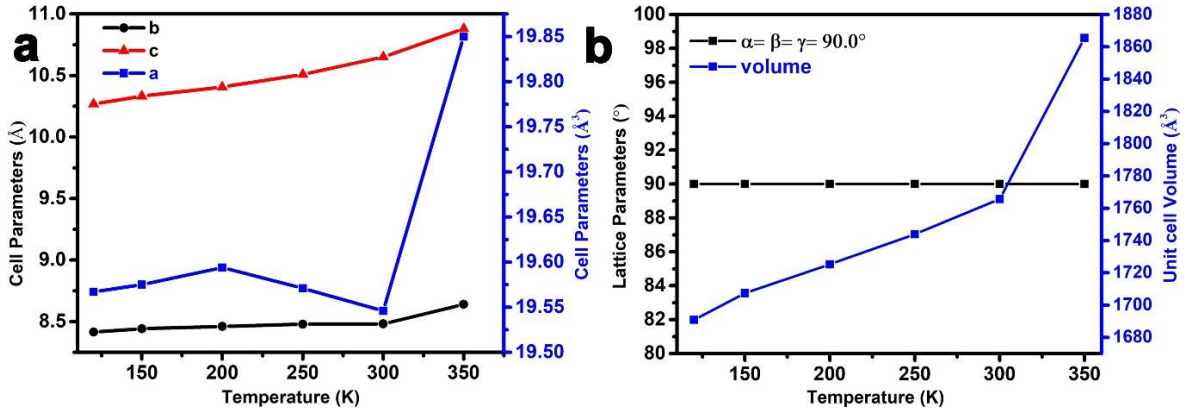

Figure A5: Variable temperature single crystal X-ray diffraction data of **2**.

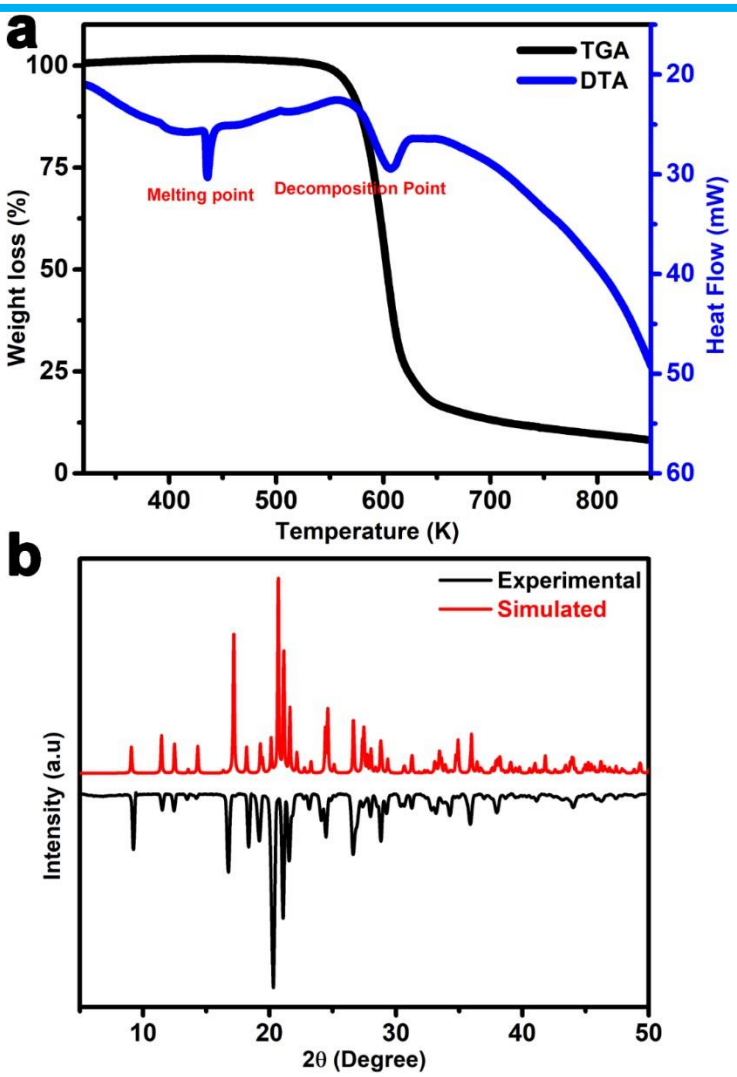

Figure A6: The (a) TGA/DTA and (b) PXRD profiles of **2**.

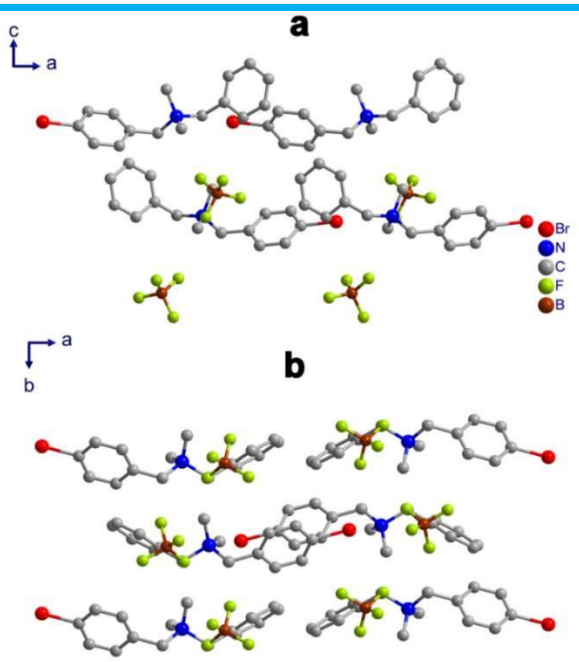

Figure A7: Packing diagram of **2** along (a) *b*-axis and (b) *c*-axis.

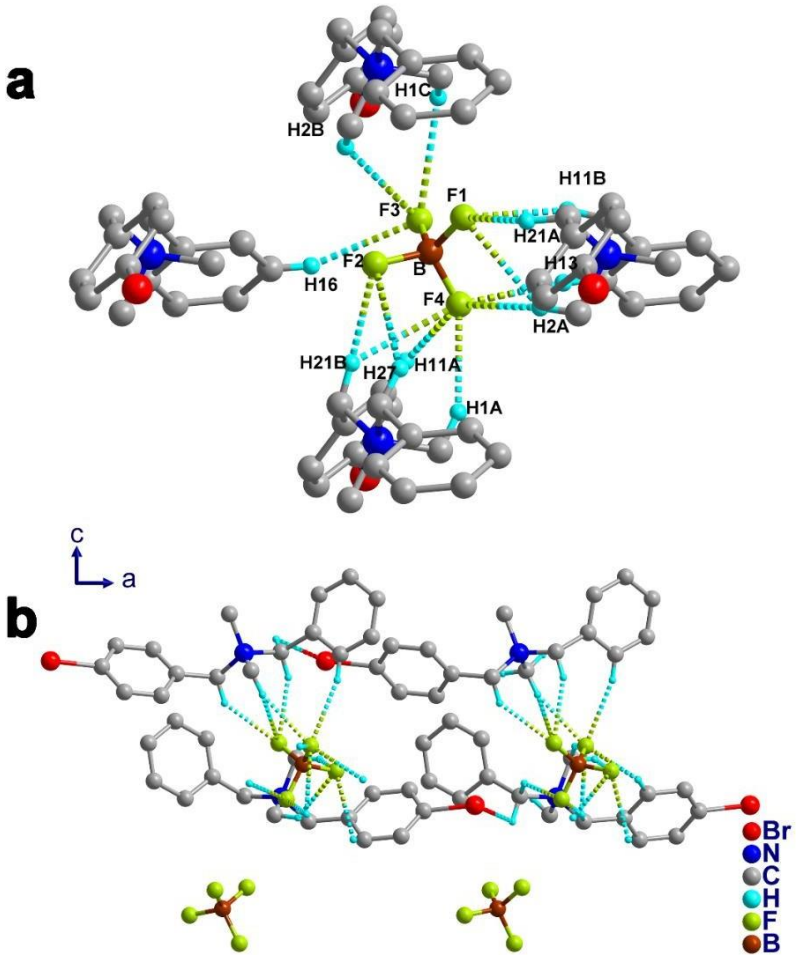

Figure A8: Non-classical C-H···F hydrogen bonding interactions in **2** at 120 K.

Table S4. X-ray crystallographic non-classical interactions for **2**.

D-H..A (1)	D-H (Å)	H…A (Å)	D-A (Å)	Angle (DHA)	Symmetry operations
C1-H1A…F4	0.979 (68)	2.433 (43)	3.348 (80)	155.56 (408)	1-X, 1-Y, 0.5+Z
C26-H27..F4	0.949 (70)	2.573 (52)	3.416 (88)	154.01 (444)	1-X, 1-Y, 0.5+Z
C21-H21B..F4	0.990 (68)	2.746 (42)	3.500 (81)	133.27 (416)	1-X, 1-Y, 0.5+Z
C2-H2A…F4	0.979 (73)	2.512 (51)	3.424 (89)	154.47 (442)	1-X, 1-Y, 0.5+Z
C13-H13…F4	0.950 (82)	2.575 (44)	3.480 (92)	163.37 (500)	1-X, 1-Y, 0.5+Z
C16-H16…F3	0.950 (82)	2.697 (51)	3.570 (105)	152.86 (576)	0.5-X, -0.5+Y,0.5+Z 0.5-
C2-H2B…F3	0.958(78)	2.633 (48)	3.416 (93)	136.85 (435)	X, -0.5+Y,0.5+Z
C1-H1C…F3	0.960 (78)	2.827 (51)	3.563 (92)	132.76 (418)	1-X, 1-Y, 0.5+Z
C21-H21B…F2	0.970 (76)	2.397 (42))	3.350 (87)	167.17 (46)	X, -1+Y, Z
C11-H11A…F2	0.969 (69)	2.749 (42)	3.520 (81)	136.88 (415)	X, -1+Y, Z
C2-H2A…F1	0.960 (73)	2.782 (47)	3.509 (89)	139.03 (451)	0.5-X, -0.5+Y, 0.5+Z
C21-H21A..F1	0.969 (82)	2.400 (56)	3.222 (97)	142.26 (494)	0.5-X, -0.5+Y, 0.5+Z
C11-H11B…F1	0.963 (72)	2.375 (52)	3.257 (88)	151.06 (443)	0.5-X, -0.5+Y, 0.5+Z
C11-H11A…Br	0.969 (69)	3.029 (7)	3.576 (70)	117.02 (407)	0.5-X, -0.5+Y, 0.5+Z

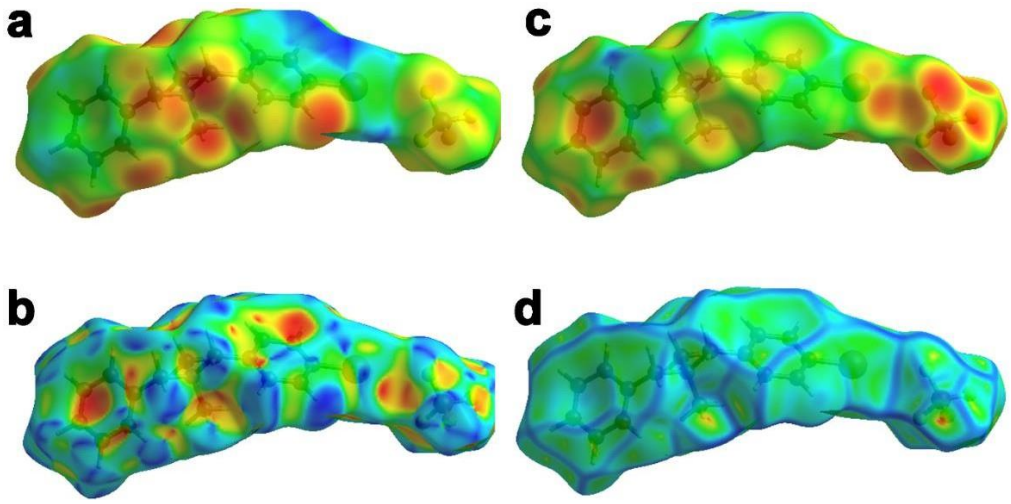

Figure A9: The 3D colour mapping derived from the Hirshfeld surface analysis of **2** showing (a) d_i, (b) d_e, (c) shape index, (d) curvedness.

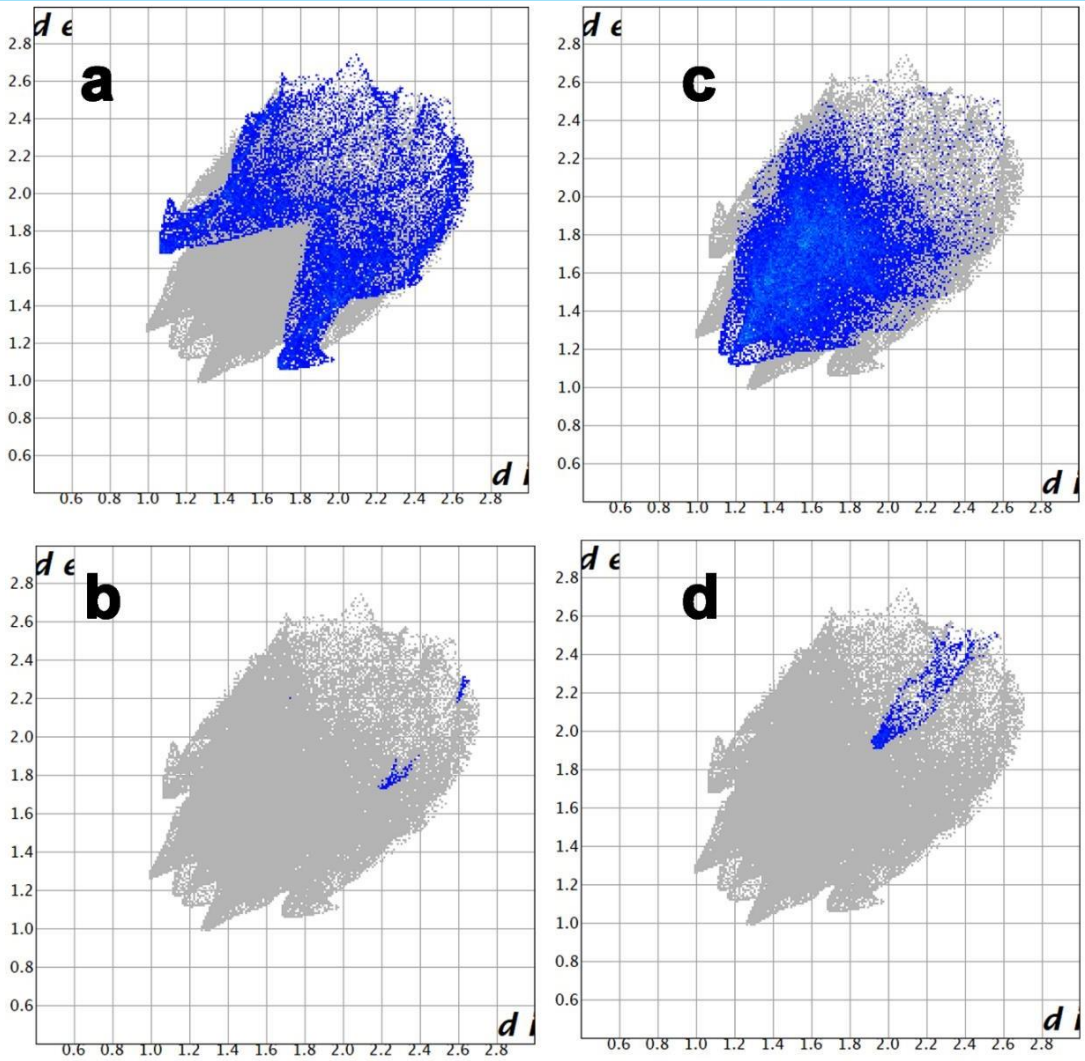

Figure A10. 2D fingerprint (d_e vs d_i) plots of **2** showing the percentages of (a) (C···H/H···C 16.3%) (b) (C···F/F···C 0.1 %), (c) (H···H 29.3%), and (d) (C···C 0.8 %).

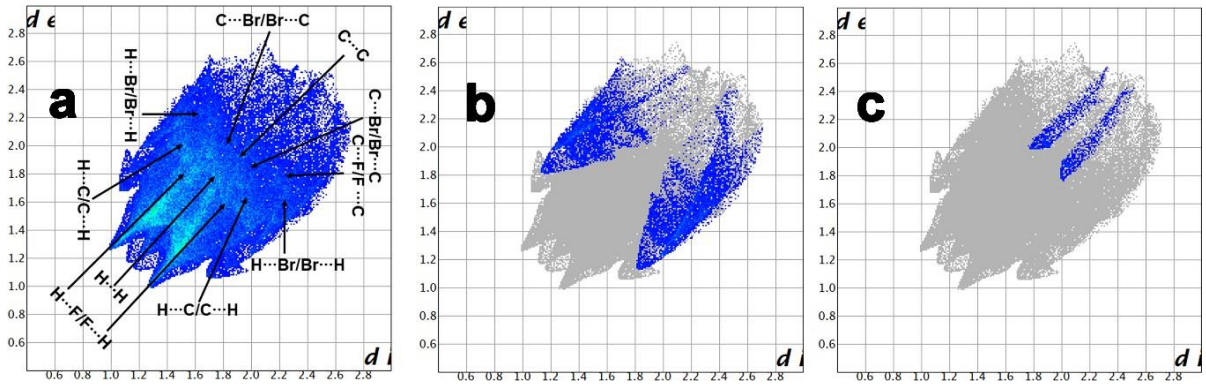

Figure A11. 2D fingerprint (d_e vs d_i) plots of **2** showing (a) all interactions. Percentages of (b) (H···Br/Br···H 10.8 %) and (c) (C···Br/Br···C 1.3%) interactions.

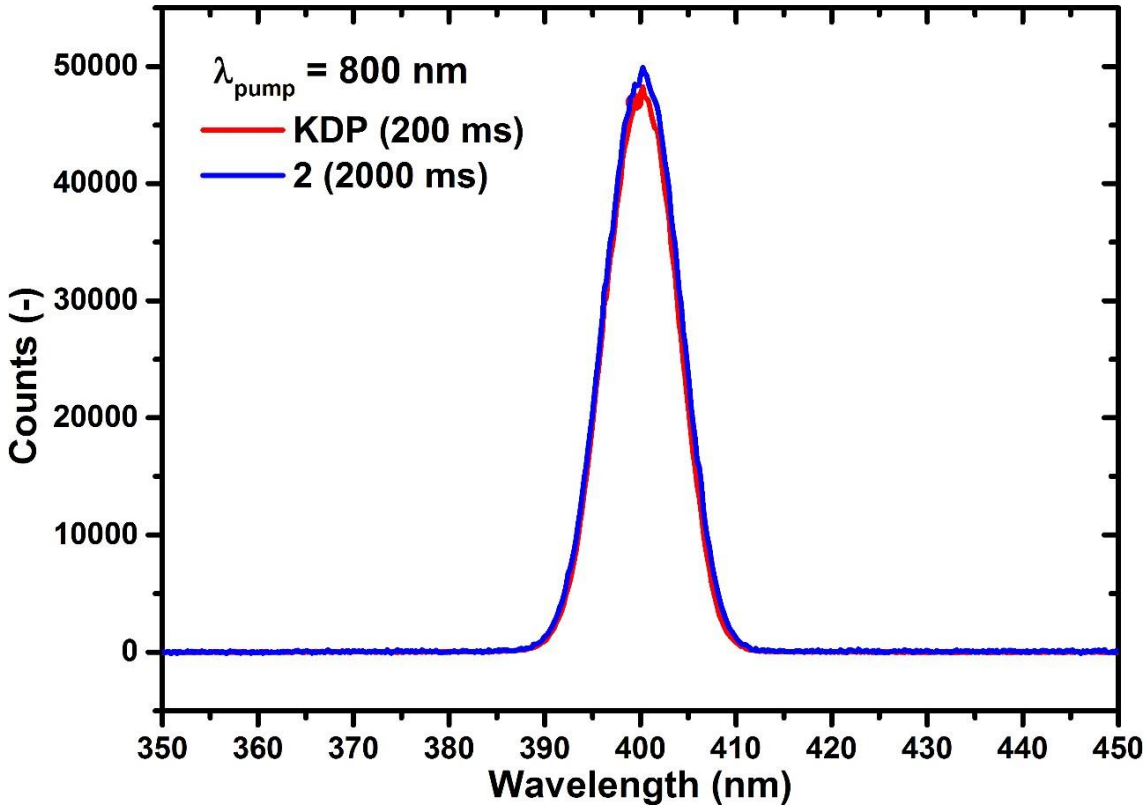

Figure A12: Spectra of second-harmonic generation (SHG) signal of **2** and its comparison with KDP.

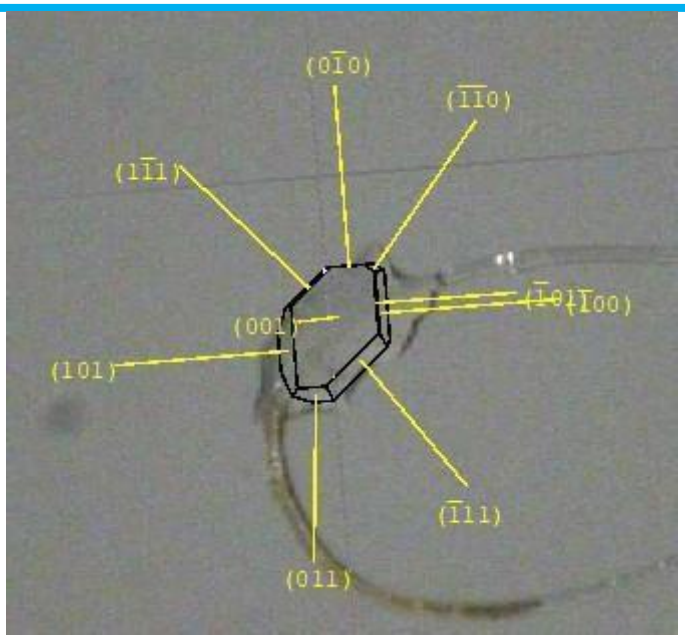

Figure A13: Face indexing on the crystal of **2** representing [0,0, 1] direction on which ferroelectric measurement was performed.

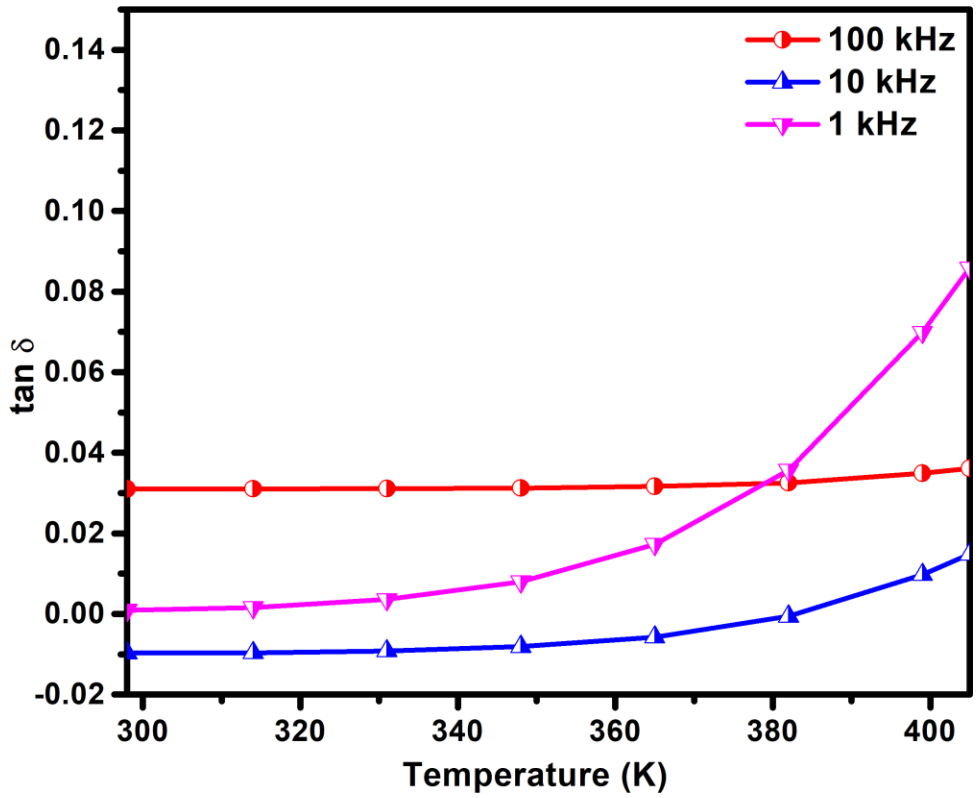

Figure A14: Temperature dependant dielectric loss plot of **2**.

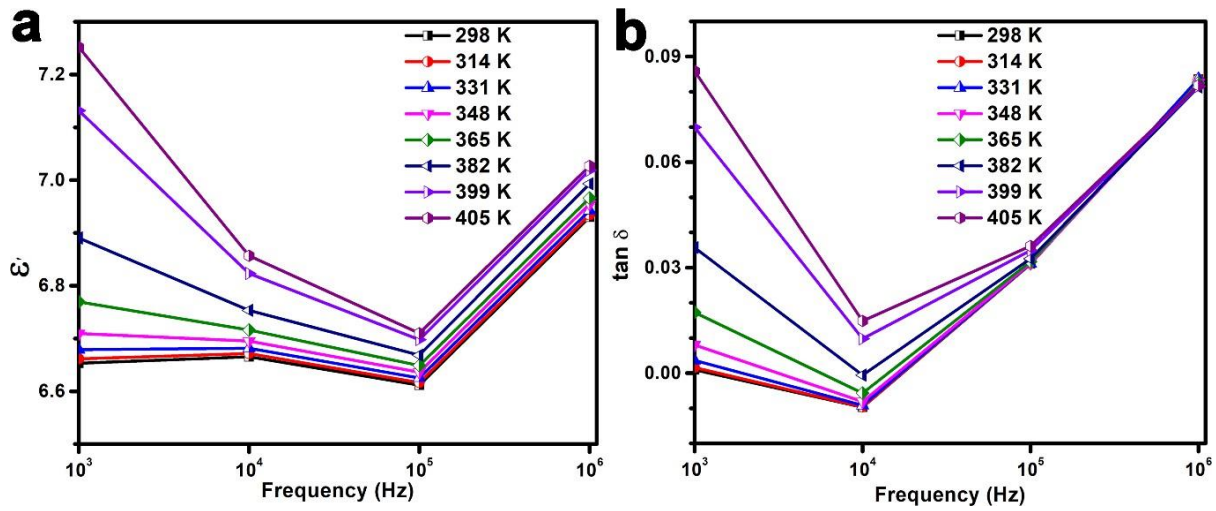

Figure A15: Frequency dependant (a) dielectric permittivity and (b) dielectric loss plots of **2**.

Appendix 5

Figure A16: Photograph of the displayed d_{33} measurement details of **2** in piezometer.

Table S5. Detailed weight percentage calculations for **2**-TPU composites.

Composite Materials (%)	2 (in mg)	TPU (in mg)
5	22.36	425
10	47.22	425
15	75.00	425
20	106.25	425

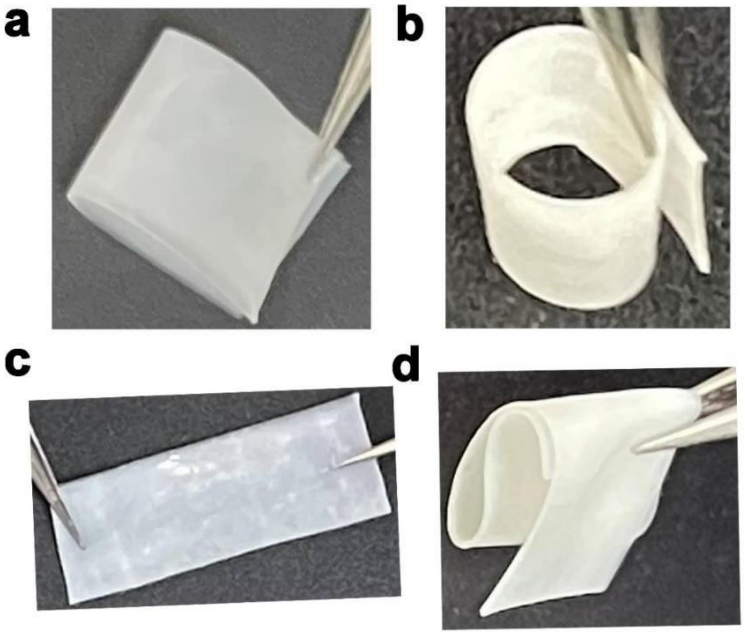

Figure A17: A representative **2**-TPU composite film showing (a) bending, (b) folding, (c) stretching, and (d) two-fold bending operations.

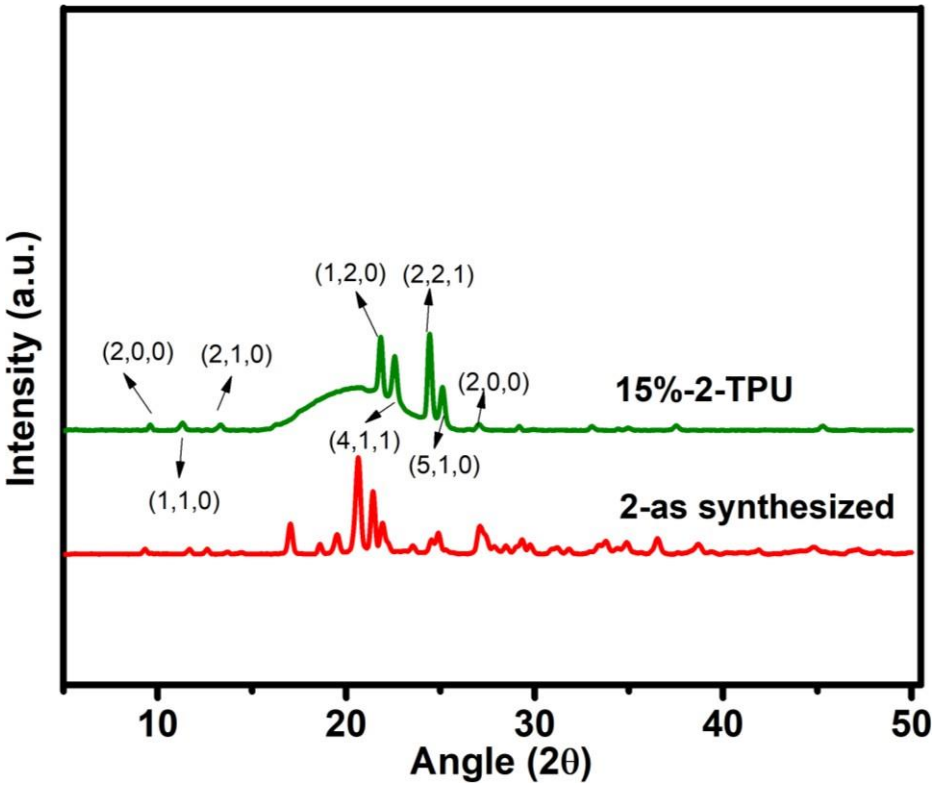

Figure A18: PXRD profiles of **2** and 15 wt % **2**-TPU along with the identified *hkl* peaks.

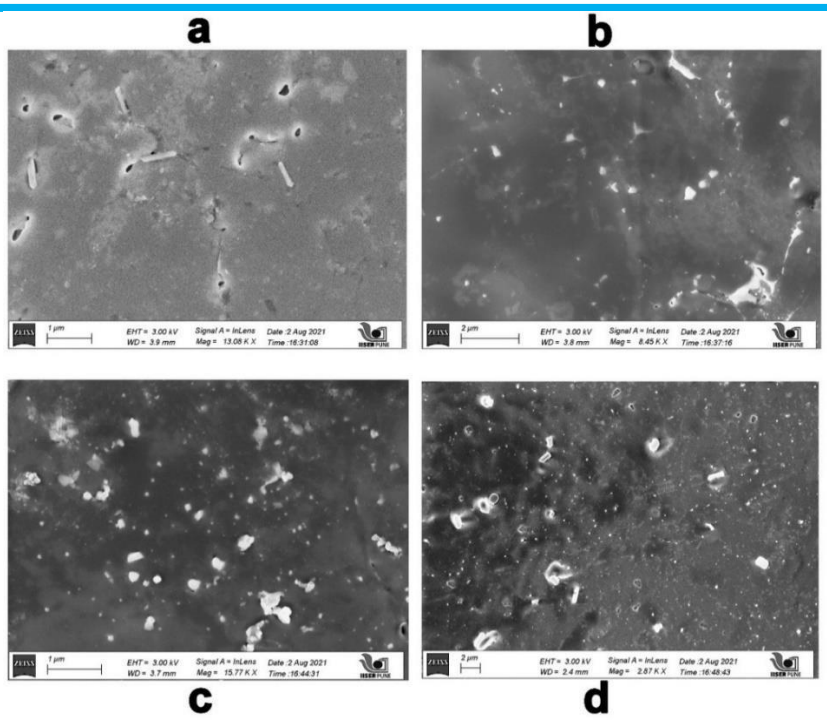

Figure A19: SEM images of **2**-TPU composites, a, b, c, and d correspond to 5, 10, 15 and 20 wt % **2**-TPU composites, respectively.

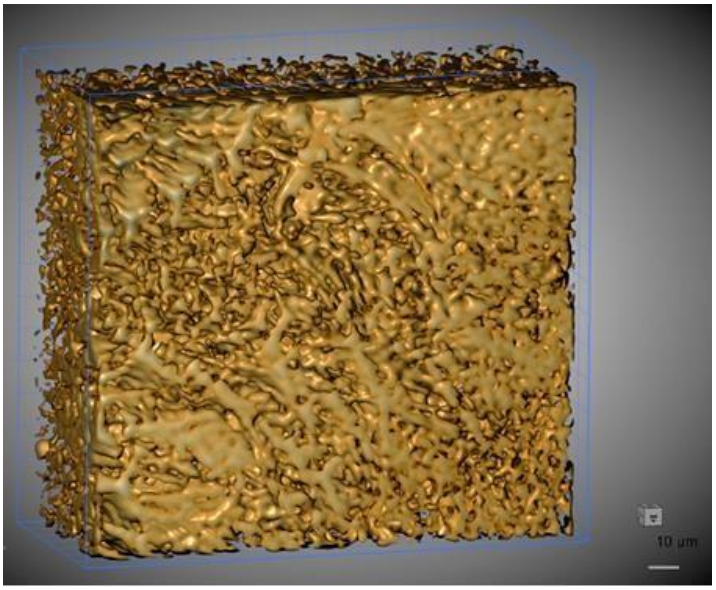

Figure A20: The X-ray 3D-microtomography image of the 20 wt % **2**-TPU composite film showing the agglomeration of the crystallites of **2**.

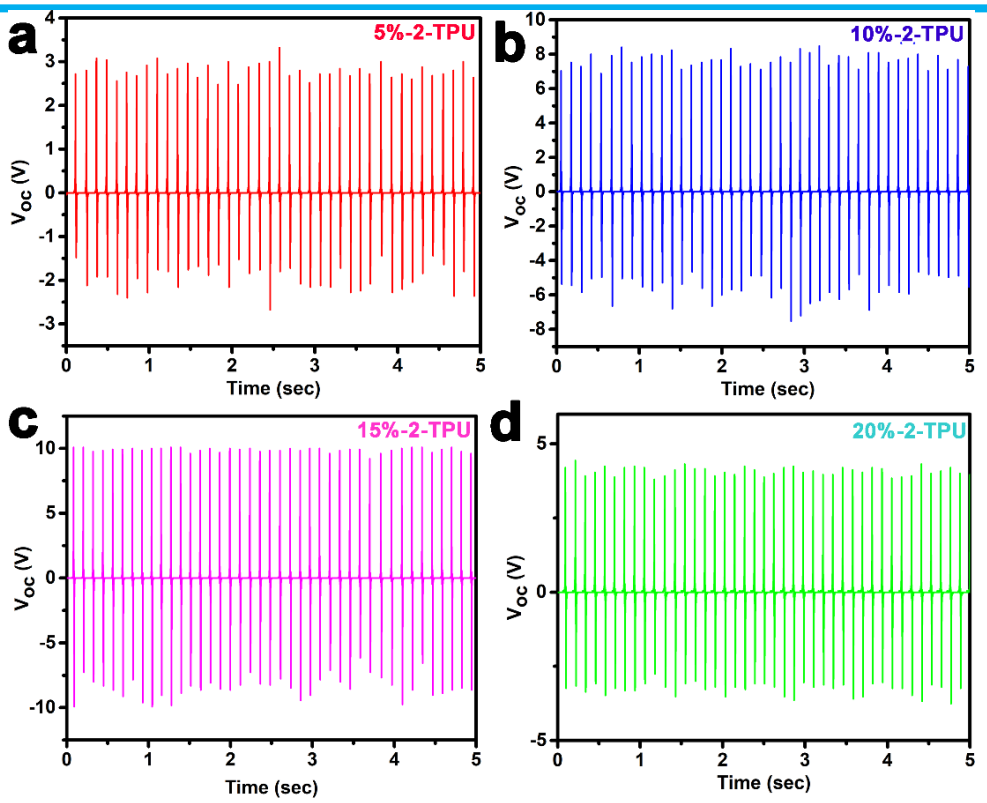

Figure A21: Output voltage profiles of all **2**-TPU composite films**.**

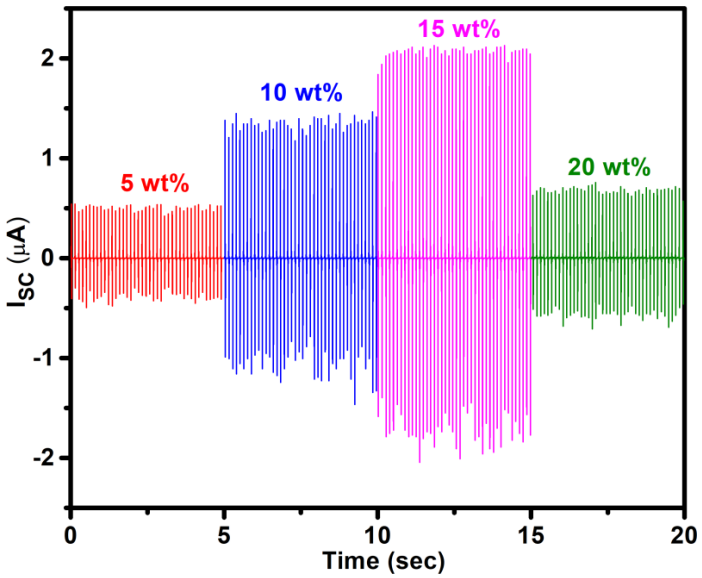

Figure A22: Comparative calculated output current profiles of **2**-TPU composite devices.

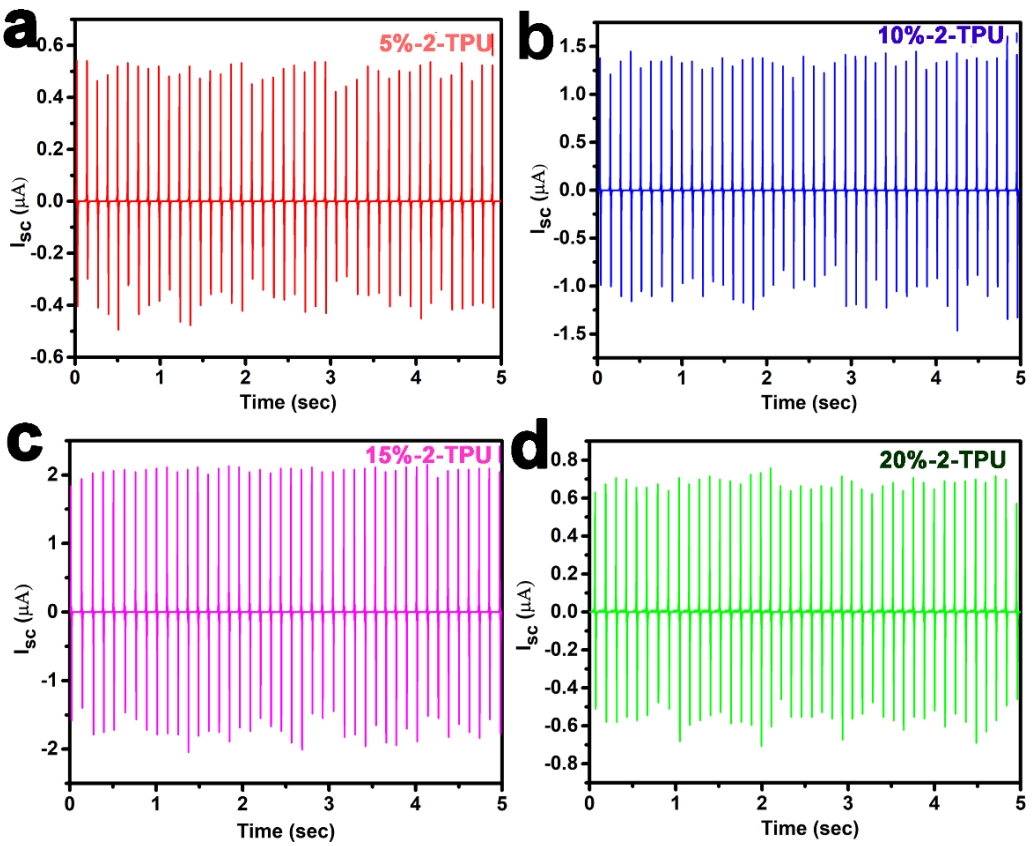

Figure A23: The calculated output currents of all **2**-TPU composite films.

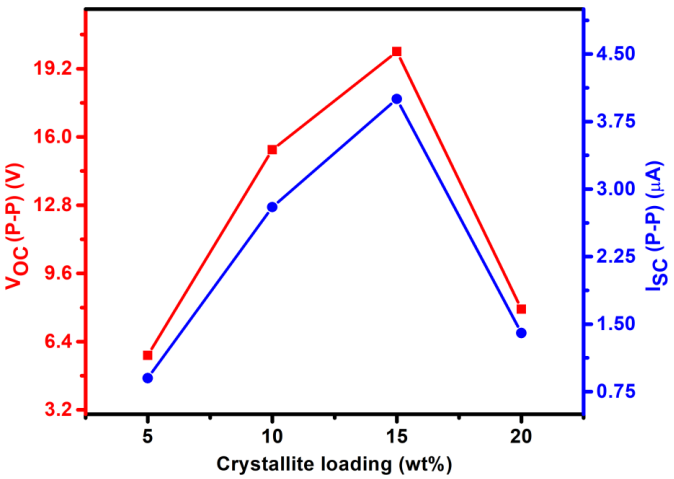

Figure A24: Comparative diagram showing the observed trends in V_{OC} and I_{SC} values of **2**-TPU composite devices.

Table A5.6. Comparison of the mechanical energy harvesting output performance 2-TPU with other organic composite energy harvesters

Organic Salt /Polymer	V_{PP} (V)	I_{PP} (μA)	**current density** ($\mu A\ cm^{-2}$)	**power density** ($\mu W\ cm^{-3}$)	**Force Freq.**	**Area** (cm^2)	$E_{\%}$	**Ref.**
DPDP·PF_6/PDMS	8.5	0.28	0.28	1.74	15 N 10 Hz	1.3 x 3	-	1
DPDP·BF_4/TPU	8.95	0.89	0.23	10.16	22 N 8 Hz	1.3 x 3	-	2
TPAP·BF_4/TPU	7.37	0.61	0.16	4.77	22 N 8 Hz	1.3 x 3	-	2
TIAP·BF_4/TPU	4.75	0.41	0.11	2.16	22 N 8 Hz	1.3 x 3	-	2
DPDP·PF_6/TPU	6.73	0.47	0.12	2.83	22 N 8 Hz	1.3 x 3	-	2
3NA/PCL	7	0.07	0.0175	0.122	3 N 3 Hz	4	-	3
Boc-FF/PLLA	30	0.3	0.075	2.3	1.5 N 3 Hz	4.0	-	4
Boc-FF/PCL	22	-	-	-	1.5 N 3 Hz	4.0	-	4
Boc-FF/PMMA	8	-	-	-	1.5 N 3 Hz	4.0	-	4
2-TPU	20	4	1.1	21.1	14.4 N 9 Hz	1.2 × 3	0.27	This work

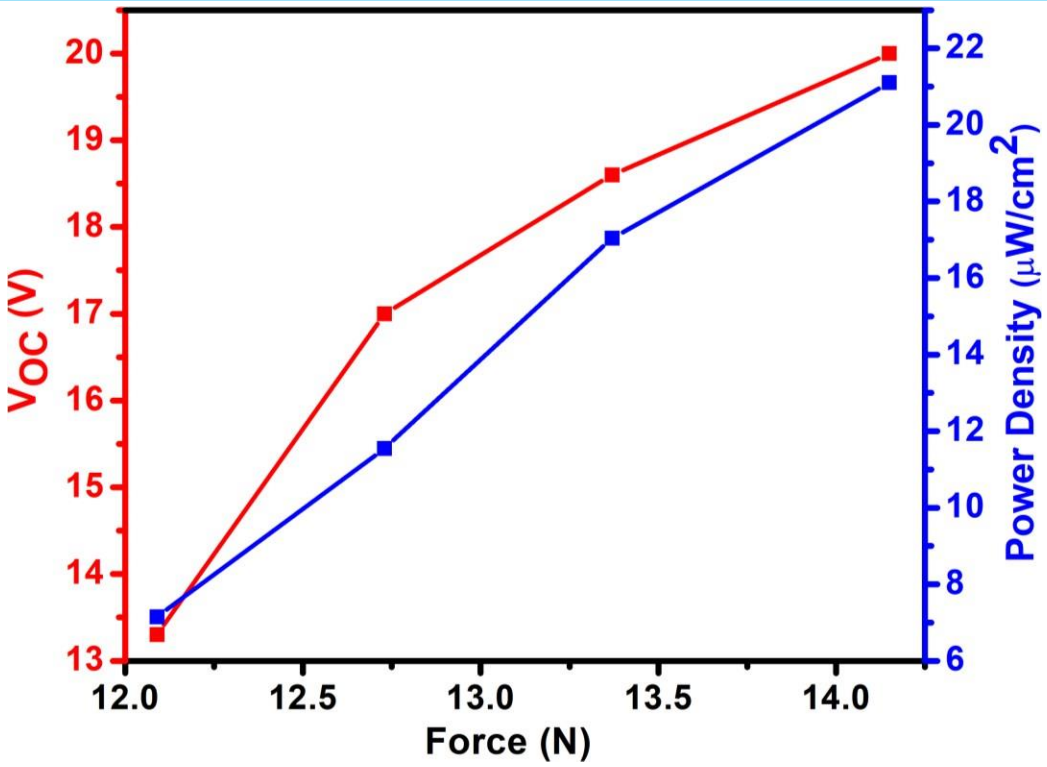

Figure A25: The voltage and power density plot of the 15 wt % **2**-TPU composite device as a function of four different external loads (12.09, 12.73, 13.37 and 14. 15 N).

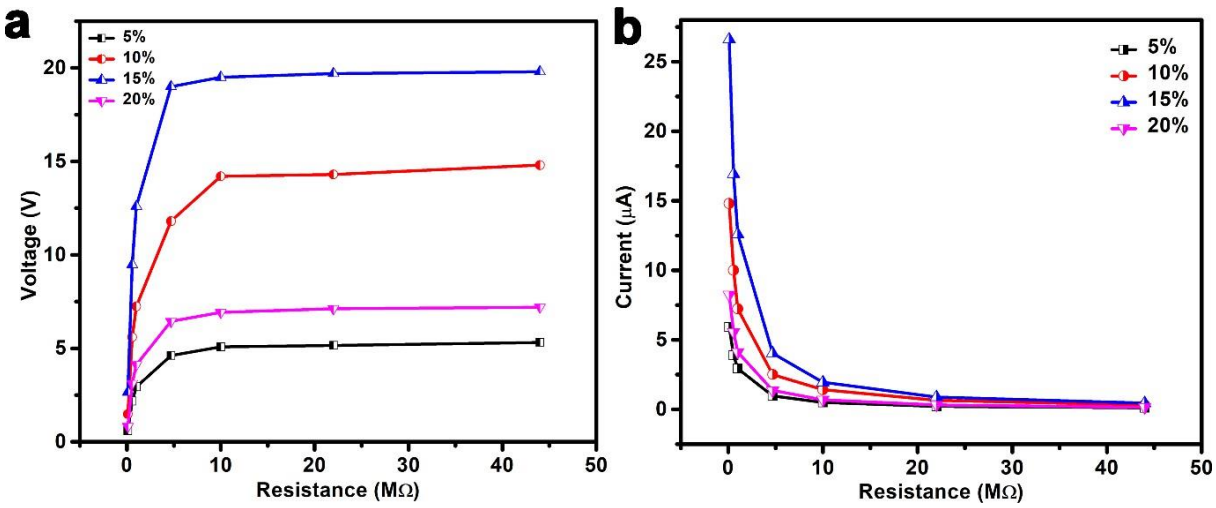

Figure A26: The comparative output (a) voltage and (b) current data for all the **2**-TPU composite devices under various load resistances.

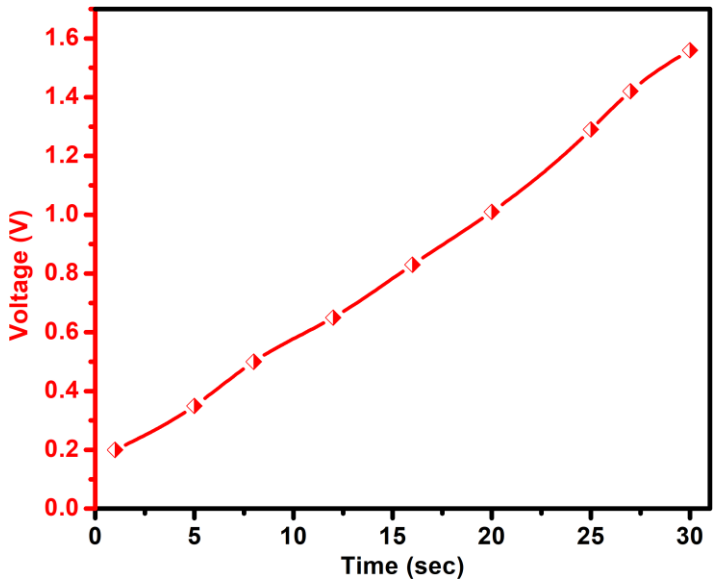

Figure A27: Stored voltages in a 100 µF capacitor by employing the 15 wt % **2**-TPU composite device at different time intervals. The solid curves tracing the points are guide to the eye.

Energy conversion efficiency calculation

Energy harvesting efficiency is the ratio between power consumed on external load resistance and input mechanical power and has been calculated by adopting the procedure outlined below.[5]

Electrical energy, $E_e = \frac{V^2}{R}\Delta t$ .....(1)

Mechanical energy, $E_m = \int_0^t F\, d(t)dt$ .....(2)

Where, V is the applied voltage, R is the applied load resistance, F is the applied force, d is the distance travelled during application of force and t is the generation time.

Energy conversion efficiency, $E_{\%} = \frac{Ee}{E_m} \times 100$ .....(3)

In our case, V, R, F, d and t are 19 V, 4.7 MΩ, 14.15 N, 2 mm and 0.11 s, respectively.

Substituting all these values in the above equation (3) , the energy conversion efficiency ($E_{\%}$) is calculated to be 0.27 %.

End of Thesis